Ion Transport and Solvation in Next Generation Battery Electrolytes: Molecular Simulation Studies

A Thesis

Submitted For the Degree of

DOCTOR OF PHILOSOPHY

in the Faculty of Science

by

Srimayee Mukherji

CHEMISTRY AND PHYSICS OF MATERIALS UNIT
JAWAHARLAL NEHRU CENTRE FOR ADVANCED SCIENTIFIC RESEARCH
Bangalore – 560 064, India

FEBRUARY 2023

To my parents and my grandmother

DECLARATION

I hereby declare that the matter embodied in the thesis entitled "**Ion Transport and Solvation in Next Generation Battery Electrolytes: Molecular Simulation Studies**" is the result of investigations carried out by me at the Chemistry and Physics of Materials Unit, Jawaharlal Nehru Centre for Advanced Scientific Research, Bangalore, India under the supervision of Prof. S. Balasubramanian and that it has not been submitted elsewhere for the award of any degree or diploma.

In keeping with the general practice in reporting scientific observations, due acknowledgement has been made whenever the work described is based on the findings of other investigators. Any omission that might have occurred by oversight or error of judgement is regretted.

Srimayee Mukherji

CERTIFICATE

I hereby certify that the matter embodied in this thesis entitled "**Ion Transport and Solvation in Next Generation Battery Electrolytes: Molecular Simulation Studies**" has been carried out by Mr. Srimayee Mukherji at the Chemistry and Physics of Materials Unit, Jawaharlal Nehru Centre for Advanced Scientific Research, Bangalore, India under my supervision and that it has not been submitted elsewhere for the award of any degree or diploma.

Prof. S. Balasubramanian
(Research Supervisor)

Acknowledgements

I thank JNCASR for providing the research facilities, student fellowship, and the right environment to conduct my research.

I am immensely grateful to my supervisor, Prof. Balasubramanian, for giving me the opportunity to conduct research in his group. I am extremely thankful for the excellent guidance, patience, support, and mentoring, that I have received from him. I thank him for the most insightful and useful courses in Physical Chemistry, and FORTRAN Programming, that he taught me. He has provided all of us excellent computational facilities in his laboratory. I have been most fortunate to be his student.

I thank Prof. Premkumar Senguttuvan and Prof. Chandrabhas Narayana for teaching me about experiments through our collaborations. I thank my fellow student collaborators Nikhil, Disha, Rahul Kumar, Bhaskar, Rishikesh, Vinita, and Anjana.

I thank past CPMU chairs, and present CPMU chair Prof. Sundaresan. I am grateful to Prof. Vidhyadhiraja, Prof. Chandrabhas Narayana, and Prof. Waghmare, for making the transition to Prof. Balasubramanian's lab smooth.

I thank Prof. Rajesh Ganapathy, under whom I conducted my Master's research work. I learnt much from him. I am thankful to Prof. Ajay Sood for the opportunity to work with him during my Master's research.

I especially thank Nikhil, Srinath, and Nimish, for teaching me much during my first year in Prof. Balasubramanian's lab. I thank Disha for helping me in conducting the work in Chapter 5 of my thesis.

I thank all the Professors for the courses that they have taught me at JNCASR.

I thank my colleagues at the JNCASR computational facility - Anoop, Suresh, and Raghul. Special thanks to Basavaraju for all the help provided.

I thank all the JNCASR academic, administrative, and hostel staff, for their services and help.

I am grateful to all current members of the lab - Srinath, Nikhil, Nimish, Sudarshan, Anjali, Megha, Disha, Oishika, and Shivanand, and past members - Dr. Divya, Dr. Sudip, Dr. Abhishek, and Rahul Kumar, for their help and fellowship.

I remember and thank all my teachers from school and college.

I am grateful for the love that I receive from my friends - Shayan, Meghana, Nikita, Dibyashree di, Pragya, Raagya, Manodeep, Divya Chalapathi, Divya G, Nalina, Pavitra, Anirudh, Anaranya, Shikha, Ekashmi, Sagar, Sanchit, and many more. I am especially indebted and very grateful to Shayan for help in putting together this thesis document. I am also thankful to Pavitra and Sagar for their help. I am very thankful to Santanu for his immense support during the period over which the work for this thesis was done.

I thank my parents, and my grandmother for their unswerving love, support, and encouragement.

I acknowledge the Param Yukti facility under the National Supercomputing Mission at Jawaharlal Nehru Centre For Advanced Scientific Research for the computational resources. I thank the CCMS Supercomputing facility.

I particularly acknowledge the developers of GROMACS, VMD, PLUMED, CP2K, and PACKMOL softwares.

Preface

Environmental and geopolitical compulsions have led to a large increase in interest in non-fossil fuel sources of energy over the past few decades. Central to all these alternative energy sources is the necessity to store the generated power for later use and distribution. This happens primarily through energy storage devices such as batteries. Improvement in battery technology has therefore been a major aim of modern industrial and scientific research. Of the three main components of a battery- the cathode, the anode, and the electrolyte, research hitherto has focused primarily on improvement of cathode technology. The work in this thesis is concerned with understanding the liquid structure and transport phenomena in battery electrolytes possibly leading to improvement of the electrolyte technology. A good liquid electrolyte must have several properties: high ionic conductivity, good chemical and thermal stability, large electrochemical window, and non-flammability. The most common lithium-ion battery electrolyte today is the 1M lithium hexafluorophosphate ($LiPF_6$) salt in a mixture of organic carbonate solvents, which is a low concentration electrolyte (LCE) designed to maximise electrical conductivity and electrochemical performance. However, the low salt concentration makes many carbonate solvent based LCEs particularly flammable due to the large number of free solvent molecules. LCEs also suffer from parasitic reactions at the electrodes. In contrast, high concentration electrolytes (HCEs) generally have a high salt concentration of 3-5 M in the electrolyte, and are non-flammable and hence safe for operation. HCEs have large electrochemical window, large voltage and high energy density, and anion-derived stable solid electrolyte interphase that reduces parasitic reactions at electrodes. These advantages of HCEs find their roots primarily in the drastic reduction in the number of free-solvent molecules from LCEs. However, because of their high salt concentration, the cost of HCE batteries is relatively high, and their electrolytes have large shear viscosity and hence low ionic conductivity. This has prevented the widespread adoption of HCEs in industry. In order to conquer these shortcomings of HCEs, it is important to recognise that the structure of HCEs and transport phenomena in HCEs are different from those in LCEs. Therefore, a detailed study into the structure and transport properties and phenomena of HCEs needs to be carried out. Molecular level understanding and statistically reliable explanations are often best obtained from

computational investigations.

This thesis presents computational studies of battery solvents and electrolytes with special emphasis to HCEs. Transport properties and mechanisms of these electrolytes are investigated and rationalised based on insights gleaned from the liquid structure. Computational methods employed are classical force-field based molecular dynamics (MD) simulations, density functional theory (DFT) based ab initio molecular dynamics (AIMD) simulations, and quantum chemical cluster calculations. Results from the simulations are compared against experimental data wherever available. For example, in this thesis, the trajectories of classical MD and *ab initio* (AIMD) simulations are used to find radial distribution functions, from which the structure of solvation shells of alkali ions are inferred. The population of different types of alkali-ion solvation shells are also estimated from the trajectories. Through Green-Kubo relations, several transport properties such as shear viscosity, ionic conductivity, and diffusion coefficients are estimated. Also, time correlation functions such as the spatio-temporal van Hove correlation function indicate the emergence of non-diffusive transport phenomena (for example, hopping). Steered molecular dynamics and Umbrella sampling methods are used to calculate energy barriers to hopping. This thesis employs these techniques, and goes back and forth between structure and transport of electrolytes based on their interdependence. Electrolytes that use the organic solvent sulfolane are studied, as also electrolytes that use a mixture of an organic and an aqueous solvent that has potential to be useful in rechargeable aqueous zinc ion batteries.

The interdependent study of structure and transport in this thesis is now outlined briefly in terms of its chapters. **Chapter 2** presents a refinement of the force field to capture the structure and transport through accurate estimation of physicochemical properties of liquid sulfolane, a promising battery solvent. **Chapter 3** employs the force field developed in Chapter 2 to find evidence for Li-ion hopping in HCEs and to characterise hop events and hop energy barriers. **Chapter 4** contains three sub-chapters. **Chapter 4A** provides a description of the methods used for the force-field refinement of the bis(fluorosulfonyl)imide anion. Employing the force field for the anion presented in Chapter 4A, **Chapter 4B** reports the liquid state structure and transport in Na-ion and Li-ion based HCEs. **Chapter 4C** studies mixed alkali-ion electrolytes for theoretical interest and as a means to improve the transport properties of pure Na-ion HCEs. **Chapter 5** confirms the presence of cation pair complexes in Li and Na-based HCEs through AIMD simulations. AIMD simulations, quantum chemical geometry optimization, and frequency calculations are employed to understand the stability of these clusters. In a work carried out in collaboration with experimentalists, **Chapter 6** describes how the addition of propylene carbonate (PC) as a cosolvent to water remedies challenges faced at both electrodes in rechargeable aqueous zinc ion batteries.

Contents

List of Figures

List of Tables

Chapter 1

Introduction

1.1 Battery solvents and Battery electrolytes

In a world of increasing energy demands, the need for progressively better energy storage systems (ESS) is important [1–5]. Batteries are crucial ESS without which meeting the energy demands of today's world in a regulated fashion is not possible [6–11]. The need for safer batteries and those that cater to higher energy densities is growing [12–18].

Up to this point, the majority of the effort in boosting the performance of batteries has come from improvements in the cathode technology [19]. However, other components of the battery such as the anode and the electrolyte can also be engineered for improved battery characteristics. As an illustrative example of a battery system of the present generation, a Li-ion battery is shown in Figure 1.1.

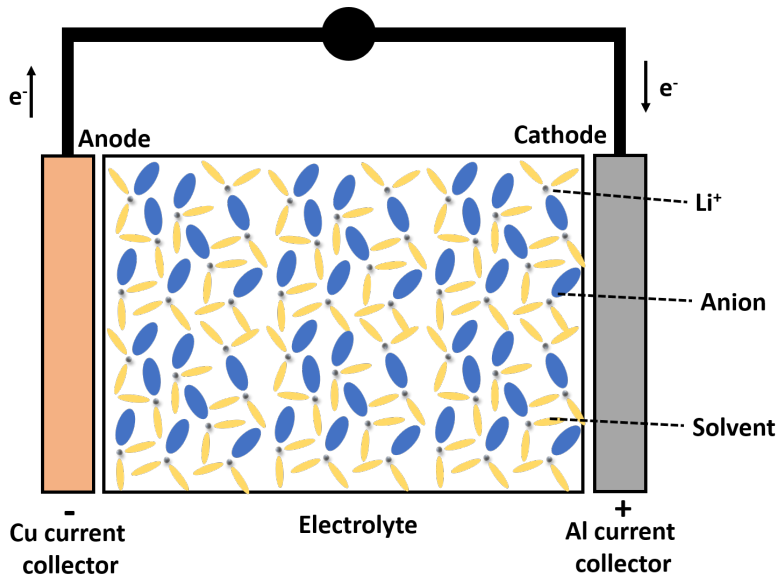

Figure 1.1: Components of a Li-ion battery.

An electrolyte is a medium between the two electrodes that serves the purpose of charge conduction through ion transport. Apart from being a good medium for transport of ions, the electrolyte must be such that it remains stable under the reductive and oxidative influences of the electrodes [20].

There is a need for batteries with higher rate, higher energy density, longer calendar life, lesser dendritic growth [21], and lesser parasitic reactions at electrodes. There is also a need for electrolytes with larger ionic conductivity and more safety (i.e. less flammability). Motivated by these needs, in recent times, research in engineering electrolytes for superior batteries has also begun to pick up pace [19].

A battery electrolyte is typically composed of a salt dissolved in solvent. Depending on the composition of the electrolyte or the type of solvent, battery electrolytes can be of many types, such as organic, aqueous, solid state, polymer gel, ionic liquid and deep eutectic electrolytes to name a few. The best marketable technology for battery electrolytes has for very long been 1 M lithium hexafluorophosphate ($LiPF_6$) salt in a mixture of organic carbonate solvents, for example, ethylene carbonate (EC) mixed with linear carbonate esters such as dimethyl carbonate (DMC) [12].

This thesis primarily investigates electrolytes based on a promising polar aprotic organic solvent, viz., sulfolane. Chapter 6 of the thesis investigates a mixture of organic and aqueous solvent-based electrolytes for rechargeable aqueous zinc batteries.

1.2 Need for high concentration electrolytes (HCEs)

Battery electrolytes employed today use approximately 1 M concentration of salt dissolved in the electrolyte. These are prototypical low concentration electrolytes (LCEs). The 1 M concentration is chosen primarily for maximizing the ionic conductivity of the electrolyte. Although this technology has been in place for over two decades, it has severe shortcomings. Battery solvents are very often carbonate solvents which are flammable. Safety is therefore a major concern with batteries based on low concentration electrolytes. Further, batteries based on low concentration electrolytes also have a narrow electrochemical window (4.4 V) which make them unsuitable for any high voltage or high energy-density applications. However, looking at power demands today, the future in batteries lies in offering high-voltage applicability.

High concentration electrolytes (HCEs) are a very promising alternative to conventional electrolytes. HCEs usually have a salt concentration of 3-5 M [12, 22], although in some cases may even exceed 5 M [12, 23]. Similar to LCEs, depending on the solvent type, HCEs can have organic solvent [24–26, 26–28], ionic liquids (IL) solvent [29–31], and

aqueous (water-in-salt [32–34]) solvent-based electrolytes. Some advantages of HCEs are depicted in Figure 1.2. To state these explicitly [12, 20]:

(i) HCEs have a high reductive and oxidative stability [26, 28, 35–45].

(ii) HCEs have significantly lowered flammability and volatility, and enhanced thermal stability. Therefore batteries based on HCEs are safer [46].

(iii) HCE batteries offer high rate [26–28, 47].

(iv) HCE batteries that have a large carrier density [12].

(v) HCE batteries have longer cycling life [25, 40].

(vi) HCEs prevent several parasitic side-reactions at the electrodes [12].

(vii) HCEs prevent dendritic growth on the anode [39].

(viii) HCEs allow formation of an anion-derived ion-conducting and electron insulating solid electrolyte interphase (SEI) on the anode instead of a solvent-derived SEI.

However, HCEs have some disadvantages as well which are still preventing their large-scale applicability [20]:

(i) HCEs contain a large amount of salt. Very often, this makes the electrolyte very viscous and results in a low ionic conductivity [26].

(ii) Due to the large viscosity of HCEs, the wetting time of the electrolyte on the separator and the electrodes is very large [12].

(iii) Due to the scarcity of lithium in the Earth's crust, and due to the use of a large amount of salt in HCEs, the cost of such batteries is relatively high.

In order to overcome the challenges faced by HCEs, it is important to first understand the liquid structure and transport phenomena in HCEs against those in LCEs. The next sections of this chapter are dedicated to what is known in literature of HCEs hitherto.

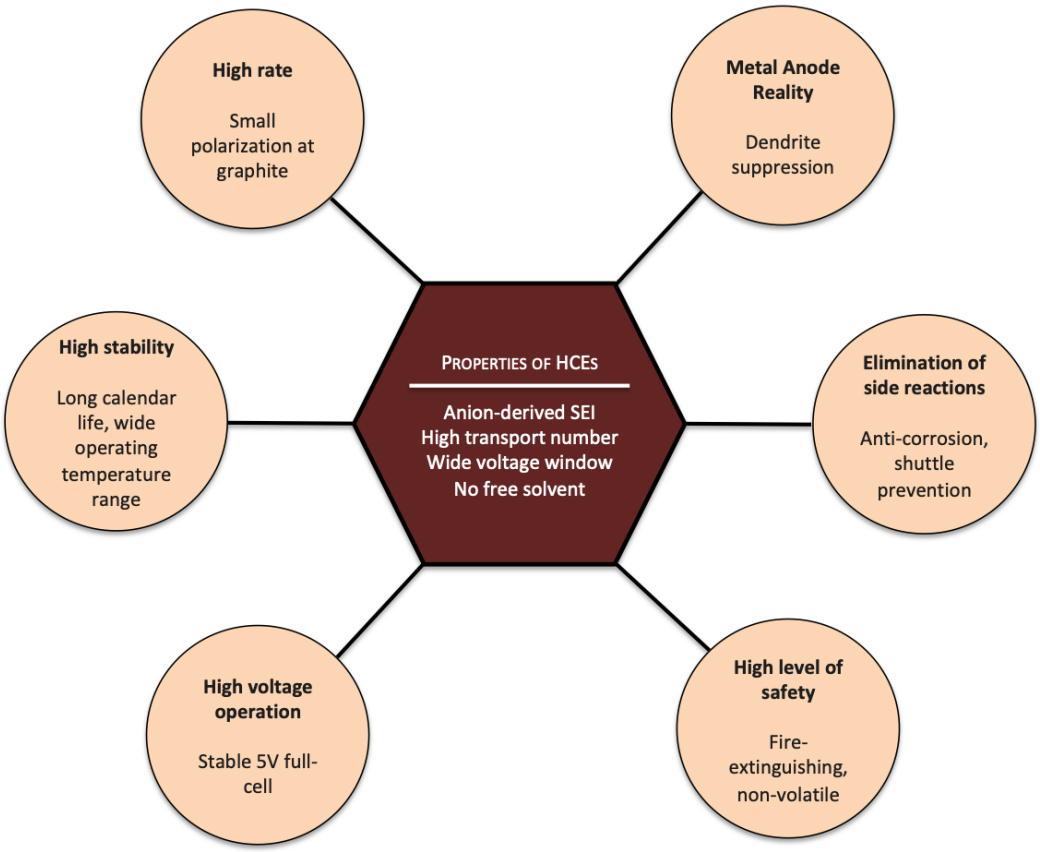

Figure 1.2: Advantages of using HCEs. Adapted from Ref. 12.

1.3 Brief overview of what is known about the structure and transport of HCEs

1.3.1 Intermolecular structure of HCEs as opposed to that of LCEs

Aprotic solvents are Lewis bases and primarily interact with cations (Lewis acids) by solvating them closely. Anions are also Lewis bases and compete with solvent molecules to interact with cations. In protic solvents, such as water, the solvent molecules closely interact with both cations and anions. However, a competition between solvent molecules and anions to solvate cations continues to be operational.

At low salt concentrations, cations are solvated primarily by solvent molecules. This is

due to the sheer number dominance of solvent molecules over anions at low salt concentrations [20]. In LCEs, cations and anions are separated by solvent molecules. Such pairs of cation and anions are then called solvent separated ion pairs (SSIPs) (Figure 1.3, left). The cation and anion of a SSIP are not typically interacting with each other [48–53].

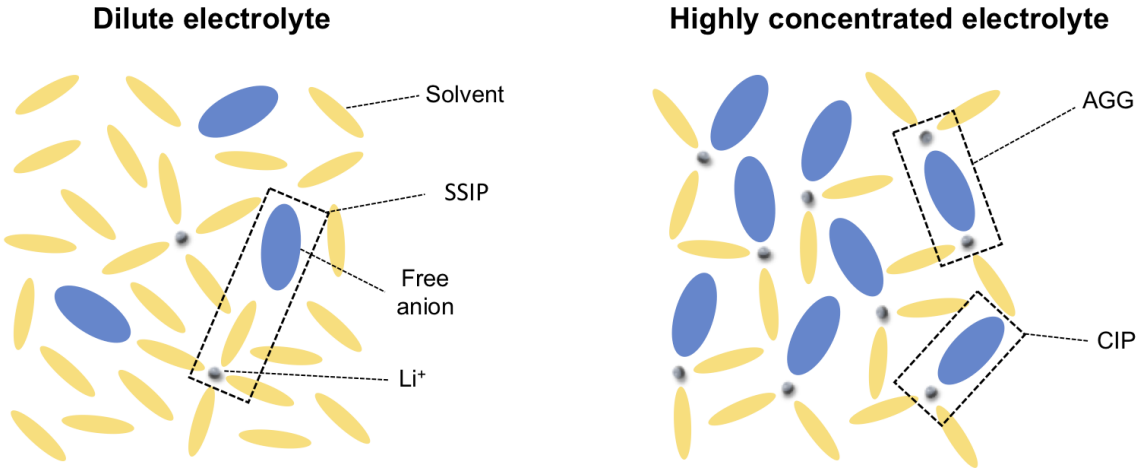

Figure 1.3: Left: Typical liquid structure of a low concentration electrolyte with solvent separated ion-pairs (SSIPs). Right: Typical liquid structure of a high concentration electrolyte with contact-ion pairs (CIPs) [54, 55] and aggregates (AGGs) [56, 57]. Adapted from Ref. 26.

At high salt concentrations, due to the anions being present in the electrolyte in large numbers, solvent molecules and anions compete strongly with each other to interact with cations. The more strongly the salt dissociates in the solvent, more the competition (between solvent molecules and anions) is won by solvent molecules, and therefore fewer the free solvent molecules in the electrolyte. Yet, in HCEs, due to the larger number of anions in the electrolyte, cation-anion contact pairs (CIP) are also found. CIPs in turn can extend in space to form aggregates (AGGs, also known as agglomerates) (Figure 1.3, right).

Given this structural information of HCEs and LCEs, the following is noted: In LCEs, since the number of salt formula units is much smaller than the number of solvent molecules, a large number of solvent molecules are free as opposed to the situation in HCEs.

The implications of this are the following:

(i) Advances and issues in developing salt-concentrated battery electrolytes

(ii) Cations being primarily solvated by solvent molecules implies the formation of a solvent derived SEI, which is very often unstable, electrode passivating, and which allows for dendritic growth.

(iii) A large number of free solvent molecules leads to several parasitic reactions at the electrodes.

Structurally, why HCEs do not suffer from the aforementioned issues by the merit of having fewer free solvent molecules is therefore clear.

1.3.2 Transport in HCEs as opposed to that in LCEs

In LCEs, the viscosity of the electrolyte is low and therefore ions and molecules are able to diffuse with ease. During the diffusion of metal ions, they drag their nearest solvation shell neighbours along with themselves. This mode of transport is called vehicular or diffusive mode of transport [58] (Figure 1.4(a)).

When the viscosity of liquid state electrolyte is excessively high, and in solid state electrolytes as well, the ions and molecules are too trapped for effective diffusion across the bulk of the electrolyte. In such a scenario, small and light metal ions can hop out of their solvation shell cages [58]; in contrast to vehicular diffusion in LCEs, the metal ions do not drag along their solvation shell cages (Figure 1.4(b)); rather, they exchange one or more ligands in the process of hopping.

In most liquid HCEs, the viscosity is moderately high and a combination of vehicular and structural modes of diffusion/transport is operational [58–62]. As viscosity increases in going from LCEs to HCEs, and with the increase in caging of alkali ions, hopping becomes an increasingly prominent mode of transport. Hopping occurs over and above a slow diffusion of the cages of alkali-ions [58] (Figure 1.4(c)).

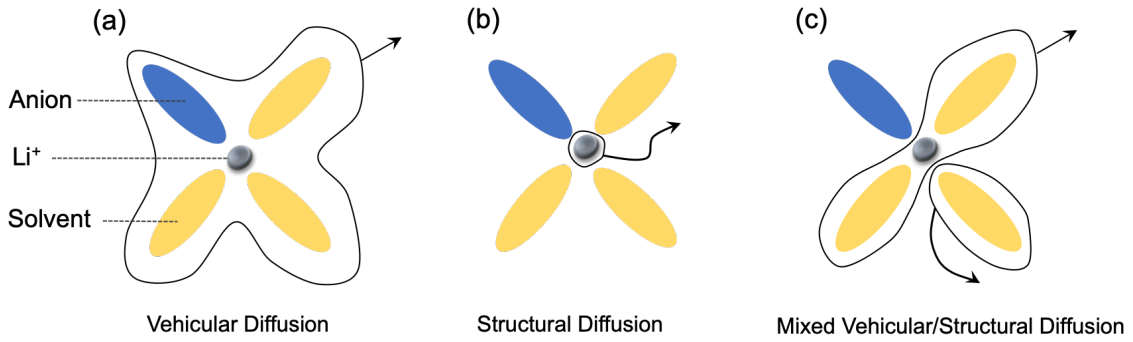

Figure 1.4: Various modes of ionic transport in electrolytes: (a) Vehicular diffusion, (b) Structural mode of transport, and (c) a mix of structural and vehicular modes of transport. Adapted from Ref. 58.

Looking further into structural diffusion or hopping, it has been proposed that hopping would typically involve one or more ligands (nearest solvation shell members to the alkali-ion) to be exchanged [63].

Some structural features may be conducive to the long distance transport through hopping. The following section discusses this briefly through two examples.

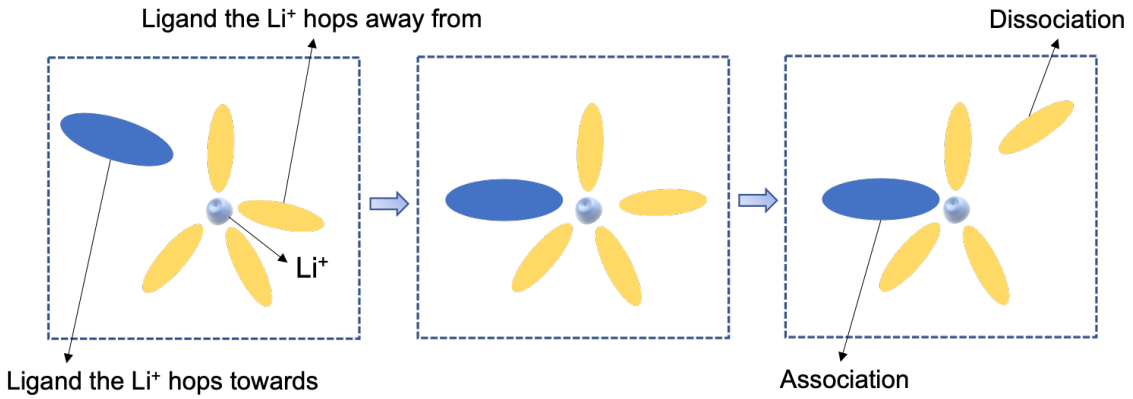

Figure 1.5: Ligand exchange involved in hopping. Adapted from Ref. 63.

1.3.3 Structural features helpful towards long-distance percolation of metal ions in HCEs

In archetypical HCEs, Na-ions which are within 5 Å of each other connect to form network structures which comprise extended AGG structures [64]. It is speculated that such networks may aid Na-ion (or alkali-ion) transport in general in HCEs.

In water-in-salt electrolytes (HCEs where water is the solvent), water is seen to be distributed non-homogeneously in the form of channels. Li-ions are seen to transport faster through these percolating channels [65, 66].

Given this background, this thesis contains further investigations into the liquid structure and transport of HCEs. The structure and transport of water based LCEs is also investigated. To this end, the computational techniques used are discussed in the next sections.

1.4 Computational techniques used to investigate electrolytes in this thesis

1.4.1 Classical Molecular Dynamics (MD) simulations

Molecular Dynamics (MD) simulations are one of two important classical mechanics methods for molecular simulations [67–76], the other being Monte Carlo (MC) simulations. MD simulations today are well suited for studying a wide variety of systems such as biological systems [77–80], systems that self-assemble [81, 82], metal organic frameworks [83, 84],

crystals [85–89], and complex liquids such as ionic liquids [90, 91], deep eutectic solvents [91–94], mixtures [95, 96], glasses [97–99], and many more. The first pioneering MD simulations were those conducted by Alder and Wainwright [100, 101] for a system of hard spheres, and then by Rahman for a system of Lennard-Jones particles [102, 103]. MD simulations have come a long way since these landmark simulations in terms of the system complexity, the system size, the simulation time, the realism of the force field, the quality of thermostats and barostats, etc., and thus provide quantitative predictions and inferences that are nearly accurate, today.

Based on specified inter-atomic interaction parameters leading to the calculation of force on every atom, classical MD simulations finally yield the position and velocity of atoms at every timestep. Force on an atom can be obtained through the gradient of potential energy (Equation 1.1).

$$\mathbf{F_i} = -\nabla_i U \tag{1.1}$$

From Newton's laws of motion it is known that:

$$\mathbf{F_i} = m_i \frac{d^2\mathbf{r_i}}{dt^2} \tag{1.2}$$

Combining Equations 1.1 and 1.2, we get:

$$m_i \frac{d^2\mathbf{r_i}}{dt^2} = -\nabla_i U \tag{1.3}$$

Newton's equation of motion (Equation 1.3) is solved to obtain velocities and positions from forces. This describes how the trajectory for an NVE (microcanonical) ensemble is obtained. When the coupling thermostat and barostat (depending on the ensemble) degrees of freedom are also considered, trajectories in NVT and NPT ensembles can also be generated.

With the initial configuration, initial momenta of all atoms, and all inter-atomic interaction parameters, evolving the system of atoms in time is a cyclic process (Figure 1.6).

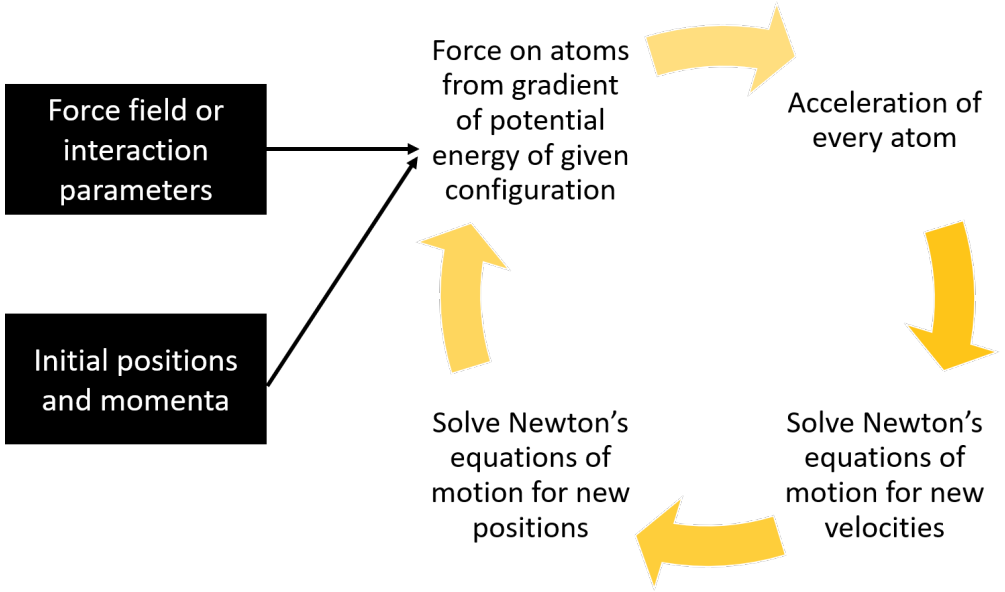

Figure 1.6: The cyclic process involved in generating a MD trajectory.

In this thesis, classical MD has been used to study battery solvents and electrolytes in detail. Using MD simulations, one can study sufficiently large system sizes for sufficiently long periods of time, which are particularly well suited for the study of liquids, especially for their structure, dynamics, and bulk properties. The properties predicted from MD simulations are very often in good agreement with experiments for a good force field model. A parallel between the procedures followed in experiments and in simulations is shown in Figure 1.7.

The simulations package used to this end is GROMACS [104–106]. These simulations are based on classical mechanics, with electrons in the ground state, pair-additive force fields, truncated long-range interactions, and periodic boundary conditions.

The three important ingredients required for an MD simulation are:

(i) force field parameters for inter-atomic interaction,

(ii) initial atomic positions and momenta, and

(iii) thermostat and barostat.

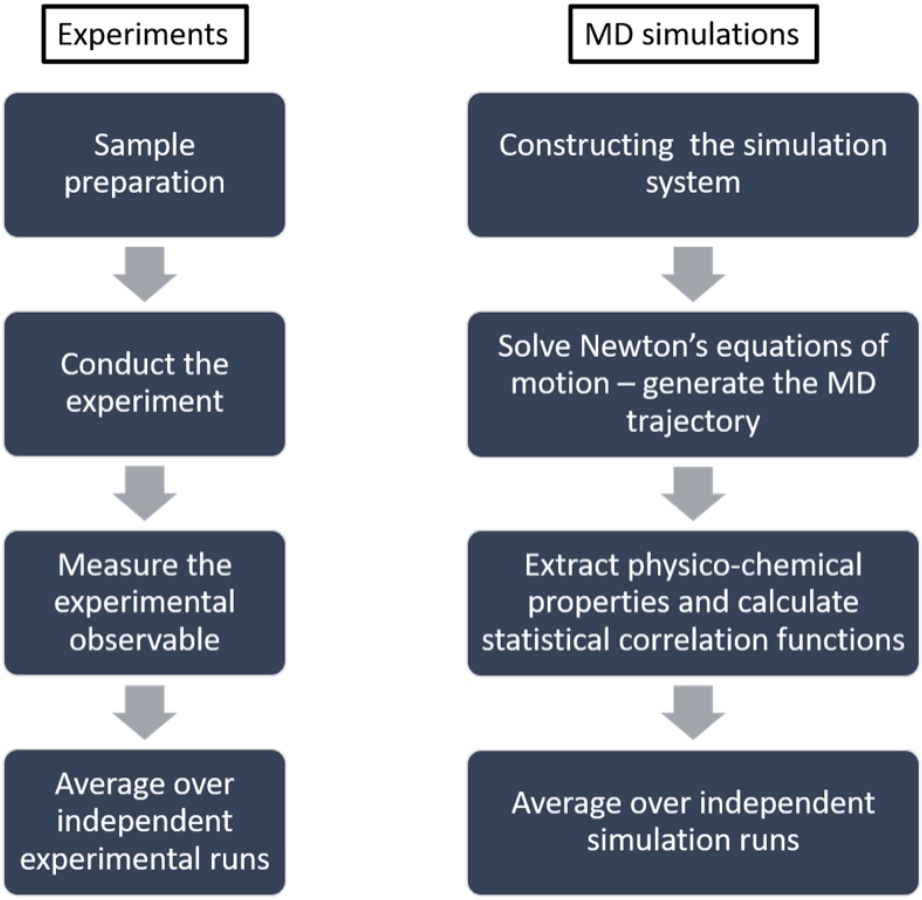

Figure 1.7: Parallel procedures of experiments and MD simulations.

Initial atomic positions and momenta

A configuration containing all the required molecules is generally created through a random packing of molecules and ions with a tolerance (minimum distance) criterion on the distance between any two atoms. One such software for random packing is PACKMOL [107]. This software has been used throughout this thesis.

This packed configuration is energy minimized within the force-field framework. This energy minimized configuration is used as the initial atomic configuration (positions) for the MD simulation (Figure 1.6).

The initial momenta follow the Maxwell-Boltzmann distribution of velocities.

Interatomic potentials and force fields

The total potential energy of the system is of the form:

$$U = \sum_{\text{bonds}} \frac{1}{2} k_r (r_{ij} - r_0)^2 + \sum_{angles} \frac{1}{2} k_\theta (\theta_{ijk} - \theta_0)^2 + \sum_{\text{torsions}} \sum_{n} k_{\phi,n} [1 + cos(n\phi_{ijkl} - \phi_s)] + \sum_{\text{non-bonded pairs}} \left[\frac{q_i q_j}{4\pi\epsilon_0 r_{ij}} + 4\epsilon_{ij} \left(\frac{\sigma_{ij}}{r_{ij}^{12}} - \frac{\sigma_{ij}}{r_{ij}^{6}} \right) \right] \tag{1.4}$$

The first three terms correspond to intramolecular potential energies, i.e. bonded energy terms. The bonded energy terms of Equation 1.4 are bond, bond angle, and dihedral deformation terms, respectively. r_0 and θ_0 are the equilibrium bond length and bond angle values. k_r, k_θ, and k_ϕ are the bond, bond angle, and the dihedral angle deformation constants. n and ϕ_s are the multiplicity and phase respectively. The ultimate and penultimate terms of Equation 1.4 are the non-bonded energy terms, viz. the Coulombic electrostatic energy and the van der Waals energy (represented as Lennard-Jones energy) terms, respectively. q_i is the partial charge on atom i. r_{ij} is the distance between atoms i and j, σ_{ij} is the interatomic distance at which the Lennard-Jones potential energy is zero. ϵ_{ij} marks the minimum in the Lennard-Jones energy. σ_{ij} and ϵ_{ij} are calculated using combination rules such as the Lorentz-Berthelot rules [108, 109], defined as

$$\sigma_{ij} = \frac{\sigma_{ii} + \sigma_{jj}}{2} \tag{1.5}$$

and

$$\epsilon_{ij} = \sqrt{\epsilon_{ii}\epsilon_{jj}} \tag{1.6}$$

where r_0, θ_0, q_i, q_j, ϵ, σ, $k_{\phi,s}$, ϕ_s, and the combination rules comprise the force-field parameters for an MD simulation. These parameters can be refined to arrive at a good force field model for a compound.

Molecular force field models for MD simulations need to be validated empirically for their accuracy, and used with caution while predicting structural and dynamic properties. For this reason, starting from a generic force field, refinement to the force field parameters is often necessary to make reliable predictions and make accurate inferences about the system of interest. Force fields for ionic liquids have been developed and/or refined earlier [110–112]. These liquids can also serve as battery solvents [64, 113–115]. In this thesis, Chapter 2 is based on obtaining a more realistic force field for an organic solvent, sulfolane.

The force fields used in this thesis are either:

(i) refined from those existing in literature based on the Optimized Potentials for Liquid

Simulations (OPLS) [116–118] force-field or Mondal-Balasubramanian (MB) [111] force-fields, or

(ii) General Amber force field (GAFF) [119], or

(iii) TIP 3P for water [120].

Nuclei have a cloud of electron density surrounding them. For classical MD, atoms are assigned net atomic charges (NAC) for electrostatic interactions. This implies that the electron density around nuclei needs to be partitioned and assigned to the different atoms as their NAC.

There exist several atomic population analysis methods which result in slightly different atomic site charges. Density derived electrostatic and chemical charge (DDEC6) method was proposed as the default method for quantum programs over some other methods for the following reasons:

(i) Mulliken [121] and Davidson-Løwdin [122] methods: these have no mathematical limits as the basis set is systematically refined towards completeness. The Mulliken charge method is extremely sensitive to the basis set being used.

(ii) Bader's quantum chemical topology method: this method can result in non-nuclear attractors which lead to undefined NACs [123].

(iii) Electrostatic potential fitting techniques (ESP [124], Chelp [125], Chelpg [126], REPEAT [127]): these methods lack fair conformational transferability, and assign unrealistic charge values to certain buried atoms. RESP is an improvement over these charge methods but often leads to various plausible charge values [128]. This method has been employed in Chapter 6 of this thesis along with GAFF.

(iv) Original Hirshfeld method [129–132]: typically, this method underestimates NAC values.

(v) The Natural Population Analysis (NPA) [133]: this method involves the generation of localized orbitals. Plane-wave basis functions are a challenge towards their application.

Density derived electrostatic and chemical (DDEC) charges

The work presented in this thesis extensively uses/derives the density derived electrostatic and chemical (DDEC) [134] charges, and hence this charge technique has been briefly

discussed here. As opposed to the aforementioned atomic population analysis method, the DDEC [129, 134–137] charge method meets some performance goals in assigning NACs:

(i) one assigned electron distribution for each atom,

(ii) core electrons assigned only to the host atom,

(iii) atomic site charges are functionals of the total electron density distribution,

(iv) the electron distribution assigned gives an efficiently converging multipole expansion,

(v) atomic site charges typically follow Pauling scale electronegativity trends,

(vi) transferrability of atomic site charges across conformations,

(vii) fast and robust convergence towards a unique solution, and

(viii) linear scaling in computational cost with system size.

This thesis uses the following atomic site charges:

(i) density derived electrostatic and chemical charges (DDEC6),

(ii) charges from Ref. [24] (OPLS-AA based force), and

(iii) restrained electrostatic potential (RESP) charges [138] with GAFF [119] (Chapter 6).

Temperature and pressure coupling

While NVE (N: microcannonical-constant number, V: volume, E: energy) ensembles may be easier to simulate, they do not correspond to the thermodynamic conditions employed in experiments. NPT (P: pressure, T: temperature) and NVT (V: volume) ensembles are more realistic. To maintain constant average temperature and pressure in the system, it needs to be coupled to a thermostat (for constant temperature) and barostat (for constant pressure). Several thermostats are used for NPT and NVT simulations in literature. Some examples are:

(i) Berendsen temperature coupling [139],

(ii) Velocity-rescaling temperature coupling [140],

(iii) Andersen thermostat [141], and

(iv) Nosé-Hoover temperature coupling [142, 143].

In this thesis, the Nosé-Hoover thermostat and the velocity-rescaling thermostat were used. Several barostats are used for NPT simulations in literature. Some examples are:

(i) Berendsen pressure coupling [139],

(ii) Parrinello-Rahman pressure coupling [144],

(iii) Surface-tension coupling, and

(iv) MTTK pressure control algorithms [145].

In this thesis, the Berendsen barostat for NPT equilibration and the Parrinello-Rahman barostat for NPT production were used.

1.4.2 *Ab-initio* Molecular Dynamics (AIMD) simulations

These simulations explicitly treat electronic structure on-the-fly during otherwise-classical MD simulations. Car-Parrinello dynamics (CPMD) is an example of AIMD [146]. AIMD simulations have been used to study metal-organic frameworks [83], ionic liquids [147, 148], organic liquids [149], supramolecular systems, and a variety of other systems. In AIMD, bulk conditions are obtained using periodic boundary conditions (PBC).

AIMD does not depend on empirical (force-field) parameters as does classical MD; rather, it depends on the accuracy of the quantum mechanical (QM) representation involved. QM techniques are used to solve the Kohn-Sham equation followed by Newton's equations of motion to obtain the trajectory of atoms. In some more detail, the AIMD procedure is as follows [72].

The standard Hamiltonian of the system for the electronic ($\mathbf{r_i}$) and nuclear ($\mathbf{R_I}$) degrees of freedom is given by [150]:

$$\begin{aligned}\hat{\mathbf{H}} &= -\sum_I \frac{\hbar^2}{2M_I}\nabla_I^2 - \sum_i \frac{\hbar^2}{2m_e}\nabla_i^2 + \sum_{i<j}\frac{e^2}{|\mathbf{r_i}-\mathbf{r_j}|} - \sum_{I,i}\frac{e^2 Z_I}{|\mathbf{R_I}-\mathbf{r_i}|} + \sum_{I<J}\frac{e^2 Z_I Z_J}{|\mathbf{R_I}-\mathbf{R_J}|} \\ &= -\sum_I \frac{\hbar^2}{2M_I}\nabla_I^2 - \sum_i \frac{\hbar^2}{2m_e}\nabla_i^2 + V_{n-e}(\mathbf{r_i}, \mathbf{R_I}) \\ &= -\sum_I \frac{\hbar^2}{2M_I}\nabla_I^2 + \hat{\mathbf{H}}_\mathbf{e}(\mathbf{r_i}, \mathbf{R_I}) \end{aligned} \tag{1.7}$$

where Z is the nuclear charge, i and j are different electrons, I and J are different nuclei, M_I and m_e are the masses, and $\mathbf{R_i}$ and $\mathbf{r_I}$ are the coordinates, of the nucleus and the electron, respectively. The terms in the first line of Equation 1.7 correspond to the kinetic energy of the nucleus, the kinetic energy of the electrons, the inter-electron repulsion energy,

the nucleus-electron attraction interaction energy, and the inter-nuclear repulsion potential energy, respectively.

A simplification, known as the Born-Oppenheimer (BO) approximation, assumes that the Hamiltonian and the wave function can be separated into a nuclear and an electronic part, i.e. $\hat{\mathbf{H}} = \hat{\mathbf{H}}_\mathbf{n} + \hat{\mathbf{H}}_\mathbf{e}$ and $\psi = \psi_n \psi_e$, where n and e represent nucleus and electrons, respectively. This simplification can be invoked by restricting the total electronic wave function ψ to the ground state wave function ψ_0 of $\hat{\mathbf{H}}_\mathbf{e}$ at each instant of time, which is obtained by solving the time-independent electronic Schrödinger equation

$$\hat{\mathbf{H}}_\mathbf{e}\psi_0 = E_0\psi_0 \tag{1.8}$$

where $E_0(\mathbf{R_I(t)})$ specifies the ground-state Born-Oppenheimer potential energy surface on which the nuclei move, and

$$\hat{\mathbf{H}}_\mathbf{e} = -\sum_i \frac{1}{2}\nabla_i^2 - \sum_{i,\alpha} \frac{Z_\alpha}{|\mathbf{r_i} - \mathbf{R}_\alpha|} + \sum_{i<j} \frac{1}{|\mathbf{r_i} - \mathbf{r_j}|} \tag{1.9}$$

Quantum mechanical methods such as Hartree-Fock (HF) [151] or DFT [152] are concerned with Equation 1.9. In the BO approximation, the nuclei move according to the classical Newtonian equations of motion:

$$M_I \ddot{R}_I(t) = -\nabla_I \min_{\psi_0}\{\langle\psi_0|\hat{\mathbf{H}}_\mathbf{e}|\psi_\mathbf{0}\rangle\} \tag{1.10}$$

This is the Born-Oppenheimer molecular dynamics (BOMD) method, which is the most common AIMD technique.

Despite the BO approximation separating the electronic and nuclear motions, the SCF calculation of every step is time consuming. The CPMD [146] type of AIMD simulation counters this drawback of BOMD. In this thesis, we have used the BOMD type of AIMD simulation, using the CP2K software [153].

1.4.3 Quantum chemical calculations for molecules and small clusters

Quantum chemical calculations are generally carried out for small systems by considering the electronic structure. Various quantum chemical techniques exist. In the post-Hartree-Fock (HF) approach, the energy of a system is obtained from the wave function, which is solved. In contrast, in the Density Functional Theory (DFT) [74, 76] approach, the energy of the system is obtained as a functional of the electron density that is determined. This thesis uses HF for geometry optimization with electrostatic potential calculation for

the purpose of determining density derived electrostatic and chemical (DDEC) charges. Møller–Plesset perturbation theory (MP) is a post-HF level of theory that adds electron correlation through Rayleigh–Schrödinger perturbation theory (RS-PT) [154] up to second order. In this thesis, the MP2 method [73] was used to obtain accurate ground state energies and molecular optimized geometries. For obtaining ground state energies, free energies, and optimized geometries for somewhat larger systems containing a cluster of molecules and ions, the DFT approach was employed.

DFT and post-HF scale as N^3 and N^4 with the number of electrons, N [76]. Hence, DFT is computationally less expensive for larger system sizes and hence often preferred. Inclusion of Grimme's dispersion corrections is often required for accurate predictions from DFT calculations [155]. In this thesis, small cluster calculations were geometry optimized using this technique with frequency calculations.

Gaussian software [156] and Gaussview viewing tool [157] were used for quantum calculations of molecules and small clusters.

1.5 Free energy techniques used in this thesis

1.5.1 Steered molecular dynamics (SMD)

SMD is a useful free-energy method employed in studying the free-energy profile in several scenarios/processes, for e.g., in pulling a ligand from the active site of a protein, or varying the distance between different ligands, or a group away from an interface or wall [158–161]. In the SMD technique, a force is applied to the system to take from state A to state B [162]. A suitable collective variable (CV) is chosen along which the system (or a part) is pulled at constant velocity or constant force. This technique has been applied to a wide variety of cases to extract potentials of mean force [163–170].

The SMD free energy technique is based on the Jarzynski equality [171–174] (Equation 1.11).

$$e^{-\beta \Delta F_{AB}} = \langle e^{-\beta W_{AB}} \rangle \tag{1.11}$$

ΔF is the free energy difference between initial and final states A and B, respectively. W_{AB} is the non-equilibrium work done to take the system from state A to state B. $\beta = \frac{1}{k_B T}$, where k_B is the Boltzmann constant, and T, temperature. Several independent trajectories are generated for the system going from state A to state B starting from different initial configurations. Calculating W_{AB} over all these trajectories, and taking an average of $e^{-\beta W_{AB}}$ over all independent runs, ΔF may be calculated.

In this thesis, SMD has been used to verify whether Li-ion hopping is activated or not by calculating the free energy barrier for Li-ion hopping in HCEs.

1.5.2 Umbrella sampling

The umbrella sampling method [175–177] involves dividing the reaction coordinate for the chosen CV into several windows. At each window, a harmonic potential is applied to constrain the system within the range of reaction coordinate assigned to that window. The constrained part of the system is allowed to sample various states staying within the umbrella. The remainder of the system relaxes to equilibrium around the umbrella. All the umbrella windows are merged through the weighted histogram analysis method (WHAM) [178–183]. WHAM gives us the desired free energy profile. In the present thesis, umbrella sampling was used to obtain the free-energy profiles for Li-ion hopping in crystal HCEs in Chapter 3.

1.5.3 Metadynamics

Metadynamics is an enhanced sampling technique which can be used to reconstruct the free energy surface [184–189] as a function of several CVs. This technique is particularly useful in accelerating the sampling of rare-events [86, 190]. Metadynamics samples rare events by filling the free energy basins with bias potentials. This free energy method is useful in the study of a wide variety of systems, especially biomolecular systems [191]. Metadynamics has also been used to arrive at the potential of mean force for a variety of systems including the study of the binding strength of ion-pairs in electrolytes [192].

In this thesis, metadynamics has not been used to reconstruct the free energy surface. Rather, it has been used for sampling/observing Li-ion hops in crystal HCEs. Crystal Li-ion hops would otherwise occur over timescales which are too computationally expensive to carry out.

1.6 Physico-chemical properties and transport properties

This thesis focuses on the interdependence of the liquid structure and transport and leverages it to understand the nature of electrolytes.

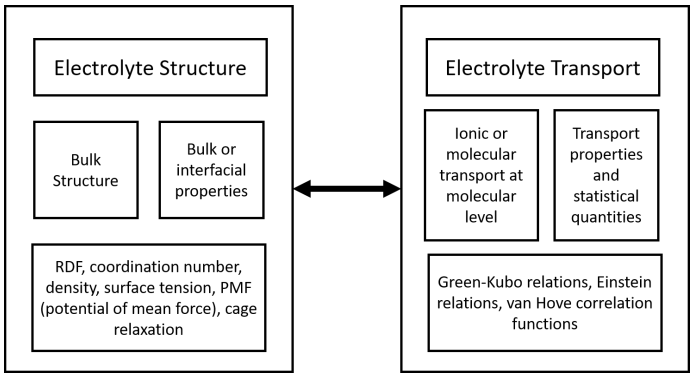

Figure 1.8: The structure-transport interdependence seen in this thesis.

1.6.1 Density

Mass density is defined as the mass per unit volume of a substance. In this thesis, the substance is either a battery solvent, e.g., sulfolane, or a battery electrolyte e.g., $LiBF_4$ in sulfolane. A commonly agreed upon acceptable upper limit on the error in density obtained from MD simulations with respect to experiments is 3% [193–196].

1.6.2 Heat of vapourization

An estimate of the strength of intermolecular interactions present in a liquid can be captured through the heat of vapourization [196].

Heat of vapourization (ΔH_{vap}) is defined as [197]:

$$\Delta H_{vap} = E_{gas} - E_{liq} + RT \tag{1.12}$$

E_{liq} is the average total energy per molecule in the liquid phase. E_{gas} is the average total energy per molecule in the gas phase. R is the gas constant and T is the temperature.

1.6.3 Surface tension

Surface tension is the energy required to increase the surface area of the liquid by unit area. Surface tension arises from an imbalance of intermolecular attractive forces that exist for molecules on the surface of a liquid relative to the molecules in the bulk [193].

Surface tension, γ, can be computed as [111]:

$$\gamma = \frac{l_z}{4}(2P_{zz} - P_{xx} - P_{yy}) \tag{1.13}$$

Here, P_{xx}, P_{yy}, and P_{zz} are the diagonal components of the pressure tensor. l_z is the length of the box along the direction in which there is a liquid-air interface.

1.6.4 Transport properties

Transport properties have been repeatedly calculated/estimated throughout this thesis. Time correlation functions are statistical quantities particularly useful to this end. A general time correlation function between two variables A and B can be defined as [198]:

$$C_{AB}(t) = \langle A(t_0)B(t_0+t)\rangle = \lim_{\tau\to\infty}\frac{1}{\tau}\int_0^\tau A(t_0)B(t_0+t)dt_0 \tag{1.14}$$

where the average is taken over all time origins and an ensemble average is considered. When $A = B$, the correlation function becomes an auto-correlation function, e.g., velocity auto-correlation function.

Time correlation functions provide a vivid idea of the dynamics operational in the system [199]. Further, the time integrals of these functions often yield experimentally measurable transport properties/coefficients, e.g., diffusion coefficient is the time integral of the velocity auto correlation function. Furthermore, the Fourier transforms of some of these functions lead to various experimental spectra. For example, the intensity corresponding to the elastic and coherent neutron scattering is proportional to the Fourier transform of the pair correlation function, $g(r)$. Therefore, time correlation functions serve as an important link between properties calculated from simulations and those obtained from experiments.

At equilibrium, the correlation function is invariant under translation of time origin t_0.

$$C_{AB}(t) = \langle A(t_0)B(t_0+t)\rangle = \langle A(t_0+s)B(t_0+s+t)\rangle \tag{1.15}$$

When $t = 0$, the dynamic correlation function reduces to a static correlation function, defined:

$$C_{AB}(0) = \langle A(t_0)B(t_0)\rangle = \lim_{\tau\to\infty}\frac{1}{\tau}\int_0^\tau A(t_0)B(t_0)dt_0 \tag{1.16}$$

Equation 1.16 forms the normalization factor for the dynamic correlation function.

The time correlation function can be used in its normalized form (Equation 1.17).

$$\hat{C}_{AB}(t) = \frac{\langle A(t_0)B(t_0+t)\rangle}{\langle A(t_0)B(t_0)\rangle} \tag{1.17}$$

Computationally, transport properties can be obtained from Green-Kubo relations [200, 201]. These are relations between correlation functions of microscopic quantities calculated at equilibrium and macroscopic coefficients [202, 203].

Linear response theory provides an understanding of these relations as response of the systems to weak perturbations. Linear response theory can be used to provide an interpretation of these formulae in terms of the response of the system to a weak perturbation [199].

Green–Kubo relations are infinite time integrals of equilibrium time correlation functions (Equation 1.18 [199]).

$$\gamma = \int_0^\infty dt \langle \dot{A}(t)\dot{A}(0)\rangle \tag{1.18}$$

Here γ is a transport coefficient. A is a dynamical variable whose time derivative is taken.

With every Green-Kubo relation there is an associated Einstein relation. An Einstein relation is another expression which can be used at large time intervals for calculation of transport properties [199, 204].

$$\langle (A(t) - A(0))^2 \rangle = 2t\gamma \tag{1.19}$$

as $t \to \infty$. Alternatively,

$$\gamma = \lim_{t\to\infty} \frac{d}{dt}\frac{1}{2}\langle (A(t) - A(0))^2 \rangle \tag{1.20}$$

Self-diffusion coefficient, shear viscosity, and ionic conductivity are the three transport properties calculated in this thesis either using the Green-Kubo or Einstein formulation [201, 205–207].

Self-diffusion coefficient

The mean squared displacement of particles $\langle |\Delta \mathbf{r}|^2 \rangle$ is proportional to a power β of the time interval, t (Equation 1.21).

$$\langle |\Delta \mathbf{r}|^2 \rangle \propto t^\beta \tag{1.21}$$

When $\beta = 1$, the dynamics of the system is said to be diffusive.

The Green-Kubo relation for self-diffusion coefficient in three dimensions is [199]:

$$D = \frac{1}{3}\int_0^\infty dt \langle \mathbf{v_i}(t) \cdot \mathbf{v_i}(0)\rangle \tag{1.22}$$

where $\mathbf{v_i}(t)$ is the velocity of each particle or centre of mass of each molecule.

The Einstein relation for self-diffusion coefficient is [199]:

$$D = \lim_{t\to\infty} \frac{d}{dt}\frac{1}{6}\langle|\mathbf{r_i}(t) - \mathbf{r_i}(0)|^2\rangle \tag{1.23}$$

where $\mathbf{r_i}$(t) is the position vector of the i^{th} particle/atom.

In this thesis, the Einstein relation for diffusion coefficient has been used.

Shear viscosity

Shear viscosity can be calculated through a variety of methods [208].

It can be computed from the Green-Kubo relation using [199, 201, 205]:

$$\eta = \frac{V}{k_B T}\int_0^\infty dt\langle P_{\alpha\beta}(t)P_{\alpha\beta}(0)\rangle \tag{1.24}$$

where $\alpha \neq \beta$ defines the off-diagonal elements of the pressure tensor. V is the volume of the system. T is temperature, and k_B is the Boltzmann constant.

In this thesis, we use the Green-Kubo relation for the calculation of shear viscosity.

Ionic conductivity

The Green-Kubo relation for the calculation of ionic conductivity, σ, is [209]:

$$\sigma = \frac{1}{V k_B T}\int_0^\infty \langle \mathbf{j(t)} \cdot \mathbf{j(0)}\rangle dt \tag{1.25}$$

Here, T and V are the temperature and the volume of the system, respectively. $j(t)$ is charge flux. It is defined as:

$$\mathbf{j(t)} = \sum_{i=1}^{n} z_i e \mathbf{v_i}(t) \tag{1.26}$$

v_i and $z_i e$ are velocity and charge on ion i, respectively. Ionic conductivity can also be calculated through the Einstein relation. The Einstein for the molar conductivity can be expressed as [210]:

$$\Lambda = \frac{N_0 e^2}{6 n k_B T}\lim_{t\to\infty}\frac{d}{dt}\sum_i\sum_j z_i z_j \langle[\mathbf{R_i}(t) - \mathbf{R_i}(0)] \cdot [\mathbf{R_j}(t) - \mathbf{R_j}(0)]\rangle \tag{1.27}$$

Here, N_0 is the Avagadro number, k_B is the Boltzmann constant, e is elementary charge, T, temperature, z_i is the charge on the cation or anion, $\mathbf{R_i}$(t) is the postion vector of the i^{th}

ion, and n, the number of (cation-anion) pairs.

Equation 1.27 takes into account correlations in displacement between self and non-self pairs of ions. Therefore the total molar conductivity takes all pairs of (cation-cation), (cation-anion), (anion-anion) pairs into account.

The Nernst-Einstein molar ionic conductivity takes only self correlations into account (Equation 1.28) [210]:

$$\Lambda_{NE} = \frac{N_0 e^2}{k_B T}(D_{anion} + D_{cation}) \tag{1.28}$$

Here, D_{cation} and D_{anion} are the diffusion coefficients of the cation and anion, respectively.

The ionic conductivity can be calculated from the molar conductivity as [211]:

$$\Lambda = \sigma / c \tag{1.29}$$

where c is the molar concentration of the electrolyte or the concentration of the salt in the electrolyte.

In this thesis, we use the Einstein relation for the calculation of ionic conductivity.

1.7 Overview of some useful statistical quantities

1.7.1 Radial distribution function

The radial distribution function, $g(r)$ is proportional to the probability of finding an atom in a shell dr located at a distance r from a reference position. $g(r)$ represents the distribution of target atomic species around a reference atomic species and tells us of the local ordering of the target atom type around the reference atom type [68].

The number of atoms found in a shell $dn(r)$ located between distances r and $r + dr$ is:

$$dn(r) = \frac{N}{V} g(r) 4\pi r^2 dr \tag{1.30}$$

N is the total number of target atoms, and V is the volume of the system.

The volume of the shell of thickness dr (Figure 1.9) can be approximated to:

$$V_{shell} = \frac{4}{3}\pi(r + dr)^3 - \frac{4}{3}\pi r^3 \approx 4\pi r^2 dr \tag{1.31}$$

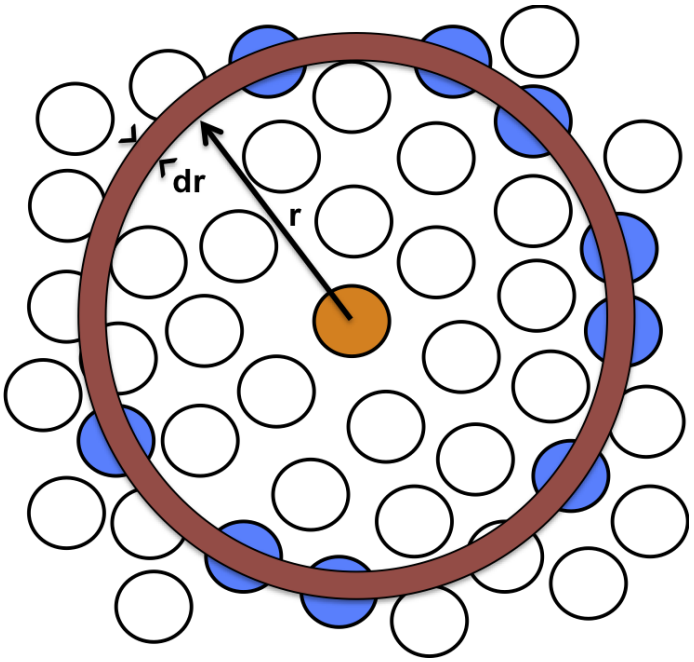

Figure 1.9: Looking at the space around the central particle in the form of shells of thickness dr. Adapted from Ref. 212.

When more than one chemical species is involved:

$$g_{AB}(r) = \frac{dn_{AB}(r)}{4\pi r^2 dr \rho_A} \tag{1.32}$$

where $\rho_A = \frac{N_A}{V} = \frac{Nc_A}{V}$. c_A is the concentration of the species A.

An example of $g(r)$ of oxygen of water (OW) (target) around the zinc ions (Zn^{2+}) (reference) in a rechargeable aqueous zinc ion battery electrolyte is shown in Figure 1.10.

The running integral of $g(r)$ (as defined in Equation 1.33), gives the running coordination number $n(r)$ or $cn(r)$. The running coordination number represents how many of the target atoms have been accounted for as a function of radial distance r from the reference atom.

$$n(r) = \int_0^r \rho_B g(r) 4\pi r^2 dr \tag{1.33}$$

Also,

$$\int_0^\infty \rho_A g(r) 4\pi r^2 dr = N_A \tag{1.34}$$

If reference and target atoms are of the same type, and N is the number of such atoms, then,

$$n(r) = \int_0^r \rho g(r) 4\pi r^2 dr \tag{1.35}$$

where, ρ is the density of the species being considered.

Also

$$\int_0^\infty \rho g(r) 4\pi r^2 dr = N - 1 \tag{1.36}$$

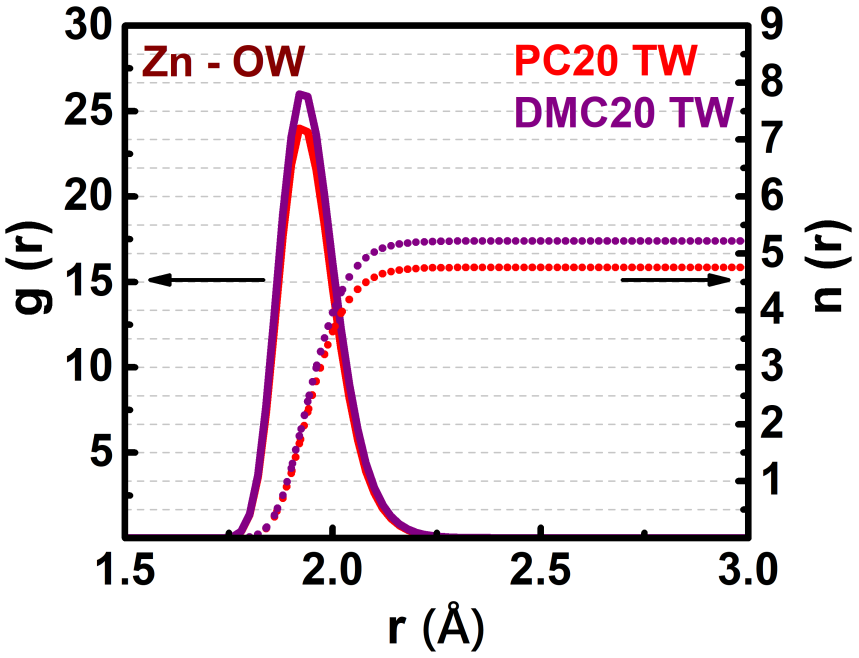

Figure 1.10: Radial distribution function $g(r)$ and coordination numbers $n(r)$ of Zn^{2+} (reference) and OW (target) pair for a $Zn(OTf)_2$ based aqueous electrolyte containing propylene carbonate (PC) and dimethyl carbonate (DMC) as cosolvent.

1.7.2 Non-Gaussian parameter

The non-Gaussian parameter is a measure of how much the dynamics of the particles is deviated from purely diffusive dynamics, i.e., a measure of the dynamic heterogeneity of transport in the system [91, 213–215]. While the time interval corresponding to the peak position represents the onset of diffusive dynamics, the height of the peak represents the extent of dynamic heterogeneity.

$$\alpha_2 = \frac{3\langle|\Delta\mathbf{R}|^4\rangle}{5\langle|\Delta\mathbf{R}|^2\rangle^2} - 1 \tag{1.37}$$

ΔR is the displacement of a particle and the average is taken over all time origins and over all particles.

1.7.3 van Hove correlation function

The van Hove distribution function $G(r,t)$ is a real-space dynamical correlation function for characterising the spatial and temporal distributions of pairs of particles in a fluid [216].

$G(r,t)$ describes both the temporal evolution and the spatial distribution of either the same particle or pairs of particles [217]. It is defined as in Equation 1.38:

$$G(r,t) = \frac{1}{N}\left\langle \sum_{i=1}^{N}\sum_{j=1}^{N} \delta(|\mathbf{R}_j(t) - \mathbf{R}_i(0)| - r) \right\rangle \tag{1.38}$$

Here, $\langle\rangle$ denotes average over all time origins. N is the total number of particles in the system. $\mathbf{R}_j(t)$ is the position of the j^{th} particle at time t.

$G(r,t)$ can be split into "self" and "distinct" parts, G_s(r,t) and G_d(r,t), respectively.

$$\begin{aligned} G(r,t) &= \frac{1}{N}\left\langle \sum_{i=1}^{N} \delta(|\mathbf{R}_i(t) - \mathbf{R}_i(0)| - r) \right\rangle + \frac{1}{N}\left\langle \sum_{i=1}^{N}\sum_{j\neq i} \delta(|\mathbf{R}_j(t) - \mathbf{R}_i(0)| - r) \right\rangle \\ &\equiv G_s(r,t) + G_d(r,t) \end{aligned} \tag{1.39}$$

The self part of the van Hove correlation function,

$$G_s(r,t) = \frac{1}{N}\left\langle \sum_{i=1}^{N} \delta(|\mathbf{R}_i(t) - \mathbf{R}_i(0)| - r) \right\rangle \tag{1.40}$$

represents the probability of finding a particle i at time t at a distance r away from its position at time $t = 0$. The self part of the van Hove correlation function can detect the presence of significant hopping present in the system [23, 218], as well as non-Gaussian dynamics in the system when compared to systems with purely diffusive dynamics [219]. $G_s(r,t)$ at the single particle level can also show hopping (Chapter 3 and 4B). A sudden change in particle position (large displacement over a short time as shown in Chapter 3 and Chapter 4B) with absolute time is a sure signature of single particle hop [220].

In a system where hopping is also a prominent mode of transport, the presence of humps and valleys in G_s(r,t) as a function of radial distance r for a given time interval t, is indicative of the presence of hopping. Humps in G_s(r,t) are indicative of pockets in radial distances at which probability of finding the particular species is more over time interval t. Valleys in G_s(r,t) are indicative of pockets in radial distances at which probability of finding the particular species is less over time interval t. Such humps and valleys in G_s(r,t) can exist only if the species hops.

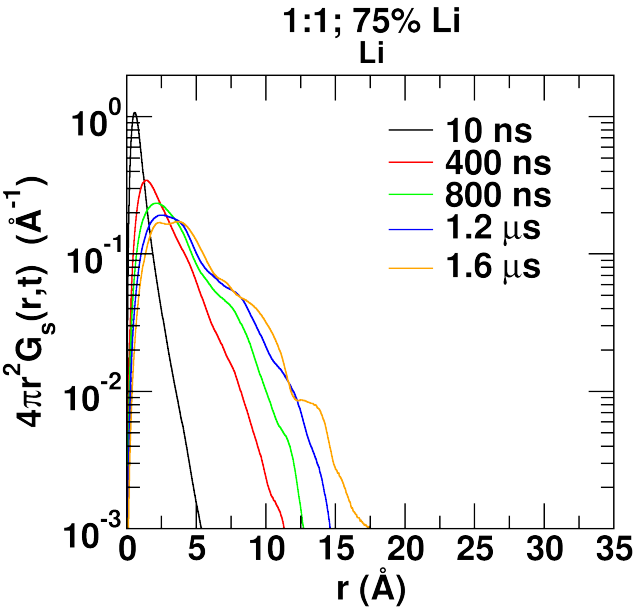

Figure 1.11: Self part of van Hove correlation function G_s(r,t) as a function of radial distance r for Li-ions in an HCE.

Alongside G_s(r,t) of the system as is, it is useful to look at a system which is purely diffusive with the same diffusion coefficient as the real data. This comparison allows us to understand how dynamically heterogeneous the real data is. A system displaying purely diffusive dynamics follows the Equation 1.41 [221]:

$$G_s(r,t) = \frac{e^{\frac{-r^2}{4Dt}}}{4Dt^{\frac{3}{2}}} \tag{1.41}$$

Here, D is the diffusion coefficient of species we are looking at the G_s(r,t) of.

The distinct part of the van Hove correlation function,

$$G_d(r,t) = \frac{1}{N}\left\langle \sum_{i=1}^{N}\sum_{j\neq i}\delta(|\mathbf{R}_j(t) - \mathbf{R}_i(0)| - r)\right\rangle \tag{1.42}$$

represents the probability of finding a particle j at time t a distance r away from the position particle i was at time $t = 0$.

$G_d(r,0)/\rho = g(r)$, where ρ is the density of particle of type j, and $g(r)$ is the radial distribution function of target type j around reference type i. Humps in $G_d(r,t)$ between the position of the first peak of $g(r)$ and $r = 0$, indicate pockets of radial distances that j is more likely to be found at time interval t with respect to the initial position occupied by i. Likewise, valleys in $G_d(r,t)$ indicate pockets of radial distances that j is less likely to be found at time interval t with respect to the initial position occupied by i [222, 223].

1.7.4 Cage relaxation time correlation functions

The solvation shell members around an alkali-ion were monitored. The number and identity of the solvation shell neighbours defined the cage identity.

Continuous cage relaxation time correlation function

In this thesis, the following definition for the continuous cage relaxation time correlation function, $S(t)$ was used:

$$S(t) = \langle s(t_0 + t)m(t_0 + t)\rangle \tag{1.43}$$

$S(t)$ is sensitive to the change in cage identity at any time instant $t_0 + t$ following a time origin t_0. Average is taken over all time origins t_0 and all cage centers (alkali ions). $s(t_0 + t)$ = 1 if the cage identity at $t_0 + t$ is the same as that at t_0. Else, it is 0. $m(t_0 + t)$ = 1 if the cage identity was maintained intact at all times investigated from t_0 to $t_0 + t$. Else, it is 0.

Intermittent cage relaxation time correlation function

The intermittent cage relaxation correlation function, $C(t)$, is defined here as:

$$C(t) = \langle s(t_0 + t)\rangle \tag{1.44}$$

$C(t)$ allows for more leeway than $S(t)$ in cage identity. If the cage identity at t_0 and $t_0 + t$ has remained the same, $C(t_0 + t)$ is given the value 1. Else, it is given 0. $C(t)$ is not sensitive to the cage identity between times t_0 and $t_0 + t$.

From $S(t)$ and $C(t)$ as defined, it is expected for $S(t)$ to decay faster than $C(t)$.

These cage relaxation time correlation functions can be fit to a linear combination of exponentials (Equation 1.45).

$$f(t) = \sum_{i=1}^{N} A_i e^{\frac{-t}{\tau_i}} \tag{1.45}$$

where A_i and τ_i are parameters that need to be fit.

1.7.5 Velocity auto-correlation function & vibrational density of states

The velocity auto-correlation function (VACF) represents the extent of correlation between the velocity of the same particle separated by time interval t [224].

It is defined as:

$$C_v(t) = \frac{\langle \mathbf{v}(t+t_0) \cdot \mathbf{v}(t_0) \rangle}{\langle \mathbf{v}(t_0) \cdot \mathbf{v}(t_0) \rangle} \tag{1.46}$$

Here again, average is taken over all time origins t_0 and over all atoms of the species being considered.

From Newton's laws of motion and by definition of VACF (Equation 1.46), C_v(t) for a non-interacting system (without forces) would be 1 at all time intervals t.

Whereas, in the presence of weak inter-atomic forces, over time, the forces would have the effect of velocity de-(auto)-correlating the system. In this case, VACF (C_v(t)) shows an exponential decay. The system is thought to lose memory of its initial velocity state with time. Such an exponential decay can be expected in the case of atoms of a gas.

Lastly, when the inter-atomic forces are large, such as in dense systems (crystals and liquids), one expects a damped oscillatory behaviour. Due to an ordered structure in crystals, and fixed mean position of atoms, and fixed environments, atomic vibrations about their mean position is largely regular apart from small perturbation forces that act over time. Therefore there is a damped oscillatory behaviour. In amorphous solids and liquids, the damping is larger due to the presence of diffusion and a more irregular and fluctuating vibrational environments. In a more dense system, where the atoms are more caged, the oscillations (although damped) will be more pronounced in comparison to that of a less dense system.

One example of VACF for Li and Na-ions in HCEs is shown in Figure 1.12. Li-ions have a tighter and smaller solvation shell in comparison to that of Na-ions. Thus, Li-ions have a much larger frequency of rattling in their cages as compared to Na-ions.

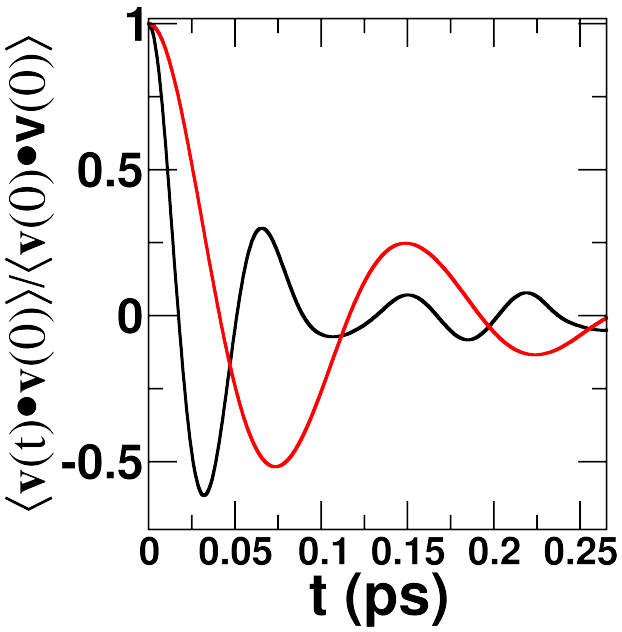

Figure 1.12: Velocity auto correlation function for alkali ions in HCEs; Li (black), Na (red).

1.8 Some relevant experimental techniques and definitions

Experimental work for Chapter 6 presented in this thesis was carried out by the group of Prof. Premkumar Senguttuvan.

Electrochemical parameters:

Working electrode: The electrode on which all the electrochemical events of interest in a cell are carried out.
Counter electrode: The electrode that is used to complete the electrochemical circuit.
Reference electrode: The electrode with reference to which the change in potential of the working electrode is measured [225].
Theoretical Voltage: The standard potential of a cell, which can be obtained experimentally or can be calculated using the formula: *Reduction potential of the cathode – Reduction potential of the anode*
Theoretical capacity: The total electric power involved in the electrochemical reaction
Coulombic efficiency (CE): The ratio of discharge capacity over charge capacity of a

cell [226], expressible as:

$$CE = \frac{Discharge\ capacity}{Charge\ capacity} = \frac{Total\ number\ of\ Zn\ ions\ back\ to\ the\ cathode}{Total\ number\ of\ Zn\ ions\ departing\ the\ cathode} \tag{1.47}$$

Important techniques:

Cyclic voltammetry (CV): A technique used to investigate the redox processes of a molecular species [225]. Potential is swept between a range of values at a definite rate at the working electrode, and the current density produced in this process is plotted as a function of potential.

Chronopotentiometry: A galvanostatic technique used to study the chemical reaction mechanism and the kinetics of a reaction. In this transient technique, the system is perturbed from its equilibrium state to a new steady state, and electrochemical information is gained during its relaxation time.

Electrochemical impedance spectroscopy (EIS): A technique used to gain insight into various physical and electronic properties of a electrochemical system, in which the system is perturbed from its equilibrium state with a small amplitude a.c. potential, and the output current is measured [227].

Fourier Transform Infrared spectroscopy (FTIR): Used, along with Raman spectroscopy, to determine the change in stretching frequency of various functional groups in the electrolytes [228, 229].

X-ray photoelectron (XPS) or electron spectroscopy for chemical analysis (ESCA): Surface sensitive techniques used to analyze the chemical or electronic state of the elements present on the surface of the material up to a depth of 1-10 nm [230]. In these, the kinetic/binding energy of electrons along with the number of electrons ejected from the surface of the sample is measured by irradiating the sample with a beam of X-rays. The binding energy of every element is unique, and this is used to determine the formal oxidation state and the concentration of the element on the surface [231].

X-ray diffraction (XRD): A nondestructive technique used to characterize structure, phase and orientation of crystalline materials [232–234]. The crystalline material acts as a three dimensional diffraction grating for the X-rays that are generated from a cathode ray tube. The diffraction pattern produce by the constructive interference of the X-rays provides information about the periodic arrangement of atoms and molecules in the materials.

Scanning electron microscope (SEM): A type of microscopy used to analyse the surface

morphology of the material with a resolution of 10 nm [235]. Most SEMs are integrated with EDX (energy dispersive X-ray) spectrometers to allow qualitative chemical analysis of the specimen, taking benefit of characteristic X-rays generated by the incident electron beam.

Inductively coupled plasma optical emission spectroscopy (ICP-OES): An analytical technique used to determine the concentration of various elements in an unknown system [236]. ICP-OES uses a plasma torch consisting of ionic gases at a very high temperature to excite the atoms of the sample, and the detector measures the light emitted by the sample as it comes to the ground state.

1.9 Additional computational techniques

A large number of analyses were conducted on the MD trajectories through in-house FORTRAN codes. These codes were written to calculate transport properties such as the diffusion constant (from mean-squared displacement), ionic conductivity, and viscosity. Codes were also written for calculating the radial distribution function, the potential of mean force (through the Jarzynski equality), dynamic correlation functions such as the self and distinct part of the van Hove correlation functions, the cage relaxation time auto-correlation function, the non-Gaussian parameter, solvation shell type populations, free-water percentage, and the velocity auto-correlation function.

Bash scripting and Tcl scripting were also used for some minor calculations.

1.10 Scope of the thesis

A brief outline of the remaining chapters of the thesis, followed by a more detailed description of each chapter comprise the scope of this thesis.

Chapter 2 presents a refinement of the force field to capture the transport and physicochemical properties of liquid sulfolane, a promising battery solvent. **Chapter 3** employs the force field developed in **Chapter 2** to find evidence for Li-ion hopping in HCEs and to characterize hop events and hop energy barriers. **Chapter 4** contains three sub-chapters. **Chapter 4A** provides a description of the methods used for the force-field refinement of the bis-(fluorosulfonyl)imide anion. Employing the force field for the anion presented in Chapter 4A, **Chapter 4B** reports the liquid state structure and transport of Na-ion and Li-ion based HCEs. **Chapter 4C** studies mixed alkali ion electrolytes as a means to improve the transport properties of pure Na-ion HCEs. **Chapter 5** confirms the presence

of bicationic complexes in Li and Na-based HCEs through AIMD simulations. AIMD simulations, quantum chemical geometry optimization, and frequency calculations are employed to understand the stability of these clusters. In a work carried out in collaboration with experimentalists, **Chapter 6** describes how the addition of propylene carbonate (PC) as a cosolvent to water remedies challenges faced at both electrodes in rechargeable aqueous zinc ion batteries.

Chapter 2: Due to sulfolane's amphiphilic nature, high oxidative and thermal stability, and optimal solvation power of cations, it shows much promise as an upcoming solvent in battery electrolytes. Hence, an all-atom force field that quantitatively captures its transport properties is essential. A refined force field that yields significantly improved estimates for self-diffusion constant and shear viscosity is presented. Prediction for physicochemical properties such as density, surface tension, and heat of vaporization are in good agreement with experiments as well. While the site charges of the molecule were obtained by periodic DFT calculations of the bulk liquid, quantum potential energy scans are used to refine the Lennard-Jones parameters. The near-neighbor structure in liquid sulfolane is characterized by an antiparallel arrangement of molecular dipoles.

Chapter 3: Based on the ratio of diffusion coefficients of various species, ion hopping is believed to be a significant mode of transport for small ions (Li-ions) in liquid high concentration electrolytes (HCEs). Herein, its microscopic signatures are determined through the self part of the van Hove space-time correlation function. The long and short time imprints of hopping in HCEs are shown using $LiBF_4$-in-sulfolane mixtures as models. Li-ions prefer to transit to previously occupied Li-ion sites. Hopping in the liquid matrix is an activated process, and its free energy barrier and transition state structure are determined. Nanoscale compositional heterogeneity was observed in HCEs, as evidenced by the presence of anion bridged Li-ion chains. Further, the simulations shed light on the composition, stiffness, and lifetime of the solvation shell of Li ions.

Chapter 4: The bis(flurosulfonyl)imide (FSI) anion is currently used widely in HCEs. An improved force field for the FSI anion is presented in **Chapter 4A**. The FSI force field was found to be generic enough to be applicable to two different classes of systems, viz., Li and Na salts in sulfolane and ionic liquids such as $[C_2MIM]FSI$. In **Chapter 4B**, using the force field for FSI obtained in **Chapter 4A**, a comparative study of the structure and transport of lithium and sodium based HCEs is made. It is observed that diffusion coefficients of various species in Na-ion based HCEs are about an order of magnitude smaller than in Li-ion based ones. Li-ions diffuse faster than Na ions since they have a smaller solvation shell radius. They also have a higher propensity to hop, again due to their relative size and a larger Einstein frequency – the cage rattling frequency. In **Chapter 4C**, with a view to reducing the consumption of Li salt, the enhancement of transport properties

of sodium HCE through lithium doping is studied. It is found that the transport properties of all species in the HCE are improved by replacing a fraction of Na-ions with Li-ions. The non-Gaussian parameter of ions demonstrates the system to be dynamically heterogeneous. At the time interval corresponding to its maximum, as the Li-content in the electrolyte increases, the fraction of Li-ions increases for which the translational displacement is larger than that predicted by pure diffusion. Therefore, Li-ions carried an increasing fraction of the total current as the Li-content of the electrolyte was increased (increasing transference numbers of Li). The cage relaxation time of Li-ions decreases with increasing Li-ion fraction while that for Na-ion is nearly independent of it.

Chapter 5: The presence of ligand-bridged cation pair complexes in HCEs observed in classical MD simulations presented in **Chapter 4B** are further investigated in this chapter. Their presence in both Li-ion HCE and Na-ion HCE models is confirmed through AIMD simulations. It is found that cation pair complexes composed of Na-ions are more probable than those composed of Li-ions. The dependence of the free energy of formation of cation pair complexes on the number of shared ligands was determined. The chemical identity of the cations and of the shared ligands as well as their composition decide the stability of a cation pair complex.

Chapter 6: Aqueous rechargeable zinc-ion batteries are limited in their scope, due to poor Coulombic efficiencies, dendritic growth on zinc anode, and structural degradation and dissolution of oxide cathode. Given that 'free water' (water molecules unassociated with any other species) is implicated in parasitic reactions at either electrode, the introduction of a polar co-solvent, propylene carbonate (PC), is shown to reduce the amount of free water in the system through the formation of PC-water hydrogen bonds. Using PC as a co-solvent also modulates the composition of the Zn-ion primary solvation shell by replacing water molecule(s) with the organic carbonate and/or the anion. These chief observations from the simulations offer a microscopic explanation for the significant enhancement in battery characteristics upon the addition of PC to the electrolyte observed in experiments.

Bibliography

[1] Haisheng Chen, Thang Ngoc Cong, Wei Yang, Chunqing Tan, Yongliang Li, and Yulong Ding. Progress in electrical energy storage system: A critical review. *Progress in Natural Science*, 19(3):291–312, 2009.

[2] Przemyslaw Komarnicki, Pio Lombardi, and Zbigniew Styczynski. Electric energy storage system. In *Electric Energy Storage Systems*, pages 37–95. Springer, 2017.

[3] Haoran Zhao, Qiuwei Wu, Shuju Hu, Honghua Xu, and Claus Nygaard Rasmussen. Review of energy storage system for wind power integration support. *Applied Energy*, 137:545–553, 2015.

[4] Neal S Wade, PC Taylor, PD Lang, and PR Jones. Evaluating the benefits of an electrical energy storage system in a future smart grid. *Energy Policy*, 38(11):7180–7188, 2010.

[5] Hao Qian, Jianhui Zhang, Jih-Sheng Lai, and Wensong Yu. A high-efficiency grid-tie battery energy storage system. *IEEE Transactions on Power Electronics*, 26(3):886–896, 2010.

[6] Yayun Zheng, Di Wang, Shubham Kaushik, Shaoning Zhang, Tomoki Wada, Jinkwang Hwang, Kazuhiko Matsumoto, and Rika Hagiwara. Ionic Liquid Electrolytes for Next-generation Electrochemical Energy Devices. *EnergyChem*, page 100075, 2022.

[7] Richard York. Do alternative energy sources displace fossil fuels? *Nature Climate Change*, 2(6):441–443, 2012.

[8] Dieter Helm. The future of fossil fuels—is it the end? *Oxford Review of Economic Policy*, 32(2):191–205, 2016.

[9] Omar Ellabban, Haitham Abu-Rub, and Frede Blaabjerg. Renewable energy resources: Current status, future prospects and their enabling technology. *Renewable and Sustainable Energy Reviews*, 39:748–764, 2014.

[10] Dolf Gielen, Francisco Boshell, Deger Saygin, Morgan D Bazilian, Nicholas Wagner, and Ricardo Gorini. The role of renewable energy in the global energy transformation. *Energy Strategy Reviews*, 24:38–50, 2019.

[11] Patrick Moriarty and Damon Honnery. Can renewable energy power the future? *Energy Policy*, 93:3–7, 2016.

[12] Yuki Yamada, Jianhui Wang, Seongjae Ko, Eriko Watanabe, and Atsuo Yamada. Advances and issues in developing salt-concentrated battery electrolytes. *Nature Energy*, 4(4):269–280, 2019.

[13] Chao Zhang, Yi-Li Wei, Peng-Fei Cao, and Meng-Chang Lin. Energy storage system: Current studies on batteries and power condition system. *Renewable and Sustainable Energy Reviews*, 82:3091–3106, 2018.

[14] Faramarz Faraji, Abbas Majazi, Kamal Al-Haddad, et al. A comprehensive review of flywheel energy storage system technology. *Renewable and Sustainable Energy Reviews*, 67:477–490, 2017.

[15] Srdjan M Lukic, Jian Cao, Ramesh C Bansal, Fernando Rodriguez, and Ali Emadi. Energy storage systems for automotive applications. *IEEE Transactions on Industrial Electronics*, 55(6):2258–2267, 2008.

[16] Tobias Placke, Richard Kloepsch, Simon Dühnen, and Martin Winter. Lithium ion, lithium metal, and alternative rechargeable battery technologies: the odyssey for high energy density. *Journal of Solid State Electrochemistry*, 21(7):1939–1964, 2017.

[17] Ashish Rudola, Anthony JR Rennie, Richard Heap, Seyyed Shayan Meysami, Alex Lowbridge, Francesco Mazzali, Ruth Sayers, Christopher J Wright, and Jerry Barker. Commercialisation of high energy density sodium-ion batteries: Faradion's journey and outlook. *Journal of Materials Chemistry A*, 9(13):8279–8302, 2021.

[18] Yi Chen, Tianyi Wang, Huajun Tian, Dawei Su, Qiang Zhang, and Guoxiu Wang. Advances in lithium–sulfur batteries: from academic research to commercial viability. *Advanced Materials*, 33(29):2003666, 2021.

[19] Kang Xu. Electrolytes and interphases in Li-ion batteries and beyond. *Chemical Reviews*, 114(23):11503–11618, 2014.

[20] Yuki Yamada and Atsuo Yamada. Superconcentrated electrolytes for lithium batteries. *Journal of the Electrochemical Society*, 162(14):A2406, 2015.

[21] Inhyuk Jang and Arun Yethiraj. Effect of diffusion constant on the morphology of dendrite growth in lithium metal batteries. *The Journal of Chemical Physics*, 154(23):234705, 2021.

[22] Wilberth A Narvaez, Sanghyun J Park, and Benjamin J Schwartz. Hydrated electrons in high-concentration electrolytes interact with multiple cations: A simulation study. *The Journal of Physical Chemistry B*, 2022.

[23] Srimayee Mukherji, Nikhil VS Avula, Rahul Kumar, and Sundaram Balasubramanian. Hopping in High Concentration Electrolytes-Long Time Bulk and Single-Particle Signatures, Free Energy Barriers, and Structural Insights. *The Journal of Physical Chemistry Letters*, 11(22):9613–9620, 2020.

[24] Kaoru Dokko, Daiki Watanabe, Yosuke Ugata, Morgan L Thomas, Seiji Tsuzuki, Wataru Shinoda, Kei Hashimoto, Kazuhide Ueno, Yasuhiro Umebayashi, and Masayoshi Watanabe. Direct evidence for Li ion hopping conduction in highly concentrated sulfolane-based liquid electrolytes. *The Journal of Physical Chemistry B*, 122(47):10736–10745, 2018.

[25] Kaoru Dokko, Naoki Tachikawa, Kento Yamauchi, Mizuho Tsuchiya, Azusa Yamazaki, Eriko Takashima, Jun-Woo Park, Kazuhide Ueno, Shiro Seki, Nobuyuki Serizawa, et al. Solvate ionic liquid electrolyte for Li–S batteries. *Journal of the Electrochemical Society*, 160(8):A1304, 2013.

[26] Yuki Yamada, Keizo Furukawa, Keitaro Sodeyama, Keisuke Kikuchi, Makoto Yaegashi, Yoshitaka Tateyama, and Atsuo Yamada. Unusual stability of acetonitrile-based superconcentrated electrolytes for fast-charging lithium-ion batteries. *Journal of the American Chemical Society*, 136(13):5039–5046, 2014.

[27] R Petibon, CP Aiken, L Ma, D Xiong, and JR Dahn. The use of ethyl acetate as a sole solvent in highly concentrated electrolyte for Li-ion batteries. *Electrochimica Acta*, 154:287–293, 2015.

[28] Yuki Yamada, Makoto Yaegashi, Takeshi Abe, and Atsuo Yamada. A superconcentrated ether electrolyte for fast-charging Li-ion batteries. *Chemical Communications*, 49(95):11194–11196, 2013.

[29] Ju Sun, Luke A O'Dell, Michel Armand, Patrick C Howlett, and Maria Forsyth. Anion-derived solid-electrolyte interphase enables long life Na-ion batteries using superconcentrated ionic liquid electrolytes. *ACS Energy Letters*, 6(7):2481–2490, 2021.

[30] Fangfang Chen, Patrick Howlett, and Maria Forsyth. Na-ion solvation and high transference number in superconcentrated ionic liquid electrolytes: a theoretical approach. *The Journal of Physical Chemistry C*, 122(1):105–114, 2018.

[31] Khryslyn Arano, Srdan Begic, Fangfang Chen, Dmitrii Rakov, Driss Mazouzi, Nicolas Gautier, Robert Kerr, Bernard Lestriez, Jean Le Bideau, Patrick C Howlett, et al. Tuning the formation and structure of the silicon electrode/ionic liquid electrolyte interphase in superconcentrated ionic liquids. *ACS Applied Materials & Interfaces*, 13(24):28281–28294, 2021.

[32] Zhujie Li, Roza Bouchal, Trinidad Mendez-Morales, A-L Rollet, Cecile Rizzi, Steven Le Vot, Frédéric Favier, Benjamin Rotenberg, Oleg Borodin, Olivier Fontaine, et al. Transport properties of Li-tfsi water-in-salt electrolytes. *The Journal of Physical Chemistry B*, 123(49):10514–10521, 2019.

[33] Zhujie Li, Guillaume Jeanmairet, Trinidad Méndez-Morales, Benjamin Rotenberg, and Mathieu Salanne. Capacitive performance of water-in-salt electrolytes in supercapacitors: A simulation study. *The Journal of Physical Chemistry C*, 122(42):23917–23924, 2018.

[34] Trinidad Mendez-Morales, Zhujie Li, and Mathieu Salanne. Computational screening of the physical properties of water-in-salt electrolytes. *Batteries & Supercaps*, 4(4):646–652, 2021.

[35] Kazuaki Matsumoto, Kazuhiko Inoue, Kentaro Nakahara, Ryota Yuge, Takehiro Noguchi, and Koji Utsugi. Suppression of aluminum corrosion by using high concentration litfsi electrolyte. *Journal of Power Sources*, 231:234–238, 2013.

[36] Dennis W McOwen, Daniel M Seo, Oleg Borodin, Jenel Vatamanu, Paul D Boyle, and Wesley A Henderson. Concentrated electrolytes: decrypting electrolyte properties and reassessing al corrosion mechanisms. *Energy & Environmental Science*, 7(1):416–426, 2014.

[37] Kazuki Yoshida, Megumi Nakamura, Yuichi Kazue, Naoki Tachikawa, Seiji Tsuzuki, Shiro Seki, Kaoru Dokko, and Masayoshi Watanabe. Oxidative-stability enhancement and charge transport mechanism in glyme–lithium salt equimolar complexes. *Journal of the American Chemical Society*, 133(33):13121–13129, 2011.

[38] Ted M Pappenfus, Wesley A Henderson, Boone B Owens, Kent R Mann, and William H Smyrl. Complexes of lithium imide salts with tetraglyme and their polyelectrolyte composite materials. *Journal of the Electrochemical Society*, 151(2):A209, 2004.

[39] Soon-Ki Jeong, Hee-Young Seo, Dong-Hak Kim, Hyun-Kak Han, Jin-Gul Kim, Yoon Bae Lee, Yasutoshi Iriyama, Takeshi Abe, and Zempachi Ogumi. Suppression of dendritic lithium formation by using concentrated electrolyte solutions. *Electrochemistry Communications*, 10(4):635–638, 2008.

[40] Liumin Suo, Yong-Sheng Hu, Hong Li, Michel Armand, and Liquan Chen. A new class of solvent-in-salt electrolyte for high-energy rechargeable metallic lithium batteries. *Nature Communications*, 4(1):1–9, 2013.

[41] Jiangfeng Qian, Wesley A Henderson, Wu Xu, Priyanka Bhattacharya, Mark Engelhard, Oleg Borodin, and Ji-Guang Zhang. High rate and stable cycling of lithium metal anode. *Nature Communications*, 6(1):1–9, 2015.

[42] Yuki Yamada, Yasuyuki Takazawa, Kohei Miyazaki, and Takeshi Abe. Electrochemical lithium intercalation into graphite in dimethyl sulfoxide-based electrolytes: effect of solvation structure of lithium ion. *The Journal of Physical Chemistry C*, 114(26):11680–11685, 2010.

[43] Yuki Yamada, Kenji Usui, Ching Hua Chiang, Keisuke Kikuchi, Keizo Furukawa, and Atsuo Yamada. General observation of lithium intercalation into graphite in ethylene-carbonate-free superconcentrated electrolytes. *ACS Applied Materials & Interfaces*, 6(14):10892–10899, 2014.

[44] Soon-Ki Jeong, Minoru Inaba, Yasutoshi Iriyama, Takeshi Abe, and Zempachi Ogumi. Electrochemical intercalation of lithium ion within graphite from propylene carbonate solutions. *Electrochemical and Solid-State Letters*, 6(1):A13, 2002.

[45] Soon-Ki Jeong, Minoru Inaba, Yasutoshi Iriyama, Takeshi Abe, and Zempachi Ogumi. Interfacial reactions between graphite electrodes and propylene carbonate-based solutions: Electrolyte-concentration dependence of electrochemical lithium intercalation reaction. *Journal of Power Sources*, 175(1):540–546, 2008.

[46] Kazuki Yoshida, Mizuho Tsuchiya, Naoki Tachikawa, Kaoru Dokko, and Masayoshi Watanabe. Change from glyme solutions to quasi-ionic liquids for binary mixtures consisting of lithium bis (trifluoromethanesulfonyl) amide and glymes. *The Journal of Physical Chemistry C*, 115(37):18384–18394, 2011.

[47] Jianhui Wang, Yuki Yamada, Keitaro Sodeyama, Ching Hua Chiang, Yoshitaka Tateyama, and Atsuo Yamada. Superconcentrated electrolytes for a high-voltage lithium-ion battery. *Nature Communications*, 7(1):1–9, 2016.

[48] Rudolph A Marcus and Norman Sutin. Electron transfers in chemistry and biology. *Biochimica et Biophysica Acta (BBA)-Reviews on Bioenergetics*, 811(3):265–322, 1985.

[49] Koichi Fumino, Peter Stange, Verlaine Fossog, Rolf Hempelmann, and Ralf Ludwig. Gleichgewicht zwischen kontakt-und solvensseparierten ionenpaaren in mischungen von protischen ionischen flüssigkeiten und molekularen lösungsmitteln durch polarität kontrolliert. *Angewandte Chemie*, 125(47):12667–12670, 2013.

[50] Christoph Lambert and Paul von Ragué Schleyer. Are polar organometallic compounds "carbanions"? the gegenion effect on structure and energies of alkali-metal compounds. *Angewandte Chemie International Edition in English*, 33(11):1129–1140, 1994.

[51] Jian-Ming Lü, Sergiy V Rosokha, Sergey V Lindeman, Ivan S Neretin, and Jay K Kochi. "separated" versus "contact" ion-pair structures in solution from their crystalline states: dynamic effects on dinitrobenzenide as a mixed-valence anion. *Journal of the American Chemical Society*, 127(6):1797–1809, 2005.

[52] Mario El Kazzi, Izabela Czekaj, Erik J Berg, Petr Novák, and Matthew A Brown. Investigation of Li-ion solvation in carbonate based electrolytes using near ambient pressure photoemission. *Topics in Catalysis*, 59(5):628–634, 2016.

[53] S Merkel, D Stern, J Henn, and D Stalke. Solvent-separated and contact ion pairs of parent lithium trimethyl zincate. *Angewandte Chemie International Edition*, 48(34):6350–6353, 2009.

[54] Raymond M Fuoss. Ionic association. III. the equilibrium between ion pairs and free ions. *Journal of the American Chemical Society*, 80(19):5059–5061, 1958.

[55] S Winstein, E Clippinger, AH Fainberg, R Heck, and GC Robinson. Salt effects and ion pairs in solvolysis and related reactions. III. common ion rate depression and exchange of anions during acetolysis. *Journal of the American Chemical Society*, 78(2):328–335, 1956.

[56] Jiangtao Hu, Yuchen Ji, Guorui Zheng, Weiyuan Huang, Yuan Lin, Luyi Yang, and Feng Pan. Influence of electrolyte structural evolution on battery applications: Cationic aggregation from dilute to high concentration. *Aggregate*, 3(1):e153, 2022.

[57] Zhou Yu, Nitash P Balsara, Oleg Borodin, Andrew A Gewirth, Nathan T Hahn, Edward J Maginn, Kristin A Persson, Venkat Srinivasan, Michael F Toney, Kang Xu, et al. Beyond local solvation structure: nanometric aggregates in battery electrolytes and their effect on electrolyte properties. *ACS Energy Letters*, 7(1):461–470, 2021.

[58] Julian Self, Kara D Fong, and Kristin A Persson. Transport in superconcentrated lipf6 and libf4/propylene carbonate electrolytes. *ACS Energy Letters*, 4(12):2843–2849, 2019.

[59] Vikas Dubey, Archita Maiti, and Snehasis Daschakraborty. Predicting the solvation structure and vehicular diffusion of hydroxide ion in an anion exchange membrane using nonreactive molecular dynamics simulation. *Chemical Physics Letters*, 755:137802, 2020.

[60] Vikas Dubey and Snehasis Daschakraborty. Translational jump-diffusion of hydroxide ion in anion exchange membrane: Deciphering the nature of vehicular diffusion. *The Journal of Physical Chemistry B*, 126(12):2430–2440, 2022.

[61] Dominik Marx, Amalendu Chandra, and Mark E Tuckerman. Aqueous basic solutions: hydroxide solvation, structural diffusion, and comparison to the hydrated proton. *Chemical Reviews*, 110(4):2174–2216, 2010.

[62] Tamar Zelovich, Leslie Vogt-Maranto, Michael A Hickner, Stephen J Paddison, Chulsung Bae, Dario R Dekel, and Mark E Tuckerman. Hydroxide ion diffusion in anion-exchange membranes at low hydration: insights from ab initio molecular dynamics. *Chemistry of Materials*, 31(15):5778–5787, 2019.

[63] Masaki Okoshi, Chien-Pin Chou, and Hiromi Nakai. Theoretical analysis of carrier ion diffusion in superconcentrated electrolyte solutions for sodium-ion batteries. *The Journal of Physical Chemistry B*, 122(9):2600–2609, 2018.

[64] Fangfang Chen and Maria Forsyth. Elucidation of transport mechanism and enhanced alkali ion transference numbers in mixed alkali metal–organic ionic molten salts. *Physical Chemistry Chemical Physics*, 18(28):19336–19344, 2016.

[65] Oleg Borodin, Liumin Suo, Mallory Gobet, Xiaoming Ren, Fei Wang, Antonio Faraone, Jing Peng, Marco Olguin, Marshall Schroeder, Michael S Ding, et al. Liquid structure with nano-heterogeneity promotes cationic transport in concentrated electrolytes. *ACS Nano*, 11(10):10462–10471, 2017.

[66] James A Given and George Stell. A percolation theory of ionic clustering in electrolytes. *The Journal of Chemical Physics*, 106(3):1195–1209, 1997.

[67] Dennis C Rapaport and Dennis C Rapaport Rapaport. *The art of molecular dynamics simulation*. Cambridge University Press, 2004.

[68] MP Allen and DJ Tildesley. Computer simulation of liquids: Oxford university press. 1989.

[69] Daan Frenkel, Berend Smit, and Mark A Ratner. *Understanding molecular simulation: From algorithms to applications*, volume 2. Academic press San Diego, 1996.

[70] Mark Tuckerman. *Statistical mechanics: theory and molecular simulation*. Oxford University Press, 2010.

[71] Attila Szabo and Neil S Ostlund. *Modern quantum chemistry: Introduction to advanced electronic structure theory*. Courier Corporation, 2012.

[72] Dominik Marx and Jürg Hutter. *Ab initio molecular dynamics: Basic theory and advanced methods*. Cambridge University Press, 2009.

[73] G Martin-Head, JA Pople, and MJ Frisch. MP2 energy evaluation by direct methods. *Chem. Phys. Lett*, 153:503–506, 1988.

[74] Klaus Capelle. A bird's-eye view of density-functional theory. *Brazilian Journal of Physics*, 36:1318–1343, 2006.

[75] G Cicccotti, D Frenkel, and IR McDonald. Simulations of liquids and solids–molecular dynamics and Monte Carlo methods in statistical mechanics, 1987.

[76] David S Sholl and Janice A Steckel. *Density functional theory: A practical introduction*. John Wiley & Sons, 2011.

[77] Sudarshan Behera, Sudip Das, and Sundaram Balasubramanian. An atomistic view of solvent-free protein liquids: The case of Lipase A. *Physical Chemistry Chemical Physics*, 23(12):7302–7312, 2021.

[78] Amit Kumawat and Suman Chakrabarty. Hidden electrostatic basis of dynamic allostery in a pdz domain. *Proceedings of the National Academy of Sciences*, 114(29):E5825–E5834, 2017.

[79] Samuel S Cho, Govardhan Reddy, John E Straub, and D Thirumalai. Entropic stabilization of proteins by TMAO. *The Journal of Physical Chemistry B*, 115(45):13401–13407, 2011.

[80] Govardhan Reddy and D Thirumalai. Dissecting ubiquitin folding using the self-organized polymer model. *The Journal of Physical Chemistry B*, 119(34):11358–11370, 2015.

[81] Aritra Sarkar, Ranjan Sasmal, Charly Empereur-Mot, Davide Bochicchio, Srinath VK Kompella, Kamna Sharma, Shikha Dhiman, Balasubramanian Sundaram, Sarit S Agasti, Giovanni M Pavan, et al. Self-sorted, random, and block supramolecular copolymers via sequence controlled, multicomponent self-assembly. *Journal of the American Chemical Society*, 142(16):7606–7617, 2020.

[82] Srabani S Mishra, Srinath VK Kompella, Shobhana Krishnaswamy, Sundaram Balasubramanian, and Dillip K Chand. Low-symmetry self-assembled coordination complexes with exclusive diastereoselectivity: Experimental and computational studies. *Inorganic Chemistry*, 59(17):12884–12894, 2020.

[83] Abhishek Sharma, Nimish Dwarkanath, and Sundaram Balasubramanian. Thermally activated dynamic gating underlies higher gas adsorption at higher temperatures in metal–organic frameworks. *Journal of Materials Chemistry A*, 9(48):27398–27407, 2021.

[84] Nimish Dwarkanath, Sourav Palchowdhury, and S Balasubramanian. Unraveling the sorption mechanism of CO_2 in a molecular crystal without intrinsic porosity. *The Journal of Physical Chemistry B*, 123(34):7471–7481, 2019.

[85] R Martoňák, Alessandro Laio, and Michele Parrinello. Predicting crystal structures: the Parrinello-Rahman method revisited. *Physical Review Letters*, 90(7):075503, 2003.

[86] Roman Martoňák, Davide Donadio, Artem R Oganov, and Michele Parrinello. Crystal structure transformations in SiO_2 from classical and ab initio metadynamics. *Nature Materials*, 5(8):623–626, 2006.

[87] Kartik Sau and P Padma Kumar. Role of ion–ion correlations on fast ion transport: Molecular dynamics simulation of $Na_2Ni_2TeO_6$. *The Journal of Physical Chemistry C*, 119(32):18030–18037, 2015.

[88] Supriya Roy and P Padma Kumar. Influence of Si/P ordering on Na^+ transport in NASICONs. *Physical Chemistry Chemical Physics*, 15(14):4965–4969, 2013.

[89] Krishnanjan Pramanik, Kartik Sau, and P Padma Kumar. Role of framework flexibility in ion transport: A molecular dynamics study of LiM_2^{IV} $(PO_4)_3$. *The Journal of Physical Chemistry C*, 124(7):4001–4009, 2020.

[90] Nikhil VS Avula, Anirban Mondal, and Sundaram Balasubramanian. Charge environment and hydrogen bond dynamics in binary ionic liquid mixtures: A computational study. *The Journal of Physical Chemistry Letters*, 9(12):3511–3516, 2018.

[91] Anuradha Das, Suman Das, and Ranjit Biswas. Fast fluctuations in deep eutectic melts: Multi-probe fluorescence measurements and all-atom molecular dynamics simulation study. *Chemical Physics Letters*, 581:47–51, 2013.

[92] Rupesh Verma and Tamal Banerjee. Liquid–liquid extraction of lower alcohols using menthol-based hydrophobic deep eutectic solvent: experiments and cosmo-sac predictions. *Industrial & Engineering Chemistry Research*, 57(9):3371–3381, 2018.

[93] Rupesh Verma, Mood Mohan, Vaibhav V Goud, and Tamal Banerjee. Operational strategies and comprehensive evaluation of menthol based deep eutectic solvent for the extraction of lower alcohols from aqueous media. *ACS Sustainable Chemistry & Engineering*, 6(12):16920–16932, 2018.

[94] Jan Philipp Bittner, Ningning Zhang, Lei Huang, Pablo Domínguez de María, Sven Jakobtorweihen, and Selin Kara. Impact of deep eutectic solvents (dess) and individual des components on alcohol dehydrogenase catalysis: connecting experimental data and molecular dynamics simulations. *Green Chemistry*, 24(3):1120–1131, 2022.

[95] Tamisra Pal and Ranjit Biswas. Composition dependence of dynamic heterogeneity time-and length scales in [omim][bf_4]/water binary mixtures: Molecular dynamics simulation study. *The Journal of Physical Chemistry B*, 119(51):15683–15695, 2015.

[96] Juriti Rajbangshi, Kallol Mukherjee, and Ranjit Biswas. Heterogeneous orientational relaxations and translation–rotation decoupling in (choline chloride+ urea) deep eutectic solvents: Investigation through molecular dynamics simulations and dielectric relaxation measurements. *The Journal of Physical Chemistry B*, 125(22):5920–5936, 2021.

[97] Atreyee Banerjee, Suman Chakrabarty, and Sarika Maitra Bhattacharyya. Interplay between crystallization and glass transition in binary lennard-jones mixtures. *The Journal of Chemical Physics*, 139(10):104501, 2013.

[98] Ujjwal Kumar Nandi, Atreyee Banerjee, Suman Chakrabarty, and Sarika Maitra Bhattacharyya. Composition dependence of the glass forming ability in binary mixtures: The role of demixing entropy. *The Journal of Chemical Physics*, 145(3):034503, 2016.

[99] Srikanth Sastry, Pablo G Debenedetti, and Frank H Stillinger. Signatures of distinct dynamical regimes in the energy landscape of a glass-forming liquid. *Nature*, 393(6685):554–557, 1998.

[100] Berni Julian Alder and Thomas Everett Wainwright. Phase transition for a hard sphere system. *The Journal of Chemical Physics*, 27(5):1208–1209, 1957.

[101] Berni J Alder and Thomas Everett Wainwright. Studies in molecular dynamics. i. general method. *The Journal of Chemical Physics*, 31(2):459–466, 1959.

[102] Aneesur Rahman. Correlations in the motion of atoms in liquid argon. *Physical Review*, 136(2A):A405, 1964.

[103] Aneesur Rahman and Frank H Stillinger. Molecular dynamics study of liquid water. *The Journal of Chemical Physics*, 55(7):3336–3359, 1971.

[104] Henk Bekker, HJC Berendsen, EJ Dijkstra, S Achterop, R Vondrumen, David VANDERSPOEL, A Sijbers, H Keegstra, and MKR Renardus. Gromacs-a parallel computer for molecular-dynamics simulations. In *4th International Conference on Computational Physics (PC 92)*, pages 252–256. World Scientific Publishing, 1993.

[105] Berk Hess, Carsten Kutzner, David Van Der Spoel, and Erik Lindahl. Gromacs 4: algorithms for highly efficient, load-balanced, and scalable molecular simulation. *Journal of Chemical Theory and Computation*, 4(3):435–447, 2008.

[106] Mark James Abraham, Teemu Murtola, Roland Schulz, Szilárd Páll, Jeremy C Smith, Berk Hess, and Erik Lindahl. GROMACS: High performance molecular simulations through multi-level parallelism from laptops to supercomputers. *SoftwareX*, 1:19–25, 2015.

[107] Leandro Martínez, Ricardo Andrade, Ernesto G Birgin, and José Mario Martínez. Packmol: A package for building initial configurations for molecular dynamics simulations. *Journal of Computational Chemistry*, 30(13):2157–2164, 2009.

[108] Hendrik Antoon Lorentz. Ueber die anwendung des satzes vom virial in der kinetischen theorie der gase. *Annalen der Physik*, 248(1):127–136, 1881.

[109] Daniel Berthelot. Sur le mélange des gaz. *Compt. Rendus*, 126(3), 1898.

[110] Jesse G McDaniel, Chang Yun Son, and Arun Yethiraj. Ab initio force fields for organic anions: Properties of [BMIM][TFSI],[BMIM][FSI], and [BMIM][OTf] ionic liquids. *The Journal of Physical Chemistry B*, 122(14):4101–4114, 2018.

[111] Anirban Mondal and Sundaram Balasubramanian. Quantitative prediction of physical properties of imidazolium based room temperature ionic liquids through determination of condensed phase site charges: A refined force field. *The Journal of Physical Chemistry B*, 118(12):3409–3422, 2014.

[112] Nikhil VS Avula, Anwesa Karmakar, Rahul Kumar, and Sundaram Balasubramanian. Efficient parametrization of force field for the quantitative prediction of the physical properties of ionic liquid electrolytes. *Journal of Chemical Theory and Computation*, 17(7):4274–4290, 2021.

[113] Gongyue Huang, Haijin Zhu, Luca Porcarelli, Yady García, Luke A O'Dell, and Maria Forsyth. Study of ion transport in novel protic polymerized ionic liquids and composites. *Macromolecular Chemistry and Physics*, page 2200124, 2022.

[114] Meisam Hasanpoor, Damien Saurel, Rosalía Cid Barreno, Kilian Fraysse, María Echeverría, Maria Jáuregui, Francisco Bonilla, George W Greene, Robert Kerr, Maria Forsyth, et al. Morphological evolution and solid–electrolyte interphase formation on $LiNi_{0.6}Mn_{0.2}Co_{0.2}O_2$ cathodes using highly concentrated ionic liquid electrolytes. *ACS Applied Materials & Interfaces*, 14(11):13196–13205, 2022.

[115] Hyungook Yoon, Adam S Best, Maria Forsyth, Douglas R MacFarlane, and Patrick C Howlett. Physical properties of high Li-ion content n-propyl-n-methylpyrrolidinium bis (fluorosulfonyl) imide based ionic liquid electrolytes. *Physical Chemistry Chemical Physics*, 17(6):4656–4663, 2015.

[116] William L Jorgensen and Julian Tirado-Rives. Chemical theory and computation special feature: potential energy functions for atomic-level simulations of water and organic and biomolecular systems. In *Proceedings of the National Academy of Science*, volume 102, pages 6665–6670, 2005.

[117] Leela S Dodda, Jonah Z Vilseck, Julian Tirado-Rives, and William L Jorgensen. 1.14* CM1A-LBCC: localized bond-charge corrected CM1A charges for condensed-phase simulations. *The Journal of Physical Chemistry B*, 121(15):3864–3870, 2017.

[118] William L Jorgensen and Julian Tirado-Rives. Potential energy functions for atomic-level simulations of water and organic and biomolecular systems. *Proceedings of the National Academy of Sciences*, 102(19):6665–6670, 2005.

[119] Junmei Wang, Romain M Wolf, James W Caldwell, Peter A Kollman, and David A Case. Development and testing of a general amber force field. *Journal of Computational Chemistry*, 25(9):1157–1174, 2004.

[120] William L Jorgensen, Jayaraman Chandrasekhar, Jeffry D Madura, Roger W Impey, and Michael L Klein. Comparison of simple potential functions for simulating liquid water. *The Journal of Chemical Physics*, 79(2):926–935, 1983.

[121] James X Mao. Atomic charges in molecules: a classical concept in modern computational chemistry. *Journal of Postdoctoral Research*, 2(2), 2014.

[122] George Bruhn, Ernest R Davidson, Istvan Mayer, and Aurora E Clark. Löwdin population analysis with and without rotational invariance. *International journal of quantum chemistry*, 106(9):2065–2072, 2006.

[123] WL Cao, C Gatti, PJ MacDougall, and RFW Bader. On the presence of non-nuclear attractors in the charge distributions of Li and Na clusters. *Chemical Physics Letters*, 141(5):380–385, 1987.

[124] Brent H Besler, Kenneth M Merz Jr, and Peter A Kollman. Atomic charges derived from semiempirical methods. *Journal of Computational Chemistry*, 11(4):431–439, 1990.

[125] Lisa Emily Chirlian and Michelle Miller Francl. Atomic charges derived from electrostatic potentials: A detailed study. *Journal of Computational Chemistry*, 8(6):894–905, 1987.

[126] Curt M Breneman and Kenneth B Wiberg. Determining atom-centered monopoles from molecular electrostatic potentials. the need for high sampling density in formamide conformational analysis. *Journal of Computational Chemistry*, 11(3):361–373, 1990.

[127] Christopher I Bayly, Piotr Cieplak, Wendy Cornell, and Peter A Kollman. A well-behaved electrostatic potential based method using charge restraints for deriving atomic charges: The RESP model. *The Journal of Physical Chemistry*, 97(40):10269–10280, 1993.

[128] Carlos Campañá, Bastien Mussard, and Tom K Woo. Electrostatic potential derived atomic charges for periodic systems using a modified error functional. *Journal of Chemical Theory and Computation*, 5(10):2866–2878, 2009.

[129] Thomas A Manz and David S Sholl. Improved atoms-in-molecule charge partitioning functional for simultaneously reproducing the electrostatic potential and chemical states in periodic and nonperiodic materials. *Journal of Chemical Theory and Computation*, 8(8):2844–2867, 2012.

[130] Aleksandr V Marenich, Steven V Jerome, Christopher J Cramer, and Donald G Truhlar. Charge model 5: An extension of hirshfeld population analysis for the accurate description of molecular interactions in gaseous and condensed phases. *Journal of Chemical Theory and Computation*, 8(2):527–541, 2012.

[131] Patrick Bultinck, Christian Van Alsenoy, Paul W Ayers, and Ramon Carbó-Dorca. Critical analysis and extension of the Hirshfeld atoms in molecules. *The Journal of Chemical Physics*, 126(14):144111, 2007.

[132] Ernest R Davidson and Subhas Chakravorty. A test of the Hirshfeld definition of atomic charges and moments. *Theoretica Chimica Acta*, 83(5):319–330, 1992.

[133] Alan E Reed, Robert B Weinstock, and Frank Weinhold. Natural population analysis. *The Journal of Chemical Physics*, 83(2):735–746, 1985.

[134] Thomas A Manz and Nidia Gabaldon Limas. Introducing DDEC6 atomic population analysis: Part 1. Charge partitioning theory and methodology. *RSC Advances*, 6(53):47771–47801, 2016.

[135] Thomas A Manz and David S Sholl. Chemically meaningful atomic charges that reproduce the electrostatic potential in periodic and nonperiodic materials. *Journal of Chemical Theory and Computation*, 6(8):2455–2468, 2010.

[136] Thomas A. Manz. Introducing DDEC6 atomic population analysis: Part 3. comprehensive method to compute bond orders. *RSC Adv.*, 7:45552–45581, 2017.

[137] Nidia Gabaldon Limas and Thomas A Manz. Introducing DDEC6 atomic population analysis: part 2. computed results for a wide range of periodic and nonperiodic materials. *RSC advances*, 6(51):45727–45747, 2016.

[138] Michael Schauperl, Paul S Nerenberg, Hyesu Jang, Lee-Ping Wang, Christopher I Bayly, David L Mobley, and Michael K Gilson. Non-bonded force field model with advanced restrained electrostatic potential charges (RESP2). *Communications Chemistry*, 3(1):1–11, 2020.

[139] Herman JC Berendsen, JPM van Postma, Wilfred F Van Gunsteren, ARHJ DiNola, and Jan R Haak. Molecular dynamics with coupling to an external bath. *The Journal of Chemical Physics*, 81(8):3684–3690, 1984.

[140] Giovanni Bussi, Davide Donadio, and Michele Parrinello. Canonical sampling through velocity rescaling. *The Journal of Chemical Physics*, 126(1):014101, 2007.

[141] Hans C Andersen. Molecular dynamics simulations at constant pressure and/or temperature. *The Journal of Chemical Physics*, 72(4):2384–2393, 1980.

[142] Shūichi Nosé. A molecular dynamics method for simulations in the canonical ensemble. *Molecular Physics*, 52(2):255–268, 1984.

[143] William G Hoover. Canonical dynamics: Equilibrium phase-space distributions. *Physical Review A*, 31(3):1695, 1985.

[144] Shuichi Nosé and ML Klein. Constant pressure molecular dynamics for molecular systems. *Molecular Physics*, 50(5):1055–1076, 1983.

[145] Glenn J Martyna, Mark E Tuckerman, Douglas J Tobias, and Michael L Klein. Explicit reversible integrators for extended systems dynamics. *Molecular Physics*, 87(5):1117–1157, 1996.

[146] Richard Car and Mark Parrinello. Unified approach for molecular dynamics and density-functional theory. *Physical Review Letters*, 55(22):2471, 1985.

[147] Jindal K Shah. Ab initio molecular dynamics simulations of ionic liquids. In *Annual Reports in Computational Chemistry*, volume 14, pages 95–122. Elsevier, 2018.

[148] Jindal K Shah and Edward J Maginn. Molecular simulation of ionic liquids: Where we are and the path forward. *Ionic Liquids Further UnCOILed: Critical Expert Overviews*, pages 149–192, 2014.

[149] Anjali Gaur and Sundaram Balasubramanian. Liquid ethylene glycol: Prediction of physical properties, conformer population and interfacial enrichment with a refined non-polarizable force field. *Physical Chemistry Chemical Physics*, 24(18):10985–10992, 2022.

[150] Dominik Marx and Jurg Hutter. Ab initio molecular dynamics: Theory and implementation. *Modern methods and algorithms of quantum chemistry*, 1(301-449):141, 2000.

[151] Juan S Gómez-Jeria. A new set of local reactivity indices within the Hartree-Fock-Roothaan and density functional theory frameworks. *Canadian Chemical Transactions*, 1(1):25–55, 2013.

[152] Walter Kohn and Lu Jeu Sham. Self-consistent equations including exchange and correlation effects. *Physical Review*, 140(4A):A1133, 1965.

[153] Jürg Hutter, Marcella Iannuzzi, Florian Schiffmann, and Joost VandeVondele. CP2K: Atomistic simulations of condensed matter systems. *Wiley Interdisciplinary Reviews: Computational Molecular Science*, 4(1):15–25, 2014.

[154] Christian Brouder, Gérard HE Duchamp, Frédéric Patras, and Gábor Z Tóth. The Rayleigh-Schrödinger perturbation series of quasi-degenerate systems. *International Journal of Quantum Chemistry*, 112(10):2256–2266, 2012.

[155] Stephan Ehrlich, Jonas Moellmann, Werner Reckien, Thomas Bredow, and Stefan Grimme. System-dependent dispersion coefficients for the DFT-D3 treatment of adsorption processes on ionic surfaces. *ChemPhysChem*, 12(17):3414–3420, 2011.

[156] MJ ea Frisch, GW Trucks, HB Schlegel, GE Scuseria, MA Robb, JR Cheeseman, G Scalmani, VPGA Barone, GA Petersson, HJRA Nakatsuji, et al. Gaussian 16, 2016.

[157] Roy Dennington, Todd Keith, John Millam, et al. Gaussview, version 5. 2009.

[158] Manel Balsera, Sergey Stepaniants, Sergei Izrailev, Yoshitsugu Oono, and Klaus Schulten. Reconstructing potential energy functions from simulated force-induced unbinding processes. *Biophysical Journal*, 73(3):1281–1287, 1997.

[159] Barry Isralewitz, Jerome Baudry, Justin Gullingsrud, Dorina Kosztin, and Klaus Schulten. Steered molecular dynamics investigations of protein function. *Journal of Molecular Graphics and Modelling*, 19(1):13–25, 2001.

[160] Barry Isralewitz, Mu Gao, and Klaus Schulten. Steered molecular dynamics and mechanical functions of proteins. *Current Opinion in Structural Biology*, 11(2):224–230, 2001.

[161] Hui Lu and Klaus Schulten. Steered molecular dynamics simulations of force-induced protein domain unfolding. *Proteins: Structure, Function, and Bioinformatics*, 35(4):453–463, 1999.

[162] Sergei Izrailev, Sergey Stepaniants, Barry Isralewitz, Dorina Kosztin, Hui Lu, Ferenc Molnar, Willy Wriggers, and Klaus Schulten. Steered molecular dynamics. In *Computational molecular dynamics: challenges, methods, ideas*, pages 39–65. Springer, 1999.

[163] Sanghyun Park and Klaus Schulten. Calculating potentials of mean force from steered molecular dynamics simulations. *The Journal of Chemical Physics*, 120(13):5946–5961, 2004.

[164] Justin R Gullingsrud, Rosemary Braun, and Klaus Schulten. Reconstructing potentials of mean force through time series analysis of steered molecular dynamics simulations. *Journal of Computational Physics*, 151(1):190–211, 1999.

[165] Sergei Izrailev, Sergey Stepaniants, Manel Balsera, Yoshi Oono, and Klaus Schulten. Molecular dynamics study of unbinding of the avidin-biotin complex. *Biophysical Journal*, 72(4):1568–1581, 1997.

[166] Helmut Grubmüller, Berthold Heymann, and Paul Tavan. Ligand binding: molecular mechanics calculation of the streptavidin-biotin rupture force. *Science*, 271(5251):997–999, 1996.

[167] Barry Isralewitz, Sergei Izrailev, and Klaus Schulten. Binding pathway of retinal to bacterio-opsin: a prediction by molecular dynamics simulations. *Biophysical Journal*, 73(6):2972–2979, 1997.

[168] Willy Wriggers and Klaus Schulten. Investigating a back door mechanism of actin phosphate release by steered molecular dynamics. *Proteins: Structure, Function, and Bioinformatics*, 35(2):262–273, 1999.

[169] Siewert-Jan Marrink, Oliver Berger, Peter Tieleman, and Fritz Jähnig. Adhesion forces of lipids in a phospholipid membrane studied by molecular dynamics simulations. *Biophysical Journal*, 74(2):931–943, 1998.

[170] Hui Lu, Barry Isralewitz, Andre Krammer, Viola Vogel, and Klaus Schulten. Unfolding of titin immunoglobulin domains by steered molecular dynamics simulation. *Biophysical Journal*, 75(2):662–671, 1998.

[171] Christopher Jarzynski. Nonequilibrium equality for free energy differences. *Physical Review Letters*, 78(14):2690, 1997.

[172] Christopher Jarzynski. Equilibrium free-energy differences from nonequilibrium measurements: A master-equation approach. *Physical Review E*, 56(5):5018, 1997.

[173] Jan Liphardt, Sophie Dumont, Steven B Smith, Ignacio Tinoco Jr, and Carlos Bustamante. Equilibrium information from nonequilibrium measurements in an experimental test of Jarzynski's equality. *Science*, 296(5574):1832–1835, 2002.

[174] Sanghyun Park, Fatemeh Khalili-Araghi, Emad Tajkhorshid, and Klaus Schulten. Free energy calculation from steered molecular dynamics simulations using jarzynski's equality. *The Journal of Chemical Physics*, 119(6):3559–3566, 2003.

[175] Glenn M Torrie and John P Valleau. Monte Carlo free energy estimates using non-boltzmann sampling: Application to the sub-critical Lennard-Jones fluid. *Chemical Physics Letters*, 28(4):578–581, 1974.

[176] Glenn M Torrie and John P Valleau. Nonphysical sampling distributions in Monte Carlo free-energy estimation: Umbrella sampling. *Journal of Computational Physics*, 23(2):187–199, 1977.

[177] Johannes Kästner. Umbrella sampling. *Wiley Interdisciplinary Reviews: Computational Molecular Science*, 1(6):932–942, 2011.

[178] Shankar Kumar, John M Rosenberg, Djamal Bouzida, Robert H Swendsen, and Peter A Kollman. The weighted histogram analysis method for free-energy calculations on biomolecules. i. the method. *Journal of Computational Chemistry*, 13(8):1011–1021, 1992.

[179] Benoît Roux. The calculation of the potential of mean force using computer simulations. *Computer Physics Communications*, 91(1-3):275–282, 1995.

[180] Christian Bartels and Martin Karplus. Multidimensional adaptive umbrella sampling: Applications to main chain and side chain peptide conformations. *Journal of Computational Chemistry*, 18(12):1450–1462, 1997.

[181] Christian Bartels. Analyzing biased Monte Carlo and molecular dynamics simulations. *Chemical Physics Letters*, 331(5-6):446–454, 2000.

[182] Emilio Gallicchio, Michael Andrec, Anthony K Felts, and Ronald M Levy. Temperature weighted histogram analysis method, replica exchange, and transition paths. *The Journal of Physical Chemistry B*, 109(14):6722–6731, 2005.

[183] Alan Grossfield. Wham: the weighted histogram analysis method, version 2.0. 9. *Available at membrane. urmc. rochester. edu/content/wham. Accessed November*, 15:2013, 2013.

[184] Alessandro Laio and Michele Parrinello. Escaping free-energy minima. *Proceedings of the National Academy of Sciences*, 99(20):12562–12566, 2002.

[185] Marcella Iannuzzi, Alessandro Laio, and Michele Parrinello. Efficient exploration of reactive potential energy surfaces using car-parrinello molecular dynamics. *Physical Review Letters*, 90(23):238302, 2003.

[186] Giovanni Bussi, Alessandro Laio, and Michele Parrinello. Equilibrium free energies from nonequilibrium metadynamics. *Physical Review Letters*, 96(9):090601, 2006.

[187] Bernd Ensing, Marco De Vivo, Zhiwei Liu, Preston Moore, and Michael L Klein. Metadynamics as a tool for exploring free energy landscapes of chemical reactions. *Accounts of Chemical Research*, 39(2):73–81, 2006.

[188] Alessandro Laio and Francesco L Gervasio. Metadynamics: A method to simulate rare events and reconstruct the free energy in biophysics, chemistry and material science. *Reports on Progress in Physics*, 71(12):126601, 2008.

[189] Xubo Lin. Applications of molecular dynamics simulations in drug discovery. In *Advances in Protein Molecular and Structural Biology Methods*, pages 455–465. Elsevier, 2022.

[190] Vladimir N Uversky. *Dancing protein clouds: Intrinsically disordered proteins in health and disease, Part A*. Academic Press, 2019.

[191] Alessandro Barducci, Riccardo Chelli, Piero Procacci, Vincenzo Schettino, Francesco L Gervasio, and Michele Parrinello. Metadynamics simulation of prion protein: β-structure stability and the early stages of misfolding. *Journal of the American Chemical Society*, 128(8):2705–2710, 2006.

[192] Tyler K Lytle, Ajay Muralidharan, and Arun Yethiraj. Why lithium ions stick to some anions and not others. *The Journal of Physical Chemistry B*, 125(17):4447–4455, 2021.

[193] Carl Caleman, Paul J Van Maaren, Minyan Hong, Jochen S Hub, Luciano T Costa, and David Van Der Spoel. Force field benchmark of organic liquids: Density, enthalpy of vaporization, heat capacities, surface tension, isothermal compressibility, volumetric expansion coefficient, and dielectric constant. *Journal of Chemical Theory and Computation*, 8(1):61–74, 2012.

[194] George Kaminski, Erin M Duffy, Tooru Matsui, and William L Jorgensen. Free energies of hydration and pure liquid properties of hydrocarbons from the OPLS all-atom model. *The Journal of Physical Chemistry*, 98(49):13077–13082, 1994.

[195] George Kaminski and William L Jorgensen. Performance of the AMBER94, MMFF94, and OPLS-AA force fields for modeling organic liquids. *The Journal of Physical Chemistry*, 100(46):18010–18013, 1996.

[196] Junmei Wang and Tingjun Hou. Application of molecular dynamics simulations in molecular property prediction. 1. density and heat of vaporization. *Journal of Chemical Theory and Computation*, 7(7):2151–2165, 2011.

[197] Srimayee Mukherji, Nikhil VS Avula, and Sundaram Balasubramanian. Refined force field for liquid sulfolane with particular emphasis to its transport characteristics. *ACS Omega*, 5(43):28285–28295, 2020.

[198] Daan Frenkel and Berend Smit. *Understanding molecular simulation: from algorithms to applications*, volume 1. Elsevier, 2001.

[199] Michael P Allen and Dominic J Tildesley. *Computer simulation of liquids*. Oxford University Press, 2017.

[200] Melville S Green. Markoff random processes and the statistical mechanics of time-dependent phenomena. ii. irreversible processes in fluids. *The Journal of Chemical Physics*, 22(3):398–413, 1954.

[201] Ryogo Kubo. Statistical-mechanical theory of irreversible processes. I. General theory and simple applications to magnetic and conduction problems. *Journal of the Physical Society of Japan*, 12(6):570–586, 1957.

[202] Hyun-Myung Chun, Qi Gao, and Jordan M Horowitz. Nonequilibrium Green-Kubo relations for hydrodynamic transport from an equilibrium-like fluctuation-response equality. *Physical Review Research*, 3(4):043172, 2021.

[203] Jean-Pierre Hansen and Ian R McDonald. Theory of simple liquids. *Physics Today*, 41(10):89–90, 1988.

[204] Debra J Searles and Denis J Evans. The fluctuation theorem and Green–Kubo relations. *The Journal of Chemical Physics*, 112(22):9727–9735, 2000.

[205] Melville S Green. Brownian motion in a gas of noninteracting molecules. *The Journal of Chemical Physics*, 19(8):1036–1046, 1951.

[206] Melville S Green. Comment on a paper of Mori on time-correlation expressions for transport properties. *Physical Review*, 119(3):829, 1960.

[207] Ryogo Kubo, Mario Yokota, and Sadao Nakajima. Statistical-mechanical theory of irreversible processes. II. Response to thermal disturbance. *Journal of the Physical Society of Japan*, 12(11):1203–1211, 1957.

[208] Berk Hess. Determining the shear viscosity of model liquids from molecular dynamics simulations. *The Journal of Chemical Physics*, 116(1):209–217, 2002.

[209] Manish Agarwal and Charusita Chakravarty. Evaluation of collective transport properties of ionic melts from molecular dynamics simulations. *Journal of Chemical Sciences*, 121(5):913–919, 2009.

[210] Wei Zhao, Frédéric Leroy, Berit Heggen, Stefan Zahn, Barbara Kirchner, Sundaram Balasubramanian, and Florian Müller-Plathe. Are there stable ion-pairs in room-temperature ionic liquids? Molecular dynamics simulations of 1-n-butyl-3-methylimidazolium hexafluorophosphate. *Journal of the American Chemical Society*, 131(43):15825–15833, 2009.

[211] Peter Atkins, Peter William Atkins, and Julio de Paula. *Atkins' Physical Chemistry*. Oxford University Press, 2014.

[212] The radial distribution functions: definitions . https://isaacs.sourceforge.net/phys/rdfs.html. Accessed: 2022-09-25.

[213] AZMS Rahman, KS Singwi, and A Sjölander. Theory of slow neutron scattering by liquids. I. *Physical Review*, 126(3):986, 1962.

[214] R Zorn. Deviation from gaussian behavior in the self-correlation function of the proton motion in polybutadiene. *Physical Review B*, 55(10):6249, 1997.

[215] Suman Chakrabarty, Dwaipayan Chakrabarti, and Biman Bagchi. Power law relaxation and glassy dynamics in lebwohl-lasher model near the isotropic-nematic phase transition. *Physical Review E*, 73(6):061706, 2006.

[216] Léon Van Hove. Correlations in space and time and born approximation scattering in systems of interacting particles. *Physical Review*, 95(1):249, 1954.

[217] Paul Hopkins, Andrea Fortini, Andrew J Archer, and Matthias Schmidt. The van Hove distribution function for brownian hard spheres: Dynamical test particle theory and computer simulations for bulk dynamics. *The Journal of Chemical Physics*, 133(22):224505, 2010.

[218] Jiajia Li, Ruiyao He, Hao Yuan, Fang Fang, Guobing Zhou, and Zhen Yang. Molecular insights into the effect of asymmetric anions on lithium coordination and transport properties in salt-doped poly (ionic liquid) electrolytes. *Macromolecules*, 55(15):6703–6715, 2022.

[219] Sayantan Acharya, Ujjwal Kumar Nandi, and Sarika Maitra Bhattacharyya. Fickian yet non-Gaussian behaviour: A dominant role of the intermittent dynamics. *The Journal of Chemical Physics*, 146(13):134504, 2017.

[220] Arnab Mukherjee, Sarika Bhattacharyya, and Biman Bagchi. Pressure and temperature dependence of viscosity and diffusion coefficients of a glassy binary mixture. *The Journal of Chemical Physics*, 116(11):4577–4586, 2002.

[221] Junko Habasaki, Carlos Leon, and KL Ngai. Dynamics of glassy, crystalline and liquid ionic conductors. *Top Appl Phys*, 132:355–410, 2017.

[222] S Balasubramanian and KJ Rao. Preferential paths in alkali ion migration and the mixed alkali effect in silicate glasses. *The Journal of Physical Chemistry*, 97(35):8835–8838, 1993.

[223] S Balasubramanian and KJ Rao. A molecular dynamics study of the mixed alkali effect in silicate glasses. *Journal of Non-Crystalline Solids*, 181(1-2):157–174, 1995.

[224] V Balakrishnan. The velocity autocorrelation function. In *Elements of Nonequilibrium Statistical Mechanics*, pages 31–46. Springer, 2021.

[225] Noémie Elgrishi, Kelley J Rountree, Brian D McCarthy, Eric S Rountree, Thomas T Eisenhart, and Jillian L Dempsey. A practical beginner's guide to cyclic voltammetry. *Journal of Chemical Education*, 95(2):197–206, 2018.

[226] Jie Xiao, Qiuyan Li, Yujing Bi, Mei Cai, Bruce Dunn, Tobias Glossmann, Jun Liu, Tetsuya Osaka, Ryuta Sugiura, Bingbin Wu, et al. Understanding and applying coulombic efficiency in lithium metal batteries. *Nature Energy*, 5(8):561–568, 2020.

[227] Edward P Randviir and Craig E Banks. Electrochemical impedance spectroscopy: An overview of bioanalytical applications. *Analytical Methods*, 5(5):1098–1115, 2013.

[228] Theophanides Theophile. *Infrared spectroscopy: Materials science, engineering and technology*. BoD–Books on Demand, 2012.

[229] Peter James Lingane and Dennis G Peters. Chronopotentiometry. *CRC Critical Reviews in Analytical Chemistry*, 1(4):587–634, 1971.

[230] Kevin N Wood and Glenn Teeter. Xps on Li-battery-related compounds: analysis of inorganic sei phases and a methodology for charge correction. *ACS Applied Energy Materials*, 1(9):4493–4504, 2018.

[231] X Zhang and M Cresswell. Chapter 3—materials characterization of inorganic controlled release. *Inorganic Controlled Release Technology*, pages 57–91, 2016.

[232] WL Bragg. Report of the philosophical society. *Nature*, 90:402, 1912.

[233] William Lawrence Bragg. The specular reflection of x-rays. *Nature*, 90(2250):410–410, 1912.

[234] William Henry Bragg. X-rays and crystals. *Nature*, 90(2243):219–219, 1912.

[235] Thomas L Hayes and RFW Pease. The scanning electron microscope: principles and applications in biology and medicine. *Advances in Biological and Medical Physics*, 12:85–137, 1968.

[236] Gregory P Holmes-Hampton, Wing-Hang Tong, and Tracey A Rouault. Biochemical and biophysical methods for studying mitochondrial iron metabolism. In *Methods in Enzymology*, volume 547, pages 275–307. Elsevier, 2014.

Chapter 2

A refined force field for liquid sulfolane with particular emphasis on its transport characteristics

2.1 Introduction

Sulfolane (IUPAC: thiolane 1,1-dioxide, CAS: 126-33-0) is an indispensable industrial solvent. Since sulfolane is a member of the sulfone class of molecules, it is also commonly referred to as tetramethylene sulfone. Liquid sulfolane has high thermal stability and a wide liquidus range, making it a very useful solvent for several high-temperature reactions even in the presence of strong acids and bases [1]. Sulfolane is particularly useful in the separation of aromatic hydrocarbons from a mixture of hydrocarbons, and in the sulfinol process of purifying natural gas through the removal of carbon dioxide, hydrosulfuric acid, and a few other sulfur-containing compounds [1]. In recent times, however, liquid sulfolane is also being studied for its benefits as a solvent in lithium(Li)-ion and sodium(Na)-ion batteries [2–7]. High oxidative stability, thermal stability, and relative permittivity (43.3 [8]) of sulfolane, make it a strong prospective solvent candidate for electrolytes in highly-stable, high-voltage batteries [2–4]. Certain high salt concentration electrolytes formed with sulfolane in Li-S batteries have proven particularly promising. In these batteries, sulfolane behaves as a *sparingly soluble* solvent for Li_2S_X. These batteries are stable with better cycling, high-durability, and high energy density [5]. Combined with hydrofluoroethers,

Work reported in this chapter was published with the same title in *ACS Omega* **2020**, *5*, 28285–28295 (https://doi.org/10.1021/acsomega.0c04243)

sulfolane has the added advantage of enhancing the diffusivity and rate-capability in these Li-S batteries [5].

Active research in the use of high concentrations of a lithium (or sodium) salts in sulfolane as battery electrolytes are in progress since these super-concentrated electrolytes address both the increased energy and safety requirements for next-generation rechargeable batteries [2, 5]. However, it is also important to note that sulfone based electrolytes have certain disadvantages in being used as a battery component. Some of these are their high melting point (except sulfolane with melting point $T_m = 301.55K$) [1], high viscosity (of liquid-sulfolane - 10.35 mPa·s at 303.15 K [1]), inferior wettability of electrodes and separators, and formation of unstable solid-electrolyte interface (SEI) materials [9]. These challenges can be overcome, however. For example, sulfolane in combination with non-solvating fluorinating ether overcomes these challenges in addition to providing high-efficiency cycling of Li-metal even at high Li salt concentrations [10].

The broad applicability of sulfolane partially finds its footing in its 'two-in-one' structure- a ring composed predominantly of carbon atoms and a SO_2 crown. Although aprotic, the SO_2 group of sulfolane is the source of its significant dipole moment (5.65 Debye from MP2 level calculations carried out in this work). The massive dipole moment contributes to its high relative permittivity of 43.3 [8], when compared to other dipolar aprotic solvents. Sulfolane's ring of carbon atoms and its large dielectric constant come with a twin-benefit. Sulfolane is miscible in several polar organic compounds, and at the same time, as a solvent, it solvates many inorganic compounds [1, 11]. Examining its SO_2 group more closely, the vibrational spectrum of SO_2 in sulfolane is very typical of most sulfones and is therefore also of wide interest in understanding this class of compounds [12]. Keeping these in mind, a comprehensive understanding of sulfolane's physicochemical nature, and exploring the full utility of this promising multipurpose solvent is important. Apart from experiments, this necessity can also be met through computational studies on sulfolane by providing molecular level insights into its properties, which may serve as new directions for future experimental studies.

In the past, molecular simulations, molecular dynamics (MD) simulations and configurational bias Monte Carlo simulations have used general and refined force fields to accurately capture several, if not all experimentally reported thermophysical and thermochemical properties of substances [13–23]. However, a force field that accurately captures the transport properties of sulfolane and whose potential energy surface (PES) is in good agreement with that obtained from quantum calculations is currently absent. The availability of such a force field is of paramount importance to realizing the utility of sulfolane-based battery electrolytes. The simulations of Aparicio and coworkers in Ref. 24 on sulfolane

reproduces the density, heat of vaporization, and self-diffusion constant in fair comparison with experiments; however, the shear viscosity predicted by the model is half of that of the experimental value, which is somewhat surprising as the self-diffusion coefficient predicted by the model too is 23% lesser than the experimental value. Furthermore, the electric dipole moment of a single molecule of sulfolane calculated from the model is just 3.9 Debye when compared to the value calculated from MP2 level quantum calculations of 5.65 Debye (*vide infra*). Thus, our continued search for a more physicochemically meaningful and quantitatively reliable force field for sulfolane is not out of place.

While general, all-purpose force fields capture relatively simpler physical properties such as the density of such solvents, quantitatively accurate force fields for transport properties of sulfolane are required, which can enable molecular simulations to provide insights and directions to experimental research on a near-equal footing. The work presented in this chapter is aimed in that direction.

In this study, we aim to arrive at an effective force field parameter set for sulfolane with particular emphasis on selecting appropriate non-bonded descriptors such as site charges and Lennard-Jones parameters for use in molecular simulations. The atomic-site charges in a liquid can, in principle, be considerably different from those obtained through quantum gas-phase calculations [21]. To derive liquid phase atomic-site charges for our MD simulations of bulk sulfolane, quantum Density Functional Theory (DFT) optimizations of independent snapshots obtained from the liquid phase of sulfolane were carried out. These snaphshots were selected from MD simulations using a generic force field and gas-phase DDEC6 [25] charges (see computational methods). Later, this electron density was partitioned to atomic site charges through the well-established density-derived electrostatic and chemical (DDEC6) charge partitioning method [25]. Correspondingly, we have also modified the Lennard-Jones interaction parameters to improve the match to quantum potential energy surface scans between a pair of molecules. In addition to refining the non-bonding parameters, we have derived the equilibrium values for bond-lengths and bond-angles through single-molecule quantum geometry optimizations at MP2 level of theory. The dihedral parameters used in Ref. 2 were retained in the current study. We find, our force field parameters, while being the closest in reproducing quantum potential energy scans, predict properties such as density, heat of vaporization nearly at par with force fields such as the Optimized Potentials for Liquid Simulations (OPLS) force field [15]. This refined force field predicts diffusivity and viscosity, and interfacial properties of sulfolane in better agreement with experiments than other force fields. As a test of the applicability of the refined parameters, in the results section, we provide a comparison between the values of several experimentally determined properties against those predicted by our force field and two other general force fields. We also calculate various properties of sulfolane as a

function of temperature and compare them against values reported from experiments.

2.2 Computational methods

The non-planar nature of sulfolane molecule is illustrated in Figure 2.1 which also provides atom labels.

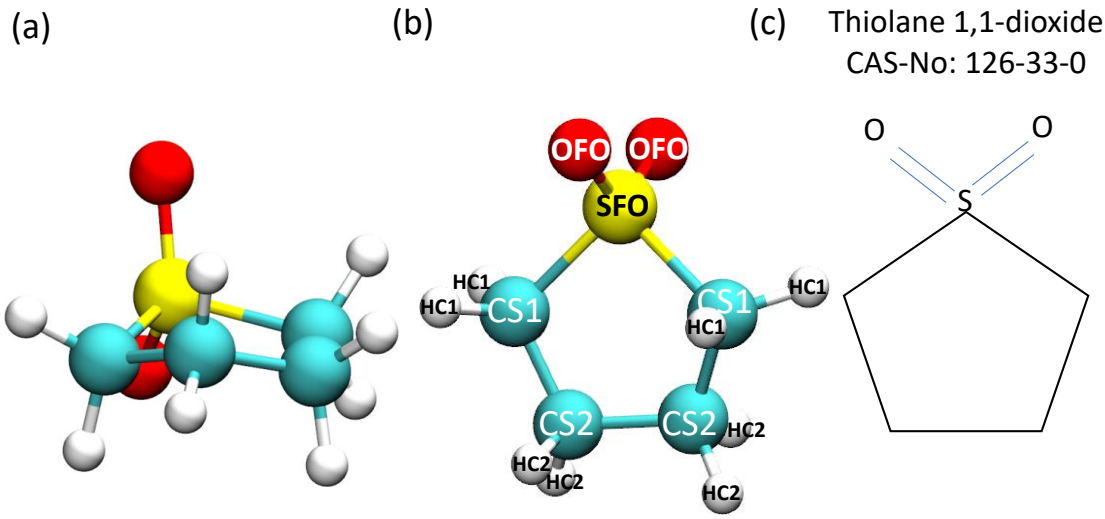

Figure 2.1: (a) Molecular structure of sulfolane. (b) Atom types of sulfolane. (c) Chemical identifiers of compound sulfolane.

Liquid sulfolane modelled at 303K and 1 bar using the force field described in Ref. 2 yielded a reasonably accurate density of 1284 kg·m^{-3}. However, the self-diffusion coefficient of sulfolane using the force field of Ref. 2 ($D_{\mathrm{Ref.2}}$ was calculated to be 6.0×10^{-13} m^2·s^{-1}) was more than two orders of magnitude lesser than the experimental value of $D_{exp,extrapolated} = 14.72 \times 10^{-11}$ m^2·s^{-1} obtained of extrapolation from experimental data in Ref. 2. As a consequence of the underestimation of diffusivity, the viscosity of sulfolane was inestimable from molecular simulations even when calculated through a long MD trajectory of 25 ns duration.

To investigate the applicability of OPLS force field of sulfolane, we first obtained its parameters from the LigPArGen Server [26–28]. Although we found that the OPLS force field with the 1.14*CM1A-LBCC charges [27] estimates many physical properties of liquid sulfolane well, the viscosity calculated using this force field was around twice the experimentally reported value of 10.05 mPa·s [29]. Hence, a refined force field for sulfolane capturing its transport properties accurately, remained a necessity.

We started the force field refinement of sulfolane using the parameters used in Ref. 2 as our initial guess.

$$U = \frac{1}{2}\sum_{bonds} k_b(r-r_0)^2 + \frac{1}{2}\sum_{angles} k_\theta(\theta-\theta_0)^2 + \sum_{dihedrals}\sum_{n=1}^{\{multiplicity} k_\phi(1+cos(n\phi-\phi_s)) + \sum_i\sum_{j\neq i} 4\epsilon_{ij}\left[\left(\frac{\sigma_{ij}}{r_{ij}}\right)^{12} - \left(\frac{\sigma_{ij}}{r_{ij}}\right)^{6}\right] + \frac{1}{4\pi\epsilon_0}\sum_i\sum_{j\neq i}\frac{q_i q_j}{r_{ij}} \quad (2.1)$$

The total potential energy of the system is a sum total of energies from non-bonded contributions such as the Coulombic and the Lennard-Jones interactions and those from the bonded contributions of bond, angle and dihedral-angle excitations (Equation 2.1). We refine the Coulombic and Lennard-Jones interactions, bond and angle equilibrium values to arrive at the refined set of parameters reported here. r_0 is equilibrium bond-length, k_b is bond force-constant, θ_0 is equilibrium bond-angle, k_θ is angle force-constant, ϕ, k_ϕ, and ϕ_s are dihedral parameters. σ_{ij} and ϵ_{ij} are LJ parameters, r_{ij} is the distance between the centers of the i^{th} and j^{th} atoms. ϵ_0 is the permittivity of free-space and q_i is the atomic site charge of the i^{th} atom.

2.2.1 Non-bonded parameters

1. Deriving atomic-site charges

Method of refining atomic-site charges (DDEC) used here has earlier been employed to refine parameters for imidazolium cation based ionic liquids. Refined for imidazolium cation–PF_6^- anion pair, these parameters were found to be transferable across a family of imidazolium-based ionic liquids [21, 30, 31]. The fact that this procedure, when systematically applied to two very different kinds of liquids has yielded reliable parameters (property predictions are comparable to experimentally measured values) prompts us to believe that this procedure can now be used to refine force field parameters for many different classes of liquids. It is also possible that the refined force field for sulfolane reported here is extendable with minor modifications to the entire class of sulfone compounds.

In order to derive atomic-site charges from DFT calculations of liquid sulfolane, seven independent snapshots were chosen from a NVT MD run. This MD run used the force field of Ref. 2 barring the atomic-site charges. Atomic-site charges used were obtained for a single sulfolane molecule from DDEC6 [25] calculations post a quantum optimization using B3LYP/6-311g(d (Table A.1). These gas-phase DDEC6 charges obtained were used

in the MD simulation contained twenty-six sulfolane molecules in liquid-phase at 303 K. The linear dimension of the NPT equilibrated box was 16.3 Å. These snapshots were then geometry optimized within quantum density functional theory using CP2K software (version 6.1) [32] with the Perdew, Burke, and Ernzerhof (PBE) exchange-correlation functional [33] and Grimme's D3 empirical van der Waals corrections [34]. A convergence criterion of 10^{-6} a.u. for the gradient of electronic wave functions, and 5×10^{-3} a.u. for the force on the nuclei, were employed. The core-electrons and nuclei were accounted for using the Geodecker–Teter–Hutter (GTH) pseudopotentials [35, 36]. All valence electrons were represented by triple-ζ double-polarized basis sets with an energy cutoff of 320 Ry. The coordinates obtained from this minimization were used to obtain valence electron density at the same level of theory. This density was stored in a cube file and was used to obtain DDEC6 liquid phase atomic charges using Chargemol software (Version 3.5) [37]. The atomic-site charge distribution over seven snapshots were fairly narrow (see Appendix Figure A.1) and hence their mean was utilizable. More detailed discussions on the applicability of this procedure followed in deriving condensed-phase charges can be found in Ref. 30. Site charges were averaged over all the molecules of a snapshot as well as over all the seven snapshots to arrive at the final liquid phase DDEC6 charges employed in the refined force field simulations. These charges are presented in Table 2.1. Charges from Ref. 2 and those from OPLS [27] are also provided for the sake of completeness.

Atom type	Ref. 2	OPLS	This work
SFO	1.56000	1.22980	1.067020
OFO	-0.78000	-0.57030	-0.562630
CS1	-0.12000	-0.46675	-0.324400
CS2	-0.12000	-0.16105	-0.135542
HC1	0.06000	0.16740	0.142387
HC2	0.06000	0.12420	0.102144

Table 2.1: Atomic site charges q(e) of sulfolane derived from quantum calculations of bulk liquid and used in the simulations reported here. Charges from Ref. 2 and of the OPLS force field [26–28] are provided for the sake of completeness.

2. Refinement of Lennard-Jones parameters

The Lennard-Jones (LJ) parameters were obtained by conducting several trials to fit quantum chemical rigid potential energy surface (PES) scans of a pair of sulfolane molecules as a function of the distance between them. The PES scans were performed using Gaussian 16 software [38]. These scans were performed in gas phase along two different directions of

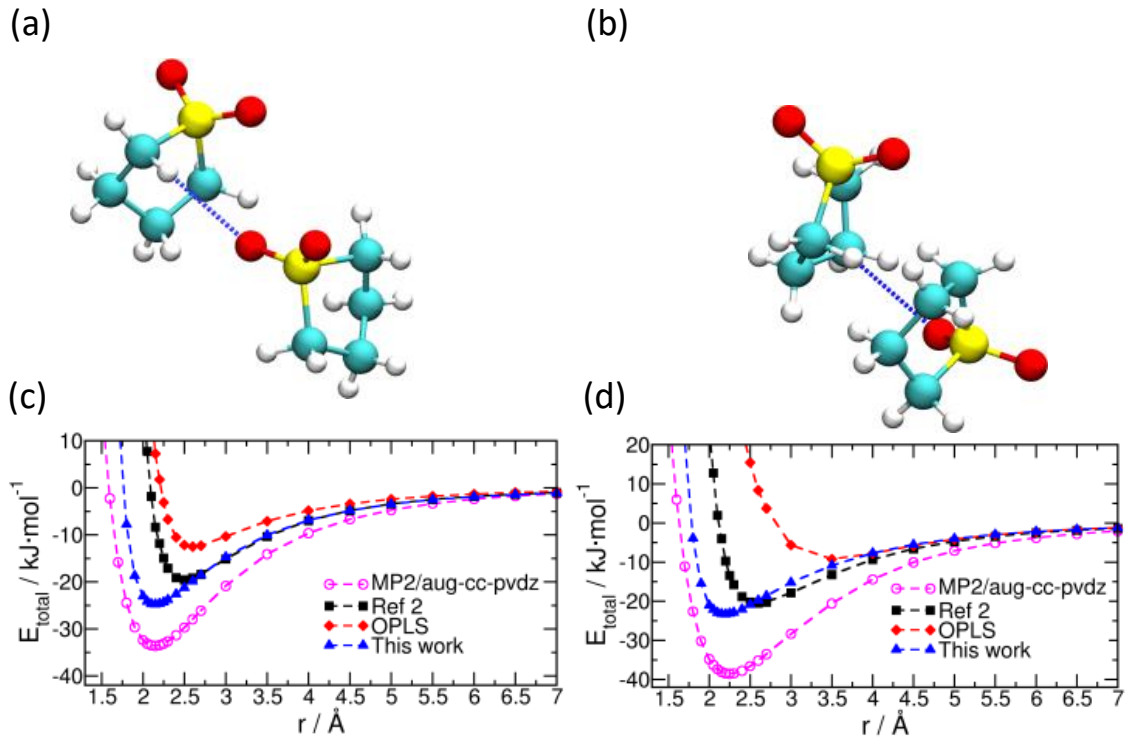

Figure 2.2: (a) & (b) Directions along which a pair of sulfolane molecules are made to approach each other during the potential energy scan (PES). (c) & (d) Corresponding PE surfaces.

approach of the molecules (shown in Figure 2.2(a) and (b)). The two initial configurations for gas-phase calculations were created in GaussView software (version 5.0.9. [39]). Subsequently, the LJ parameters employed in Ref. 2 were suitably modified through several trials so that the total potential energy calculated with the force field matches the quantum chemical PES as closely as possible (shown in Figure 2.2(c) and (d)). Since the PES calculations were carried out in gas phase, the gas-phase DDEC6 site charges presented in Table A.1 were used to arrive at the refined LJ parameters. The LJ parameters of Ref. 2, OPLS, and our refined force field (used henceforth in this work) are provided in Table 2.2. The PES of both OPLS and of Ref. 2 are much shallower when compared to the MP2 result.

The bonded parameters (bond stretch, and angle bending) used in the current chapter are provided in the Appendix Tables A.2 and A.3. Sulfolane, being a cyclic molecule, was anticipated to have large dihedral energy barriers compared to k_BT, where k_B is the Boltzmann constant and T, temperature (303 to 398) K. Hence, we do not expect that at these temperatures, the dihedral angles deviate much from the equilibrium structure. Hence, dihedral parameters were adopted as is from Ref. 2 without any refinement.

Atom type	σ			ϵ		
	Ref. 2	OPLS	This work	Ref. 2	OPLS	This work
SFO	3.55	3.55	3.80	1.046	1.046	2.000
OFO	2.96	2.96	2.90	0.879	0.711	0.711
CS1	3.50	3.50	3.55	0.276	0.276	0.100
CS2	3.50	3.50	3.50	0.276	0.276	0.100
HC1	2.50	2.50	2.00	0.126	0.126	0.050
HC2	2.50	2.50	2.50	0.126	0.126	0.067

Table 2.2: Lennard-Jones (LJ) parameters for all the force fields studied - σ_{ii} (Å) and ϵ_{ii} (kJ·mol^{-1}) of equation 2.1. Those of Ref. 2 and of OPLS [26–28] are provided for the sake of completeness.

2.2.2 Molecular dynamics simulations of liquid sulfolane

Liquid sulfolane was modelled using these refined parameters. Classical MD simulations were performed using GROningen MAchine for Chemical Simulations, i.e., GROMACS package [40–42] (version 2018.3). Particle–particle mesh Ewald (PPPM) solver was used to calculate the long-range electrostatic interactions [43]. A precision of 10^{-5} was used for the same. The leap-frog algorithm, with a time step of 1 fs, was used to evolve the system in time. Atom coordinates were dumped at an interval of 1 ps. C–H covalent bonds were held constrained with the LINCS (Linear Constraint Solver) algorithm present in GROMACS [44]. Verlet algorithm used by GROMACS was employed for neighbor lists [45]. Van der Waals and Coulomb cutoff distances were both taken to be 12Å, with a neighbor list up to 14Å. Interactions between different atom types was defined using geometric mean, i.e., $\sigma_{ij} = (\sigma_{ii}\sigma_{jj})^{1/2}$ and $\epsilon_{ij} = (\epsilon_{ii}\epsilon_{jj})^{1/2}$. The same combining rules are used by OPLS and our calculations using the force field in Ref. 2. 1-2 and 1-3 pairs interact via bond stretch and bending interactions only. For the non-bonding interaction involving 1-4 pairs, a scale factor of 0.5 is applied to both the Lennard-Jones and Coulomb interactions. For all remaining atom pairs, the scale factor for non-bonding interactions is 1.0. Long-range energy and pressure dispersion corrections were applied. The Nosé–Hoover thermostat [46] was employed with a coupling time-constant of 0.5 ps. NVT production trajectories were used for a majority of the analyses. Berendsen [47] and Parrinello-Rahman barostats [48, 49] were used for constant-temperature and constant-pressure NPT equilibration, and NPT production runs, respectively. In either case, a coupling time-constant of 2 ps was used. The barostat was coupled to the system every 10 steps when using the Berendsen barostat and every step with the Parrinello-Rahman barostat. An initial configuration of 800 sulfolane molecules was generated using the packing optimization for the automated generation of starting configurations for molecular

dynamics simulations (Packmol-Version 18.002) software [50]. Minimization using the steepest gradient method was followed by constant-NPT equilibration of the system for 10 ns. Constant-NPT production runs of 25 ns followed this. After that, constant-NVT equilibration for 10 ns were performed. In the OPLS force field framework and that of the refined force field reported here, the NVT productions runs at 303 K were of duration 50 ns each. Only in the case of the simulations carried out using the force field of Ref. 2 at 303 K, owing to its sluggishness, an NVT production of 1 μs was required to reach the diffusive regime.

Liquid sulfolane was simulated at several temperatures in the range (303 K to 398 K) using the refined force field. NVT production runs of 50 ns were conducted for simulations at 303 K, 25 ns at 323 K and 348 K, and over 12 ns at 373 K and 398 K. Other details for these runs remain the same as those for the one performed at 303 K.

Periodic boundary conditions were applied along all three directions. The NPT equilibrated box-lengths to accommodate 800 sulfolane molecules for various force fields studied here, and for the various temperatures at which the refined force field was studied, are given in Appendix Table A.4. Visualization was carried out in Visual Molecular Dynamics (VMD) software [51].

2.3 Results and Discussion

All percentage deviations mentioned are calculated from the corresponding experimental value, unless stated otherwise. All expanded uncertainties (U) are those calculated on the average value of the property reported.

2.3.1 Density

Average density for each force field studied was calculated by considering 25 ns of the NPT production run (after NPT equilibration) (Table 2.3). The data was divided into five blocks of 5 ns duration each. Method of calculating expanded uncertainty (U) on the mean have been provided in Appendix A. The NPT equilibrated box-lengths are provided in Table A.4. As shown in Table 2.3, percentage errors in density ($\Delta\rho$) with respect to the experimental density, defined $\Delta\rho = \frac{(\rho_{sim}-\rho_{exp})}{\rho_{exp}} \times 100$ for all force fields are within 3%.

The force field also predicts the temperature dependence of the density of liquid sulfolane rather well. These values are provided in (Table 2.4 and Figure 2.3).

Force field	ρ_{sim} [a]	$\Delta\rho$ (%)
Force field of Ref. 2	1297.15 ± 1.8	2.71
OPLS	1250.00 ± 0.3	-1.02
This work	1292.28 ± 0.4	2.33
Literature	1262 [52], 1262.3 [29]	–
	1261.9 [53], 1260.4 [54]	–
	1260.4 [55], 1260.80 [56]	–

[a] The expanded uncertainty (U) is reported at 95% level of confidence.

Table 2.3: Density ρ_{sim} (kg·m^{-3}) of liquid sulfolane estimated by all force fields at temperature T = 303 K and pressure p = 1 bar. Experimental density at the same state point is ρ_{exp} = 1262.9 kg·m^{-3} (Ref. 57)

Temperature / K	$\rho_{\text{This work}}$ [a,b]	ρ_{exp}	$\Delta\rho$ (%)
303	1292.28 ± 0.4	1262.9 [57]	2.33
313	1280.66 ± 0.4	1254.1 [57]	2.12
323	1268.89 ± 0.5	1245.2 [57]	1.90
348	1239.15 ± 0.7	1222.9 [53]	1.33
373	1208.09 ± 0.4	1200.9 [53]	0.60
398	1177.21 ± 0.4	1178.9 [53]	-0.14

[a] The expanded uncertainty (U) is reported at 95% level of confidence.
[b] Density data follows a linear fit, y = mx + c, with m = -1.21 kg·m^{-3}·K^{-1}, and c = 1660.18 kg·m^{-3}.

Table 2.4: Comparison between density of liquid sulfolane from this work $\rho_{\text{This work}}$ (kg·m^{-3}) with the density of sulfolane from experiments ρ_{exp} (kg· m^{-3}) in the temperature range T = (303 to 398) K, and at pressure p = 1 bar. $\Delta\rho$ is calculated with respect to the corresponding experimental value.

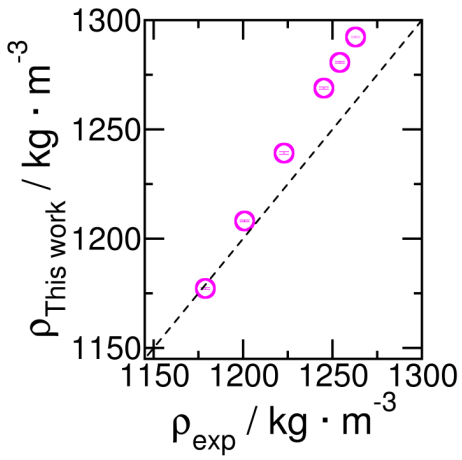

Figure 2.3: Comparison between densities predicted from this work with those from experiments in the temperature range, T = 303K - 398K and at pressure p = 1 bar.

2.3.2 Intermolecular Structure: Radial Distribution Functions

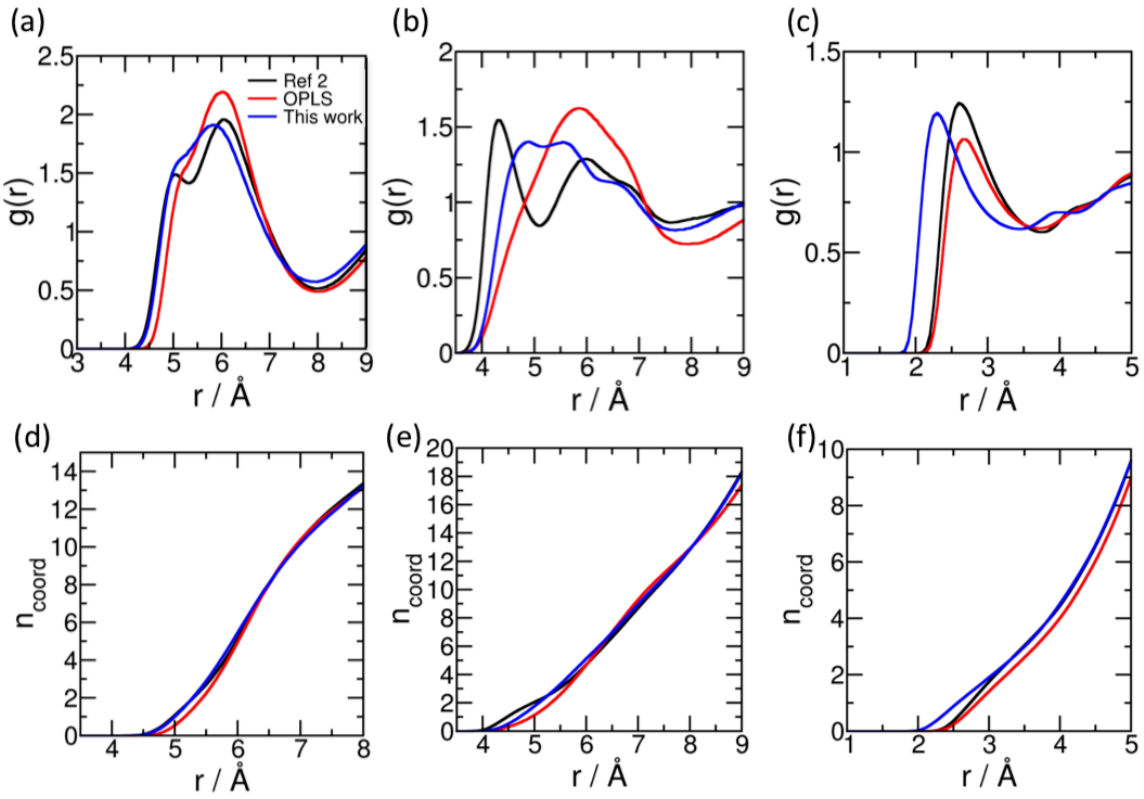

Figure 2.4: Radial distribution function between the following pairs of atoms at 303 K - (a) Center of Mass (COM)–COM, (b) SFO-SFO, and (c) OFO-HC1 (intermolecular). (d)-(f) coordination numbers corresponding to (a)-(c), respectively. Black - force field of Ref. 2, red - OPLS, and blue - this work.

The intermolecular radial distribution functions (RDF) between select pairs of sites calculated from all the three force fields at 303 K are presented in Figure 2.4. The center of mass (COM)–COM RDF (Figure 2.4(a)) and SFO-SFO RDF (Figure 2.4(b)) suggest that the first coordination shell of sulfolane ends a little short of 8 Å. Also, reminiscent of liquid argon, the first coordination shell contains 13 molecules on an average. From Figure 2.4(c), we see that the HC1 hydrogens can be found closer to the OFO oxygen in simulations using the force field reported here in comparison to the remaining two. This may be a consequence of the fact that the refined force field reported here justifiably identifies two types of hydrogens (HC1 and HC2), depending on the electronegativity of the carbon atoms (CS1 or CS2) they are attached to. Although OPLS force field too considers sulfolane to have two hydrogen and carbon atom types in terms of their charges, its LJ parameters do not distinguish between these two types. The position of the first peak of OFO-HC1 RDF obtained using the force field of Ref. 2 and that from OPLS match with each other and is at

a slightly larger distance than the one obtained from the refined force field; this observation is consistent with the respective PES presented in Figure 2.2. RDF for other atom-pairs are reported in Figure A.3.

2.3.3 Molecular Dipole Moment & Intermolecular Dipole Correlations

The dipole moment from each force field of a single sulfolane molecule was calculated using the geometry optimized structure obtained from MP2 level of theory, but with charges as prescribed by the respective force field. These values are tabulated in Table 2.5. The magnitude of dipole moment from OPLS force field and that from our force field are within 5% of the MP2 value, while that described in Ref. 2 is within 10% of the same.

Description	p / Debye	Δp (%)
MP2/aug-cc-pvdz	5.646	–
Force field of Ref. 2	6.178	9.42
OPLS	5.425	-3.91
This work	5.922	4.89

Table 2.5: Dipole moment magnitude p (Debye) of a sulfolane molecule in gas phase obtained by all force fields and a quantum chemical calculation. The dipole moment predicted from the refined force field (This work) uses the derived DDEC6 liquid phase charges reported under "This work" in Table 2.1. The experimentally determined gas-phase dipole moment is 4.69 Debye [1]. The deviation Δp has been calculated w.r.t. the MP2/aug-cc-pvdz value.

One can expect the significantly large electric dipole moment (Table 2.5) of sulfolane to influence the intermolecular structure and orientation in its liquid phase. As mentioned earlier, MP2 calculations of the single molecule yield a dipole moment value of 5.65 Debye (Figure 2.5(a)). Despite the fact that sulfolane possesses a gas phase dipole moment which is significantly higher than that of water (1.85 Debye [58]), its static dielectric constant is much lesser (43.3 [8]) than that of liquid water (76.55 at 303 K [59]) and is comparable to that of DMSO (46 [60] at 298K).

The molecular size (volume) of a sulfolane molecule is approximately 101.04 $cm^3 \cdot mol$ (167.8 $Å^3$ per molecule) obtained from single molecule gas-phase quantum calculations using Gaussian 16 software [38]. Details for this calculation are provided in Appendix A. This large molecular volume and hence large intermolecular distances even to the first solvation shell (see COM-COM pair-correlation function in Figure 2.4(a)), limits the extent of intermolecular orientational preferences that can potentially arise from its large

dipole moment; The large molecular volume of sulfolane results in its smaller dielectric-constant of in comparison to dimethyl-sulfoxide (DMSO) [1] and water. However, the large dipole-moment of sulfolane may possibly be a part of the reason behind its higher dielectric-constant in comparison to other polar aprotic solvents [1].

Figure 2.5(b) shows the combined probability density function, P(r,$cos\theta$), representing orientational preference and spatial distribution of dipoles of sulfolane molecules around a central sulfolane dipole. Here, r is the radial distance from the central sulfolane dipole and θ is the angle made between the central dipole and the dipole at r. P(r,$cos\theta$) is averaged over all sulfolane dipoles over a 5 ns trajectory. Figure 2.5(b)-(d) suggest that the orientational effect of a central dipole on its neighboring dipoles is limited; however, a certain degree of anti-parallel or near-antiparallel alignment of near neighbor sulfolane molecules is seen. The probability density function of dipole orientations for dipoles present between 4.5 Å and 5.5 Å from a central sulfolane molecule is shown in Figure 2.5(e). Once again, a preference for anti-parallel orientations is noticed. The increased intensity between 5.5 Å and 6 Å in Figure 2.5(b) (corresponding to Figure 2.5(f)), coincides with the first peak position of the COM-COM pair correlation function presented in Figure 2.4(a). A weak preference for a parallel orientation with the central sulfolane dipole is seen at these distances. This feature is due to a weak competition in the dipole-dipole interactions of molecules in this region with the central molecule and with molecules in the 4.5 Å to 5.5 Å region.

We also study P(r,$cos\theta$) as a function of temperature (Figure 2.6). We find that temperature does not have a significant effect on P(r,$cos\theta$) over the temperature range studied here. This, we speculate, is due to the large dipole moment of sulfolane. However, we see some decrease in number of sulfolane molecules whose dipoles align anti-parallelly to the central sulfolane dipole. Also, the various regions of the P(r,$cos\theta$) shift marginally to larger distances as a result of the decrease in density with increase in temperature.

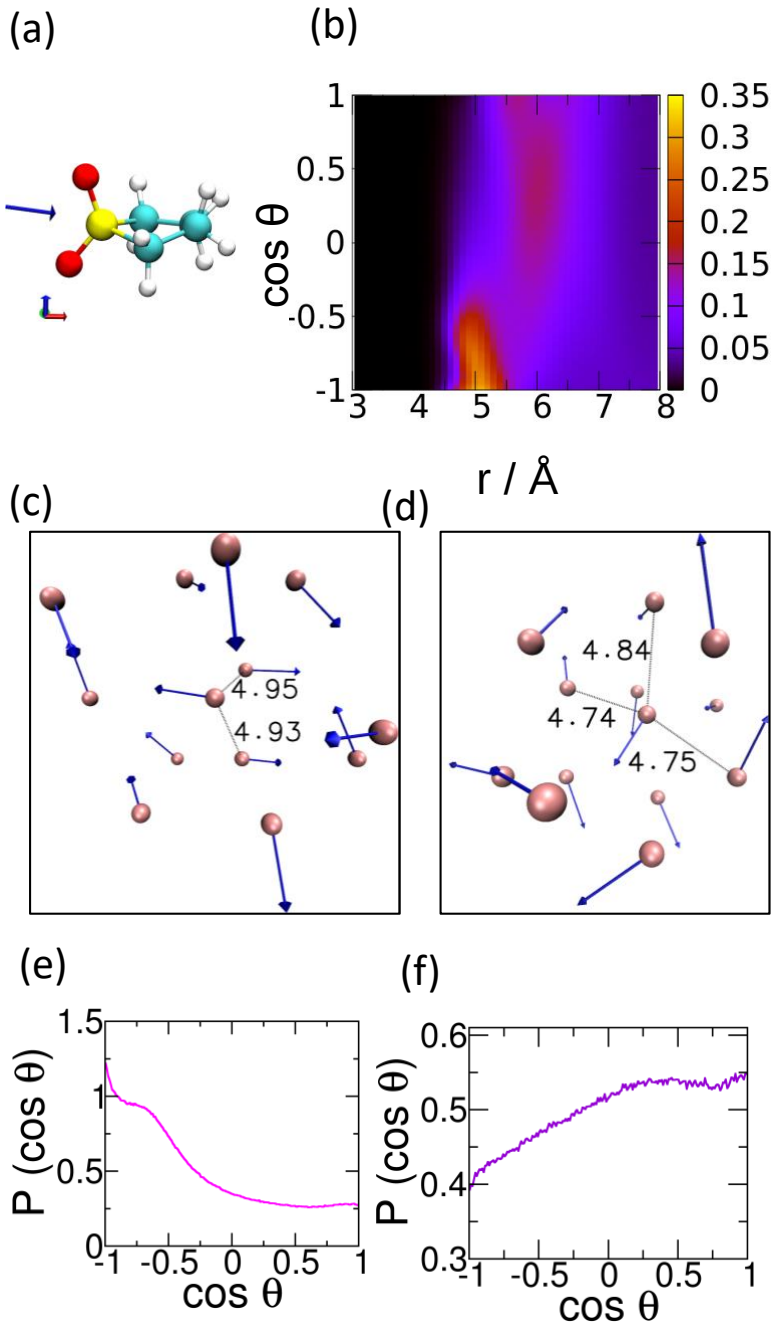

Figure 2.5: (a) Orientation of the dipole moment vector of sulfolane molecule obtained from MP2 level calculations. (b) Combined intermolecular inter-dipole orientational ($cos\theta$) and radial distance (r) probability density function (PDF), illustrating the distance dependence of dipole orientation around any central sulfolane dipole. Amongst the sulfolane dipoles within the first solvation shell (8 Å) of a central molecule, the ones closest (within 5 Å) show an orientational preference of close to 180° as in (c) and close to 130° as in (d). Pink spheres in panels (c) and (d) are molecular center of masses, and the blue arrows are molecular dipole moment vectors. Distances marked are in Angstrom. Snapshots (c) and (d) have been chosen randomly among those sulfolane molecules with twelve neighbors in the first solvation shell. Probability density function of the cosine of the angles between dipoles for a range of distances, (e) from 4.5 Å to 5.5 Å, and (f) from 5.5 Å to 6.0 Å.

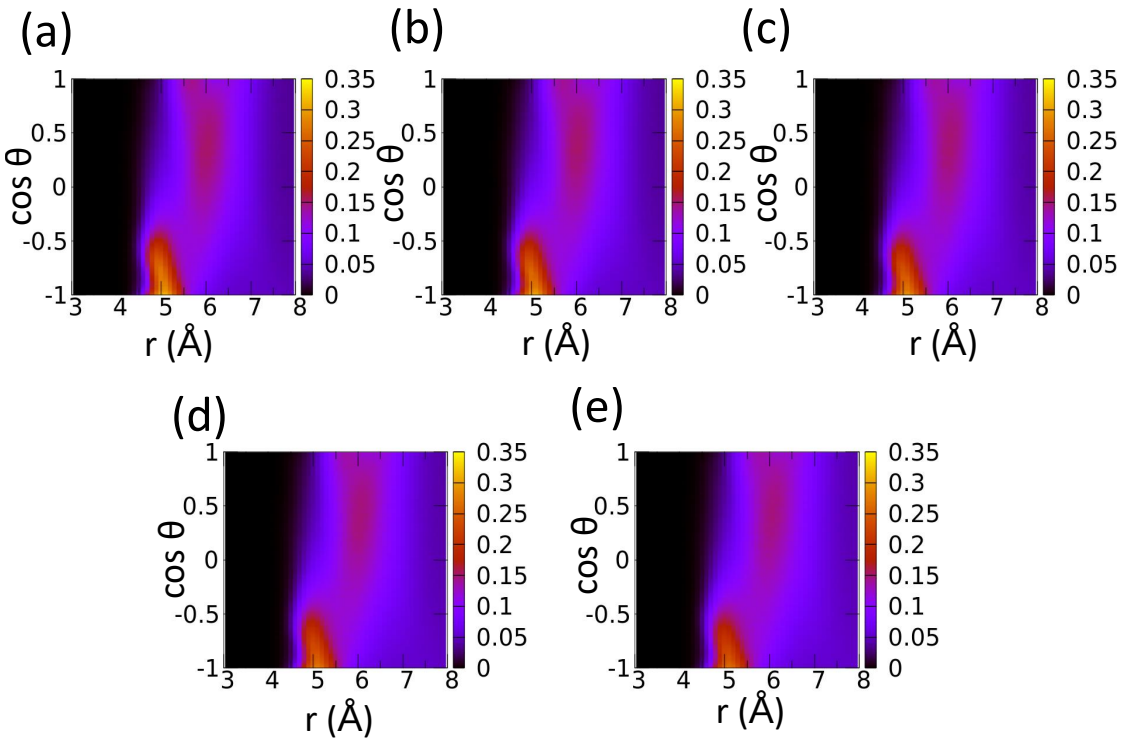

Figure 2.6: Temperature dependence of combined intermolecular inter-dipole orientational and radial distance probability density function. (a) 303 K, (b) 323 K, (c) 348 K, (d) 373 K, and (e) 398 K.

2.3.4 Heat of vaporization

The heat of vaporization provides a good estimate of the strength of intermolecular interactions present in any liquid. Assuming ideality in the gas-phase, it is defined as $\Delta H_{vap} = E_{gas} - E_{liq} + RT$ [61], where ΔH_{vap} is the heat of vaporization, E_{gas} is the average total energy of a sulfolane molecule in the gas-phase, E_{liq} is the average total energy per molecule in the liquid-phase, R is the universal gas constant, and T, temperature. The mean value of the heat of vaporization of liquid sulfolane at 303K was calculated from three independent single molecule gas-phase NVT calculations (E_{gas}) ($N_{sample} = 3$) and from a common single realization of E_{liq} for each force field. The results are tabulated in Table 2.6, and details are provided in Appendix A.

Force field	$\Delta H_{vap,sim}$ / kJ·mol^{-1}[a]	$\Delta(\Delta$ H$_{vap})$ (%)
Force field of Ref. 2	67.05 ± 0.17	0.48
OPLS	60.71 ± 0.24	-9.02
This work	59.43 ± 0.27	-10.94

[a] The expanded uncertainty (U) is reported at 95% level of confidence.

Table 2.6: Heat of vaporization ΔH (kJ·mol^{-1}) obtained using force fields at temperature T = 303 K, and pressure p = 1 bar. The experimental value using the Clapeyron and Cox equations is 66.73 kJ·mol^{-1} [62].

All the force fields yield heat of vaporization within 11% of experiment.

2.3.5 Surface tension

Details of calculation of surface tension are provided in Appendix A. The surface tension estimated from all the force fields, including the one presented here, are presented in Table 2.7. Surface tension data in literature seems to vary greatly from one experimental report to another. Thus, we desisted from calculating it as a function of temperature and limited ourselves to ambient conditions.

Force field	γ / mN·m^{-1}[a]	$\Delta\gamma$ (%)
Force field of Ref. 2	53.43 ± 4.6	50.51
OPLS	45.50 ± 1.6	28.17
This work	34.62 ± 0.5	-2.48
Literature	35.5 [63]	–
	35.5[b]	–
	47.95 [29]	–

[a] The expanded uncertainty (U) is reported at 95% level of confidence.

[b] https://m.chemicalbook.com/ChemicalProductProperty_DE_cb3852996.htm

Table 2.7: Surface tension γ (mN·m^{-1}) of liquid sulfolane at temperature T = 303 K, and pressure p = 1 bar calculated using different force fields. Experimentally determined value is γ_{exp} = 35.50 mN·m^{-1} [64].

2.3.6 Shear viscosity

Another crucial transport property to validate the transport properties obtained through force field is shear viscosity. We calculate it from the off-diagonal components of the pressure tensor from equilibrium MD simulations. The stress-stress time correlation function and the shear viscosity derived therefrom, are calculated according to the Green-Kubo method in a manner similar to Ref. 65. The Green-Kubo expression used for viscosity calculation is provided in Appendix Equation A-1. An example for the pressure tensor correlation function in time is shown in Figure A.4. Further details of the calculation are provided in Appendix A.

The running intergral of shear viscosity is shown in Figure 2.7. The calculation of uncertainty U on the reported viscosity (Table 2.8) obtained from block-averaging, was obtained in a manner very similar to that of density.

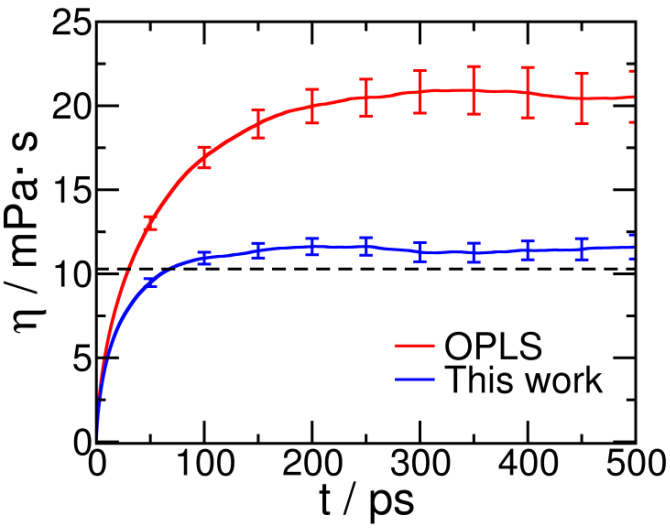

Figure 2.7: Running integral for shear viscosity of liquid sulfolane estimated from the OPLS force field and from the current work at temperature T = 303 K and pressure p = 1 bar. The dashed line is drawn at the experimental value of 10.284 mPa·s [53] for comparison.

Force field	η / mPa·s[a]	$\Delta\eta$ (%)
Force field of Ref. 2	Not estimable within 25 ns run	Not estimable
OPLS	20.47 $\pm$ 0.04	99.05
This work	11.43 $\pm$ 0.15	10.02
Literature	10.228 [55], 10.05 [29]	–
	10.30 [52], 10.074 [56]	–
	10.4010 [57]	–

[a] The expanded uncertainty (U) is reported at 95% level of confidence.

Table 2.8: Shear viscosity η (mPa·s) estimated by all force fields at temperature T = 303 K, and pressure p = 1 bar. Experimentally determined value of shear viscosity is 10.284 mPa·s [53].

We have also calculated the shear viscosity of liquid sulfolane at different temperatures, and find that the calculated values using the refined force field are in good comparison with experiments (See Table 2.9 and Figure 2.8). Running integral of the pressure time correlation function as a function of temperature is shown in Appendix Figure A.5.

Temperature / K	$\eta_{\text{This work}}$ [a,b]	η_{exp}	$\Delta\eta$ (%)
303	11.43 $\pm$ 0.15	10.284 [53]	10.02
323	6.53 $\pm$ 0.03	6.312 [53]	3.45
348	5.25 $\pm$ 0.03	3.846 [53]	36.50
373	2.05 $\pm$ 0.02	2.57 [53]	-20.23
398	1.59 $\pm$ 0.04	1.835 [53]	-13.35

[a] The expanded uncertainty (U) is reported at 95% level of confidence.

[b] The data follows the Vogel-Fulcher-Tammann (VTF) equation [66], $\eta = \eta_0 \cdot e^{\frac{B}{T-T_{VF}}}$, where η_0 = 0.0026 mPa·s, B = 2554.6092 K, and T_{VF} = 0.0 K. Since in the present case, the VTF equation reduces to the Arrhenius equation, the activation energy obtained from an Arrhenius fit is 21.24 kJ·mol^{-1}.

Table 2.9: Comparison between the shear viscosity of liquid sulfolane calculated using the force field reported here, $\eta_{\text{This work}}$ (mPa·s), with that reported in experiments η_{exp} (mPa·s) in the temperature range T = (303 to 398) K, and at pressure p = 1 bar. $\Delta\eta$ is calculated with respect to the experimental value.

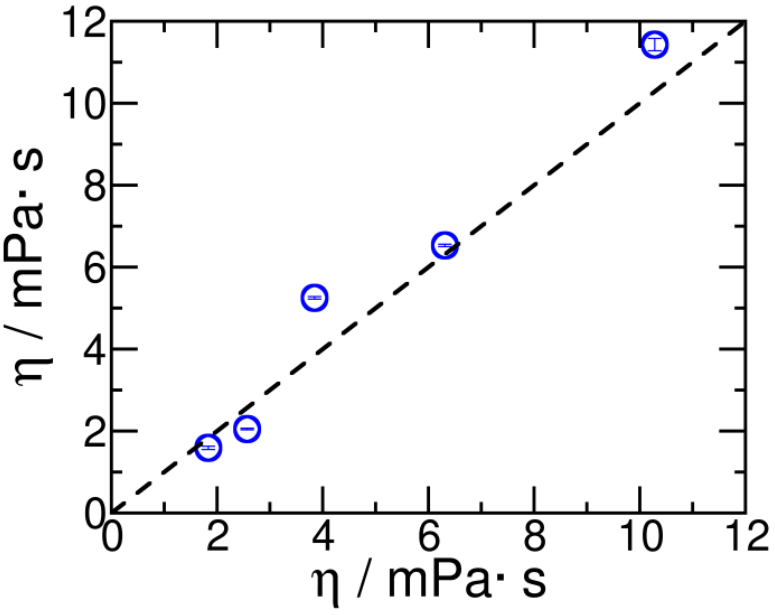

Figure 2.8: Comparison between shear viscosity predicted from this work with those reported in experiments in the temperature range, T = (303 to 398) K and at pressure p = 1 bar.

2.3.7 Self Diffusion Coefficient

The self-diffusion coefficient of sulfolane was calculated from the mean squared displacement (MSD). Reliable measurements of the experimental diffusion coefficient were not found in the literature. Thus, we estimated it by a linear extrapolation of the experimentally reported diffusivity of sulfolane in solutions of varying concentrations of $LiBF_4$ [2] to zero concentration of $LiBF_4$ at 303 K. The diffusion-constant obtained through this procedure is 14.72×10^{-11} $m^2 \cdot s^{-1}$, and is herein considered as the experimental diffusion constant, against which values from different force fields are compared. Constant NVT simulations of duration 50 ns at the equilibrated density were used to calculate the MSD for the OPLS force field and for the refined force field (see Figure 2.9). The smallest time interval for which MSD was calculated was 1 ps. The diffusive regime was determined from the time point, the exponent $\beta(t)$ defined in Appendix Equation A-2, reaches unity (2 ns to 26 ns). Further details of the calculation are provided in Appendix A.

$\langle|\Delta\mathbf{r}|^2\rangle$ (MSD) as a function of time-interval t is shown in Figure 2.9. $\beta(t)$ for sulfolane in each force field considered is shown in Appendix Figure A.6. The self-diffusion coefficients (D) calculated are provided in Table 2.10. The diffusion constant from the refined force field developed herein is closest to the experimental value.

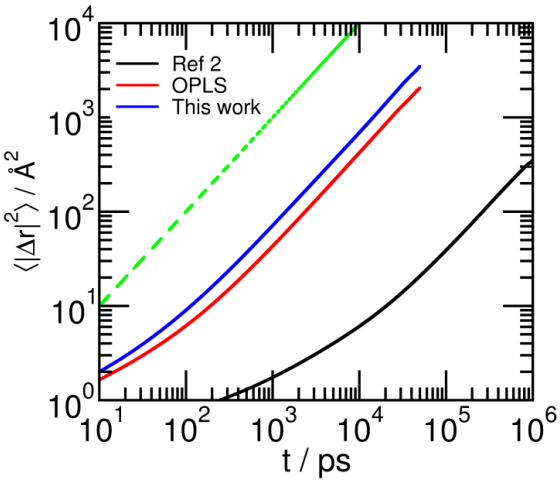

Figure 2.9: Mean square displacement of sulfolane (MSD) of center of mass(COM) as a function of time for all force fields studied in this work. The dashed green line represents the y = x line, provided here for the sake of comparison.

Force field	$D/10^{-11}$ m^2·s^{-1}[a]	Δ D (%)
Force field of Ref. 2	0.06 ± 0.001	-99.59
OPLS	7.12 ± 0.08	-51.63
This work	11.89 ± 0.4	-19.16

[a] The expanded uncertainty (U) is reported at 95% level of confidence.

Table 2.10: Self diffusion coefficient D (m^2·s^{-1}) of liquid sulfolane estimated from simulations using the three force fields, at temperature T = 303 K, and pressure p = 1 bar. Experimentally determined value of diffusion-constant obtained through extrapolation from data in Ref. 2 is 14.72×10^{-11}m^2·s^{-1}.

We also calculated the self-diffusion coefficient of sulfolane as a function of temperature. The results are provided in Table 2.11 and Figure 2.10. Experimental self-diffusion constants were not found in the literature for comparison.

Temperature / K	$D/10^{-11}$ m^2·s^{-1}[a,b]
303	11.89 ± 0.4
323	22.33 ± 0.5
348	40.83 ± 0.7
373	65.77 ± 1.2
398	103.38 ± 1.3

[a] The expanded uncertainty (U) is reported at 95% level of confidence.

[b] The data follows an exponential fit of the form : $D = A \cdot e^{\frac{-E_a}{k_B T}}$. Where activation energy E_a = 22.60 kJ·mol^{-1}, and A = 97372.59 × 10^{-11}m^2·s^{-1}.

Table 2.11: Self-diffusion coefficient of liquid sulfolane as a function of temperature as predicted from this work, D

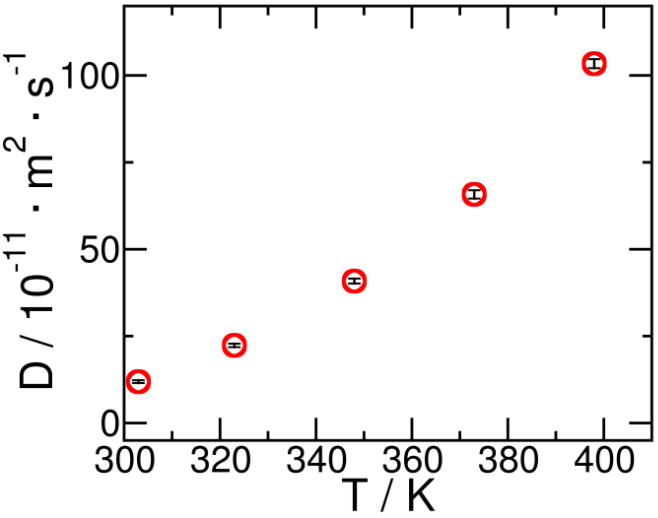

Figure 2.10: Self-diffusion coefficients of liquid sulfolane as a function of temperature in the range T = (303 to 398) K.

2.4 Conclusions

In this work, the need for a force field that quantitatively captures the transport properties of liquid sulfolane has been met. In order to achieve this, average atomic-site charges were derived for the liquid phase of sulfolane using periodic density functional theory calculations and the DDEC6 method for partitioning the electronic density into atomic site charges. Narrow atomic-site charge distributions in the liquid allowed for obtaining site

charges through DFT geometry optimizations of independent snapshots chosen from a MD trajectory.

A modification of charges necessitates a refinement of Lennard-Jones (LJ) parameters as well. Thus, chemically different atom types were identified, and their LJ-parameters were tuned so that the total potential energy of a pair of sulfolane molecules as a function of their intermolecular distance calculated within the refined force field, matches that obtained from reference quantum chemical calculations as closely as possible. Lastly, we also modified the equilibrium bond-length and bond-angles to those obtained from gas phase quantum chemical optimization of a sulfolane molecule.

Although our force field is a non-polarizable one, the values predicted by it for several physical and chemical properties such as molecular dipole moment, liquid density, viscosity, self-diffusion coefficient, and surface tension quantitatively match experimental data to a fair extent with the benefit of having computed them with much lesser computational cost as compared to simulations using ab-initio MD methods or with polarizable force fields. In particular, we stress on the remarkable agreement of self-diffusion coefficient and shear viscosity of this refined force field with experiments, since reproducing transport quantities from non-polarizable force fields has always posed a challenge [65]. We notice that the match of density and heat-of-vaporization from the refined force field with experiments is not as good as that for transport properties and surface tension. However, among other force fields studied here, the refined force field parameters reported here yield the closest match to the quantum PES scans. Also, the rigorous method used for derivation of atomic-site charges within the liquid phase of sulfolane reinforces our faith in the reliability of the refined force field, particularly for transport properties. A temperature dependent study of several physical quantities yielded results in quantitative agreement with experiments. This increased the reliability of this refined force field. The near-neighbor structure in liquid sulfolane is characterized by anti-parallel arrangement of molecular dipoles.

Several quantitative predictions regarding sulfolane assisted reactions and its viability as an emerging battery electrolyte component can now be made with fair certainty. It is also interesting to note that the refined force field for sulfolane may be applicable to the entire class of sulfone compounds with minor modifications. Investigations along these lines constitute the next chapter.

Bibliography

[1] Ulf Tilstam. Sulfolane: a versatile dipolar aprotic solvent. *Org. Process Res. Dev.*, 16(7):1273–1278, 2012.

[2] Kaoru Dokko, Daiki Watanabe, Yosuke Ugata, Morgan L Thomas, Seiji Tsuzuki, Wataru Shinoda, Kei Hashimoto, Kazuhide Ueno, Yasuhiro Umebayashi, and Masayoshi Watanabe. Direct evidence for Li ion hopping conduction in highly concentrated sulfolane-based liquid electrolytes. *The Journal of Physical Chemistry B*, 122(47):10736–10745, 2018.

[3] M Sedlarikova, Jiří Vondrak, J Maca, and K Bartusek. Sulfolane as solvent for lithium battery electrolytes. *J. New Mater. Electrochem. Syst.*, 16(2), 2013.

[4] Josef Maca, Martin Frk, Zdenka Rozsivalova, and Marie Sedlarikova. Properties of sulfolane based aprotic electrolytes. *Port. Electrochim. Acta*, 31(6):321–330, 2013.

[5] Azusa Nakanishi, Kazuhide Ueno, Daiki Watanabe, Yosuke Ugata, Yoshiharu Matsumae, Jiali Liu, Morgan L Thomas, Kaoru Dokko, and Masayoshi Watanabe. Sulfolane-based highly concentrated electrolytes of Lithium bis(trifluoromethanesulfonyl)amide: ionic transport, Li-ion coordination, and Li–S battery performance. *J. Phys. Chem. C*, 123(23):14229–14238, 2019.

[6] Taisho Seita, Yoshiharu Matsumae, Jiali Liu, Ryoichi Tatara, Kazuhide Ueno, Kaoru Dokko, and Masayoshi Watanabe. Graphite–lithium sulfide battery with a single-phase sparingly solvating electrolyte. *ACS Energy Lett.*, 5:1–7, 2019.

[7] Yukihiro Okamoto, Seiji Tsuzuki, Ryoichi Tatara, Kazuhide Ueno, Kaoru Dokko, and Masayoshi Watanabe. High transference number of na ion in liquid-state sulfolane solvates of Sodium bis(fluorosulfonyl)amide. *J. Phys. Chem. C*, 124(8):4459–4469, 2020.

[8] Joe W Vaughn and Conrad F Hawkins. Physical properties of tetrahydrothiophene-1,1-dioxide and 3-methyltetrahydrothiophene-1,1-dioxide. *J. Chem. Eng. Data*, 9(1):140–142, 1964.

[9] Kang Xu. Nonaqueous liquid electrolytes for lithium-based rechargeable batteries. *Chemical Reviews*, 104(10):4303–4418, 2004.

[10] Xiaodi Ren, Shuru Chen, Hongkyung Lee, Donghai Mei, Mark H Engelhard, Sarah D Burton, Wengao Zhao, Jianming Zheng, Qiuyan Li, and Michael S Ding. Localized high-concentration sulfone electrolytes for high-efficiency lithium-metal batteries. *Chem*, 4(8):1877–1892, 2018.

[11] Urszula Domańska, Warren C Moollan, and Trevor M Letcher. Solubility of sulfolane in selected organic solvents. *J. Chem. Eng. Data*, 41(2):261–265, 1996.

[12] JE Katon and WR Feairheller Jr. The vibrational spectra and molecular configuration of sulfolane. *Spectrochim. Acta*, 21(1):199–201, 1965.

[13] Christian D Berweger, Wilfred F van Gunsteren, and Florian Müller-Plathe. Force field parametrization by weak coupling. re-engineering SPC water. *Chem. Phys. Lett.*, 232(5-6):429–436, 1995.

[14] Haiyan Liu, Florian Mueller-Plathe, and Wilfred F van Gunsteren. A force field for liquid dimethyl sulfoxide and physical properties of liquid dimethyl sulfoxide calculated using molecular dynamics simulation. *J. Chem. Eng. Data*, 117(15):4363–4366, 1995.

[15] William L Jorgensen, David S Maxwell, and Julian Tirado-Rives. Development and testing of the opls all-atom force field on conformational energetics and properties of organic liquids. *J. Am. Chem. Soc.*, 118(45):11225–11236, 1996.

[16] Wei Zhao, Hossein Eslami, Welchy Leite Cavalcanti, and Florian Mueller-Plathe. A refined all-atom model for the ionic liquid 1-n-butyl 3-methylimidazolium bis(trifluoromethylsulfonyl)imide [BMIM][NTf_2]. *Z. Phys. Chem.*, 221(11-12):1647–1662, 2007.

[17] Neeraj Rai, Jake L Rafferty, Amitesh Maiti, and J Ilja Siepmann. Prediction of the bubble point pressure for the binary mixture of ethanol and 1,1,1,2,3,3,3-heptafluoropropane from gibbs ensemble Monte Carlo simulations using the trappe force field. *Fluid Phase Equilib.*, 260(2):199–211, 2007.

[18] Neeraj Rai, Alexander J Wagner, Richard B Ross, and J Ilja Siepmann. Application of the trappe force field for predicting the hildebrand solubility parameters of organic solvents and monomer units. *J. Chem. Theory Comput.*, 4(1):136–144, 2008.

[19] Wei Zhao, Frédéric Leroy, Berit Heggen, Stefan Zahn, Barbara Kirchner, Sundaram Balasubramanian, and Florian Müller-Plathe. Are there stable ion-pairs in room-temperature ionic liquids? Molecular dynamics simulations of 1-n-butyl-3-methylimidazolium hexafluorophosphate. *Journal of the American Chemical Society*, 131(43):15825–15833, 2009.

[20] Neeraj Rai, Surya P Tiwari, and Edward J Maginn. Force field development for actinyl ions via quantum mechanical calculations: an approach to account for many body solvation effects. *J. Phys. Chem. B*, 116(35):10885–10897, 2012.

[21] Anirban Mondal and Sundaram Balasubramanian. A molecular dynamics study of collective transport properties of imidazolium-based room-temperature ionic liquids. *J. Chem. Eng. Data*, 59(10):3061–3068, 2014.

[22] Becky L Eggimann, Yangzesheng Sun, Robert F DeJaco, Ramanish Singh, Muhammad Ahsan, Tyler R Josephson, and J Ilja Siepmann. Assessing the quality of molecular simulations for vapor–liquid equilibria: An analysis of the trappe database. *J. Chem. Eng. Data*, 65(3):1330–1344, 2019.

[23] Jingyi L Chen, Bai Xue, Krishnan Mahesh, and J Ilja Siepmann. Molecular simulations probing the thermophysical properties of homogeneously stretched and bubbly water systems. *J. Chem. Eng. Data*, 64(9):3755–3771, 2019.

[24] Alberto Gutiérrez, Mert Atilhan, and Santiago Aparicio. Microscopic characterization of CO_2 and H_2S removal by sulfolane. *Energy Fuels*, 31(9):9800–9813, 2017.

[25] Thomas A Manz and Nidia Gabaldon Limas. Introducing DDEC6 atomic population analysis: Part 1. Charge partitioning theory and methodology. *RSC Advances*, 6(53):47771–47801, 2016.

[26] William L Jorgensen and Julian Tirado-Rives. Potential energy functions for atomic-level simulations of water and organic and biomolecular systems. *Proceedings of the National Academy of Sciences*, 102(19):6665–6670, 2005.

[27] Leela S Dodda, Jonah Z Vilseck, Julian Tirado-Rives, and William L Jorgensen. 1.14* CM1A-LBCC: localized bond-charge corrected CM1A charges for condensed-phase simulations. *The Journal of Physical Chemistry B*, 121(15):3864–3870, 2017.

[28] Leela S Dodda, Israel Cabeza de Vaca, Julian Tirado-Rives, and William L Jorgensen. Ligpargen web server: an automatic OPLS-AA parameter generator for organic ligands. *Nucleic acids research*, 45(W1):W331–W336, 2017.

[29] Sara Ahmad Kelayeh, Amir Hossein Jalili, Cyrus Ghotbi, Masih Hosseini-Jenab, and Vahid Taghikhani. Densities, viscosities, and surface tensions of aqueous mixtures of sulfolane+ triethanolamine and sulfolane+ diisopropanolamine. *J. Chem. Eng. Data*, 56(12):4317–4324, 2011.

[30] Anirban Mondal and Sundaram Balasubramanian. Quantitative prediction of physical properties of imidazolium based room temperature ionic liquids through determination of condensed phase site charges: A refined force field. *The Journal of Physical Chemistry B*, 118(12):3409–3422, 2014.

[31] Nikhil VS Avula, Anirban Mondal, and Sundaram Balasubramanian. Charge environment and hydrogen bond dynamics in binary ionic liquid mixtures: A computational study. *The Journal of Physical Chemistry Letters*, 9(12):3511–3516, 2018.

[32] Jürg Hutter, Marcella Iannuzzi, Florian Schiffmann, and Joost VandeVondele. CP2K: Atomistic simulations of condensed matter systems. *Wiley Interdisciplinary Reviews: Computational Molecular Science*, 4(1):15–25, 2014.

[33] John P Perdew, Kieron Burke, and Matthias Ernzerhof. Generalized gradient approximation made simple. *Phys. Rev. Lett.*, 77(18):3865, 1996.

[34] Stefan Grimme. Semiempirical gga-type density functional constructed with a long-range dispersion correction. *J. Comput. Chem.*, 27(15):1787–1799, 2006.

[35] Stefan Goedecker, Michael Teter, and Jürg Hutter. Separable dual-space gaussian pseudopotentials. *Phys. Rev. B*, 54(3):1703, 1996.

[36] Christian Hartwigsen, Sephen Gœdecker, and Jürg Hutter. Relativistic separable dual-space gaussian pseudopotentials from H to Rn. *Phys. Rev. B*, 58(7):3641, 1998.

[37] Nidia Gabaldon Limas and Thomas A Manz. Introducing DDEC6 atomic population analysis: part 4. efficient parallel computation of net atomic charges, atomic spin moments, bond orders, and more. *RSC Adv.*, 8(5):2678–2707, 2018.

[38] MJ ea Frisch, GW Trucks, HB Schlegel, GE Scuseria, MA Robb, JR Cheeseman, G Scalmani, VPGA Barone, GA Petersson, HJRA Nakatsuji, et al. Gaussian 16, 2016.

[39] Roy Dennington, Todd Keith, John Millam, et al. Gaussview, version 5. 2009.

[40] Henk Bekker, HJC Berendsen, EJ Dijkstra, S Achterop, R Vondrumen, David VANDERSPOEL, A Sijbers, H Keegstra, and MKR Renardus. Gromacs-a parallel computer for molecular-dynamics simulations. In *4th International Conference on Computational Physics (PC 92)*, pages 252–256. World Scientific Publishing, 1993.

[41] Berk Hess, Carsten Kutzner, David Van Der Spoel, and Erik Lindahl. Gromacs 4: algorithms for highly efficient, load-balanced, and scalable molecular simulation. *Journal of Chemical Theory and Computation*, 4(3):435–447, 2008.

[42] Mark James Abraham, Teemu Murtola, Roland Schulz, Szilárd Páll, Jeremy C Smith, Berk Hess, and Erik Lindahl. GROMACS: High performance molecular simulations through multi-level parallelism from laptops to supercomputers. *SoftwareX*, 1:19–25, 2015.

[43] Tom Darden, Darrin York, and Lee Pedersen. Particle Mesh Ewald: An n log (n) method for Ewald sums in large systems. *J. Chem. Phys.*, 98(12):10089–10092, 1993.

[44] Berk Hess, Henk Bekker, Herman JC Berendsen, and Johannes GEM Fraaije. LINCS: A linear constraint solver for molecular simulations. *J. Comput. Chem.*, 18(12):1463–1472, 1997.

[45] Szilárd Páll and Berk Hess. A flexible algorithm for calculating pair interactions on simd architectures. *Comput. Phys. Commun.*, 184(12):2641–2650, 2013.

[46] Shūichi Nosé. A molecular dynamics method for simulations in the canonical ensemble. *Molecular Physics*, 52(2):255–268, 1984.

[47] Herman JC Berendsen, JPM van Postma, Wilfred F Van Gunsteren, ARHJ DiNola, and Jan R Haak. Molecular dynamics with coupling to an external bath. *The Journal of Chemical Physics*, 81(8):3684–3690, 1984.

[48] Michele Parrinello and Aneesur Rahman. Polymorphic transitions in single crystals: A new molecular dynamics method. *Journal of Applied physics*, 52(12):7182–7190, 1981.

[49] Shuichi Nosé and ML Klein. Constant pressure molecular dynamics for molecular systems. *Molecular Physics*, 50(5):1055–1076, 1983.

[50] Leandro Martínez, Ricardo Andrade, Ernesto G Birgin, and José Mario Martínez. Packmol: A package for building initial configurations for molecular dynamics simulations. *Journal of Computational Chemistry*, 30(13):2157–2164, 2009.

[51] William Humphrey, Andrew Dalke, and Klaus Schulten. VMD – Visual Molecular Dynamics. *J. Mol. Graphics*, 14:33–38, 1996.

[52] Amir Hossein Jalili, Mohammad Shokouhi, Farid Samani, and Masih Hosseini-Jenab. Measuring the solubility of CO_2 and H_2S in sulfolane and the density and viscosity of saturated liquid binary mixtures of (Sulfolane+ CO_2) and (Sulfolane+ H_2S). *J. Chem. Thermodyn.*, 85:13–25, 2015.

[53] Jerry F Casteel and Paul G Sears. Dielectric constants, viscosities, and related physical properties of 10 liquid sulfoxides and sulfones at several temperatures. *J. Chem. Eng. Data*, 19(3):196–200, 1974.

[54] Florentino Murrieta-Guevara, Esther Rebolledo-Libreros, and Arturo Trejo. Gas solubility of carbon dioxide and hydrogen sulfide in mixtures of sulfolane with monoethanolamine. *Fluid Phase Equilib.*, 86:225–231, 1993.

[55] Jacinto Águila-Hernández, Arturo Trejo, Blanca Estela García-Flores, and René Molnar. Viscometric and volumetric behaviour of binary mixtures of sulfolane and n-methylpyrrolidone with monoethanolamine and diethanolamine in the range 303–373 K. *Fluid Phase Equilib.*, 267(2):172–180, 2008.

[56] Changsheng Yang, Wali Yu, and Peisheng Ma. Densities and viscosities of binary mixtures of ethylbenzene+ n-methyl-2-pyrrolidone, ethylbenzene+sulfolane, and styrene+octane from (303.15 to 353.15) K and atmospheric pressure. *J. Chem. Eng. Data*, 50(4):1197–1203, 2005.

[57] Francisca Maria Rodrigues Mesquita, Filipe Xavier Feitosa, Martin Aznar, Hosiberto B de Sant'Ana, and Rílvia S Santiago-Aguiar. Density, viscosities, and excess properties for binary mixtures of sulfolane+ alcohols and sulfolane+ glycols at different temperatures. *J. Chem. Eng. Data*, 59(7):2196–2206, 2014.

[58] Shepard A Clough, Yardley Beers, Gerald P Klein, and Laurence S Rothman. Dipole moment of water from stark measurements of H_2O, HDO, and D_2O. *J. Chem. Phys.*, 59(5):2254–2259, 1973.

[59] CG Malmberg and AA Maryott. Dielectric constant of water from 0^o to 100^o c. *J. Res. Natl. Bur. Stand. (U. S.)*, 56(1):1, 1956.

[60] Eric W Prestbo and Jeanne L McHale. Static dielectric constants and kirkwood correlation factors of dimethyl sulfoxide/carbon tetrachloride solutions. *J. Chem. Eng. Data*, 29(4):387–389, 1984.

[61] C Krekeler, F Dommert, J Schmidt, YY Zhao, Christian Holm, R Berger, and Luigi Delle Site. Electrostatic properties of liquid 1, 3-dimethylimidazolium chloride: role of local polarization and effect of the bulk. *Phys. Chem. Chem. Phys.*, 12(8):1817–1821, 2010.

[62] Michal Fulem, Kvetoslav Ruzicka, and Martin Ruzicka. Recommended vapor pressures for thiophene, sulfolane, and dimethyl sulfoxide. *Fluid Phase Equilibria*, 303(2):205–216, 2011.

[63] John A Dean. *Lange's Handbook of Chemistry 15th ed*. McGraw-Hill, New York, 1999.

[64] Raymond Eller Kirk, Donald Frederick Othmer, Martin Grayson, and David Eckroth. Encyclopedia of Chemical Technology. 1978.

[65] Yong Zhang, Akihito Otani, and Edward J Maginn. Reliable viscosity calculation from equilibrium molecular dynamics simulations: A time decomposition method. *J. Chem. Theory Comput.*, 11(8):3537–3546, 2015.

[66] Zbigniew H Stachurski. *Fundamentals of amorphous solids: Structure and properties*. John Wiley & Sons, 2015.

Chapter 3

Hopping in high concentration electrolytes - Long time bulk and single-particle signatures, free energy barriers, and structural insights

3.1 Introduction

From Chapter 2, we learnt that sulfolane shows great promise as a battery solvent in terms of its high voltage operation applicability, high thermal stability, and high solvation ability. We employ the refined force field developed in Chapter 2 for sulfolane towards realising lithium-ion (Li-ion) high concentration electrolytes (HCEs) in this chapter. This enabled us to study structure and transport of Li-ion electrolytes in general and Li-ion hopping in HCEs in particular. HCEs have myriad advantages. One of the ways to achieve safer high-voltage Li-ion batteries is to use HCEs, which reduces flammability [1, 2]. Further, anion-derived solid electrolyte interphase (SEI) formed in HCEs enable greater stability and longer term cycling compared to present-day dilute electrolyte batteries wherein solvent-derived SEI is generated [2–10]. High-energy density and voltage needs are also met by HCEs (*solvent-in-salt electrolytes*). Some specific advantages of using HCEs are: increased battery life-span [11], higher Coulombic efficiency [12], ultrafast charging [13], prevention of solvent degradation [13, 14], larger and more stable electrochemical windows [15],

Work reported in this chapter was published with the same title in *J. Phys. Chem. Lett.* **2020**, *11*, 9613-9620 (https://doi.org/10.1021/acs.jpclett.0c02995)

higher rate capability [16], and higher transport numbers of alkali ions [17, 18]. Although HCEs are generally thought to suffer from the drawback of low ionic conductivity, this drawback has been overcome in part recently by an appropriate choice of anions in mixed-anion HCEs [19], and in part by adding a non-solvating and/or low-viscosity additive solvent [20–22]. Most HCEs, however, continue to suffer from low ionic conductivities.

In HCEs, Li-ions are conceived to be a part of solvent or anion bridged chain-like electrolyte structures for ligand exchange [23–25]. Presence of ion-aggregated (AGG) structures are also thought to facilitate Li-ion transport [26–28]. Further, HCEs do not obey the Stokes-Einstein relation [23, 29]. Li-ions are less mobile than the solvent molecules and counterions at low concentrations of salt; however, at high concentrations, the converse is true. An ion hopping mechanism in HCEs has been proposed to explain these characteristics [23]; however, at present, the process is yet to be comprehensively characterised microscopically and thus remains elusive. Ion hopping has also been identified as one probable mode of transport for small ions in polymeric ionic-liquids, making this mode of transport of increasing relevance [30].

In the present study, we aimed to increase our understanding of such HCEs (solvent-in-salt) electrolytes appreciably, with a particular emphasis to understanding the "hopping" phenomenon using $LiBF_4$ in sulfolane as a case study [23, 31]. The salt $LiBF_4$ and solvent sulfolane were particularly chosen for a direct comparison with extensive experiments on the same [23].

In this chapter, we defined a Li-ion "hop" to be a motion of a Li-ion which occurs within a few picoseconds and involves a ligand/nearest-neighbor exchange. Depending on the concentration of the electrolyte and the nature of the salt and solvent, ligand-exchange may occur over a few picoseconds to hundreds of picoseconds [24, 29]. We did not refer to these ligand-exchanges that occur over beyond a few picoseconds as being hops; rather, such events are likely to arise from a combination of hopping and diffusive motions (in varying proportions). The umbrella term, *hop+diffusive* is used henceforth to refer to them. This chapter reports signatures of "hopping" over a large range of timescales, i.e, from a few picoseconds corresponding to a single hop to microsecond timescales corresponding to averaged bulk-imprints of hop-events. The latter is important due to the highly viscous nature of the medium at high salt concentrations. We also obtained an understanding of the following - preferred locations to which Li-ions *hop+diffuse*, concentration dependence of the composition of the solvation shell of Li-ions, structural and dynamic heterogeneity, and structural relaxation in these electrolytes. Most importantly, through steered molecular dynamics (SMD) simulations, we obtained the free energy barrier for the hopping of Li-ions making this the first attempt, to our knowledge, in the calculation of ion-hopping barriers in a liquid matrix (barring H^+ hopping [32–38]). MD simulations of the $LiBF_4$:SUL=1:1

crystal were also carried out in order to draw parallels between the structure of crystal HCEs and liquid HCEs as well as to study hopping in both systems.

3.2 Methodology and Simulation Details

In the present study, the lithium salt employed is lithium tetrafluoroborate ($LiBF_4$), and the solvent used is sulfolane. Figure 3.1 shows the structure of these molecules along with the atom types considered in our study.

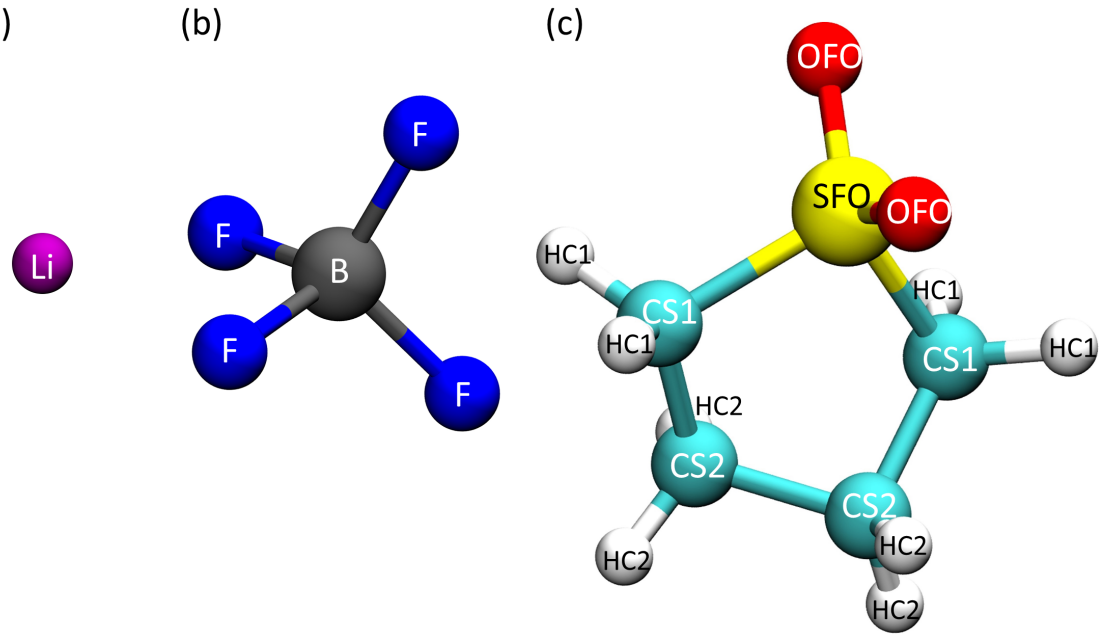

Figure 3.1: (a) Lithium ion (Li-ion), (b) Tetrafluoroborate anion (BF_4), and (c) Sulfolane molecule (SUL) (solvent).

3.2.1 Force-field details

The atom types, Lennard-Jones (LJ) parameters, and bonded parameters used for $LiBF_4$ are the same as in Ref. 23. Atomic site charges and LJ parameters for $LiBF_4$ are given in Table 3.1. The atomic site charges used for $LiBF_4$ were derived using the $LiBF_4$:SUL = 1:1 crystal structure available in the Cambridge Structure Database (CSD) as CCDC 1866668 and reported in Ref. 23. The electron density distribution of this unit cell was calculated through quantum density functional theory using CP2K software [39]. Perdew, Burke, and Ernzerhof (PBE) exchange-correlation functional [40] and Grimme's D3 empirical van der

Waals corrections [41] were employed. The core-electrons and nuclei were represented using the Geodecker–Teter–Hutter (GTH) pseudopotentials [42, 43]. All valence electrons were represented by triple–ζ double-polarized basis sets with an energy cut-off of 320 Ry. This electron density stored in a cube file was used as input to Chargemol [44] software for partition to atomic site DDEC6 charges [45]. The charges over all atoms of the same atomic type were averaged to obtain the charges used in our liquid phase simulations (Table 3.1).

Atom type	Charge (e^-)	σ (Å)	ϵ (kJ/mol)
Li	0.82	1.46	0.799144
B	1.10	3.5814	0.397480
F	-0.48	2.95	0.255224

Table 3.1: Atom types, atomic site charges, and Lennard-Jones parameters of $LiBF_4$ used in this work.

The force-field parameters for sulfolane used in this study are the refined parameters reported in Chapter 2.

Li-BF_4-SUL crystal

The same force field parameters used for simulating the liquid phase were used here, except for a small change in the atomic site charges of F atoms. In the liquid phase, all the four F atoms of a BF_4 ion are equivalent, but the same is not true in the crystal phase where two of the fluorine atoms coordinate with Li ions while the other two do not (see Figure B.1 crystal structure). So two different atomic site charges were used for these two different types of fluorine atoms as shown in Table 3.2.

Atom type	Charge (e^-)
Li	0.82
B	1.10
F1 (non-coordinating)	-0.448
F2 (coordinating)	-0.512

Table 3.2: Atom types and atomic site charges of $LiBF_4$ used in this work for the simulation of the crystal.

3.2.2 Molecular dynamics (MD) simulation details

Concentrations of $LiBF_4$ in sulfolane for which experimental data have been reported (as in Ref. 23) were chosen for our simulations in order to conduct a concentration dependent study, while at the same time ensuring that insights gleaned from our simulations are realistic to a fair extent. To this end, PACKMOL software [46] was used to generate random configurations of the constituents at each concentration. GROMACS-2018.3 package [47–49] was employed to generate the MD trajectories. Insights on the structure and on various equilibrium properties were gleaned from the analysis at each of these concentrations. These trajectories were utilized to investigate various aspects of Li-ion hopping in highly-concentrated electrolytes. The temperature and pressure for all production runs were 303 K and 1 bar, respectively. Most analyses were carried out with in-house FORTRAN codes.

A timestep of 1 fs was used to integrate the equations of motion using the leap-frog algorithm. All C-H bonds of sulfolane were constrained using the LINCS algorithm [50] in GROMACS. The Lennard-Jones (LJ) and Coulomb cut-off distances were fixed at 12 Å, and the neighbor list cut-off was extended to 14 Å. Long-range interactions were accounted for using particle–particle mesh Ewald (PPPM) method [51]. 1-2, 1-3 non-bonding interactions were set to zero. For 1-4 pairs, non-bonding LJ and Coulombic interactions were included with a scale factor of 0.5. For all other atom-pairs, a scale factor of 1.0 was used. Geometric mean was employed as the combining rule for calculating the interaction between different atom types. Long-range dispersion corrections to energy and pressure were applied.

The random packing at each concentration was energy minimised within the force-field which was followed by constant-NPT equilibration run using Berendsen barostat [52] and Nosé–Hoover thermostat [53]. Following this, a constant-NPT production run using Parrinello-Rahman Barostat [54, 55] and Nosé–Hoover thermostat was carried out. The average density estimated from the NPT production run was used to run constant-NVT equilibration and finally, the constant-NVT production run. For the Nosé–Hoover thermostat [53], a coupling time-constant of 0.5 ps was used, and the system was coupled to the thermostat every 10 timesteps. For the Berendsen [52] and the Parrinello-Rahman barostats [54, 55], a coupling time constant of 2 ps used. Either barostat was coupled with the system once every 10 timesteps and every 1 timestep, respectively, for high ($>$1 M) concentration and low concentration systems. More than one independent run is required at moderate to high concentrations of $LiBF_4$ to infer any reliable and statistically significant conclusions in these sluggish systems. To create independent NVT production runs, in addition to the NVT runs mentioned earlier, the average box size obtained from NPT at 303 K was also NVT thermalized at two other temperatures, viz., 340 K and 350 K for 2 ns. These systems were then annealed back to 303 K followed by short NVT equilibration

runs for 10 ns at 303 K. Following this, independent NVT production runs at 303 K were run. A total of three independent NVT trajectories were analyzed to arrive at the averaged transport properties. Electrolyte concentration of 4.26 M was simulated at three different temperatures, viz., 303 K, 333.15 K, and 363.15 K, as experimental physicochemical properties were reported for this concentration and the aforementioned temperatures in Ref. 23. The number of molecules of each compound at every concentration of $LiBF_4$, the temperature of the system, the corresponding box-size, and the run-lengths for MD runs carried out are provided in Tables B.1 and 3.3, respectively. To simulate a bulk environment, periodic boundary conditions were applied along all three axes. Vizualizations were made using the Visual Molecular Dynamics (VMD) software [56].

Li-BF_4-SUL crystal

First, the system was energy minimised in the force field framework and then warmed from 5 K to 223 K in the NVT ensemble at a heating rate of 20 K/ns. Nosé–Hoover thermostat with coupling time constant 1 ps was used for the NVT simulation. After sufficient equilibration in the NVT ensemble, the final configuration was used to start the NPT simulation at 303 K. Parinello-Rahman with anisotropic coupling (each side is independently coupled) and Nosé–Hoover thermostat with coupling time constants of 10 ps and 1 ps, respectively, were used for the NPT simulation. All other simulation protocols are the same as in the previous section. The NPT simulation was run for 10 ns and the last 5 ns was used for analysis.

Simulations of the crystal of two different sizes cryst-216 and cryst-120 (see above), were performed. The larger system (cryst-216) was used for structural analysis and the smaller system (cryst-120) was used to estimate the free energy of Li hopping.

3.2.3 MD run duration details

The trajectory lengths for NPT equilibration, NPT production, NVT production, and the number of independent NVT production trajectories simulated at each concentration are as in Table 3.3. All the runs in Table 3.3 were conducted at temperature T = 303 K, and pressure P = 1 bar.

Salt conc. (M)	Molar ratio $LiBF_4$:SUL	Temperature (K)	Force field used	NPT equilibration duration (ns)	NPT production duration (ns)	No. of independent NVT runs	Each NVT prod. duration (ns)
5.76	1:1.35	303	This work	20	400	3	1 run for 2005 and 2 runs for 1005
5.76	1:1.35	303	Ref. 23	10	400	1	1005
4.26	1:2.00	303	This work	10	120	3	1005
4.26	1:2.00	333.15	This work	10	120	1	700
4.26	1:2.00	363.15	This work	10	50	1	100
3.04	1:3.00	303	This work	10	100	3	500
2.36	1:4.00	303	This work	10	80	3	80
1.25	1:8.00	303	This work	10	60	3	60
1.00	1:10.08	303	This work	12.8	60	3	60
1.00	1:10.08	303	Ref. 23	12.8	60	1	60
0.51	1:20.00	303	This work	10	20	1	60
0.21	1:50.00	303	This work	5	10	1	50
0.00	0:800	303	Ref. 57	10	25	1	50
0.00	0:800	303	Ref. 23	10	25	1	1000

Table 3.3: MD run-length details.

3.3 Results and Discussion

This chapter reports several different aspects of the structure, transport, and hopping phenomenon in HCEs. The main results have been illustrated and discussed in detail in the main body of the chapter. Several system details, physico-chemical properties, and details of each analyses are provided in the appendix and are referred to in the main body of the chapter.

3.3.1 Force field validation, proof & characteristics of Li-ion hopping

The force-field is validated by comparing densities, ionic conductivities, and self-diffusion coefficients at various concentrations of $LiBF_4$ in sulfolane (Tables B.3, B.4, and B.5, respectively) with the experimental data of Ref. 23. Results for these quantities from our force-field are in fair comparison with experiments (Figures 3.2(a) and (b)). The transference number of Li-ions increases with increase in Li-salt concentration, and its values are in excellent agreement with experimental data [23] (Table B.6). Ionic conductivity was also calculated with respect to temperature at 4.26 M (Figure B.2(d)). The activation energy calculated from the Arrhenius fit to the data from our simulations is 3.22 kcal/mol (Figure B.2), which is in good agreement with the experimental value of 3.16 kcal/mol [23].

This match further validated the force-field used here. Insights from simulations of crystals to aid the understanding of liquids are rare in the literature. We also examined characteristics of hopping events in the crystal and draw parallels to those in HCEs.

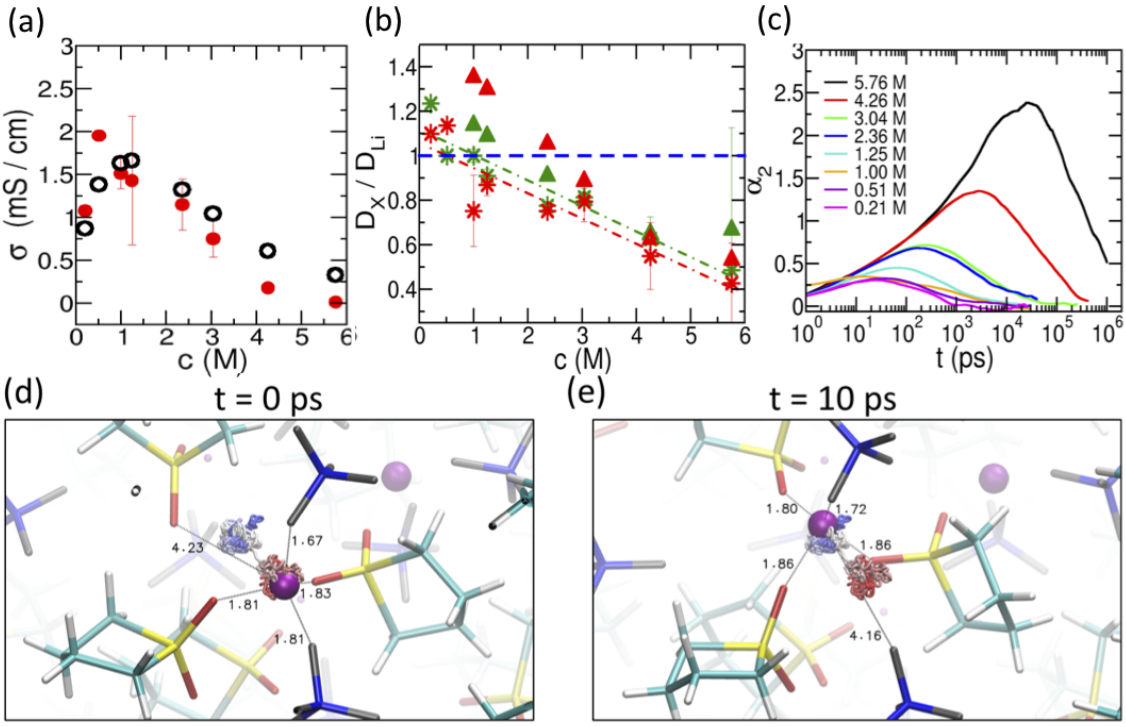

Figure 3.2: (a) Ionic conductivity obtained from our simulations and those reported in experiments of Ref. 23 at 303 K and 1 bar. c is the concentration of $LiBF_4$ in liquid sulfolane. Black: Experiments, Red: Simulations (b) Ratio of self-diffusion coefficient of BF_4 anion (green) and sulfolane solvent (red) to that of lithium (Li) ions from our simulations (stars) and from experiments (up triangles) of Ref. 23. The dashed lines for the simulation data are a guide to the eye. (c) Non-Gaussian parameter α_2 at different concentrations of $LiBF_4$. Snapshots from the simulation of the solution at 5.76 M concentration show the environment around a Li-ion (d) before a hop and (e) after the hop. The time difference between the two snapshots is 10 ps. Purple sphere: Lithium. Stick models show sulfolane molecule (yellow-S, red-O, cyan-C and white-H), and BF_4 anion (blue-B, and gray-F). Distances (in Å) of the Li-ion to its initial and final coordinating ligands atoms are mentioned beside the corresponding bond. The trajectory of the Li-ion during the hop is overlayed on both snapshots (d) and (e) at an interval of 1 fs (small spheres). The color gradient from red to white and then to blue of these spheres represents the direction of time. Red represents an earlier time, and blue represents a later time.

Li-ions in highly viscous HCEs are expected to be heterogeneous in their dynamics. A measure of dynamic heterogeneity, the non-Gaussian parameter, α_2 of Li-ions (Equation A-5, Figure 3.2(c)) exhibits distinctly large peaks, particularly at the highest concentrations of the salt (> 4 M). While the increase in peak height of α_2 with increase in salt concentration is indicative of the growing deviation of Li-ion dynamics from a homogeneous

behavior, the position of the peak is suggestive of the time of onset of diffusive dynamics (Figures B.3(b) and (c)) [58–60]. This observation suggested that ion transport mechanisms distinctive from pure diffusion are operative at high salt concentrations. Visualisation of trajectories in this regime revealed sudden jumps ("hops") of Li-ions over an interval of a few picoseconds. Figures 3.2(d) and (e) depict one such event wherein the hopping of a Li-ion changed its coordination environment – a BF_4 anion in its first coordination shell has been replaced by a sulfolane molecule. Significant dynamic heterogeneity of Li-ions in HCEs may in part stem from the fact that Li-ions predominantly remain caged (with slow diffusive motion of the cage), and occasionally exhibit hops. However, bulk signature of hopping are required to undeniably establish their presence and importance in HCEs.

In order to investigate small ion hopping at high salt concentrations in the electrolyte, we employed the self-part of the van Hove correlation function [61], G_s(r,t), defined in Equation A-6. G_s(r,t) gives the distribution of distances by which Li-ions have moved during any chosen time interval. A purely diffusive motion follows the Gaussian distribution described in Equation A-7. The presence of humps beyond the first peak at any chosen time interval indicates hopping of Li-ions alongside diffusion (Figure 3.3(b)). They indicate that at the end of a time interval, Li-ions prefer to be found at distances corresponding to humps rather than at valleys. Multiple humps in G_s(r,t) were seen at 5.76 M and almost none are seen at 1 M or at low concentrations of salt (Figures 3.3(a) and (b). Details of this calculation are presented in the appendix (Figure B.4). Following this work, Li et al. used G_s(r,t) to explore hopping in Li salt-doped poly(ionic liquid) with different extents of asymmetry in anions [62]. As the salt concentration is increased, Li-ions become increasingly caged, leaving occasional hops as the predominant means of motion for these ions. Qualitatively consistent with predictions from experiments, in our simulations, the humps in G_s(r,t) corresponding to Li-hopping become noticeable around the same concentration of salt where D_X/D_{Li} becomes less than 1 (Figure 3.2(b)). At a given concentration, at short time intervals, Li-ions travel to larger distances than they would have done purely through diffusion (compare black colored dashed and continuous lines in Figure 3.3(a) and (b)). Over a short time interval, the number Li-ions that have hopped in HCEs are small, and the humps corresponding to their hops are smeared out by their diffusive motion.

Gleaning insights from the behavior of individual Li-ions proved equally vital. Figures 3.3(c) and (d) single Li-ion G_s(r,t)s revealed that while at low concentrations, the transport of Li-ions is primarily through diffusion, at high concentrations it is predominantly via hops. As expected from the substantial dynamic heterogeneity of Li-ions at 5.76 M (Figure 3.2(d)), we found that for a given trajectory duration, on an average, some Li-ions typically hop multiple times (Figure 3.3(c)), some others hop just once, and some remained completely caged (Figure B.6). The overall shift in the position of the first peak in all G_s(r,t)

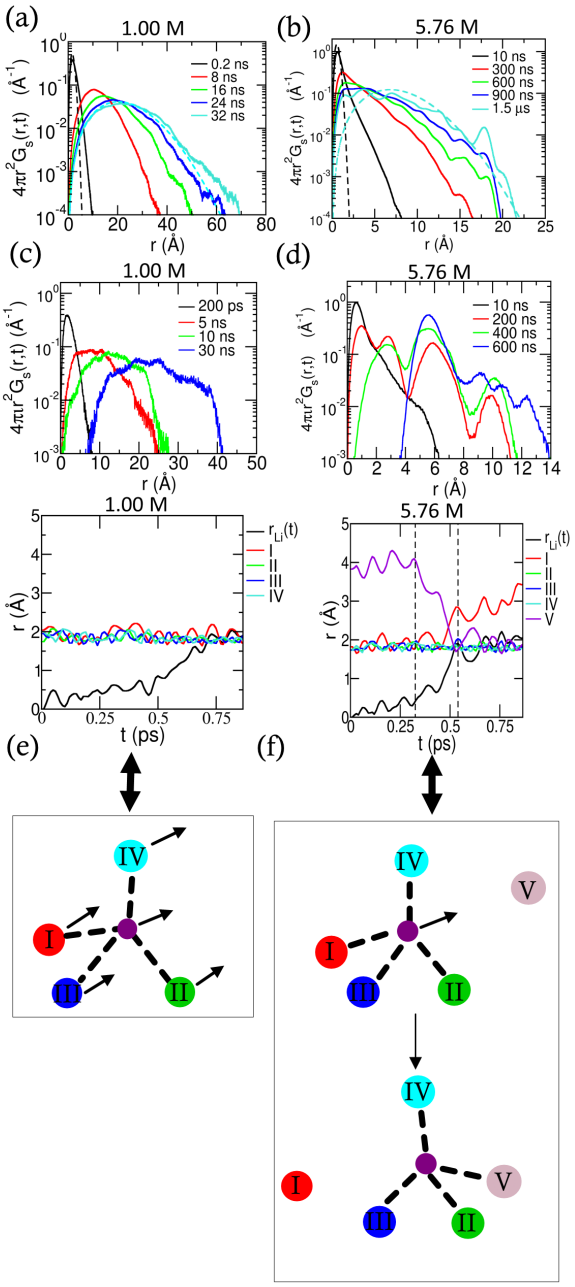

Figure 3.3: G_s(r,t) of Li-ions at (a) 1 M, and (b) 5.76 M at different time intervals. Dashed lines of the same color as the solid lines, represent G_s(r,t) for purely diffusive systems at those select time intervals. Li-ion $G_s(r,t)$ of one arbitrarily chosen Li ion at (c) 1 M, and (d) 5.76 M, at various time intervals. Radial distance $r_{Li}(t)$ of the Li-ion at time t from its position at time $t = 0$ (black), and distances between the position of the Li-ion and the position of coordinating ligand atoms at time t (other colors) at (e) 1 M, and (f) 5.76 M. For a fair comparison between the modes of transport at the two salt concentrations (1 M and 5.76 M), the Li-ions were chosen such that they have both moved 2 Å over the 1 ps duration, respectively. Schematics representing the contrasting transport behavior seen in (e) and (f) are shown below the corresponding plots. Here, the central Li-ion and its coordination environment is depicted.

towards the right with increase in time interval, corresponds to the diffusive component of the Li-ion′s motion.

Away from a time-averaged picture, we looked at a single hop event of a Li-ion. In Figures 3.3(e) and (f), we considered two Li-ions which have moved the same distance in the same duration of time in the low and high concentration electrolytes, respectively. The Li-ion at 1 M (Figure 3.3(e)) dragged along all its coordinating neighbors covering a distance of 2 Å in a gradual manner (See schematic in Figure 3.3(e)). Such Li-ions can be viewed as $[\text{Li(solvent)}_x\text{(anion)}_y]^{+z}$. At low salt concentrations, $x = 4$ and $y = 0$ is most probable (Figures B.9(a)–(d)), and Li ions of the form $[\text{Li(solvent)}_x]^+$ travel as an entire complex (Figure 3.3(e)). Since these complexes undoubtedly have a larger hydrodynamic radius than that of either the solvent or anion molecules, the lower diffusivity of Li-ions relative to the other components is partly understood. However, the Li-ion at 5.76 M (Figure 3.3(f)) made a swift change in position by moving away from one coordinating ligand and getting closer to another (hop) (schematic in Figure 3.3(f)). Such Li-ions can separate from an anion to associate with a solvent molecule and vice-versa within a few picoseconds. While the transport of the Li-ion at 1 M can be likened to diffusive/vehicular motion, the hopper at 5.76 M is an example of structural or mixed diffusion described in Ref. 63 and in the Introduction chapter in this thesis.

3.3.2 Where do the Li-ions hop to?

Clearly, in a crystal, a Li-ion is likely to hop to a vacant Li-ion site. In amorphous solids, glasses or supercooled liquids too, ions are more likely to hop to a site vacated by an ion of the same kind [64–68]. It is interesting to ask what the scenario is in liquids. To this end, we calculated the distinct part of the van Hove correlation function [61] (defined in Equation A-8) between different Li-ions (Figure 3.4).

In Figure 3.4, the $t = 0$ curves represent the pair correlation function, $g(r)$. At any concentration, G_d(r,t) should be unity for all r at t=∞. Its approach to unity, in particular, at distances less than the first peak position reveals the nature of ion transport. At low salt concentrations, at a given time interval, the probability density decreases smoothly as $r \to 0$ from the position of the first peak, implying diffusive motion of the first neighbor Li-ion towards the central Li-ion vacancy position (Figures 3.4(a) and (b)). However, at higher salt concentrations, a clear peak in the probability density at $r = 0$ is seen with a valley between it and the position of the first peak (Figures 3.4(c) and (d)). This feature indicates that the neighbor Li-ion prefers to *hop+diffuse* to the lithium vacancy site (at $r = 0$) even in a liquid, in close correspondence with hopping in a crystal. Following

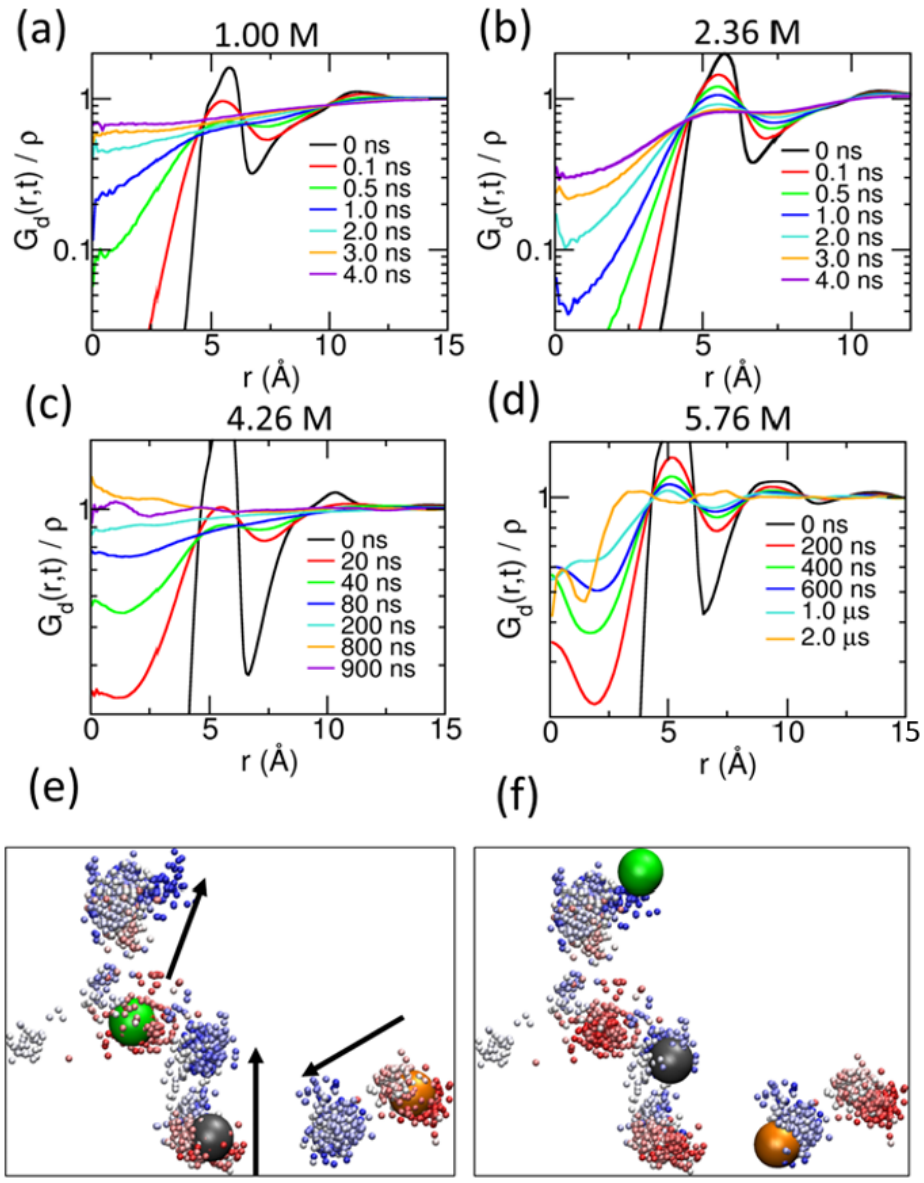

Figure 3.4: Distinct part of the van Hove correlation function between Li-ions at the following concentrations – (a) 1 M, (b) 2.36 M, (c) 4.26 M, and (d) 5.76 M. (e) and (f) show the initial and final snapshots of a 350 ns long trajectory of three different Li-ions at 5.76 M. These ions are colored green, dark gray and orange. The trajectory of these Li-ions over 350 ns have also been overlayed in the form of small spheres at an interval of 500 ps. Direction of time is from red to white and then to blue. The gross directions of motion of the three ions have been shown using arrow marks in (e).

this work, similar observations are made by Li et al. in Li salt-doped poly(ionic liquid) containing anions with different extents of asymmetry [62]. We illustrated the nature of the *hop+diffuse* motion via a concerted set of events captured from our MD simulations at 5.76 M in Figures 3.4(e) and (f). At the end of 350 ns, the orange Li-ion was on its way to occupying a site previously occupied by the gray Li-ion. The gray Li-ion hopped to a position very close to that which was previously occupied by the green Li-ion. Therefore, ions like the gray one contribute to the small hump close to 0 Å. By virtue of hopping in several steps to $r = 0$ alongside diffusion, they also contributed to the dip around 2 Å (mixed vehicular and structural diffusion [63]). The green and gray Li-ions are examples of cooperative ion transport that is at play in HCEs. For the two longest time intervals shown in Figures 3.4(c) and (d), it is seen that the peak earlier present at $r = 0$ has shifted to the right. We attributed this to the motion of the vacant site itself over long time scales.

3.3.3 Structure-transport correlation in HCEs

The varied dynamics exhibited by Li-ions in this HCE has structural underpinnings. Examination of intermolecular structure of the electrolyte through solvation shell composition and radial distribution function analyses (Figures B.9, B.10, and B.11) reveal:

(a) Li-ions at all concentrations prefer a total coordination number of four, as is well known [69],

(b) The fluorine content in the first solvation shell of Li-ions increases with increase in $LiBF_4$ concentration in line with similar findings in Refs. 70, 71, and

(c) At 5.76 M ($LiBF_4$:SUL=1:1.35), the most probable solvation shell composition of Li-ions bears a striking resemblance with that in the $LiBF_4$:SUL=1:1 (7.9 M) crystal (Figure B.1).

Interestingly however, in contrast to the crystal, 5.76 M exhibits microheterogeneity in its structure. The Li-Li g(r) (Figure B.10(a)) exhibits a left-shoulder at all concentrations, but one which is more prominent at 5.76 M. This prominence arises from distinctly proximal Li-ions. From the Li-Li ion G_d(r,t) (Figure 3.4(d)), we see that Li-ions have a preference to hop+diffuse to previously occupied Li-ion sites approximately 5 Å away. Therefore, Li-ions separated by 5 Å or lesser were of particular interest to us. We termed such Li-ions as Li*-ions, and examined their neighborhood at 5.76 M. We found Li* regions to be richer in BF_4 anion and equally poorer in sulfolane molecules, although the mole fraction of the anion in the electrolyte is lesser than that of sulfolane (Table B.1)! Whereas, the scenario in

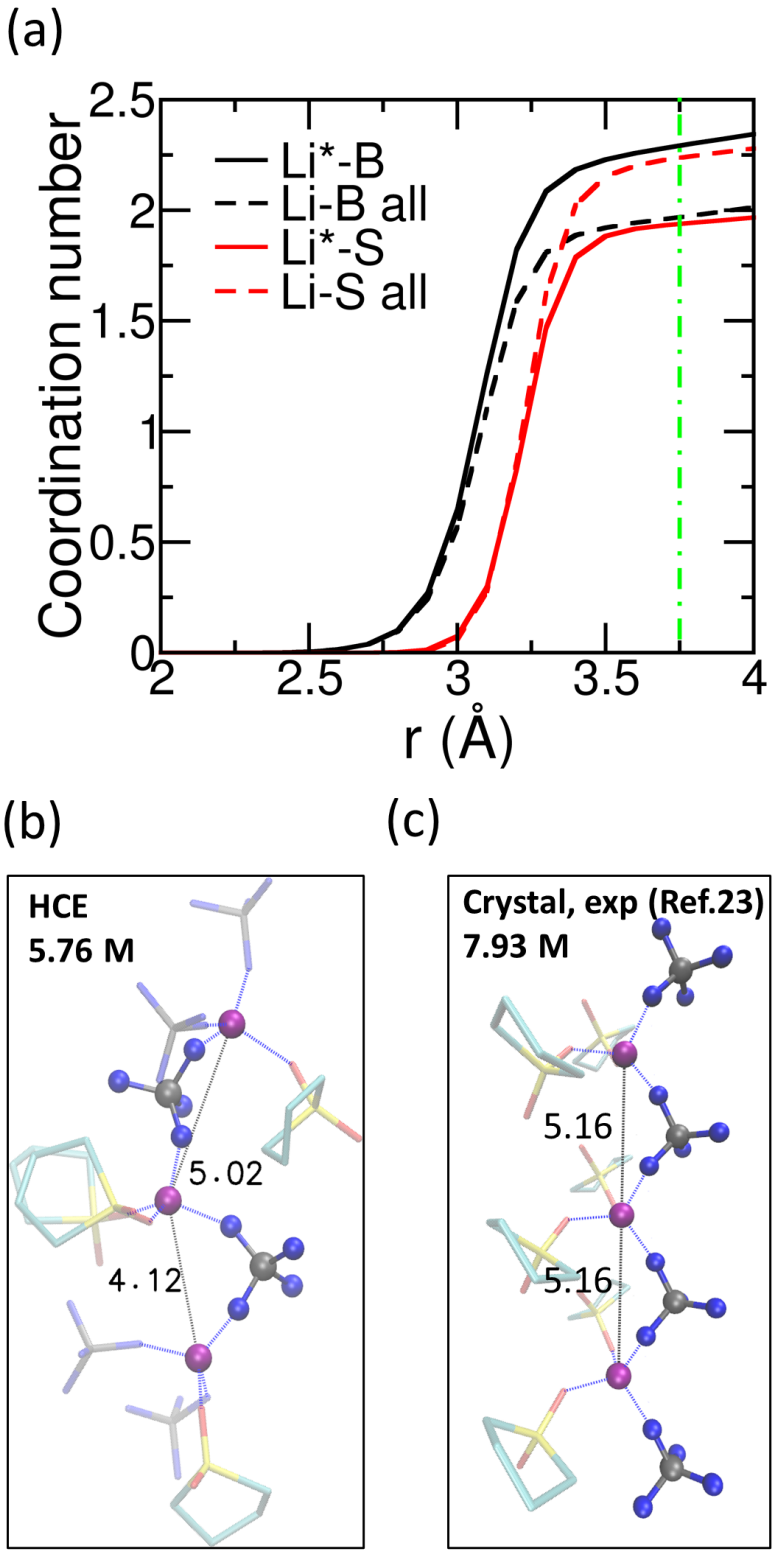

Figure 3.5: (a) Li*-S, Li-S, Li*-B, and Li-B running coordination numbers at 5.76 M. Vertical, green line is the position at which the sum of the coordination numbers with B and with S ≈ four. (b) Three Li*-ions bridged by two BF_4 anions in the liquid electrolyte at 5.76 M ($LiBF_4$:SUL = 1:1.35), observed in the simulations reported herein. (c) Three Li-ions (in purple) bridged by two BF_4 anions in $LiBF_4$:SUL = 1:1 crystal from experiments [23].

the liquid on an average (for all Li-B, Li-S), as expected, is opposite to this observation (Figure 3.5(a)). We found that two Li*-ions are predominantly bridged by a BF_4 anion (Figure 3.5(b)) [25, 72, 73]. Environments containing three or more Li*-ions connected through such bridging ligands found at 5.76 M liquid, were likened to a similar chain of Li-ions in the experimental crystal structure (Figure 3.5(b)-(c)). It is conceivable, that such bridging-ligands are the ones which a Li*-ion retains as one of its nearest neighbors when it *hops+diffuses* to a previously occupied Li*-ion site which had this ligand in common in its cage of neighbors. These findings indicate that an anion or solvent bridged network underlies the bridging-ligand-mediated transport of Li*-ions in HCEs. These findings are in line with those from the $LiBF_4$:SUL=1:1 crystal structure [23] as well as with Raman spectroscopic studies reported in Ref. 23, 25, 26. However, a more detailed study establishing these chain-like networks is required and was beyond the scope of the present thesis. However, we wish to investigate these structures in future.

3.3.4 Li-ion hopping as an activated process

Although hopping is an important transport mechanism in HCEs, it is a rare event and thus must be activated. To the best of our knowledge, ion hopping barriers have not been calculated in a liquid matrix hitherto (barring H^+ hopping/transfer [32–38] and ion diffusion barriers in glasses/supercooled liquids [74]). Herein, we estimated the free energy change for Li-ion "hopping" involving single ligand exchange, at 5.76 M. We performed steered molecular dynamics simulations (SMD) at constant velocity to estimate the free energy profile for the hopping of four Li-ions identified from the equilibrium trajectory at 5.76 M.

From visual inspection of trajectories and by examination of the free energy profiles of several hops, we find that there are roughly two kinds of hops: Those with barriers in the range of 3-4 kcal/mol and those with barriers around 2 kcal/mol. The former were found to be longer hops than the latter.

What is the nature of the transition state during the hop?

Consider the profile shown in black in Figure 3.6(a). The coordination environment of the Li-ion when it is present in the left and right basins of the profile are shown in the corresponding panels above. The snapshot below the free energy profiles is the transition state of the same Li-ion. The Li-ion is undercoordinated at the transition state (Figure 3.6(a)). The nearly flat mean coordination numbers shown in black and red in Figure 3.6(b), confirm that

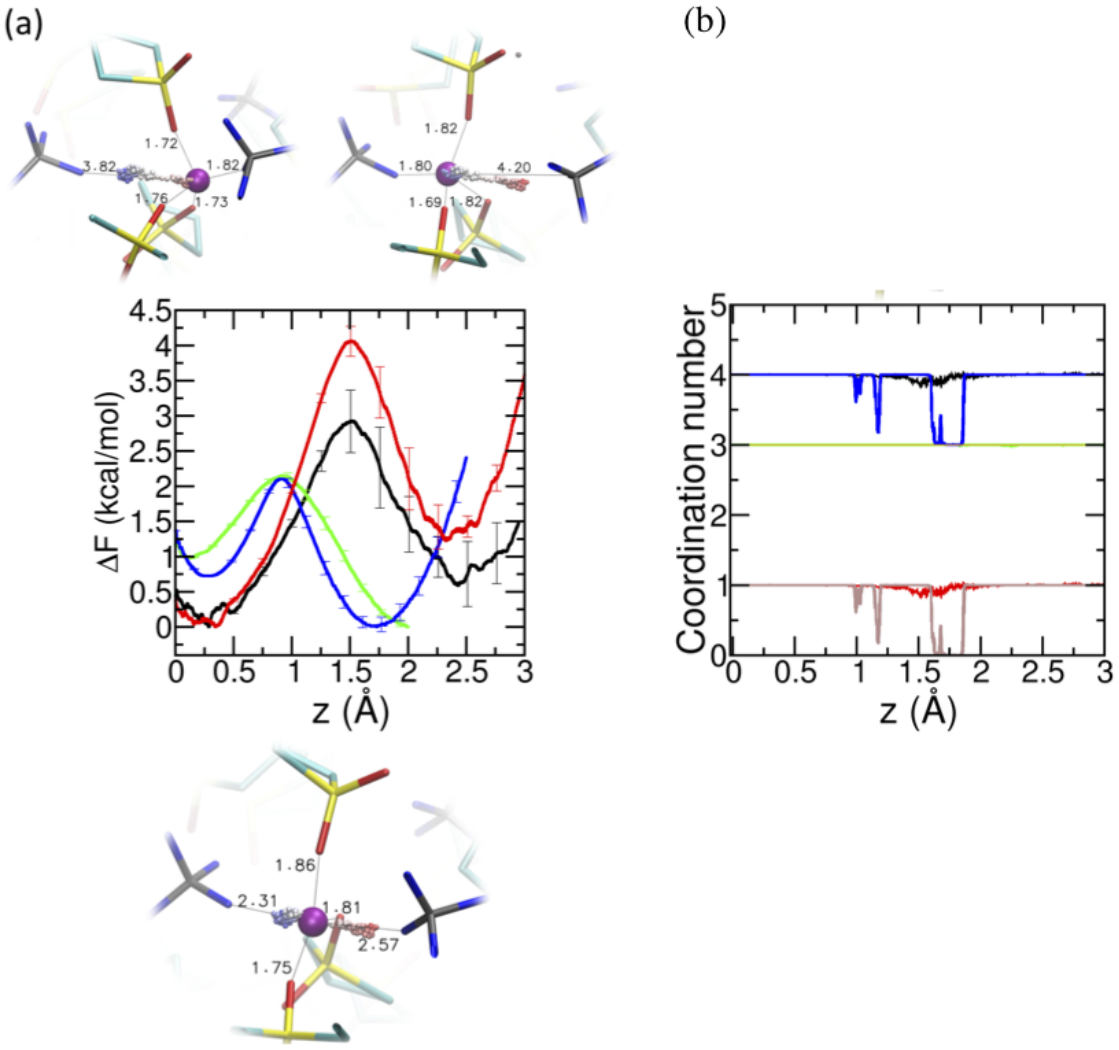

Figure 3.6: (a) Free energy profile as a function of distance along the pull direction for hops of five arbitrarily chosen lithium ions at 5.76 M, obtained through Steered Molecular Dynamics (SMD) calculations. Snapshots above and below the free energy panel pertain to the curve shown in black. Top Left: Corresponding to left basin, and Top Right: Corresponding to the right basin. Bottom: Transition State. (b) Coordination numbers of the same Li-ion as shown in above snapshots as a function of distance along the SMD pull direction. Blue and black: Total coordination number of Li-ion. Green and orange: Number of oxygens in the first solvation shell of Li-ion. Red and brown: Number of fluorines in the first solvation shell of Li-ion. Blue, green and red represent data from a single SMD run. Black, orange and red are data averaged over 200 independent SMD runs.

different SMD runs are indeed independent of each other, passing through a transition state at slightly different positions along the reaction coordinate. Given the disorder in the liquid state and the dynamic heterogeneity exhibited by the system at high salt concentrations, an ensemble of hops is likely prevalent. In the specific example illustrated as blue curve in Figure 3.6(b), one notices the ion making a few attempts to cross the transition state, yet returning back to the "reactant" state, prior to crossing it successfully. Given that the pull trajectories studied in independent SMD trajectories follow the equilibrium hop path very closely (see Figure B.13), it is envisioned that the mechanism of Li-ion hop at equilibrium too exhibits a similar characteristic. In the crystal with lithium site vacancies, hopping can take place along two different paths, both of which are characterised to be involving barriers of 6 kcal/mol and 12 kcal/mol (Figure B.16). These barriers are higher than what are calculated for the 5.76 M HCE, as they involve multiple ligand exchanges.

The nature of Li-ion transport is intimately tied to the stiffness of its coordination cage, which, in turn is dependent on the salt concentration. At 5.76 M, the intermittent cage-relaxation correlation function relaxes over timescales three-orders of magnitude larger than at 1 M (Figure B.17 and Table B.8).

3.4 Conclusions

Long-time single-particle and bulk evidence for ion-hopping in a model HCE are presented in this chapter. A large dynamic heterogeneity amongst the Li-ions was observed, which in part is attributed to caging and hopping. Hops are prominent for concentrations for which $D_X/D_{Li} \leq 1$, indicating the significant role of hopping in transport of Li-ions in HCEs. Li-ions, over long enough timescales, bear an affinity to move to previously occupied like-ion sites even in HC liquids, reminiscent of their behavior in a crystal. Intriguingly, such Li-ion sites are found to form anion-rich pockets within an electrolyte despite the larger mole fraction of solvent. Ligand-bridged chains for Li-ion transport were identified in the liquid state at the molecular-level. Crucially, we provide the first liquid-state non-H^+ ion-hopping barriers, and characterise its transition state. Ways to reduce the activation barriers without reducing salt concentration could enhance the electrical conductivity. The choice of salt and solvent should play a crucial role in determining the cage stiffness and activation energy barrier, both of which could be engineered chemically. Investigation into the characteristics of "higher-order" hops, involving multiple ligand exchanges and chain-like networks will be our future endeavor.

Despite the myriad advantages of Li-ion HCEs, given how scarce lithium is in the earth's crust, it is concerning that Li-ion batteries require large quantities of lithium salt.

Na-ion HCEs are the closest alternative to Li-ion HCEs within monovalent-ion batteries. Sodium is also about far more abundantly found in the earth's crust. Chapter 4 explores the promises and challenges faced by Na-ion HCEs alongside Li-ion HCEs and a possible way to alleviate the challenges.

Bibliography

[1] Yuki Yamada, Jianhui Wang, Seongjae Ko, Eriko Watanabe, and Atsuo Yamada. Advances and issues in developing salt-concentrated battery electrolytes. *Nature Energy*, 4(4):269–280, 2019.

[2] Jiahua Chen, Zheng Yang, Guohua Liu, Cheng Li, Jingsi Yi, Ming Fan, Huaping Tan, Ziheng Lu, and Chunlei Yang. Reinforcing concentrated phosphate electrolytes with in-situ polymerized skeletons for robust quasi-solid lithium metal batteries. *Energy Storage Materials*, 25:305–312, 2020.

[3] Amine Bouibes, Norio Takenaka, Soumen Saha, and Masataka Nagaoka. Microscopic origin of the solid electrolyte interphase formation in fire-extinguishing electrolyte: Formation of pure inorganic layer in high salt concentration. *The Journal of Physical Chemistry Letters*, 10(19):5949–5955, 2019.

[4] Qi Liu, Hongliang Xu, Feng Wu, Daobin Mu, Lili Shi, Lei Wang, Jiaying Bi, and Borong Wu. Effects of a high-concentration $LiPF_6$-based carbonate ester electrolyte for the electrochemical performance of a high-voltage layered $LiNi_{0.6}Co_{0.2}Mn_{0.2}O_2$ cathode. *ACS Applied Energy Materials*, 2(12):8878–8884, 2019.

[5] Tamene Tadesse Beyene, Bikila Alemu Jote, Zewdu Tadesse Wondimkun, Bizualem Wakuma Olbassa, Chen-Jui Huang, Balamurugan Thirumalraj, Chia-Hsin Wang, Wei-Nien Su, Hongjie Dai, and Bing-Joe Hwang. Effects of concentrated salt and resting protocol on solid electrolyte interface formation for improved cycle stability of anode-free lithium metal batteries. *ACS Applied Materials & Interfaces*, 11(35):31962–31971, 2019.

[6] Zhicheng Wang, Yiyang Sun, Yayun Mao, Fengrui Zhang, Lei Zheng, Daosong Fu, Yanbin Shen, Jianchen Hu, Huilong Dong, Jingjing Xu, et al. Highly concentrated dual-anion electrolyte for non-flammable high-voltage Li-metal batteries. *Energy Storage Materials*, 2020.

[7] Matthew Li, Chunsheng Wang, Zhongwei Chen, Kang Xu, and Jun Lu. New concepts in electrolytes. *Chemical Reviews*, 2020.

[8] Zhe Peng, Xia Cao, Peiyuan Gao, Haiping Jia, Xiaodi Ren, Swadipta Roy, Zhendong Li, Yun Zhu, Weiping Xie, Dianying Liu, et al. High-power lithium metal batteries enabled by high-concentration acetonitrile-based electrolytes with Vinylene Carbonate additive. *Advanced Functional Materials*, page 2001285, 2020.

[9] Lei Wang, Kohei Uosaki, and Hidenori Noguchi. Effect of electrolyte concentration on the solvation structure of Gold/LiTFSI-DMSO solution interface. *The Journal of Physical Chemistry C*, 2020.

[10] Sung-Ju Cho, Dae-Eun Yu, Travis P Pollard, Hyunseok Moon, Minchul Jang, Oleg Borodin, and Sang-Young Lee. Nonflammable lithium metal full cells with ultra-high energy density based on coordinated carbonate electrolytes. *iScience*, 23(2):100844, 2020.

[11] Ryoichi Tatara, David G Kwabi, Thomas P Batcho, Michal Tulodziecki, Kenta Watanabe, Hoi-Min Kwon, Morgan L Thomas, Kazuhide Ueno, Carl V Thompson, Kaoru Dokko, et al. Oxygen reduction reaction in highly concentrated electrolyte solutions of lithium bis(trifluoromethanesulfonyl)amide/dimethyl sulfoxide. *The Journal of Physical Chemistry C*, 121(17):9162–9172, 2017.

[12] Viktor Nilsson, Antonia Kotronia, Matthew Lacey, Kristina Edstrom, and Patrik Johansson. Highly concentrated LiTFSI–EC electrolytes for lithium metal batteries. *ACS Applied Energy Materials*, 3(1):200–207, 2019.

[13] Yuki Yamada, Keizo Furukawa, Keitaro Sodeyama, Keisuke Kikuchi, Makoto Yaegashi, Yoshitaka Tateyama, and Atsuo Yamada. Unusual stability of acetonitrile-based superconcentrated electrolytes for fast-charging lithium-ion batteries. *Journal of the American Chemical Society*, 136(13):5039–5046, 2014.

[14] Natalia S Katorova, Stanislav S Fedotov, Dmitry P Rupasov, Nikita D Luchinin, Benjamin Delattre, Yet-Ming Chiang, Artem M Abakumov, and Keith J Stevenson. Effect of concentrated diglyme-based electrolytes on the electrochemical performance of potassium-ion batteries. *ACS Applied Energy Materials*, 2(8):6051–6059, 2019.

[15] Xu Liu, Giuseppe Antonio Elia, Xinpei Gao, Bingsheng Qin, Huang Zhang, and Stefano Passerini. Highly concentrated KTFSI: Glyme electrolytes for K/bilayered-V_2O_5 batteries. *Batteries & Supercaps*, 2020.

[16] Kazuhisa Hirata, Yoshihiro Morita, Takeo Kawase, and Yasutaka Sumida. Effects of lithium bis(fluorosulfonyl)imide concentration on performances of lithium-ion batteries containing sulfolane-based electrolytes. *Journal of The Electrochemical Society*, 167(11):110553, 2020.

[17] Oleg Borodin, Liumin Suo, Mallory Gobet, Xiaoming Ren, Fei Wang, Antonio Faraone, Jing Peng, Marco Olguin, Marshall Schroeder, Michael S Ding, et al. Liquid structure with nano-heterogeneity promotes cationic transport in concentrated electrolytes. *ACS Nano*, 11(10):10462–10471, 2017.

[18] Fangfang Chen, Patrick Howlett, and Maria Forsyth. Na-ion solvation and high transference number in superconcentrated ionic liquid electrolytes: a theoretical approach. *The Journal of Physical Chemistry C*, 122(1):105–114, 2018.

[19] Fangfang Chen and Maria Forsyth. Computational investigation of mixed anion effect on lithium coordination and transport in salt concentrated ionic liquid electrolytes. *The Journal of Physical Chemistry Letters*, 10(23):7414–7420, 2019.

[20] Urbi Pal, Fangfang Chen, Derick Gyabang, Thushan Pathirana, Binayak Roy, Robert Kerr, Douglas R MacFarlane, Michel Armand, Patrick C Howlett, and Maria Forsyth. Enhanced ion transport in an ether aided super concentrated ionic liquid electrolyte for long-life practical lithium metal battery applications. *Journal of Materials Chemistry A*, 2020.

[21] Keitaro Takahashi, Yuki Ishino, Wataru Murata, Yasuhiro Umebayashi, Seiji Tsuzuki, Masayoshi Watanabe, Hiromitsu Takaba, and Shiro Seki. Physicochemical compatibility of highly-concentrated solvate ionic liquids and a low-viscosity solvent. *RSC Advances*, 9(43):24922–24927, 2019.

[22] Murillo Longo Martins, Robert L Sacci, Nicolette C Sanders, J Landon Tyler, Ray A Matsumoto, Ivan Popov, Wei Guo, Sheng Dai, Peter T Cummings, Alexei P Sokolov, et al. Addition of chloroform in a solvent-in-salt electrolyte: Outcomes in the microscopic dynamics in bulk and confinement. *The Journal of Physical Chemistry C*, 2020.

[23] Kaoru Dokko, Daiki Watanabe, Yosuke Ugata, Morgan L Thomas, Seiji Tsuzuki, Wataru Shinoda, Kei Hashimoto, Kazuhide Ueno, Yasuhiro Umebayashi, and Masayoshi Watanabe. Direct evidence for Li ion hopping conduction in highly concentrated sulfolane-based liquid electrolytes. *The Journal of Physical Chemistry B*, 122(47):10736–10745, 2018.

[24] Masaki Okoshi, Chien-Pin Chou, and Hiromi Nakai. Theoretical analysis of carrier ion diffusion in superconcentrated electrolyte solutions for sodium-ion batteries. *The Journal of Physical Chemistry B*, 122(9):2600–2609, 2018.

[25] Saul Perez Beltran, Xia Cao, Ji-Guang Zhang, and Perla B Balbuena. Localized high concentration electrolytes for high voltage lithium-metal batteries: Correlation between the electrolyte composition and its reductive/oxidative stability. *Chemistry of Materials*, 2020.

[26] Shinji Kondou, Morgan L Thomas, Toshihiko Mandai, Kazuhide Ueno, Kaoru Dokko, and Masayoshi Watanabe. Ionic transport in highly concentrated lithium bis(fluorosulfonyl)amide electrolytes with keto ester solvents: structural implications for ion hopping conduction in liquid electrolytes. *Physical Chemistry Chemical Physics*, 21(9):5097–5105, 2019.

[27] Jun-Ho Choi, Hochan Lee, Hyung Ran Choi, and Minhaeng Cho. Graph theory and ion and molecular aggregation in aqueous solutions. *Annual Review of Physical Chemistry*, 69:125–149, 2018.

[28] Martin Callsen, Keitaro Sodeyama, Zdenek Futera, Yoshitaka Tateyama, and Ikutaro Hamada. The solvation structure of lithium ions in an ether based electrolyte solution from first-principles molecular dynamics. *The Journal of Physical Chemistry B*, 121(1):180–188, 2017.

[29] Zhen-Kun Tang, John S Tse, and Li-Min Liu. Unusual Li-ion transfer mechanism in liquid electrolytes: a first-principles study. *The Journal of Physical Chemistry Letters*, 7(22):4795–4801, 2016.

[30] Zidan Zhang, Amir T Nasrabadi, Dipak Aryal, and Venkat Ganesan. Mechanisms of ion transport in lithium salt-doped polymeric ionic liquid electrolytes. *Macromolecules*, 53(16):6995–7008, 2020.

[31] Azusa Nakanishi, Kazuhide Ueno, Daiki Watanabe, Yosuke Ugata, Yoshiharu Matsumae, Jiali Liu, Morgan L Thomas, Kaoru Dokko, and Masayoshi Watanabe. Sulfolane-based highly concentrated electrolytes of Lithium bis(trifluoromethanesulfonyl)amide: ionic transport, Li-ion coordination, and Li–S battery performance. *J. Phys. Chem. C*, 123(23):14229–14238, 2019.

[32] Hee-Seung Lee and Mark E Tuckerman. The structure and proton transport mechanisms in the superprotonic phase of CsH_2PO_4: An *ab initio* molecular dynamics study. *The Journal of Physical Chemistry C*, 112(26):9917–9930, 2008.

[33] Gabriele Tocci and Angelos Michaelides. Solvent-induced proton hopping at a water–oxide interface. *The Journal of Physical Chemistry Letters*, 5(3):474–480, 2014.

[34] Dae-Woon Lim, Masaaki Sadakiyo, and Hiroshi Kitagawa. Proton transfer in hydrogen-bonded degenerate systems of water and ammonia in metal–organic frameworks. *Chemical Science*, 10(1):16–33, 2019.

[35] Zhuoran Long, Austin O Atsango, Joseph A Napoli, Thomas E Markland, and Mark E Tuckerman. Elucidating the Proton Transport Pathways in Liquid Imidazole with First-principles Molecular Dynamics. *The Journal of Physical Chemistry Letters*, 2020.

[36] Shinichi Miura, Mark E Tuckerman, and Michael L Klein. An *ab initio* path integral molecular dynamics study of double proton transfer in the formic acid dimer. *The Journal of Chemical Physics*, 109(13):5290–5299, 1998.

[37] Z Luz and S Meiboom. The activation energies of proton transfer reactions in water. *Journal of the American Chemical Society*, 86(22):4768–4769, 1964.

[38] Diane E Sagnella and Mark E Tuckerman. An empirical valence bond model for proton transfer in water. *The Journal of Chemical Physics*, 108(5):2073–2083, 1998.

[39] Jürg Hutter, Marcella Iannuzzi, Florian Schiffmann, and Joost VandeVondele. CP2K: Atomistic simulations of condensed matter systems. *Wiley Interdisciplinary Reviews: Computational Molecular Science*, 4(1):15–25, 2014.

[40] John P Perdew, Kieron Burke, and Matthias Ernzerhof. Generalized gradient approximation made simple. *Phys. Rev. Lett.*, 77(18):3865, 1996.

[41] Stefan Grimme. Semiempirical gga-type density functional constructed with a long-range dispersion correction. *J. Comput. Chem.*, 27(15):1787–1799, 2006.

[42] Stefan Goedecker, Michael Teter, and Jürg Hutter. Separable dual-space gaussian pseudopotentials. *Phys. Rev. B*, 54(3):1703, 1996.

[43] Christian Hartwigsen, Sephen Gœdecker, and Jürg Hutter. Relativistic separable dual-space gaussian pseudopotentials from H to Rn. *Phys. Rev. B*, 58(7):3641, 1998.

[44] Nidia Gabaldon Limas and Thomas A Manz. Introducing DDEC6 atomic population analysis: part 4. efficient parallel computation of net atomic charges, atomic spin moments, bond orders, and more. *RSC Adv.*, 8(5):2678–2707, 2018.

[45] Thomas A Manz and Nidia Gabaldon Limas. Introducing DDEC6 atomic population analysis: Part 1. Charge partitioning theory and methodology. *RSC Advances*, 6(53):47771–47801, 2016.

[46] Leandro Martínez, Ricardo Andrade, Ernesto G Birgin, and José Mario Martínez. Packmol: A package for building initial configurations for molecular dynamics simulations. *Journal of Computational Chemistry*, 30(13):2157–2164, 2009.

[47] Henk Bekker, HJC Berendsen, EJ Dijkstra, S Achterop, R Vondrumen, David VANDERSPOEL, A Sijbers, H Keegstra, and MKR Renardus. Gromacs-a parallel computer for molecular-dynamics simulations. In *4th International Conference on Computational Physics (PC 92)*, pages 252–256. World Scientific Publishing, 1993.

[48] Berk Hess, Carsten Kutzner, David Van Der Spoel, and Erik Lindahl. Gromacs 4: algorithms for highly efficient, load-balanced, and scalable molecular simulation. *Journal of Chemical Theory and Computation*, 4(3):435–447, 2008.

[49] Mark James Abraham, Teemu Murtola, Roland Schulz, Szilárd Páll, Jeremy C Smith, Berk Hess, and Erik Lindahl. GROMACS: High performance molecular simulations through multi-level parallelism from laptops to supercomputers. *SoftwareX*, 1:19–25, 2015.

[50] Berk Hess, Henk Bekker, Herman JC Berendsen, and Johannes GEM Fraaije. LINCS: A linear constraint solver for molecular simulations. *J. Comput. Chem.*, 18(12):1463–1472, 1997.

[51] Tom Darden, Darrin York, and Lee Pedersen. Particle Mesh Ewald: An n log (n) method for Ewald sums in large systems. *J. Chem. Phys.*, 98(12):10089–10092, 1993.

[52] Herman JC Berendsen, JPM van Postma, Wilfred F Van Gunsteren, ARHJ DiNola, and Jan R Haak. Molecular dynamics with coupling to an external bath. *The Journal of Chemical Physics*, 81(8):3684–3690, 1984.

[53] Shūichi Nosé. A molecular dynamics method for simulations in the canonical ensemble. *Molecular Physics*, 52(2):255–268, 1984.

[54] Michele Parrinello and Aneesur Rahman. Polymorphic transitions in single crystals: A new molecular dynamics method. *Journal of Applied physics*, 52(12):7182–7190, 1981.

[55] Shuichi Nosé and ML Klein. Constant pressure molecular dynamics for molecular systems. *Molecular Physics*, 50(5):1055–1076, 1983.

[56] William Humphrey, Andrew Dalke, and Klaus Schulten. VMD – Visual Molecular Dynamics. *J. Mol. Graphics*, 14:33–38, 1996.

[57] Srimayee Mukherji, Nikhil VS Avula, and Sundaram Balasubramanian. Refined force field for liquid sulfolane with particular emphasis to its transport characteristics. *ACS Omega*, 5(43):28285–28295, 2020.

[58] Claudio Donati, Sharon C Glotzer, Peter H Poole, Walter Kob, and Steven J Plimpton. Spatial correlations of mobility and immobility in a glass-forming lennard-jones liquid. *Physical Review E*, 60(3):3107, 1999.

[59] Junko Habasaki, Carlos Leon, and KL Ngai. *Dynamics of Glassy, Crystalline and Liquid Ionic Conductors: Experiments, Theories, Simulations*, volume 132. Springer, 2016.

[60] Alice L Thorneywork, Dirk GAL Aarts, Jürgen Horbach, and Roel PA Dullens. On the gaussian approximation in colloidal hard sphere fluids. *Soft Matter*, 12(18):4129–4134, 2016.

[61] Léon Van Hove. Correlations in space and time and born approximation scattering in systems of interacting particles. *Physical Review*, 95(1):249, 1954.

[62] Jiajia Li, Ruiyao He, Hao Yuan, Fang Fang, Guobing Zhou, and Zhen Yang. Molecular insights into the effect of asymmetric anions on lithium coordination and transport properties in salt-doped poly (ionic liquid) electrolytes. *Macromolecules*, 55(15):6703–6715, 2022.

[63] Julian Self, Kara D Fong, and Kristin A Persson. Transport in superconcentrated lipf6 and libf4/propylene carbonate electrolytes. *ACS Energy Letters*, 4(12):2843–2849, 2019.

[64] S Balasubramanian and KJ Rao. Preferential paths in alkali ion migration and the mixed alkali effect in silicate glasses. *The Journal of Physical Chemistry*, 97(35):8835–8838, 1993.

[65] S Balasubramanian and KJ Rao. A molecular dynamics study of the mixed alkali effect in silicate glasses. *Journal of Non-Crystalline Solids*, 181(1-2):157–174, 1995.

[66] Junko Habasaki, Isao Okada, and Yasuaki Hiwatari. MD study of the mixed alkali effect in a lithium-potassium metasilicate glass. *Journal of Non-Crystalline Solids*, 183(1-2):12–21, 1995.

[67] Walter Kob and Hans C Andersen. Testing mode-coupling theory for a supercooled binary Lennard-Jones mixture I: The van Hove correlation function. *Physical Review E*, 51(5):4626, 1995.

[68] Junko Habasaki and Kia L Ngai. The mixed alkali effect in ionically conducting glasses revisited: A study by molecular dynamics simulation. *Physical Chemistry Chemical Physics*, 9(33):4673–4689, 2007.

[69] Zhe Li, Grant D Smith, and Dmitry Bedrov. Li^+ solvation and transport properties in ionic liquid/lithium salt mixtures: A molecular dynamics simulation study. *The Journal of Physical Chemistry B*, 116(42):12801–12809, 2012.

[70] Juliane Fiates, Yong Zhang, Luis Fernando Mercier Franco, Edward Joseph Maginn, and Gustavo Doubek. Impact of anion shape on Li^+ solvation and on transport properties for lithium-air batteries: a molecular dynamics study. *Physical Chemistry Chemical Physics*, 2020.

[71] Irene Ruggeri, Andrea La Monaca, Francesca De Giorgio, Francesca Soavi, Catia Arbizzani, Vittorio Berbenni, Chiara Ferrara, and Piercarlo Mustarelli. Correlating Structure and Properties of Super-Concentrated Electrolyte Solutions: ^{17}O NMR and Electrochemical Characterization. *ChemElectroChem*, 6(15):4002–4009, 2019.

[72] Promit Ray, Thomas Vogl, Andrea Balducci, and Barbara Kirchner. Structural investigations on lithium-doped protic and aprotic ionic liquids. *The Journal of Physical Chemistry B*, 121(20):5279–5292, 2017.

[73] Promit Ray, Andrea Balducci, and Barbara Kirchner. Molecular dynamics simulations of lithium-doped ionic-liquid electrolytes. *The Journal of Physical Chemistry B*, 122(46):10535–10547, 2018.

[74] Collin J Wilkinson, Karan Doss, Daniel R Cassar, Rebecca S Welch, Caio B Bragatto, and John C Mauro. Predicting ionic diffusion in glass from its relaxation behavior. *The Journal of Physical Chemistry B*, 124(6):1099–1103, 2020.

Chapter 4A

Force field refinement of Bis(fluorosulfonyl)imide anion

4A.1 Introduction

The choice of salt anion in non-aqueous electrolytes greatly influences both the chemical stability and ion transport of the bulk electrolyte, and the properties of the interface between electrolyte and the electrode [1]. A number of weakly-coordinated anions, with nitrogen [2, 3], carbon [4], boron [5–8], or phosphorus [9–12] as central atoms, have been proposed. As a successor of the widely studied robust anion, bis(trifluoromethanesulfonyl)imide ($[N(SO_2CF_3)_2]^-$, $TFSI^-$, alkali metal salts and ionic liquids with bis(fluorosulfonyl)imide anion ($[N(SO_2F)_2]^-$, FSI^-) also have good physical and chemical properties, including forming stable solid-electrolyte-interphase (SEI) on electrodes [13–15]. Thus, FSI-based salts have been extensively investigated as electrolyte component to develop advanced lithium-ion batteries and rechargable lithium metal batteries [13]. In fact, LiFSI has presently been implemented as a co-salt (with 5-10 weight $\%$ of the total mass of electrolyte) to improve the performance of lithium-ion batteries for electric vehicles [16].

Various non-ionic type organic solvents have been used to prepare FSI-based electrolytes [13], including carbonates (e.g. ethylene carbonate [17]), ethers (e.g. 1,2-dimethoxy ethane, DME [18]), nitriles (e.g. acetonitrile [19]), fluorosulfonamides, sulfones (e.g. sulfolane [20]), and alkyl phosphates. For a given type of solvent, LiFSI-based electrolytes have higher ionic conductivities at room temperature than $LiPF_6$ and LiTFSI-based electrolytes [17]. This is attributed to (a) the highly flexible -SO_2-$N^{(-)}$-SO_2- structure in the FSI^- anion, resulting in weaker van der Waals interactions in FSI-based electrolytes, as indicated by their lower viscosities, and (b) the moderate size of FSI^- anion, lying between the sizes of PF_6^- and $TFSI^-$ anions [17]. The improvement in ionic conductivity with LiFSI

is greater for concentrated electrolytes [19]. Higher ionic conductivities of LiFSI-based electrolytes result in faster ion transport and should enable higher C-rate (charging rate) capability of lithium-ion batteries and rechargeable lithium metal batteries [13].

LiFSI has higher thermal stability (dissociation temperature, T_d>200^oC) [17] compared to $LiPF_6$ ($\sim$ 60^{o}C), as well as to hydrolysis [13]. Further, LiFSI-based electrolytes are compatible with electro-active materials [13], including graphite [21], silicon [22], phosphorus [23], and sulphur [24]. FSI^- anion has been demonstrated to form stable SEI layers [13] on the surface of graphite anode [25], and to achieve reversible Li^+ intercalation in conventional and concentrated (>3M) LiFSI-based electrolytes [19]. In addition, cells with LiFSI-based electrolytes have higher charge capacities and lower interfacial resistance (sum of SEI resistance and Li^+ transfer resistance) than $LiPF_6$-based electrolytes [13].

Motivated by the improved properties of conventional (dilute) LiFSI-based electrolytes, LiFSI has been studied as a salt for high-concentration electrolytes (>3 M) [13]. In these electrolytes, anions and not solvent molecules are predominantly reduced to form SEI layers [19]. The LiF-rich SEI layer formed on the Li anode can prevent the continuous reaction between electrode and electrolyte, reducing the consumption of active Li^+ ions [13].

In our studies, we desired to compare Li-ion and Na-ion high concentration electrolytes (HCEs). We were therefore in search for salts of lithium and sodium salts of a common anion which will be soluble in a common solvent. To this end, we first learnt that both LiFSI and NaFSI salts are soluble in sulfolane at 303 K temperature and 1 bar pressure [26, 27]. Inspired from this and what we learnt about the multiple benefits of the FSI anion, we fixed our choice of anion at the FSI^- anion. This sub-chapter serves mainly as a means for us to realising Li and Na-ion HCEs containing FSI^- as anion. At the same time, we wished to propose a good force field to describe the transport properties of systems containing the FSI anion.

4A.2 Methodology and Simulation Details

The bis(fluorosulfonyl)imide anion (FSI anion) is an acyclic molecule with symmetrical atom types about a central nitrogen atom (Figure 4A.1). The performance of the force field proposed here has been compared with that of the CL&P force field for the FSI anion [28] (charge-scaled) throughout this sub-chapter. Therefore the standard atom type names used by the CL&P force field were maintained herein.

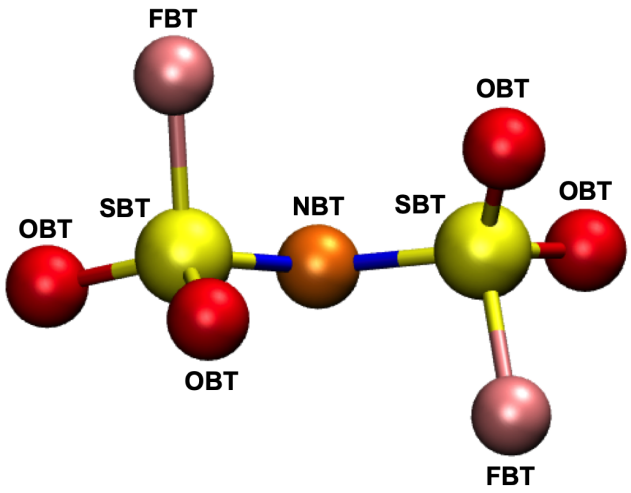

Figure 4A.1: The bis(fluorosulfonyl)imide anion (FSI anion) with atom types marked. Orange - nitrogen (NBT), yellow - sulphur (SBT), red - oxygen (OBT), pink - fluorine (FBT).

Most force fields capture the density and liquid structure well. The prediction for transport properties is often in poor agreement with experiments. In order to obtain a force field which captures transport properties better, changes to some of the parameter values in the some of the terms of the total potential energy equation were made. The total potential energy is defined:

$$U = \frac{1}{2}\sum_{bonds} k_b(r - r_0)^2 + \frac{1}{2}\sum_{angles} k_\theta(\theta - \theta_0)^2 + dihedral\,energy + \sum_i \sum_{j \neq i} 4\epsilon_{ij}\left[\left(\frac{\sigma_{ij}}{r_{ij}}\right)^{12} - \left(\frac{\sigma_{ij}}{r_{ij}}\right)^{6}\right] + \frac{1}{4\pi\epsilon_0}\sum_i \sum_{j \neq i} \frac{q_i q_j}{r_{ij}} \tag{4A.1}$$

The total potential energy of the system is a sum total of energies from non-bonded contributions such as the Coulomb and the Lennard-Jones interactions and those from the bonded contributions of bond, angle and dihedral-angle excitations of a molecule. In Equation 4A.1, q_i is the atomic site charge of the i^{th} atom, σ_{ij} and ϵ_{ij} are LJ parameters, r_{ij} is the distance between the centers of the i^{th} and j^{th} atoms, ϵ_0 is the permittivity of free-space, r_0 is equilibrium bond-length, k_b is bond force-constant, θ_0 is equilibrium bond-angle, and k_θ is angle force-constant. In this sub-chapter, the results from two force fields, viz., charge-scaled CL&P and the refined force field, were reported. The dihedral energy functional forms of the two force-fields are different. Therefore, the functional form for this term has not been included in Equation 4A.1. Under the heading "Refinement of dihedral parameters", please refer to Equations 4A.2 and Equation 4A.3 for the dihedral energy functional forms for charge scaled CL&P and the refined force field reported here, respectively. In this sub-chapter, we refine the atomic site charges and modify a few

Lennard-Jones parameters. Unlike sulfolane, the FSI anion is an acyclic molecule (anion). Therefore, in contrast to the sulfolane molecule, the dihedrals of the FSI anion are not as rigid to torsion and can be refined. In this sub-chapter, we refine the dihedral parameters of the F-S-N-S (FBT-SBT-NBT-SBT) dihedral of the FSI anion.

The force field used as a starting point for refinement is the CL&P force field [28] for the FSI anion.

4A.2.1 Chemical species studied in this sub-chapter

The systems synthesised in this thesis are LiFSI in sulfolane, NaFSI in sulfolane, and C_2MIM[FSI]. The chemical species involved are shown in Figure 4A.2.

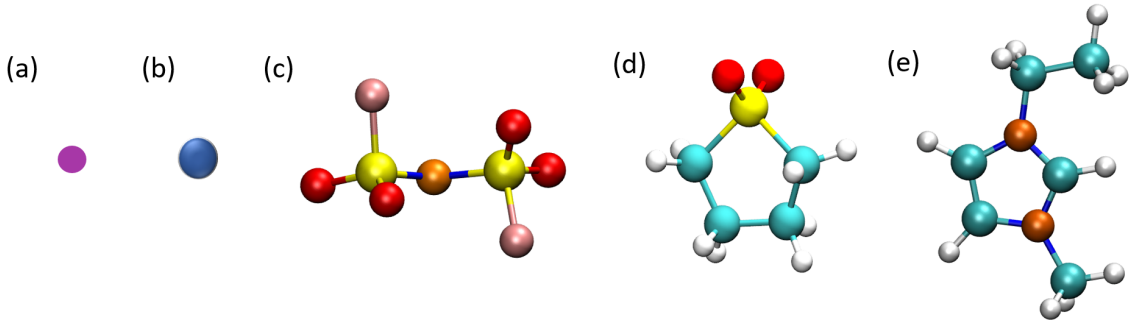

Figure 4A.2: (a) Li-ion, (b) Na-ion, (c) FSI anion, (d) Sulfolane molecule, (e) C_2MIM cation. Purple - Li-ion, blue - Na-ion, red - oxygen, cyan - carbon, yellow - sulphur, white - hydrogen, orange - nitrogen, pink - fluorine.

4A.2.2 Non-bonded parameters

Deriving atomic-site charges

Density derived electrostatic and chemical (DDEC6) atomic-site charges were dervied for the FSI anion from DFT calculations. The bis(trifluoromethanesulfonyl)imide anion (TFSI) is an anion very similar to the FSI anion excepting that the TFSI anion has CF_3 groups in the place of the fluorine atoms. Crystal DDEC6 atomic site charges for 1-Butyl-3-methylimidazolium bis(trifluoromethylsulfonyl)imide (BMIM-TFSI) cation-anion pair have been derived [29] in the past and along with other force field refinements has been shown

to capture the physico-chemical and transport properties of the ionic liquid very well [30]. Similarly, the atomic site charges for FSI anion were from the DDEC6 charges obtained for LiFSI:Sulfolane(SUL) = 1:1 crystal reported in Ref. 26. The crystal structure used as the starting point of our calculation was submitted by Dokko et al to the Cambridge Structure Database (CSD) - CCDC as 1866669 [26]. CP2K software was used for electron density distribution calculation of the unit cell of the crystal [31]. Grimme's D3 empirical van der Waals corrections [32] and Perdew, Burke, and Ernzerhof (PBE) exchange-correlation functional were used [33]. GeodeckerTeterHutter (GTH) pseudopotentials were used to represent for core-electrons [34, 35]. Triple–ζ double polarized basis sets with an energy cut-off of 320 Ry was used for valence electrons. The electron density calculated thus was used as input to Chargemol software [36] for partitioning of electron density to atomic site DDEC6 charges [37].

The total charge on the FSI anion thus derived was -0.82. Our purpose was to use the FSI force field to simulate LiFSI and NaFSI based battery electrolytes. Since we wished to maintain the partial charge on Li^+ ion at 0.82 (as in Chapter 3), the partial atomic site charges on the FSI anion atoms from both DDEC and those quoted for CL&P [28] were rescaled such that the total charge on the anion was -0.82. These scaled crystal DDEC6 and CL&P rescaled charges for each atom type of the FSI anion are presented in Table 4A.1.

Atom type	Charge scaled CL&P (e)	This work (e)
FBT	-0.1066	-0.2179
SBT	0.8364	1.3909
NBT	-0.5412	-0.7564
OBT	-0.4346	-0.6024

Table 4A.1: Atomic site charges q(e) for each atom type of the FSI anion.

Modifying the Lennard-Jones parameters

A change in atomic site charges would mean that a corresponding change in Lennard-Jones (LJ) parameters is in order. As discussed before, the FSI anion is very similar to the TFSI anion. We therefore thought that the TFSI parameters developed in our research group earlier for imidazolium based ionic liquids containing the TFSI anion [29] might be a good starting point for the LJ parameters for the FSI anion.

Since OBT is the prime interaction site of an FSI anion with an alkali-ion, we further modified the LJ parameters of OBT from that in Ref. 29 to obtain better transport properties.

These refined LJ parameters are listed in Table 4A.2.

Atom type	σ (Å)		ϵ (kJ/mol)	
	Charge-scaled CL&P [28]	This work	Charge-scaled CL&P [28]	This work
FBT	3.118	2.950	0.25540	0.09600
SBT	3.550	3.550	1.04600	0.54392
NBT	3.250	3.250	0.71128	0.41840
OBT	3.150	3.000	0.83736	0.50000

Table 4A.2: Lennard-Jones parameters from CL&P force field and the refined force field (current work) for the FSI anion.

4A.2.3 Bonded parameters

The bonded parameters include those for bonds, angles, and dihedral interactions.

Bond parameters

Bond parameters used in the refined force field were the same as those used in the CL&P force field for FSI anion [28]. These parameters are listed in Table 4A.3.

Atom type 1	Atom type 2	Equilibrium bond length r_0 (Å)	Force constant k_b (kJ mol^{-1} Å^{-2})
SBT	FBT	1.575	1879
NBT	SBT	1.570	3137
OBT	SBT	1.437	5331

Table 4A.3: Bonded length parameters for all distinct bond types present in the FSI anion.

Angle parameters

Angle parameters used in the refined force field were the same as those used in the CL&P parameterisation [28]. These parameters are listed in Table 4A.4.

Atom type 1	Atom type 2	Atom type 3	Equilibrium bond angle θ_0 (degrees/radians)	Force constant k_θ (kJ mol^{-1} rad^{-2})
FBT	SBT	NBT	103.0/1.798	902
FBT	SBT	OBT	104.1/1.817	1077
NBT	SBT	OBT	113.6/1.983	789
OBT	SBT	OBT	118.5/2.068	969
SBT	NBT	SBT	125.6/2.192	671

Table 4A.4: Bond angle parameters for all distinct bond angle types present in the FSI anion.

Refinement of dihedral parameters

All dihedrals of the FSI anion are around the S-N bond. Additionally, since FSI^- is chemically symmetric around the central nitrogen, refinement of the F-S-N-S dihedral is sufficient when setting other dihedrals types around the S-N bonds to have a force constant of 0. Therefore, we decided to refine the CL&P dihedral parameters for the F-S-N-S (FSI-SBT-NBT-SBT) dihedral starting from a force field of revised charges and LJ parameters obtained up to this point.

To refine dihedral parameters, first a FSI anion was geometry optimised at MP2/aug-cc-pvdz level of theory. A relaxed dihedral scan of the selected one of two F-S-N-S dihedrals of the FSI anion at MP2/aug-cc-pvtz level of theory/basis set was then performed. The relaxed configurations obtained for every value of the selected F-S-N-S dihedral angle is stored. These configurations are energy minimised within the force field obtained up to this point. A profile is obtained for the total potential energy as a function of the chosen dihedral angle after energy minimisation. This total potential energy profile obtained within classical MD is subtracted from the dihedral scan obtained quantum chemically earlier to yield the dihedral energy profile of the chosen dihedral. This process is to be repeated for the other F-S-N-S dihedral. An average is taken of the two dihedral energy profiles. This averaged profile is fit to a desired dihedral energy functional form to yield the revised force field parameters of a single F-S-N-S dihedral.

Dihedral parameters for the CL&P force field for FSI anion [28] are given in Table 4A.5. The dihedral parameters here fit Equation 4A.2 for Fourier dihedrals. ϕ is the dihedral angle and C_1 to C_4 can be called Fourier coefficients. This functional form takes the place of the dihedral energy term in Equation 4A.1 for the charge-scaled CL&P force field.

$$V = \frac{1}{2}[C_1(1+cos(\phi)) + C_2(1-cos(2\phi)) + C_3(1+cos(3\phi)) + C_4(1-cos(4\phi))] \quad \text{(4A.2)}$$

Atom type 1	Atom type 2	Atom type 3	Atom type 4	C_1 kJ/mol	C_2 kJ/mol	C_3 kJ/mol	C_4 kJ/mol
SBT	NBT	SBT	FBT	11.445	-15.186	-3.212	0.000
SBT	NBT	SBT	OBT	0.000	0.000	-0.015	0.000

Table 4A.5: CL&P dihedral parameters for the FSI anion [28].

Revised dihedral parameters for the force field used in this work for each value of multiplicity are given in Tables 4A.6, 4A.7, and 4A.8. The dihedral energy parameters in this case fit Equation 4A.3. ϕ is the dihedral angle, k_ϕ the dihedral force constant, ϕ_s is phase (0 for all dihedrals here), and n is multiplicity. This functional form takes the place of the dihedral energy term in Equation 4A.1 for the refined force field.

$$V = k_\phi[1 + cos(n\phi - \phi_s)] \quad \text{(4A.3)}$$

Atom type 1	Atom type 2	Atom type 3	Atom type 4	ϕ (deg)	k_ϕ (kJ/mol)	multiplicity
SBT	NBT	SBT	FBT	180	-5.0336	1
SBT	NBT	SBT	OBT	180	0.0000	1

Table 4A.6: Refined force field parameters for distinct dihedral types of the FSI anion for multiplicity = 1.

Atom type 1	Atom type 2	Atom type 3	Atom type 4	ϕ (deg)	k_ϕ (kJ/mol)	multiplicity
SBT	NBT	SBT	FBT	0	7.9869	2
SBT	NBT	SBT	OBT	0	0.0000	2

Table 4A.7: Refined force field parameters for distinct dihedral types of the FSI anion for multiplicity = 2

Atom index 1	Atom index 2	Atom index 3	Atom index 4	ϕ (deg)	k_ϕ (kJ/mol)	multiplicity
SBT	NBT	SBT	FBT	180	0.0165	3
SBT	NBT	SBT	OBT	180	0.0000	3

Table 4A.8: Refined force field parameters for distinct dihedral types of the FSI anion for multiplicity = 3

Unlike the F-S-N-S dihedral, of which there are two, there exists only one F-S-S-F (FBT-SBT-SBT-FBT) dihedral in the FSI anion. The refinement in the dihedral parameters of the F-S-N-S dihedrals are reflected in the probability density profile of the F-S-S-F dihedral. Therefore, the probability density profile of the F-S-S-F dihedral across the two force fields is shown in Figure 4A.3.

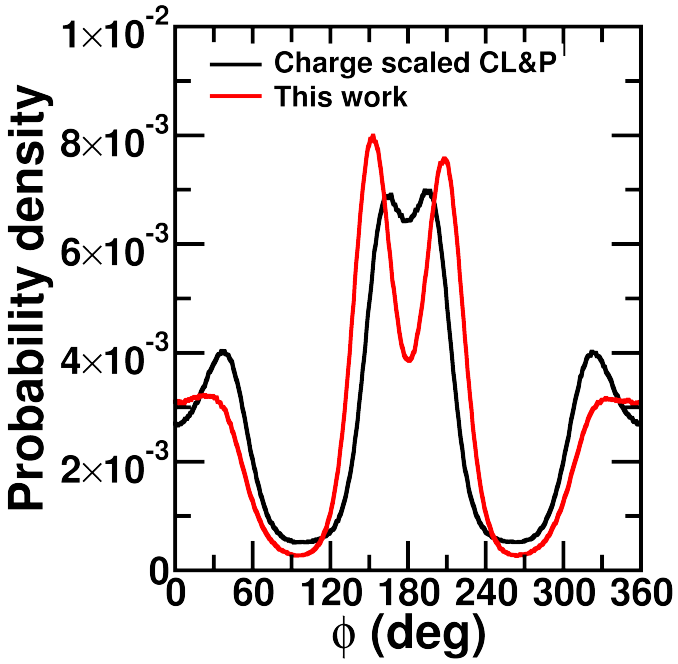

Figure 4A.3: F-S-S-F (FBT-SBT-SBT-FBT) dihedral distribution from the two force fields for LiFSI:SUL=1:3 HCE.

4A.2.4 Molecular dynamics simulations

To check the performance of force fields against experiments, classical MD simulations were carried out for LiFSI in sulfolane (1:3) system, NaFSI in sulfolane (1:1) system, and the [C_2MIM]FSI ionic liquid. To this end, PACKMOL software [38] was used to generate random configurations. GROMACS-2018.3 package [39–41] was employed to

generate the classical MD trajectories. A timestep of 1 fs was used to integrate the equations of motion using the leap-frog algorithm. All C-H bonds of sulfolane were constrained using the LINCS algorithm in GROMACS. Lennard-Jones (LJ) and Coulomb cut-off distances were fixed at 12 Å, and the neighbor list cut-off was extended to 14 Å. Long-range interactions were accounted for using particle–particle mesh Ewald (PPPM) method. 1-2, 1-3 non-bonding interactions were set to zero. For 1-4 pairs, non-bonding LJ and Coulombic interactions were included with a scale factor of 0.5. For all other atom-pairs, a scale factor of 1.0 was used. Geometric mean was employed as the combining rule for calculating the interaction between different atom types. Long-range dispersion corrections to energy and pressure were applied. The random packings were energy minimized within the force-field which was followed by constant-NPT equilibration run using Berendsen barostat and Nosé–Hoover thermostat. Following this, a constant-NPT production run using Parrinello-Rahman Barostat and Nosé–Hoover thermostat was carried out. The average density estimated from the NPT production run was used to run constant-NVT production runs. For the Nosé–Hoover thermostat, a coupling time-constant of 0.5 ps was used, and the system was coupled to the thermostat every 10 timesteps. For the Berendsen and the Parrinello-Rahman barostats, a coupling time constant of 2 ps used. Both barostats were coupled with the system once every 10 timesteps. To simulate a bulk environment, periodic boundary conditions were applied along all three axes. All visualisations were made using the Visual Molecular Dynamics software [42]. The force field for Li-ion was maintained the same as found in Chapter 3 for consistency. For sulfolane, the refined force field parameters reported in Chapter 2 were used. For the C_2MIM cation, the force field parameters were taken from Ref. 29. The charges for various atom types in C_2MIM cation are different depending on the pairing anion in Ref. 29. Those charges for the C_2MIM cation which are for the TFSI anion were chosen here after rescaling to +0.82 (since the charge on the FSI anion reported here is -0.82). The charge on the Na^+ atom was 0.82 (same as Li^+). The Lennard-Jones parameters for Na-ion were taken from Ref. 27 and stated in Table 4A.9.

Atom type	Charge (e)	σ (Å)	ϵ (kJ/mol)
Na	0.82	2.3	0.20294

Table 4A.9: Force field parameters of the Na-ion

These parameters for Li, Na, FSI ions, and sulfolane molecules have been used in Chapter 4B and 4C as well. Systems simulated in this study are described in Table 4A.10.

System	No .of molecules/ions of each type	MD simulation conditions
LiFSI:SUL = 1:3	Li^+(160), FSI^-(160), and SUL(480)	T = 303 K and P = 1 bar
NaFSI:SUL = 1:1	Na^+(160), FSI^-(160), and SUL(160)	T = 303 K and P = 1 bar
C_2MIMFSI	C_2MIM^+(250), and FSI^-(250)	T = 298 K and P = 1 bar

Table 4A.10: System details for classical MD simulations.

4A.3 Results and Discussions

Physico-chemical properties such as density, diffusion coefficient, and ionic conductivity of LiFSI:sulfolane = 1:3 were calculated using the charge scaled CL&P model and the force field reported in this study. Density of [C_2MIM]FSI too was calculated. This was done to gauge the transferability of the FSI force field proposed here across two different classes of compounds. The density of the NaFSI:SUL = 1:1 was calculated in the refined force field to check if the force field proposed here was a good choice for Na-ion HCEs as well.

4A.3.1 Density

Density was calculated for the LiFSI:SUL = 1:3 and NaFSI:SUL=1:1 HCEs at 303 K and 1 bar pressure, and that of [C_2MIM]FSI at 298 K and 1 bar pressure.

We find that the force field reported here predicts density with accuracy comparable to that of the charge-scaled CL&P force field (Table 4A.11).

Force field	ρ_{sim} (g/cc)	Deviation (%)
Charge scaled CL&P	1.487	2.00
This work	1.490	2.19

Table 4A.11: Prediction of density of LiFSI:SUL = 1:3 in different force fields. ρ_{exp} = 1.458 g/cc [26] at T = 303 K and P = 1 bar.

We checked the generality of the force field proposed here by testing the performance of our force field against experiments for two very different classes of compounds. Here, a Li-ion HCE (LiFSI:SUL=1:3), Na-ion HCE (NaFSI:SUL=1:1) form one class of compounds. A model ionic liquid ([C_2MIM]FSI) belongs to the second class of compounds. We found that the force field we proposed predicted density of both classes of compounds with fair accuracy (within 3% error) (Table 4A.12). Therefore, the FSI parameters we have proposed are transferable across these two classes of compounds.

System	ρ_{sim} (g/cc)	ρ_{exp} (g/cc)	Deviation (%)
LiFSI:SUL = 1:3 at 303 K	1.490	1.458 [26]	2.19
NaFSI:SUL = 1:1 at 303 K	1.78	1.73 [27]	2.89
[C_2MIM]FSI at 298 K	1.432	1.446 [43]	-0.97

Table 4A.12: Prediction of density of LiFSI:SUL = 1:3, NaFSI:SUL = 1:1, and [C_2MIM]FSI using the force field of this work.

4A.3.2 Diffusion coefficient

The mean squared displacements (MSD) and diffusion coefficients of the various chemical species of LiFSI:SUL = 1:3 HCE were attempted to be calculated in both force fields and compared against experimental values [26] (Figure 4A.4(a) and Table 4A.13).

From Figure 4A.4(a) we learnt that using the force field reported here, all chemical species move a distance 14 Å to 17 Å over the largest investigated time intervals. Whereas, in the charge-scaled CL&P force field various chemical species are barely able to move to between 3 Å to 5 Å over the longest time intervals investigated.

The mean of $\beta = \frac{d(log(MSD))}{d(log(t))}$ as a function of time of a particular chemical species reaching unity gives an idea of the time interval after which the molecular species enters diffusive regime from a sub-diffusive regime of dynamics. Over a 100 ns time interval, FSI anions in the force field reported here are able to transition to a near diffusive regime at 30 ns time interval. Whereas, FSI anions in the charge-scaled CL&P force field are not able to transition to the diffusive regime over the time intervals investigated (Figure 4A.4(b)). We found that the diffusion coefficients for various chemical species were not estimable within the charge-scaled CL&P force field over a 100 ns time interval.

The diffusion coefficients for the various chemical species are reported in Table 4A.13.

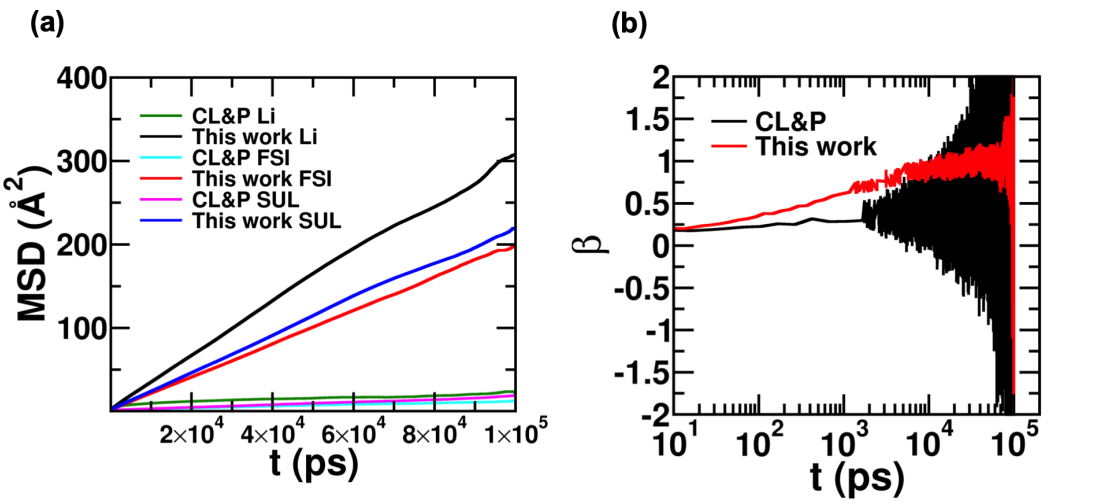

Figure 4A.4: (a) MSD versus time for all chemical species in the LiFSI:SUL=1:3 electrolyte from two force fields. (b) $\beta = \frac{d(log(MSD))}{d(log(t))}$ versus time for FSI anions for the charge-scaled CL&P force field [28] and the force field reported in this work.

Ion/ Molecule	Charge-scaled CL&P [28]	This work	Experiment	Ratio
		D_{sim} $\times 10^{-7}$cm^2/s	D_{exp} [26] $\times 10^{-7}$cm^2/s	D_{sim}/D_{exp}
Li	not estimable in 100 ns	0.537	1.630	0.330
FSI	not estimable in 100 ns	0.337	1.290	0.262
SUL	not estimable in 100 ns	0.392	1.240	0.317

Table 4A.13: Prediction of diffusion coefficient of different chemical species in LiFSI:SUL = 1:3 electrolyte.

Therefore, we found that our refined force field has made a large improvement in the estimation of diffusion coefficients of various species of the LiFSI:SUL=1:3 HCE.

4A.3.3 Ionic conductivity

The method that was used to calculate ionic conductivity is the Einstein relation discussed in Chapter 1. The ionic conductivity of LiFSI:SUL=1:3 electrolyte was not estimable in the charge-scaled CL&P force field for the same reason the diffusion coefficients of various species were not estimable over a time interval of 100 ns within the CL&P force field.

The ionic conductivity of LiFSI:SUL=1:3 HCE was estimated with good accuracy in the force field reported here (Table 4A.14). The reported ionic conductivity is only a factor

of 3.3 less than the experimentally predicted value. Prediction that is within an order of magnitude factor different from the experimentally reported value is considered good for a transport property such as ionic conductivity.

Force field	σ_{sim} (mS/cm)	$\sigma_{sim}/\sigma_{exp}$
Charge-scaled CL&P	Too viscous to be estimable in 100 ns	-
This work	0.66	0.30

Table 4A.14: Prediction of ionic conductivities of LiFSI:SUL=1:3 in different force fields. σ_{exp} = 2.19 mS/cm [26].

4A.4 Conclusions

In this sub-chapter, our aim was to arrive at a force field that captures the transport of FSI anion containing HCEs to a fair degree of accuracy. We also wanted the FSI anion force field to be transferable across two main classes of compounds, viz., Li and Na-ion battery electrolytes, and ionic liquids. To achieve this, we derived crystal phase DDEC6 charges for the experimentally reported LiFSI:SUL=1:1 crystal. Atomic site charges for FSI were extracted from the same and scaled to yield a total charge of -0.82. Next, most Lennard-Jones (LJ) parameters we used for the FSI anion were the same as those arrived at for the TFSI anion in Ref. 29. The LJ parameters for OBT (oxygen of FSI) was modified for capturing transport properties with higher accuracy. The bond and angle parameters for the FSI anion were maintained the same as in the CL&P force field [28]. We revised the dihedral parameters of the FSI anion corresponding to the changes we had made in the atomic site charges and LJ parameters. The revised force field was found to predict density with comparable accuracy as the charge-scaled CL&P force field. The main highlight in the force field parameterisation is the massive improvement in the prediction of transport properties such as diffusion coefficients, and ionic conductivity. Therefore, we propose a force field for the FSI anion which is transferable from battery electrolytes to ionic liquids, and predicts the transport properties of Li-ion HCEs well. The force field was also found applicable to Na-ion HCEs.

With a good force field for the FSI anion in hand, we wished to study the similarity and differences between Li and Na-ion based HCEs in the next sub-chapter.

Chapter 4B

Comparative study of the structure and transport of lithium and sodium based high concentration electrolytes

4B.1 Introduction

High concentration electrolytes (HCEs) use a large amount of salt as a defining feature. Lithium is scarce in the Earth's crust (0.002 %). This makes Li-ion batteries in general and Li-ion based HCE batteries in particular, very expensive. In fact, even in the Li-ion low concentration electrolyte (LCEs) battery based devices used at present, the most expensive component of the device is the battery. Sodium is thousand times more abundant in the Earth's crust than lithium (2.36 % for Na against 0.002%) [44]. Lithium-ion batteries have lithium ions in the electrolyte, and use the metals lithium (0.002 %), cobalt (0.0025 %), manganese (0.095%), and copper (0.006 %) for the cathode. On the other hand, sodium-ion batteries have sodium ions in the electrolyte and use the metals sodium (2.36 %), iron (5.63 %), nickel (0.0084 %), manganese (0.095 %), and aluminium (8.23 %) for the cathode. Thus, the raw materials for sodium-ion batteries are on the whole more abundant and widely available [44]. However, due to the larger size of Na-ion in intercalation, the specific capacity of the hard-carbon anode in a sodium-ion battery (250 mAh/g) [45] is less than that of the graphite anode in a lithium-ion battery (350 mAh/g), and consequently the specific energy of a sodium-ion battery (100-150 Wh/kg) is less than that of a lithium-ion battery (130-280 Wh/kg) [46]. It is expected though that both batteries will have comparable rate capability [47]. Na-ion batteries may therefore become more sustainable and lower in cost than Li-ion batteries, in applications where the battery energy density requirement is lower, such as short-range electric vehicles and large-scale energy storage systems [48].

Therefore, both Li-ion and Na-ion batteries have their own advantages and disadvantages. Most Na-ion electrolytes investigated up to this point are low concentration electrolytes. Given the myriad of HCEs and given the unique liquid structure and transport phenomena present in HCEs, it is worth asking how Na-ion based compare to Li-ion based HCEs. This sub-chapter studies Na-ion HCEs alongside Li-ion HCEs both as an attempt to find an alternative to a scarce metal such as lithium and also out of theoretical interest in exploring HCEs based on an alkali-ion different from Li-ion in some ways.

4B.2 Methodology and simulation details

4B.2.1 Chemical species studied in this sub-chapter

The systems synthesised in this thesis are LiFSI in sulfolane and NaFSI in sulfolane at three salt concentrations. The chemical species involved are shown in Figure 4B.1.

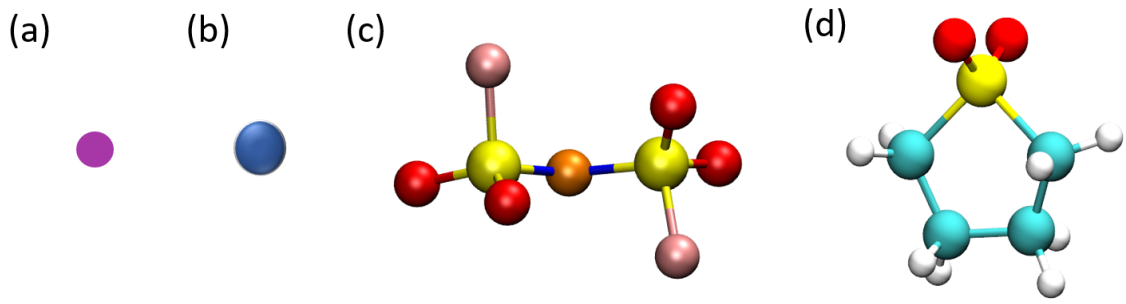

Figure 4B.1: (a) Li-ion, (b) Na-ion, (c) FSI anion, (d) Sulfolane molecule. Purple - Li-ion, blue - Na-ion, red - oxygen, cyan - carbon, yellow - sulphur, white - hydrogen, orange - nitrogen, pink - fluorine.

4B.2.2 Molecular dynamics (MD) simulation details

LiFSI in sulfolane and NaFSI in sulfolane were simulated at three salt concentrations: LiFSI/NaFSI:sulfolane = 1:1, 1:1.5, and 1:9.57. Apart from fairly low salt concentrations such as salt:solvent = 1:9.57 and lower, the most stable state of NaFSI in sulfolane at 303 K and 1 bar was crystalline at ratios except in the crystallinity gap in the range 1/1.6 $\leq$ [NaFSI]/[SUL] $\leq$ 1/0.8 [27]. LiFSI in sulfolane is most stable in liquid state atleast

up to concentrations as high as LiFSI:SUL = 1:3 [26]. This explains our choice of salt concentrations. Three independent trajectories were generated for each system. The MD simulation details are given in Tables 4B.1 and 4B.2.

System	Lithium electrolytes		Sodium electrolytes		Equilibrium NPT Box Length (Å)
	No. of Li-ions	No. of Na-ions	No. of FSI anions	No. of sulfolanes	
LiFSI:SUL = 1:1	160	0	160	160	36.27
NaFSI:SUL = 1:1	0	160	160	160	36.40
LiFSI:SUL = 1:1.5	160	0	160	240	39.16
NaFSI:SUL = 1:1.5	0	160	160	240	39.24
LiFSI:SUL = 1:9.57	160	0	160	1531	63.67
NaFSI:SUL = 1:9.57	0	160	160	1531	63.72

Table 4B.1: System details for MD simulations.

No. of salt formula units : No. of solvent molecules	NVT production trajectory length (ns)	No. of independent runs	Total trajectory length (ns)
1:1	2500	3	7500
1:1.5	1000	3	3000
1:9.57	55	3	165
			Total - 10665

Table 4B.2: MD simulation NVT production trajectory details.

PACKMOL software [38] was used to generate initial configurations of the constituents at each concentration. GROMACS-2018.3 package [39, 41, 49], was employed to generate the MD trajectories. Structural insights and various equilibrium properties were gleaned from the analysis at each of these concentrations. These trajectories were utilized to investigate various aspects of Li and Na-ion hopping in HCEs. The temperature and pressure for all production runs were 303 K and 1 bar respectively. Most analyses were carried out with in-house FORTRAN codes. A timestep of 1 fs was used to integrate the equations of motion using the leap-frog algorithm. All C-H bonds of sulfolane were constrained using the LINCS algorithm [40] in GROMACS. The Lennard-Jones (LJ) and Coulomb cut-off distances were fixed at 12Å, and the neighbor list cut-off was extended to 14 Å. Long-range interactions were accounted for using particle–particle mesh Ewald (PME) method [50]. 1-2, 1-3 non-bonding interactions were set to zero. For 1-4 pairs, non-bonding LJ and Coulombic interactions were included with a scale factor of 0.5. For

all other atom-pairs, a scale factor of 1.0 was used. Geometric mean was employed as the combining rule for calculating the interaction between different atom types. Long-range dispersion corrections to energy and pressure were applied. The random packing at each concentration was energy minimized within the force-field which was followed by constant-NPT equilibration run using Berendsen barostat [51] and Nosé–Hoover thermostat [52]. Following this, a constant-NPT production run using Parrinello-Rahman Barostat [52, 53] and Nosé–Hoover thermostat [52] was carried out. The average density estimated from the NPT production run was used to run constant-NVT equilibration and finally, the constant-NVT production run. For the Nosé–Hoover thermostat [52], a coupling time-constant of 0.5 ps was used, and the system was coupled to the thermostat every 10 timesteps. For the Berendsen [51] and the Parrinello-Rahman barostats [52, 53], a coupling time constant of 2 ps used. Parrinello-Rahman barostat was coupled with the system once every 10 timesteps and every 1 timestep respectively for high (>1 M) concentration and low concentration systems. Three independent MD runs were performed for every system. To create the two additional independent trials, density equilibrated systems at 303 K and 1 bar pressure, were heated to 340 K and 350 K, respectively, and annealed back to 303 K prior to NVT production runs. Following this, independent NVT production runs at 303 K were run. To simulate a bulk environment, periodic boundary conditions were applied along all three axes. All trajectories visualizations were made using the Visual Molecular Dynamics software [42].

4B.3 Results and Discussions

4B.3.1 Density

Lithium Bis(fluorosulfonyl)imide and Sodium Bis(fluorosulfonyl)imide were studied at three salt concentrations, viz., salt:solvent number ratios = 1:1, 1:1.5, and 1:9.57. Of these, 1:1 and 1:1.5 are HCEs whereas 1:9.57 is a prototypical low concentration electrolyte. The density of the electrolytes are tabulated in Table 4B.3.

System	Lithium electrolytes		Sodium electrolytes	
Salt:Solvent	ρ_{sim} (g/cc)	ρ_{exp} (g/cc) [26]	ρ_{sim} (g/cc)	ρ_{exp} (g/cc) [27]
1:1	1.71	*	1.78	1.73
1:1.5	1.62	*	1.686	1.63
1:9.57	1.375	1.337	1.389	1.35†

* As data from experiments were not found at salt:solvent = 1:1 and 1:1.5, it is unclear whether at these concentrations, LiFSI in sulfolane is a liquid or a crystal at 303 K and 1 bar pressure. We however simulate LiFSI in sulfolane (as a liquid) at these concentrations as well so as to parallel studies of Na-ion HCEs and to operate at the highest salt concentration limit for which data is available for either electrolyte.

† ρ = 1.35 g/cc is the experimental density of NaFSI in sulfolane at 1:10. 1:10 is nearest to the experimentally reported number ratio of NaFSI in sulfolane of 1:9.57.

Table 4B.3: Density as a function of salt concentration for Li and Na electrolytes at 303 K and 1 bar pressure.

4B.3.2 Ionic conductivity

Ionic conductivities increase with decrease in salt concentration of the electrolyte. Conductivities of lithium based electrolytes are more than an order of magnitude higher than for sodium based electrolytes in HCEs (salt:solvent = 1:1, 1:1.5) (Table 4B.4 and Figure 4B.2). The difference in conductivities between lithium and sodium based electrolytes at low salt concentration is much smaller (factor of 3, approximately). The effect of replacing all Li-ions by Na-ions on ionic transport in a salt concentration regime where one expects alkali-ion hopping (1:1 and 1:1.5) versus where alkali-ion hopping is nearly absent (1:9.57), is different.

System	Lithium electrolytes		Sodium electrolytes	
Salt:Solvent	σ_{sim} (mS/cm)	σ_{exp} (mS/cm) [26]	σ_{sim} (mS/cm)	σ_{exp} (mS/cm) [27]
1:1	0.01160	*	0.00137	0.07
1:1.5	0.12200	*	0.00499	0.23
1:9.57	1.97000	3.40	0.68100	1.89†

* As data from experiments were not found at salt:solvent = 1:1 and 1:1.5, it is unclear whether at these concentrations, LiFSI in sulfolane is a liquid or a crystal at 303 K and 1 bar pressure. We however simulate LiFSI in sulfolane (as a liquid) at these concentrations as well so as to parallel studies of Na-ion HCEs and to operate at the highest salt concentration limit for which data is available for either electrolyte.

† σ = 1.89 mS/cm is the experimental conductivity of NaFSI in sulfolane at 1:10. 1:10 is nearest to the experimentally reported number ratio of NaFSI in sulfolane of 1:9.57.

(a) At very high salt concentrations such as 1:1 (in particular) where the ionic conductivities are very small, an even more reliable prediction of the ionic conductivities from within this force field framework can only be obtained from averaging from an even larger number of runs (>3) and over even longer MD runs (> 2.5 μs).

Table 4B.4: Ionic conductivity as a function of salt concentration for Li and Na electrolytes at 303 K and 1 bar pressure averaged over three independent runs.

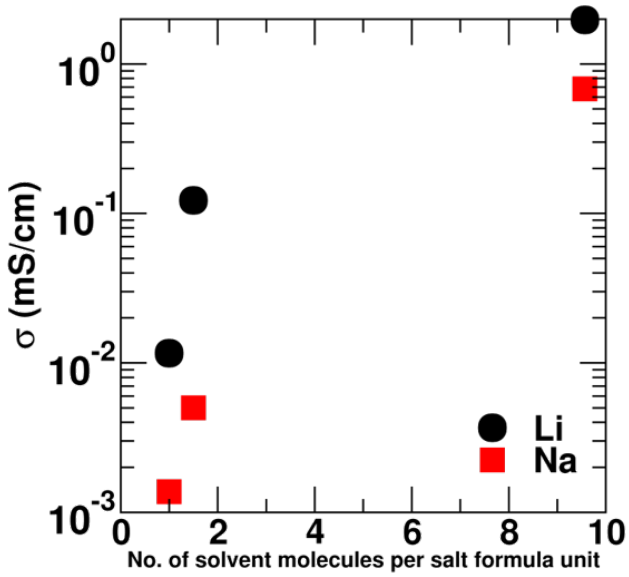

Figure 4B.2: Ionic conductivities averaged over three runs at 303 K and 1 bar pressure.

4B.3.3 Self-diffusion coefficients

In order to calculate self-diffusion coefficients, we first calculate $\beta = \frac{d(log(MSD))}{d(log(t))}$ to determine the time interval beyond which the chemical species under consideration has diffusive dynamics (Figure 4B.3(a) and (b)). The time interval required for a chemical species to enter the diffusive regime is higher in a HCE as compared to a LCE (Figure 4B.3(a) and (b)). Slopes of MSD versus time interval lines were taken over the time interval from the start of diffusive dynamics up to half of the length of the MD trajectory. β and MSD are shown in Figures 4B.3(a) and (b) and Figures 4B.3(c) and (d), respectively. The diffusion constants thus obtained are tabulated in Table 4B.5.

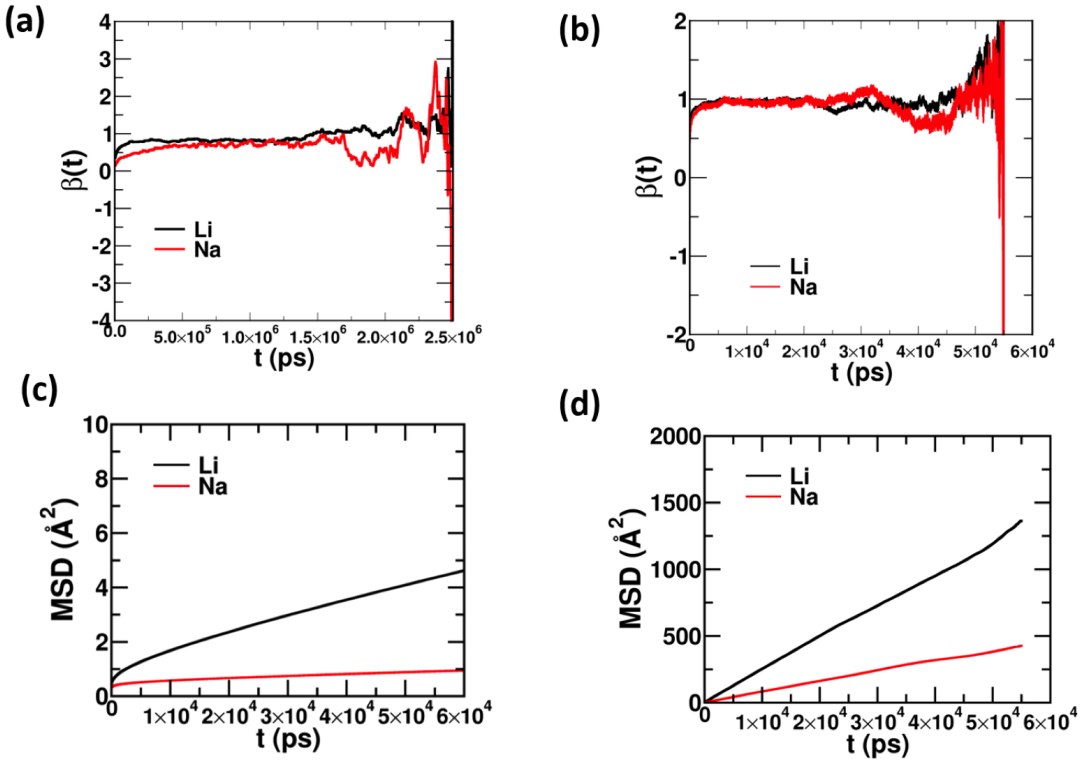

Figure 4B.3: β versus mean-squared displacement (MSD) for Li and Na-ions in salt:solvent = (a) 1:1 and (b) 1:9.57 pure alkali electrolytes. In part (a), the running average of β over 10000 ps is taken to decide the crossover to diffusive dynamics due to the large spread in the original β versus time interval data. Corresponding MSD for Li and Na-ions in salt:solvent = (c) 1:1, and (d) 1:9.57 pure alkali electrolytes. Temperature, T = 303K and pressure, P = 1 bar.

Salt:Solvent	D_{Li} $\times 10^{-7}$ cm^2/s	D_{Na} $\times 10^{-7}$ cm^2/s	$D_{FSI,Li}$ $\times 10^{-7}$ cm^2/s	$D_{FSI,Na}$ $\times 10^{-7}$ cm^2/s	$D_{SUL,Li}$ $\times 10^{-7}$ cm^2/s	$D_{SUL,Na}$ $\times 10^{-7}$ cm^2/s
1:1	0.0073	0.0007	0.0038	0.0007	0.0050	0.0008
1:1.5	0.0598	0.0037	0.0370	0.0033	0.0417	0.0037
1:9.57	4.000	1.353	3.700	2.150	3.900	2.400

At very high salt concentrations such as 1:1 (in particular) where the diffusion coefficients are very small, an even more reliable prediction of the diffusion coefficients from within this force field framework can only be obtained from averaging from an even larger number of runs (>3) and over even longer MD runs (> 2.5 μs).

Table 4B.5: Diffusion coefficients for various species present in the electrolytes at 303 K and 1 bar pressure averaged over three independent runs. $D_{FSI,Li}$ and $D_{FSI,Na}$ are the diffusion constants of FSI anion in pure lithium and sodium electrolytes, respectively. $D_{SUL,Li}$ and $D_{SUL,Na}$ are the diffusion constants of sulfolane molecule in pure lithium and sodium electrolytes, respectively.

As expected, the diffusion coefficients of all species increase with decrease in salt concentration in the electrolyte. Table 4B.5 and Figure 4B.4 show that Li-ion HCEs have nearly an order of magnitude higher diffusion coefficients for all species than Na-ion HCEs. At low salt concentrations, the difference in diffusion coefficients is not as large. This indicates that the presence of lithium instead of sodium in an electrolyte at high salt concentrations significantly improves the diffusion coefficients of all species in a way that is not as pronounced at low salt concentrations.

Next, when the ratio of the diffusion coefficients of either FSI and SUL to alkali ion is significantly less that 1, it indicates the occurrence of hopping events in the electrolyte. Diffusion coefficient ratios indicate the occurrence of hopping events in Li-ion HCEs (making Li ions considerably faster than FSI anions and sulfolane molecules), but not as much in Na-ion HCEs (Table 4B.6). This suggests Li-ions perhaps have a higher propensity to hop than Na-ions in these HCEs.

Salt:Solvent	D_{FSI}/D_{Li}	D_{FSI}/D_{Na}	D_{SUL}/D_{Li}	D_{SUL}/D_{Na}
1:1	0.52	1.00	0.68	1.14
1:1.5	0.62	0.89	0.70	1.00
1:9.57	0.93	1.59	0.98	1.77

Table 4B.6: Ratio of diffusion coefficients of alkali to anion and sulfolane at 303 K and 1 bar pressure. Data averaged over three independent runs.

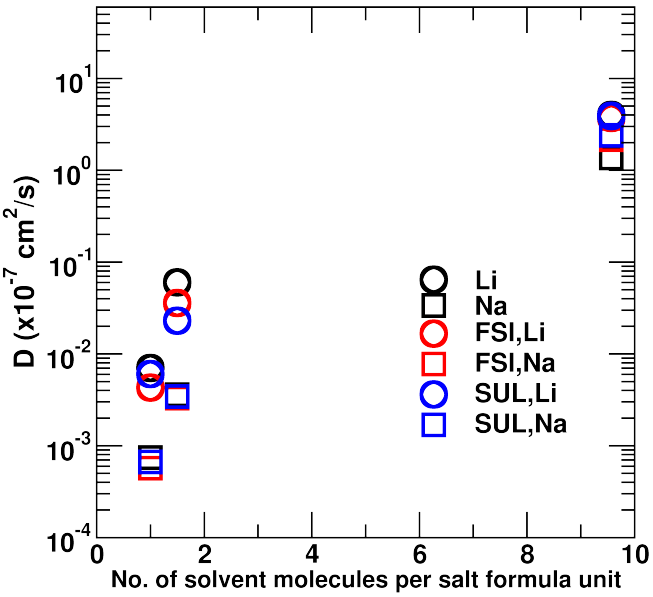

Figure 4B.4: Diffusion coefficients of different species averaged over three independent runs at 303 K and 1 bar pressure. Data averaged over three independent runs.

4B.3.4 Transference numbers

Transference numbers of all ionic species at the three salt concentrations investigated are presented in Tables 4B.7, 4B.8, and 4B.9.

System (% Li)	t_{Li}	t_{Na}	t_{FSI}
0	-	0.50	0.50
100	0.66	-	0.34

Table 4B.7: Transference numbers of various species at 303 K and 1 bar pressure at 1:1. Transference numbers averaged over three independent runs.

System (% Li)	t_{Li}	t_{Na}	t_{FSI}
0	-	0.53	0.47
100	0.63	-	0.37

Table 4B.8: Transference numbers of various species at 303 K and 1 bar pressure at 1:1.5. Transference numbers averaged over three independent runs.

System (% Li)	t_{Li}	t_{Na}	t_{FSI}
0	-	0.39	0.61
100	0.52	-	0.48

Table 4B.9: Transference numbers of various species at 303 K and 1 bar pressure at 1:9.57. Transference numbers averaged over three independent runs.

The transference numbers reported in Tables 4B.7, 4B.8, 4B.9 do not account for correlations between non-self ion-displacements. These have been calculated using self-diffusion coefficients alone. The true transference numbers ($t_{+,correlated}$) account for these correlations [54]. $t_{+,correlated}$ can be defined as : $t_{+,correlated} = \frac{\sigma_{--}\sigma_{++}-\sigma_{+-}{}^2}{\sigma_{--}(\sigma_{++}+\sigma_{--}-2\sigma_{+-})}$ [55]. Here, σ_{++}, σ_{--}, and σ_{+-} are the three components of ionic conductivity or the transport coefficients stemming from cation-cation, anion-anion, and cation-anion displacement correlations, respectively. The calculation of $t_{+,correlated}$ requires multiple (of the order of 50), and long (hundreds of nanoseconds to microseconds) trajectories. These simulations and calculations would be too computationally expensive and were therefore beyond the scope of the thesis.

We have already seen that the ionic conductivity of the Li-based electrolyte is nearly an order of magnitude more than that of the Na-based electrolytes at high salt concentrations (Figure 4B.2). Further, from the transference numbers averaged over three independent runs (Tables 4B.7, 4B.8, and 4B.9), we see that the fraction of current carried by Li-ions in LiFSI in sulfolane electrolytes is also larger than that carried by Na-ions in the NaFSI in sulfolane electrolytes. While the diffusion constants of Li are higher than those of FSI particularly in the Li-based HCEs, those of Na and FSI are the same at the corresponding salt concentrations. Further, like in the case of $LiBF_4$ in sulfolane, in FSI based HCEs too, the transference numbers of alkali increases with increase in salt concentration and due to the additional mode of transport that plays a significant role at high concentrations, viz., ion-hopping.

4B.3.5 Radial distribution functions and coordination numbers

The alkali-ion solvation shell (typically within 2 Å for Li and 3.5 Å for Na) predominantly comprises of either oxygens of sulfolane (OFO) and/or oxygens of FSI anion (OBT) (Figures 4B.5(a) and (b) as opposed to Figure 4B.6). Example of the first solvation shells of Li and Na-ions comprising of oxygens of FSI anion or sulfolane molecules is shown in Figure 4B.5(c) and (d), respectively.

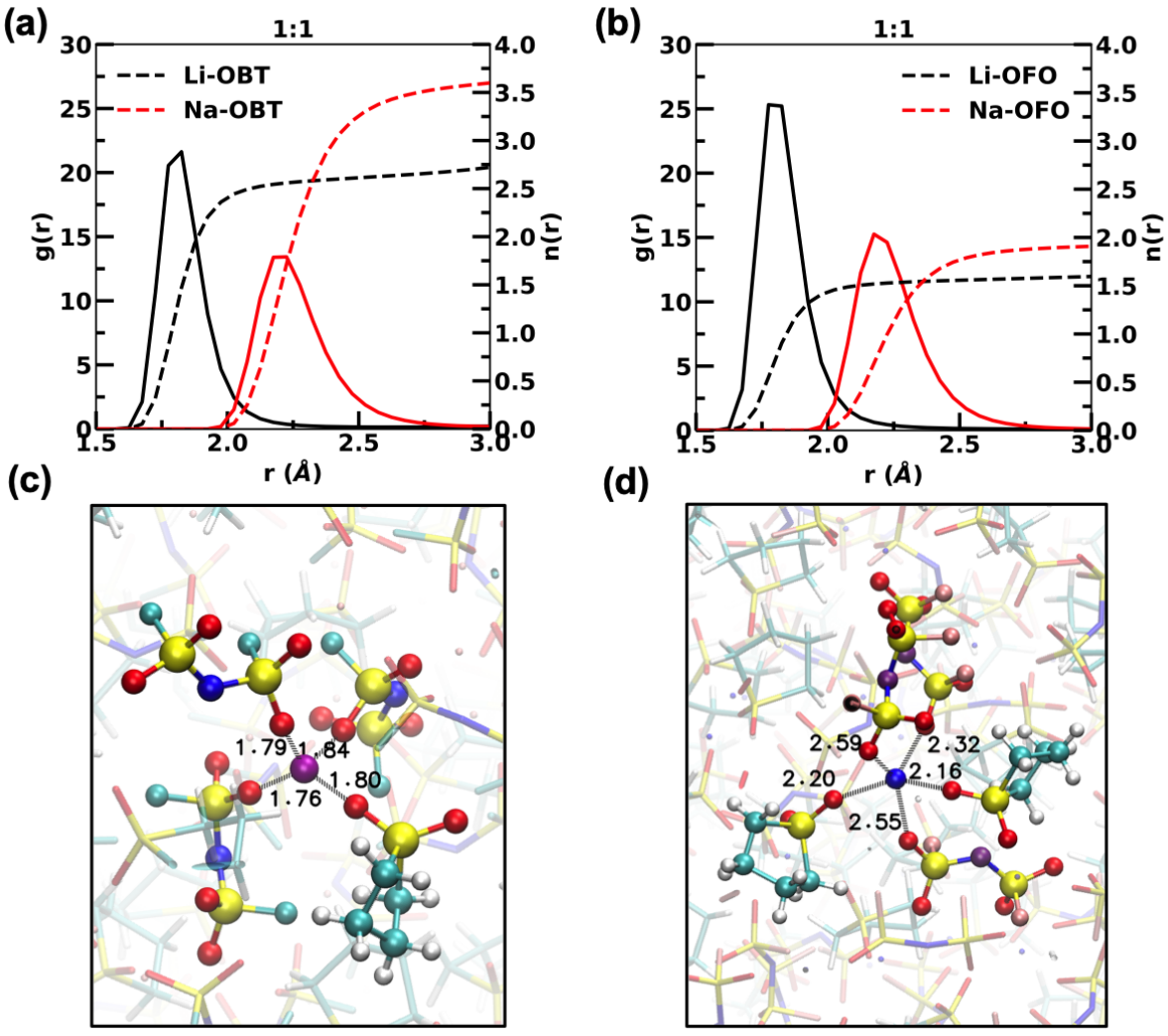

Figure 4B.5: Radial distribution functions (RDFs) and coordination numbers (n(r)) of (a) Li-OBT and Na-OBT and (b) Li-OFO and Na-OFO in 1:1 HCEs. OBT represents the oxygens of FSI anion and OFO represents the oxygens of sulfolane. Solid lines represent RDFs and dashed lines represent n(r). Data averaged over three independent runs. Example of the first solvation shells of (c) Li and (d) Na-ions in the 1:1 HCE.

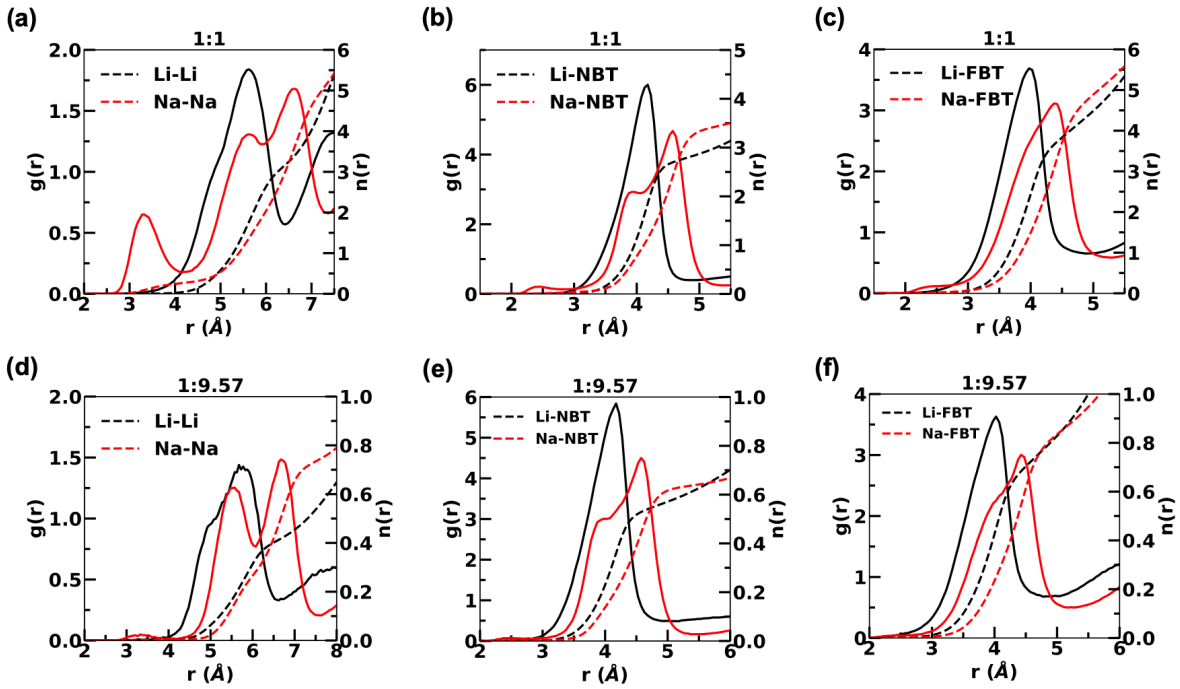

Figure 4B.6: Radial distribution functions (RDFs) and coordination numbers (n(r)) for 1:1 HCE (a) alkali-alkali pair, (b) alkali-NBT pair, and (c) alkali-FBT pair. RDFs for 1:9.57 LCE (d) alkali-alkali pair, (e) alkali-NBT pair, and (f) alkali-FBT pair. Solid lines represent RDFs and dashed lines represent n(r). Data averaged over three independent runs.

Given that OBT and OFO are the main participants in the solvation shell of both Li and Na-ions, the radial distribution function of Li-OFO/OBT and Na-OFO/OBT indicate that the solvation shell of Na-ions is looser than that of Li-ions due to the larger size of Na-ions (Figure 4B.5(a) and (b)). This can also be inferred from the velocity auto correlation function of both alkali ions shown next. A larger solvation shell for the Na-ions and their lower hop propensity as compared to the Li-ions also explains its significantly lower diffusion coefficients (and ionic conductivity of Na-based HCEs) as compared to Li-ions at the same salt concentration (Figure 4B.4 and Table 4B.5). The low ionic-conductivity of Na-based HCEs is one major challenge for the applicability of Na-HCEs which needs to be alleviated.

The RDF of Na-Na at salt:solvent = 1:1 shows a prominent pre-peak at 3.5 Å before the peak at distance between 5 Å and 6.5 Å (Figure 4B.6(a)). This peak seems to be much less prominent at 1:9.57 (Figure 4B.6(d)), and absent in the Li-based electrolytes at both salt concentrations. Also, Na-NBT and Na-FBT at 1:1 show very small pre-peaks (Figures 4B.6(b) and (c)). The corresponding pre-peaks are missing at low salt concentrations of 1:9.57 (Figure 4B.6(e) and (f)) A detailed discussion of the origin of these pre-peaks found in HCEs forms the subject matter for Chapter 5.

4B.3.6 Velocity auto-correlation function (VACF) and vibrational density of states (VDOS)

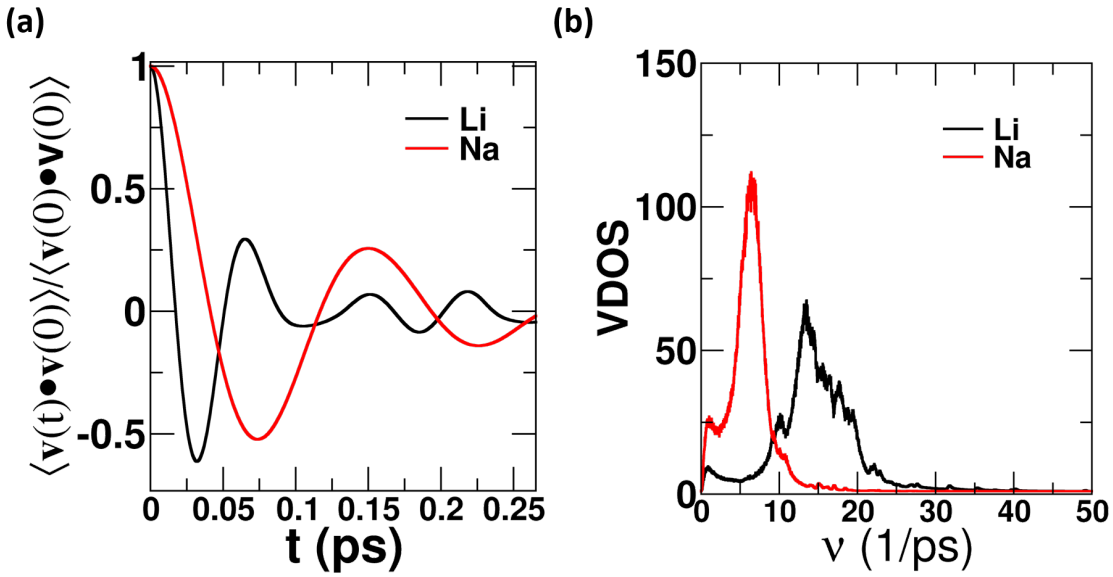

Figure 4B.7: (a) Velocity auto correlation function (VACF) of Li and Na-ions in the 1:1 HCE. (b) Corresponding density of states (VDOS) of Li and Na-ions in the 1:1 HCE. Data averaged over three independent runs.

Multiple prominent oscillations in the velocity auto correlation function (VACF) indicate the presence of cage-rattling in the 1:1 electrolyte. The larger frequency in oscillations in the case of Li-VACF in comparison to Na-VACF implies a tighter solvation shell for Li-ions as compared to those of Na-ions (Figure 4B.7(a)). As expected, the vibrational density of states (VDOS) (Figure 4B.7(b)) shows peaks at frequencies corresponding to the time period of oscillation in VACF (Figure 4B.7(a)) (Time period, T_{Li} = 0.075 ps and T_{Na} = 0.15 ps in VACF results in peaks at ν_{Li} = 13.3 ps^{-1} and ν_{Na} = 6.7 ps^{-1}, respectively in VDOS).

A larger frequency with which Li-ions rattle in their cage as compared to Na-ions amounts to a larger number of attempts being made by Li-ions to escape their cages as compared to Na-ions. Perhaps, this partially explains the higher propensity to hop of Li-ions over Na-ions and the overall faster transport of Li-ions over Na-ions.

A larger spread in the frequencies with which Li-ions rattle in their cage as opposed to Na-ions is indicated by the width of the peaks in VDOS (Figure 4B.7(b)).

4B.3.7 Solvation shell composition of alkali ions

From RDFs of various alkali-X pairs (Figures 4B.5 and 4B.6), it is clear that the first shell nearest neighbours of Li and Na-ions are predominantly oxygen atoms of sulfolane (OFO) and of FSI (OBT). Therefore, depending on the number of OFO and OBT that are present in the alkali-ion solvation shells, several solvation shell types for the alkali-ions can be realized. We found that the probability of every solvation shell type depends heavily on the alkali-ion identity and the concentration of salt in the electrolyte. (Tables 4B.10, 4B.11, 4B.12, and Figure 4B.8)

System	
Na-ions	Li-ions
(OFO:OBT)- Percentage population	
(2,4) - 17.9	(1,3) - 28.5
(1,4) - 15.4	(2,2) - 26.0
(2,3) - 14.0	(0,4) - 15.7
(3,3) - 12.7	(3,1) - 9.6
(1,5) - 11.6	-

Table 4B.10: Populations of various solvation shell types of Li and Na-ions for pure sodium (0 % Li) and pure lithium (100 % Li) at salt:solvent = 1:1 salt concentration. OFO and OBT refer to oxygens of sulfolane and FSI anion, respectively. Populations that are lesser than 9% have been omitted.

System	
Na-ions	Li-ions
(OFO:OBT)- Percentage population	
(2,3) - 17.1	(2,2) - 29.7
(3,3) - 14.4	(1,3) - 21.6
(2,4) - 12.3	(3,1) - 15.7
(1,4) - 12.2	-
(4,2) - 11.5	-
(3,2) - 11.0	-

Table 4B.11: Populations of various solvation shell types of Li and Na-ions for pure sodium (0 % Li) and pure lithium (100 % Li) at salt:solvent = 1:1.5 salt concentration. OFO and OBT refer to oxygens of sulfolane and FSI anion, respectively. Populations that are lesser than 9% have been omitted.

System	
Na-ions	Li-ions
(OFO:OBT)- Percentage population	
(6,0) - 37.9	(4,0) - 33.7
(5,1) - 28.3	(5,0) - 20.5
(5,0) - 10.9	(4,1) - 14.0
(4,1) - 9.2	-

Table 4B.12: Populations of various solvation shell types of Li and Na-ions for pure sodium (0 % Li) and pure lithium (100 % Li) at salt:solvent = 1:9.57 salt concentration. OFO and OBT refer to oxygens of sulfolane and FSI anion, respectively. Populations that are lesser than 9% have been omitted.

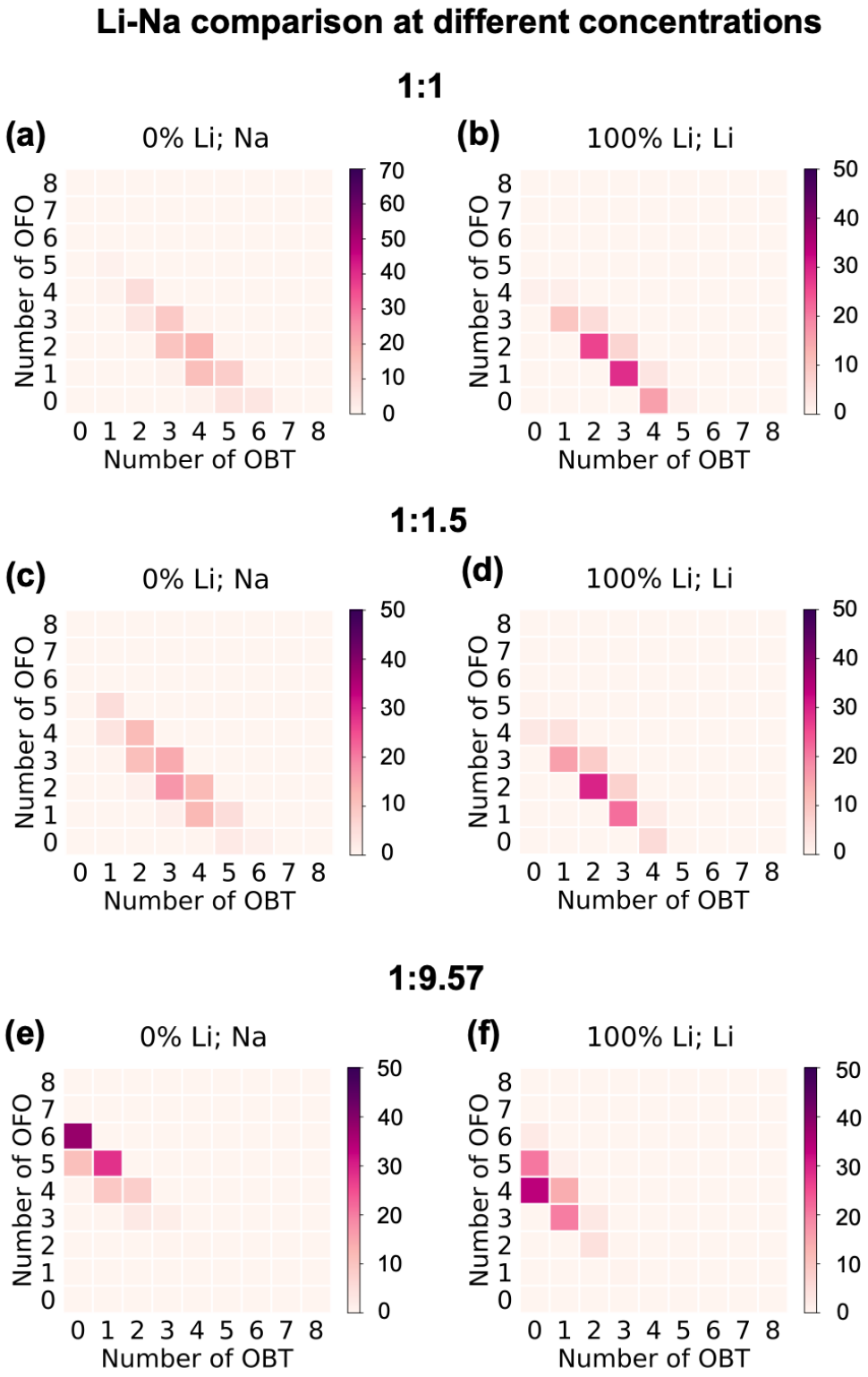

Figure 4B.8: Solvation shell composition distribution of Na and Li-ions, respectively, in pure Na (left) and pure Li (right) systems at three different salt concentrations: (a) and (b) 1:1, (c) and (d) 1:1.5, and (e) and (f) 1:9.57. OBT represents oxygens of FSI anions and OFO represents oxygens of sulfolane molecule.

The highest populations in solvation shell types of Li and Na-ions in HCEs contain a larger (or atleast an equal) number of anions than solvent molecules as one might expect for HCEs (Table 4B.10 and Table 4B.11). OBT represents oxygens of FSI anions and OFO represents oxygens of sulfolane molecule. The higher color intensity of fewer solvation shell types of Li-ions (OFO:OBT = (1,3) and (2,2)) in HCEs in comparison to all solvation shell types of Na-ions in HCEs, indicates more specificity (less diversity) in the solvation shell types of Li-ions in comparison to Na-ions (Figures 4B.8 (a) and (b), and (c) and (d)). In Li-based electrolytes, Li-ions are most likely to have a total solvation shell coordination number of 4 with OFO:OBT = (1,3) and (2,2) being most probable (Figures 4B.8(b), (d), and (f)). In Na-based electrolytes, Na-ions are most likely to have a total solvation shell coordination number of 5 or 6. OFO:OBT = (4,1), (3,2), (3,3), and (1,3) being amongst the most probable solvation shell types in Na-based HCEs (Figures 4B.8)(a) to (c)).

4B.3.8 Self-part of the van Hove correlation function G_s(r,t)

All alkali-ion G_s(r,t)

In order to identify alkali-ion hopping of Li and Na-ions and estimate its prevalence in HCEs (salt:solvent = 1:1), we calculated the self-part of the van Hove correlation function (G_s(r,t)) for Li and Na-ions (Figure 4B.9(a) and (b)). To confirm the near absence of both Li and Na-ion hopping in low concentration electrolytes, LCEs, we also calculated G_s(r,t) at salt:solvent = 1:9.57 systems (Figure 4B.9(c) and (d)).

The wiggles in the self-part of the van Hove correlation function, G_s(r,t), indicate the presence of hopping in the 1:1 Li-based HCE (Figure 4B.9(a)). Whereas, the 1:1 Na-based HCE shows milder hopping features (Figure 4B.9(b)) over the same time intervals. This might suggest a lower propensity of Na-ions to hop as was also indicated by the ratio of diffusion constants of solvent or anion to Na-ions in HCEs being close to 1 (Figure 4B.6). Further, due to the more fluid-like nature of Li-based HCEs as compared to Na-based HCEs, and a higher hopping propensity of Li-ions as compared to Na-ions in the case of HCEs, Li-ions were able to travel to much larger distances over the same time intervals as compared to Na-ions (Figure 4B.9(a) and (b)).

At 1:9.57, as expected, very little to no alkali-hopping signatures are found for both Li and Na-ion LCEs (Figure 4B.9(c) and (d)).

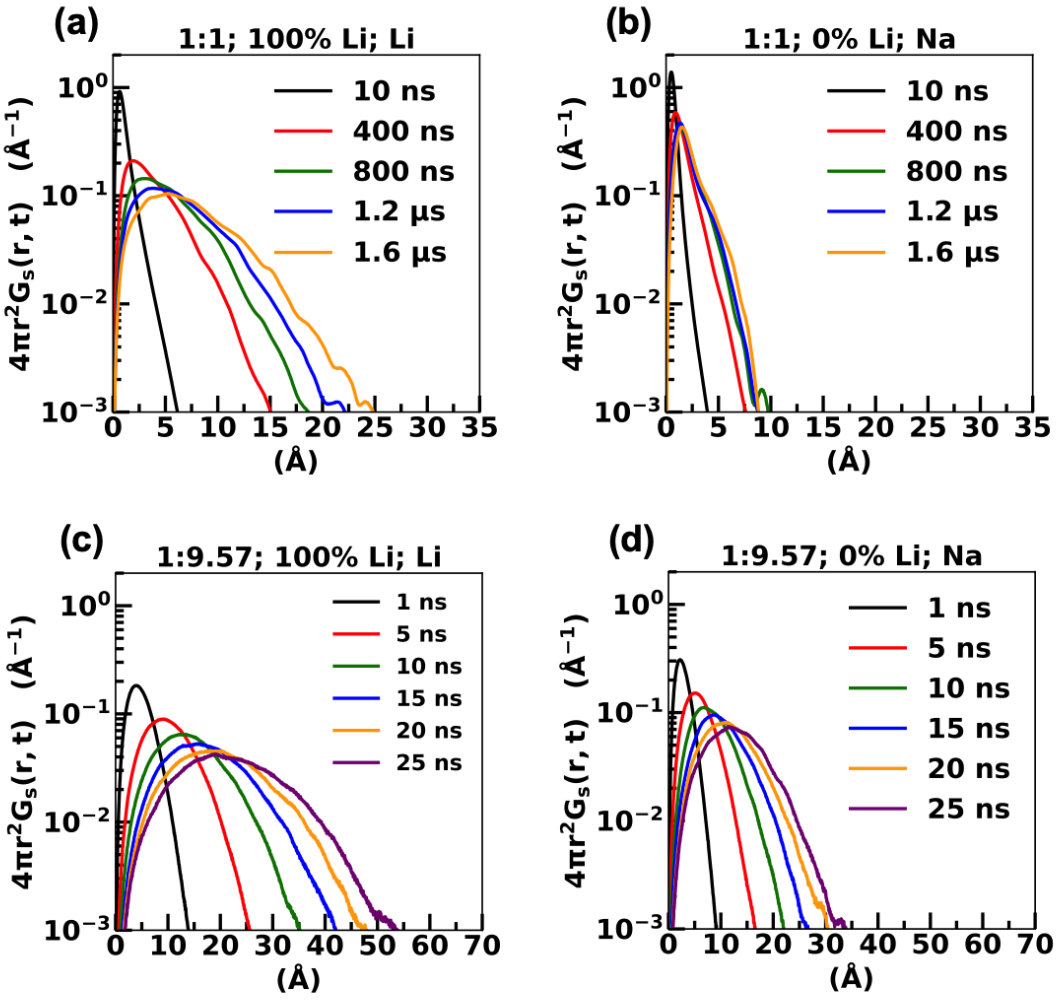

Figure 4B.9: Self-part of the van Hove correlation function $G_s(r,t)$ for pure Li and Na systems at prototypical high salt (1:1) and low salt (1:9.57) concentrations. (a) $G_s(r,t)$ for Li-ions in LiFSI:SUL=1:1, (b) $G_s(r,t)$ for Na-ions in NaFSI:SUL=1:1, (c) $G_s(r,t)$ for Li-ions in LiFSI:SUL=1:9.57, and (d) $G_s(r,t)$ for Na-ions in NaFSI:SUL=1:9.57. Data is averaged over three runs.

Single-ion $G_s(r,t)$

Ion-hopping is a single particle phenomenon, it is best established at the single-ion level. As in Chapter 3, the presence of hopping can be undeniably established by looking at the self-part of the van Hove correlation function, $G_s(r,t)$, for individual alkali-ions. We examined the difference in Li and Na-ion hopping at the single ion level (Figure 4B.10).

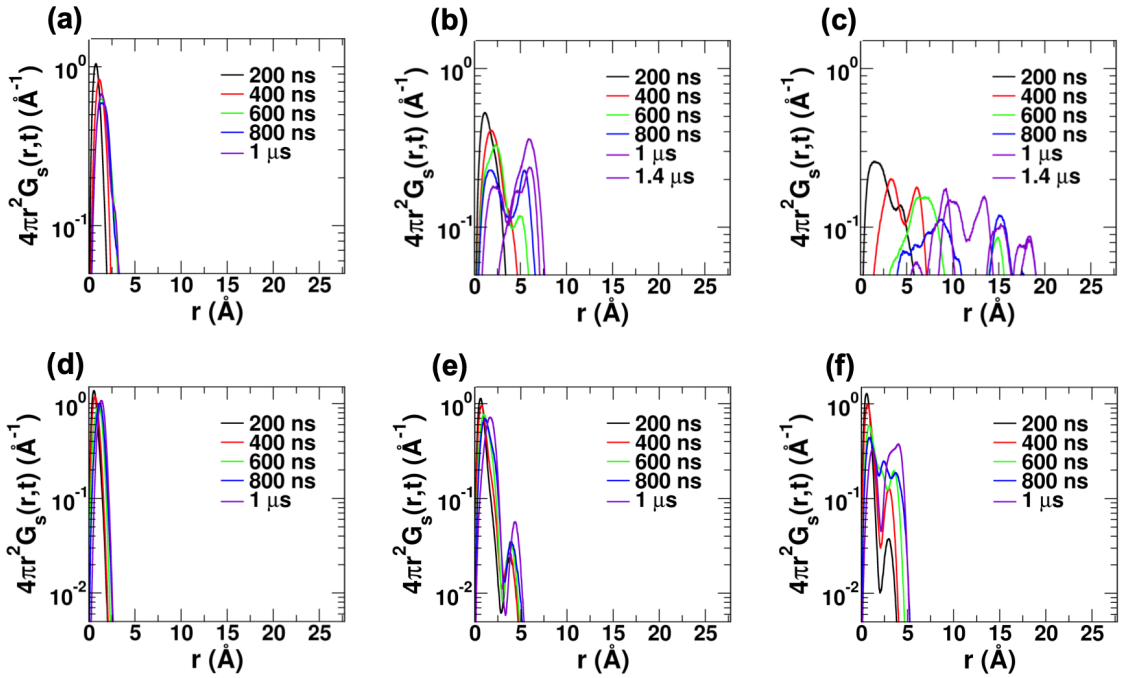

Figure 4B.10: (a) to (c) correspond to the single-ion G_s(r,t) for three arbitrarily chosen Li-ions in the LiFSI:SUL = 1:1 HCE. (d) to (f) correspond to the single-ion G_s(r,t) for three arbitrarily chosen Na-ions in the NaFSI:SUL = 1:1 HCE.

The presence of humps and valleys in the single-particle G_s(r,t) in both Li and Na-based electrolytes confirms the presence of ion-hopping in both Li and Na based alkali-ion HCEs (Figure 4B.10). Based on whether there were no additional humps, one additional hump, or multiple additional humps, we concluded that both Li and Na-ions display dynamically heterogeneity in HCEs (Figure 4B.10). The difference between the transport of Li and Na-ions is the focus of this chapter. We found that over the same time interval (1 μs), the number of Li-ions that show features of hopping is larger than that of Na-ions that show these features (Figure 4B.10(a) to (c) as opposed to (d) to (f)). A large number of Li-ions are of the type shown in Figures 4B.10(b) and (c), and fewer of the type shown in Figure 4B.10(a). The converse is true in the case of the 1:1 Na-ion HCE. A large number of Na-ions are of type in Figure 4B.10(d), and much fewer of the type of Figures 4B.10(e) and (f). While a few Li-ions were found which hopped multiple times over certain time intervals, Na-ions that hopped multiple times over the same time intervals were hard to find (Figure 4B.10(d) and (f)). Therefore, with both a higher diffusion constant and a higher propensity to hop, Li-ions were able to travel to much larger distances than Na-ions over the same time interval at the same salt concentration.

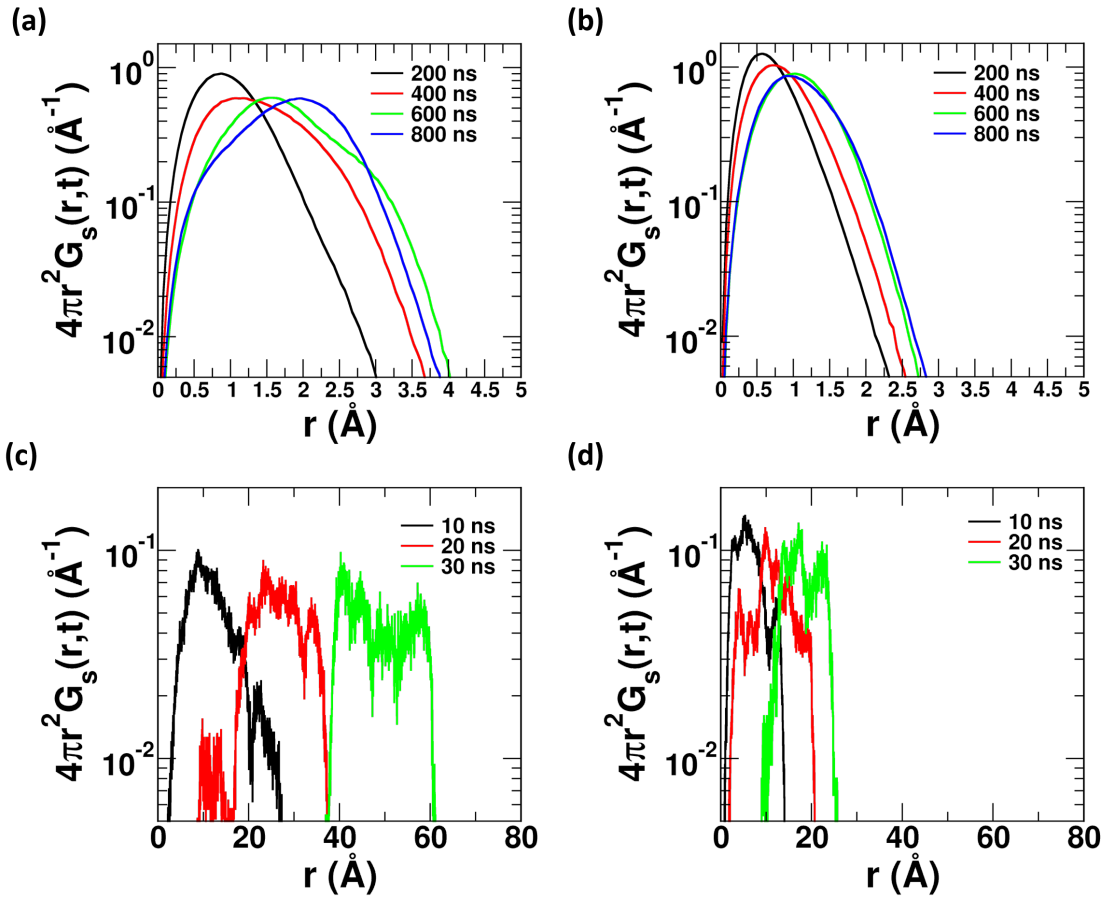

Figure 4B.11: (a) and (b) single particle G_s(r,t) for diffusive Li-ion and Na-ion, respectively in their respective pure 1:1 HCEs. (c) and (d) single particle G_s(r,t) for diffusive Li-ion and Na-ion, respectively in their respective pure 1:9.57 electrolytes.

As a further proof that alkali-ions at high salt concentrations are dynamically heterogeneous and some of them show mainly rattle in their cages and/or display diffusive behaviour even over the longest time intervals investigated, Figure 4B.11(a) and (b) show representative alkali-ions of this kind.

A prototypical low salt concentration electrolyte does not show any signatures of hopping in both the Li and Na based electrolytes. Diffusion is the main mode of transport for alkali-ions in LCEs (Figure 4B.9(c) and (d)). The curves in Figure 4B.11(c) and (d) are noisy because the MD trajectory lengths for LCEs was 55 ns as opposed to atleast 1 μs for HCEs therefore making the statistics poorer for LCEs.

4B.3.9 Single particle real time dynamics

The final proof for hopping beyond proofs at the statistical level is to see alkali-ions hop in real time. Figure 4B.12(a) and (b) shows instances of hops in real time of a Li-ion and Na-ion, respectively. Figure 4B.12(c) and (d) show a time overlayed image of the same Li and Na-ion hops, respectively.

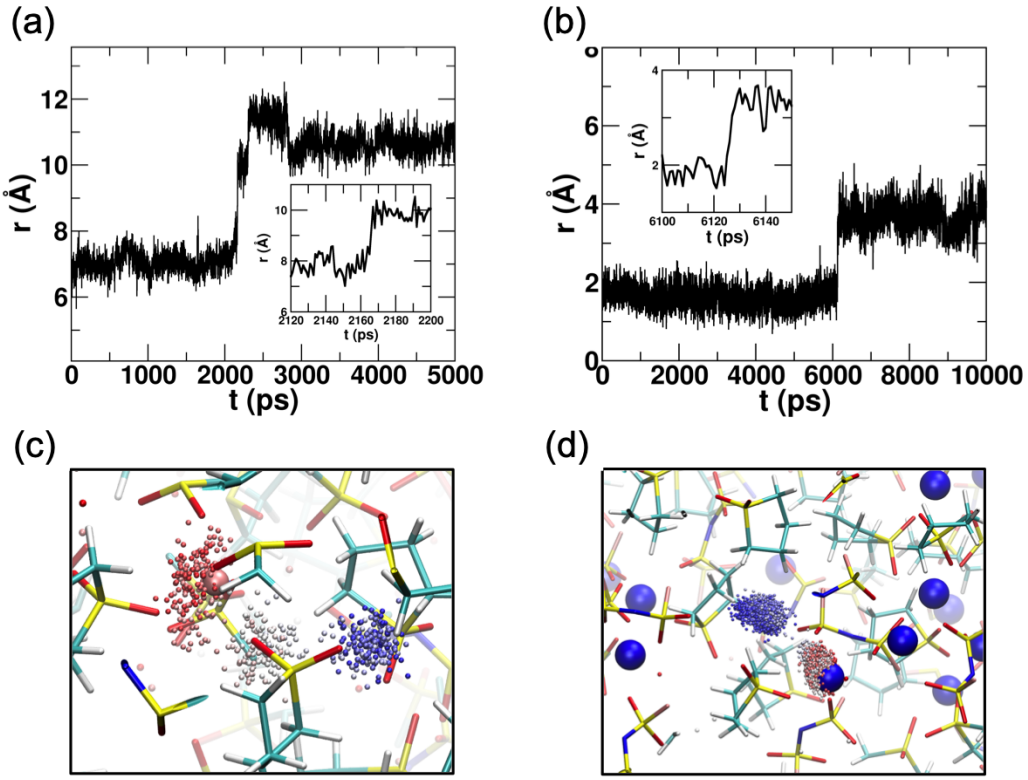

Figure 4B.12: Hopping of Li and Na ions in HCEs in real time. (a) A hop event of a Li-ion. Inset: Zooms into the time window over which the Li-ion hop occurs. (b) A hop event of a Na-ion. Inset: Zooms into the time window over which the Na-ion hop occurs. (c) and (d) represent time overlayed imaged of the same Li-ion and Na-ion hops. Each small sphere represents the alkali-ion which hops. The small spheres are separated by 1 fs in time. Blue is initial time. White intermediate times. Red later times during the hop.

4B.3.10 Distinct part of the van Hove correlation function G_d(r,t)

In Chapter 3, we found that in $LiBF_4$ in sulfolane HCEs, Li-ions preferred to *hop+diffuse* to previously occupied Li-ion sites. It would be interesting to know how Li and Na-ions

differ in this respect. To this end, we calculate the distinct part of the van Hove correlation function, $G_d(r,t)$

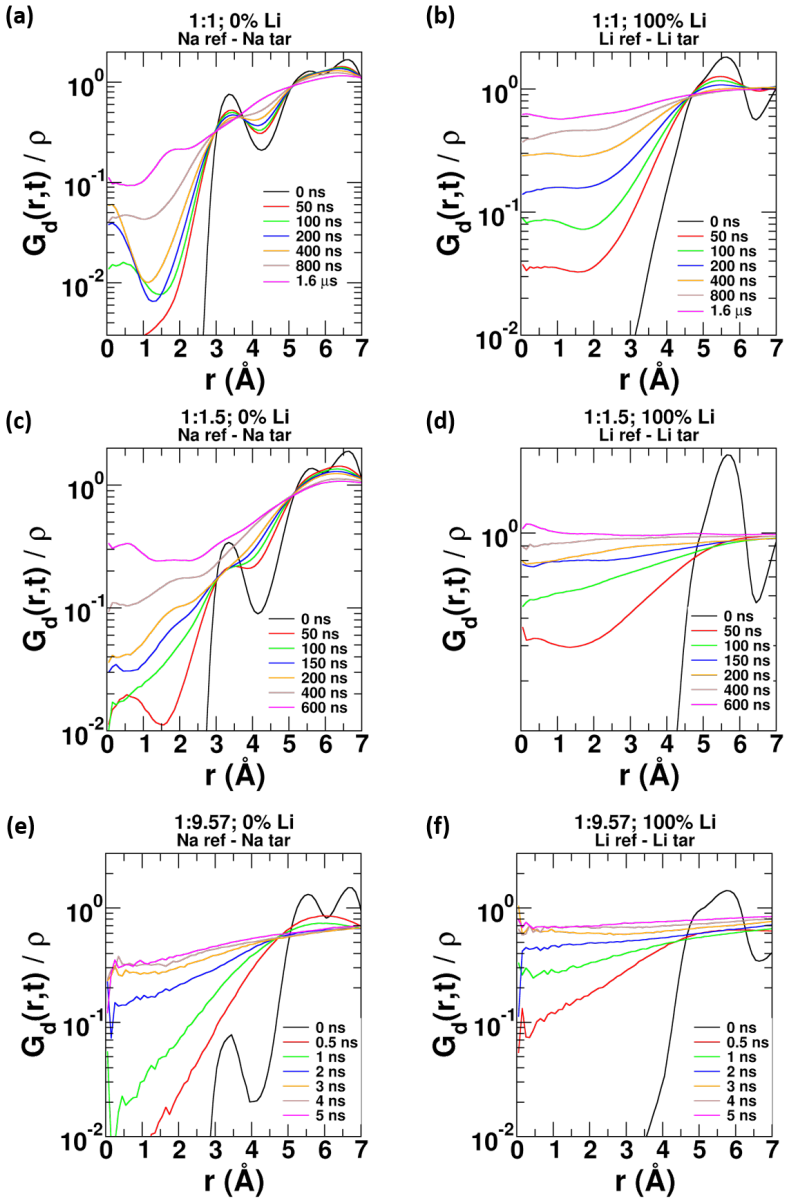

Figure 4B.13: Distinct part of the van Hove correlation function, $G_d(r,t)$ for (a) Na-reference (ref) and Na-target (tar) at NaFSI:SUL=1:1, (b) Li ref and Li tar at LiFSI:SUL=1:1, (c) Na ref and Na tar at NaFSI:SUL=1:1.5, (d) Li ref and Li tar at LiFSI:SUL=1:1.5, (e) Na ref and Na tar at NaFSI:SUL=1:9.57, and (f) Li ref and Li tar at LiFSI:SUL=1:9.57.

Distinct part of the van Hove correlation function, $G_d(r,t)$ shows that at high salt concentrations, both alkali ions have a preference to hop+diffuse to previously occupied alkali-ion sites. As we have seen before, this is indicated by a peak at r = 0 and the valley between the peak at r = 0 and the RDF first peak position at t = 0 (Figures 4B.13(a) and (b) and small time intervals in (c) and (d)). Two features come to our notice. (a) Over any time

interval, the value of $G_d(r,t)$ at r = 0 in the Li-based electrolyte is larger than that in the Na-based electrolyte. (b) The ratio of G_d(r,t) between r=0 and the bottom of the valley is nearly an order of magnitude in the Na-based 1:1 electrolyte but is much smaller in the Li-based 1:1 electrolyte.

Li-ion HCEs have more enhanced transport than the Na-based HCEs. Therefore, the diffusive component to the Li-ion motion is larger than that of Na-ions. We know that the propensity of Na-ion hopping is lower (but not absent) than that of Li-ions. Over the same time interval, due to the low diffusivity of Na-ions, a very small fraction of them can expect to move over the RDF first peak distance and those that do can predominantly do so through hopping. Whereas, in Li-based HCEs, Li-ions both have higher propensity to hop but also have higher diffusivity. The larger diffusive component to the Li-ion motion as compared to the Na-ion motion makes the $G_d(r,t)$ value in the Li-based HCE larger than the Na-based HCE over any time interval. Also, this results in a shallower valley between r = 0 and RDF first peak in Li HCE in comparison to Na HCE.

At 1:9.57, as expected, a uniform decay in $G_d(r,t)$ from the first peak in RDF to r=0, we reconfirm that ion hopping is predominantly absent and that alkali-ions predominantly move through diffusion (Figures 4B.13(e) and (f)).

4B.3.11 Non-Gaussian parameter α_2

At all salt concentrations, it is observed that the components of the Na-based electrolyte have a larger t^* (time interval corresponding to the peak in α_2) as compared to the Li-based electrolytes (Figure 4B.14). t^* indicates the time interval for the onset of diffusive motion which will be larger for a more sluggish system. Larger t^* also means that the time interval at which the onset of the maximum dynamic heterogeneity occurs, is larger.

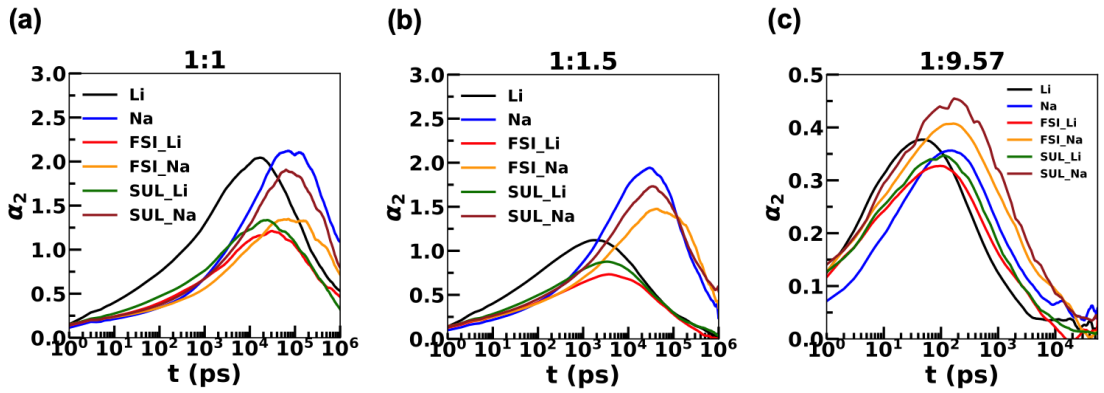

Figure 4B.14: Non-Gaussian parameter for various chemical species compared between LiFSI in sulfolane and NaFSI in sulfolane across three salt concentrations- (a) 1:1, (b) 1:1.5, and (c) 1:9.57. Data averaged over three independent runs.

4B.4 Conclusions

In conclusion, we have compared the structure and transport characteristics of LiFSI and NaFSI in sulfolane both at high and low salt concentrations. We find that the difference between the lithium and sodium based electrolytes is much more at high salt concentrations than at low salt concentrations. At high salt concentrations, we find that the transport properties such as ionic conductivity and diffusion coefficients are nearly an order of magnitude larger in Li-based HCEs as opposed to Na-based HCEs. From the transference numbers, we also find that Li-ions carry a larger fraction of the total current than the Na-ions at the same salt concentration. Through radial distribution functions (RDFs) and velocity auto-correlation functions, we find that the solvation shell of Na is looser and larger compared to the solvation shell of Li. Further, a larger solvation shell of Na-ions can accommodate many more members as compared to that of Li-ions. A typical coordination number of 4 in the case of Li-ions and between 5 to 6 is observed for the Na-ions. A pre-peak in the Na-Na, Na-NBT, Na-FBT RDFs at high salt concentrations is indicative of the presence of ligand-bridged bicationic Na-ion pairs. A more detailed study of these pairs forms the subject matter of Chapter 5. Humps and valleys in the self-part of the van-Hove correlation function (G_s(r,t)) indicate the presence of hopping in the Li-based HCE. These signatures are not so prominent in the Na-based HCE over the time interval of 1.6 μs analyzed here. However, single particle G_s(r,t)s confirm the presence of hopping in both Li and Na-ion HCEs, although perhaps more rare in Na-based HCEs. Real time hop events were also traced in either Li and Na-ion HCEs. Lastly, we find that the distribution of the squared displacements over any period of time is astoundingly broader for Li-ions

than for Na-ions in the HCEs alongside an expected larger mean. In sum, with respect to battery electrolytes, up to this point we have learnt the following. HCEs are one of the most prominent players of next generation battery electrolytes. The price of lithium per tonne has has always been high and has increased by many folds over the last decade. Sodium is roughly a 1000 times more abundant in the earth's crust and therefore much cheaper. However, the significantly slower transport properties of Na-based electrolytes that we have shown here is indicative of the highly viscous nature of Na-based HCEs. This severely hinders the wide-spread applicability of Na-ion based HCEs as a practical alternative to very expensive Li-ion based HCE batteries. One possible mid-way solution to this issue is attempted at through the detailed study of mixed alkali ion HCEs developed in the subsequent sub-chapter.

Chapter 4C

Enhancement of transport properties of sodium high concentration electrolytes through lithium doping: A study of mixed alkali high concentration electrolytes

4C.1 Introduction

High concentration electrolytes (HCEs) use a large amount of salt. Although sodium is much more abundant in the earth's crust than lithium and is suitable for HCEs in this sense, from Chapter 4B we know that sodium-ion HCEs have much lower ionic conductivities than those with lithium. Hence, pure Na-ion HCEs (in particular NaFSI in sulfolane) do not immediately seem to be viable replacements for Li-ion HCEs. We then wondered if replacing some of the Na-ions with Li-ions or mixed alkali-ion (Li-ion + Na-ion) HCEs would partially alleviate the problem. For further impetus to venture in the direction of mixed-cation electrolytes, we looked in literature to see if mixed-cation electrolytes have been envisioned before. To our delight, we found encouraging evidence for the potential that mixed-cation electrolytes hold as next-generation battery electrolytes. The concept of using mixed cation-electrolytes have just begun to gain prominence in experiments [56–58]. To the best of our knowledge, mixed-cation HCEs have not been explored very much in MD simulations. Some discussion and a few examples from studies on mixed-cation electrolytes are presented here.

It is now established that the combination of Li and Na-ions in a battery is particularly

interesting as they combine the low cost and safety of Na-ion batteries with high energy densities of Li-ion batteries [59, 60]. Such batteries are coming to be known as hybrid lithium-sodium ion batteries (HLSIBs). If the electrode material is chosen such that both Li and Na-ions are able to intercalate [60–64], then this fact compensates for the kinetic barriers in diffusion and results in high rate capability [59]. Layered electrode materials wherein alkali-ions sit in prismatic positions (P3-type) are examples of materials which can intercalate Li and Na-ions separately, and can also co-intercalate Li-Na ions reversibly [60, 65–69]. In a single cation electrolyte, the composition of the electrolyte remains constant [70]. In HLSIBs, however, where more than one kind of ion can intercalate, the composition of the electrolyte may reversibly change during the cell operation such that the total salt concentration remains the same [60]. Other than HLSIBs, other dual-cation electrolytes have also been studied. A 0.5 M Zn^{2+} + 1.0 M Na^{+} in acetonitrile electrolyte yielded a battery with a very large electrochemical window of 5.3 V [56]. In a 0.5 M Zn^{2+} + 1.0 M Na^{+} in trimethyl phosphate (TMP) electrolyte, most TMP molecules coordinate to cations which reduces the free-TMP molecules significantly and therefore improves the oxidative/reductive stability of the battery [56]. In some other studies, magnesium-lithium hybrid electrolytes have been shown to be attractive alternatives to single-cation electrolytes. In these studies, a Li-insertion cathode and a Mg anode were used alongside the hybrid electrolyte to combine the low cost and safety of Mg with the high voltage window and fast kinetics of Li-ions [71]. In yet another study of a 0.5 m $Zn(ClO_4)_2$ with 18 m $NaClO_4$ water-in-salt (WIS) electrolyte, $NaClO_4$ changes the electronic states in the electrolyte and solvation structure such that there are fewer free-water molecules finally resulting in high rate, and high cycling stability [57]. Another unique study with a Prussian Blue (PB) cathode, a $Ti_3C_2T_X$ MXene anode, and a low concentration mixture of KNO_3 and HNO_3 displayed a higher power density and enhanced H^{+} co-intercalation [58]. Overall, the use of hybrid metal-ion batteries (HMIB) shows promise for big improvements in energy storage in batteries, higher cycling stability, low cost, improved safety, and high energy density [58, 60].

In this sub-chapter, we attempted to glean insights from a computational study of mixed-cation (Li-Na) electrolytes out of theoretical interest in the novelty of the system, but also with the aim of improving the ionic conductivity of HCEs starting from a Na-ion HCE.

4C.2 Methodology and Simulation Details

4C.2.1 Chemical species studied in this sub-chapter

The systems synthesised in this thesis are LiFSI in sulfolane, NaFSI in sulfolane, and mixtures of LiFSI and NaFSI in sulfolane at three (Li+Na) concentrations (salt:solvent = 1:1, 1:1.5, and 1:9.57). The chemical species involved are shown in Figure 4C.1.

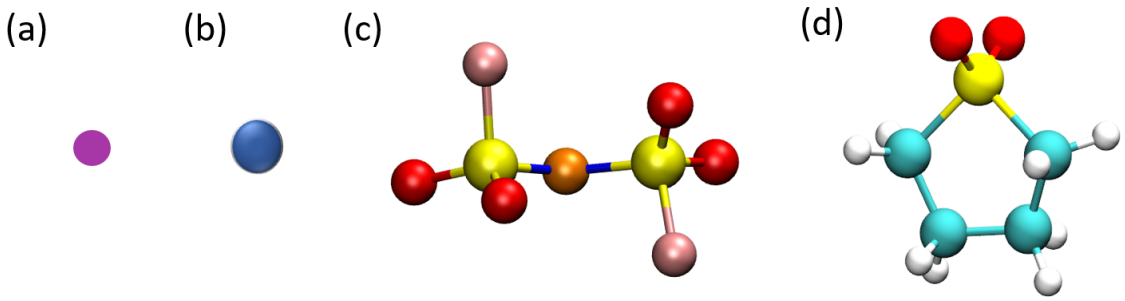

Figure 4C.1: (a) Li-ion, (b) Na-ion, (c) FSI anion, (d) Sulfolane molecule. Purple - Li-ion, blue - Na-ion, red - oxygen, cyan - carbon, yellow - sulphur, white - hydrogen, orange - nitrogen, pink - fluorine.

4C.2.2 Molecular dynamics (MD) simulation details

LiFSI and NaFSI salts were mixed in various proportions in sulfolane solvent at three concentrations, viz., salt:solvent = 1:1, 1:1.5, and 1:9.57, respectively. For each salt concentration, six mixing extents of the two alkali-ions were simulated (including pure alkali-ion systems). These were 0 %Li, 10 %Li, 25 %Li, 75 %Li, and 100 %Li. PACKMOL software [38] was used to generate random initial configurations. GROMACS-2018.3 package [39–41] was employed to carry out all the MD simulations. The force-field for the MD simulations were the same as used in Chapter 4B. A timestep of 1 fs was used to integrate the equations of motion using the leap-frog algorithm. All C-H bonds of sulfolane were constrained using the LINCS algorithm [40] in GROMACS. The Lennard-Jones (LJ) and Coulomb cut-off distances were fixed at 12 Å, and the neighbor list cut-off was extended to 14 Å. Long-range interactions were accounted for using particle–particle mesh Ewald (PPPM) method [50]. 1-2, 1-3 non-bonding interactions were set to zero. For 1-4 pairs, non-bonding LJ and Coulombic interactions were included with a scale factor of 0.5.

For all other atom-pairs a scale factor of 1.0 was used. Geometric mean was employed as the combining rule for calculating the interaction between different atom types. Long-range dispersion corrections to energy and pressure were applied. The random packing at each concentration was energy minimised within the force-field. This was followed by constant-NPT equilibration run using Berendsen barostat [51] and Nosé–Hoover thermostat [52]. Following this, a constant-NPT production run using Parrinello-Rahman Barostat [53] and Nosé–Hoover thermostat [52] was carried out. The average density estimated from the NPT production run was used to run the constant-NVT production run. For the Nosé–Hoover thermostat, a coupling time-constant of 0.5 ps was used, and the system was coupled to the thermostat every 10 timesteps. For the Berendsen and the Parrinello-Rahman barostats, a coupling time constant of 2 ps used. Parrinello-Rahman barostat was coupled with the system once every 10 timesteps and every 1 timestep for high (salt:solvent = 1:1 and 1:1.5) concentrations and low concentration systems (1:9.57), respectively. All NVT production runs used for analyses were carried out at 303 K temperature and 1 bar pressure. Three independent trials were carried out for each mixing extent at every salt concentration. For the first trial a temperature of 303 K was maintained for all simulations. To create the two additional independent trials, density equilibrated systems at 303 K and 1 bar pressure, were heated to 340 K and 350 K, respectively, and annealed back to 303 K prior to NVT production runs. To simulate a bulk environment, periodic boundary conditions were applied along all three axes. Trajectories were visualised using the Visual Molecular Dynamics software [42]. Insights into structure and transport were gleaned from the MD trajectories. Most analyses were carried out with in-house FORTRAN codes.

Force field parameters for Li are those used in Chapter 3. Those used for Na-ions are stated in Chapter 4A. FSI anion force field parameters are those refined in Chapter 4A. Sulfolane parameters used are the refined parameters set reported in Chapter 2.

System details for all mixing extents at the three salt concentrations studied are provided in Tables 4C.1, 4C.2, and 4C.3.

System (% Li)	No .of Li-ions	No. of Na-ions	No. of FSI anions	No. of SUL molecules	NPT equilibrated box-length (Å)	No. of independent trials
0	0	160	160	160	36.40	3
10	16	144	160	160	36.41	3
25	40	120	160	160	36.39	3
50	80	80	160	160	36.35	3
75	120	40	160	160	36.33	3
100	160	0	160	160	36.27	3

Table 4C.1: System details for simulations at salt:solvent=1:1. SUL stands for sulfolane molecules. All production runs used for analyses were conducted at 303 K temperature and 1 bar pressure.

System (% Li)	No .of Li-ions	No. of Na-ions	No. of FSI anions	No. of SUL molecules	NPT equilibrated box-length (Å)	No. of independent trials
0	0	160	160	240	39.24	3
10	16	144	160	240	39.19	3
25	40	120	160	240	39.24	3
50	80	80	160	240	39.21	3
75	120	40	160	240	39.17	3
100	160	0	160	240	39.16	3

Table 4C.2: System details for simulations at salt:solvent 1:1.5. SUL stands for sulfolane molecules. All production runs used for analyses were conducted at 303 K temperature and 1 bar pressure.

System (% Li)	No .of Li-ions	No. of Na-ions	No. of FSI anions	No. of SUL molecules	NPT equilibrated box-length (Å)	No. of independent trials
0	0	160	160	1531	63.72	3
10	16	144	160	1531	63.75	3
25	40	120	160	1531	63.74	3
50	80	80	160	1531	63.68	3
75	120	40	160	1531	63.70	3
100	160	0	160	1531	63.67	3

Table 4C.3: System details for simulations at salt:solvent 1:9.57. SUL stands for sulfolane molecules. All production runs used for analyses were conducted at 303 K temperature and 1 bar pressure.

No. of salt formula units : No. of solvent molecules	No. of mixing extents	NVT production trajectory length (ns)	No. of independent runs	Total trajectory length (ns)
1:1	6	2500	3	45000
1:1.5	6	1000	3	18000
1:9.57	6	55	3	990
				Total - 63990

Table 4C.4: MD simulation NVT production trajectory details.

4C.3 Results and Discussions

4C.3.1 Density

We looked at the density of various mixtures of Li and Na electrolyte mixtures at all salt concentrations investigated (Table 4C.5). It is clear that density of the mixtures monotonically decreases with increase in percentage of Li-ions in the system. Also, it was observed that the rate at which density of the electrolyte decreases with increase in percentage of Li-ions is larger for high concentration electrolytes HCEs (here salt:solvent = 1:1 and 1:1.5) as compared to that for low concentration electrolytes (LCEs) (salt:solvent = 1:9.57)) (Figure 4C.2).

System Li/(Li+Na) (%)	1:1 ρ (g/cc)	1:1.5 ρ (g/cc)	1:9.57 ρ (g/cc)
0	1.78	1.69	1.39
10	1.77	1.68	1.39
25	1.76	1.67	1.39
50	1.74	1.65	1.38
75	1.73	1.64	1.38
100	1.71	1.62	1.38

Table 4C.5: Density at various total alkali salt concentrations for various alkali mixing extents at 303 K temperature and 1 bar pressure.

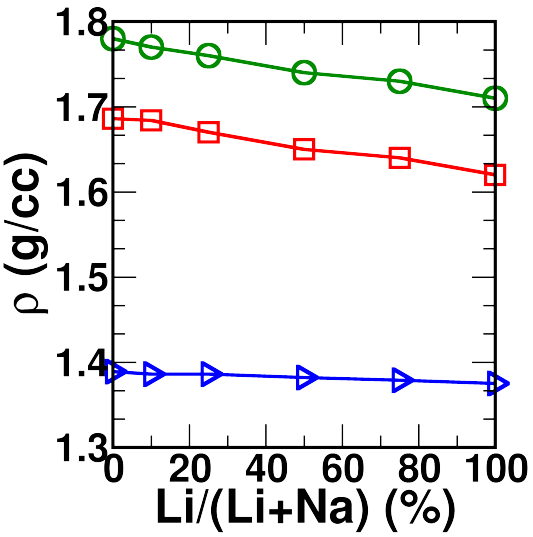

Figure 4C.2: Densities at 303 K and 1 bar pressure as a function of the percentage of Li-ions in the electrolyte for three different salt:solvent ratios investigated. Green - 1:1, red - 1:1.5, and blue 1:9.57.

4C.3.2 Self-diffusion coefficients

The self-diffusion coefficients of various ionic and molecular species for all mixing extents for all salt:solvent ratios were calculated and averaged over all three independent runs.

System Li/(Li+Na) (%)	D_{Li} $\times 10^{-7}$ cm^2/s	D_{Na} $\times 10^{-7}$ cm^2/s	D_{FSI} $\times 10^{-7}$ cm^2/s	D_{SUL} $\times 10^{-7}$ cm^2/s
0	-	0.0007	0.0007	0.0008
10	0.0010	0.0010	0.0008	0.0010
25	0.0015	0.0012	0.0010	0.0010
50	0.0027	0.0018	0.0017	0.0018
75	0.0030	0.0022	0.0017	0.0022
100	0.0073	-	0.0038	0.0050

Table 4C.6: Diffusion coefficients for various species present in the electrolytes at various mixing extents at temperature 303 K and 1 bar pressure at salt:solvent = 1:1. Data averaged over three independent runs.

System Li/(Li+Na) (%)	D_{Li} $\times 10^{-7}$ cm^2/s	D_{Na} $\times 10^{-7}$ cm^2/s	D_{FSI} $\times 10^{-7}$ cm^2/s	D_{SUL} $\times 10^{-7}$ cm^2/s
0	-	0.0037	0.0033	0.0037
10	0.0053	0.0047	0.0038	0.0047
25	0.0073	0.0050	0.0183	0.0053
50	0.0208	0.0115	0.0432	0.0140
75	0.0342	0.0162	0.0188	0.0220
100	0.0598	-	0.0358	0.0417

Table 4C.7: Diffusion coefficients for various species present in the electrolytes at various mixing extents at temperature 303 K and 1 bar pressure at salt:solvent = 1:1.5. Data averaged over three independent runs.

System Li/(Li+Na) (%)	D_{Li} $\times 10^{-7}$ cm^2/s	D_{Na} $\times 10^{-7}$ cm^2/s	D_{FSI} $\times 10^{-7}$ cm^2/s	D_{SUL} $\times 10^{-7}$ cm^2/s
0	-	1.353	2.150	2.400
10	3.350	1.373	2.317	2.583
25	3.083	1.412	2.517	2.783
50	3.367	1.658	2.633	2.967
75	3.733	1.950	3.217	3.517
100	4.000	-	3.700	3.900

Table 4C.8: Diffusion coefficients for various species present in the electrolytes at various mixing extents at temperature 303 K and 1 bar pressure at salt:solvent = 1:9.57. Data averaged over three independent runs.

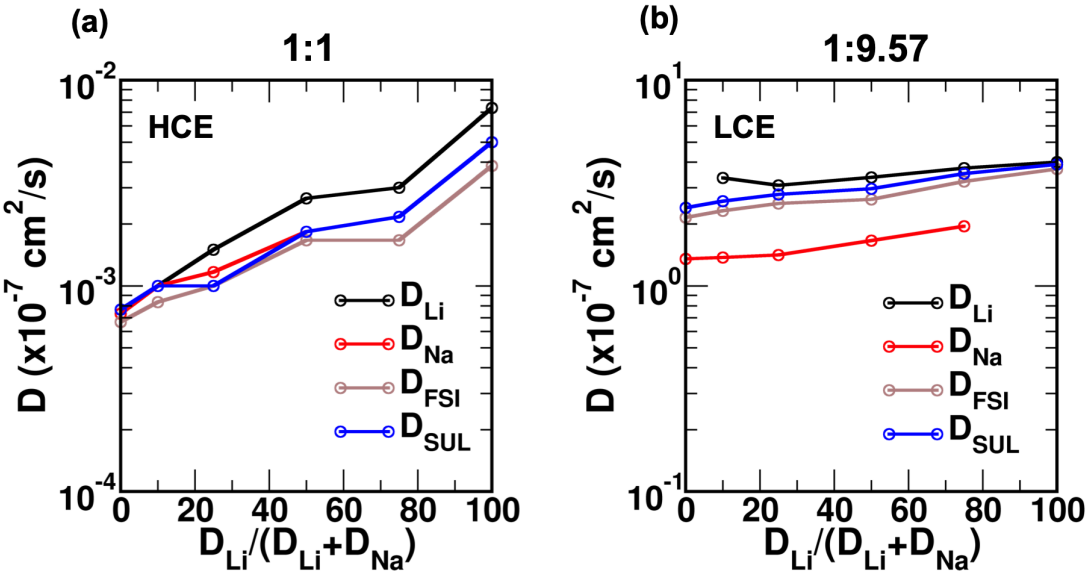

Figure 4C.3: Diffusion coefficients at prototypical (a) high salt concentration (1:1) and (b) low salt concentration systems (1:9.57) at temperature 303 K and 1 bar pressure. Data averaged over three independent runs.

In Tables 4C.6, 4C.7, and 4C.8, all values of the diffusion coefficients have been averaged over three runs. The diffusion coefficients of all species increase by roughly an order of magnitude at the high salt concentrations (salt:solvent = 1:1 and 1:1.5) in going from a pure Na-ion HCE to a pure Li-ion HCE (Figure 4C.3(a) for 1:1). Whereas, the increase is much smaller in going from the pure Na to pure Li electrolyte at 1:9.57 LCE (Figure 4C.3(b)). Like in the case of density, it was observed that the replacement of Na-ions with Li-ions has a larger effect in HCEs than LCEs.

4C.3.3 Ionic conductivity

The ionic conductivities and Nernst-Einstein conductivities (as discussed in Chapter 1) for all mixing extents at all salt concentrations were calculated and averaged over all three independent runs (Table 4C.9). The Haven ratios (defined in Equation 4C.4 [72]) were also calculated. It is the ratio of the Nernst-Einstein conductivity to the actual ionic conductivity (Chapter 1) or the ratio of self-diffusion coefficient to the conductivity diffusion coefficient.

$$H_R = \frac{D^*}{D^\sigma} = \frac{\lim_{t\to\infty} \frac{d}{dt} \sum_{i=1}^{N} (\mathbf{\Delta R}_i(t) \cdot \mathbf{\Delta R}_i(t))}{\lim_{t\to\infty} \frac{d}{dt} \sum_{i=1}^{N} (\mathbf{\Delta R_i}(t) \cdot \mathbf{\Delta R_i}(t)) + \lim_{t\to\infty} \frac{d}{dt} \sum_{i=1}^{N} \sum_{j\neq i} (\mathbf{\Delta R_i}(t) \cdot \mathbf{\Delta R_j}(t))} \tag{4C.4}$$

$\mathbf{\Delta R}_i$(t) is the displacement of the ith ion over a time interval, t. Here, N is the total number of ions.

System Li%	1:1			1:1.5		1:9.57		
	σ $\times 10^{-3}$ mS/cm	σ_{NE} $\times 10^{-3}$ mS/cm	σ_{NE}/σ	σ $\times 10^{-2}$ mS/cm	σ_{NE} $\times 10^{-2}$ mS/cm	σ mS/cm	σ_{NE} mS/cm	σ_{NE}/σ
0	1.370	2.850	2.080	0.499	1.137	0.681	1.329	1.952
10	2.660	3.729	1.402	0.767	1.397	0.884	1.473	1.779
25	2.300	4.584	1.993	0.791	3.886	0.747	1.648	2.206
50	4.140	8.006	1.934	1.940	9.663	1.010	1.956	1.937
75	5.310	9.128	1.719	2.580	7.923	1.030	2.471	2.399
100	11.600	22.977	1.981	12.200	15.640	1.970	2.929	1.487

Table 4C.9: Ionic conductivities with displacement correlations, Nernst-Einstein conductivity, and the Haven ratio σ_{NE}/σ at various total alkali salt concentrations for various alkali mixing extents at 303 K temperature and 1 bar pressure. Li % is the percentage of Li salt in the total mixture, i.e. Li/(Li+Na). Data averaged over three independent runs.

The ionic conductivity with displacement correlations and the Nernst-Einstein conductivity are as they were defined in the Appendix to Chapter 3.

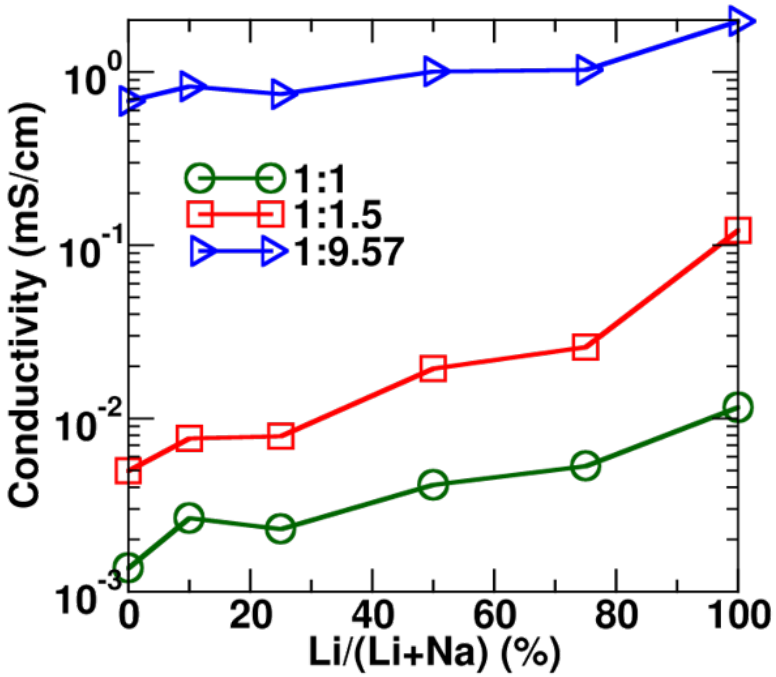

Figure 4C.4: Ionic conductivities at three salt:solvent ratios averaged over three independent runs at 303 K temperature and 1 bar pressure. Data averaged over three independent runs.

Ionic conductivities increase significantly (roughly by an order or magnitude or more) and largely systematically in going across the range of percentage of Li-ions. Like density and diffusion coefficients, the increase in conductivity in going from a pure Na-ion electrolyte to a pure Li-ion electrolyte, is significant in HCEs but not as significant in LCEs (Figure 4C.4).

Due to correlations in ion-ion displacements, particularly cation-anion displacement correlations, the actual ionic conductivities are smaller than the Nernst-Einstein (NE) conductivities. Therefore, the Haven ratio (σ_{NE}/σ) is greater than 1 for HCEs and LCEs (Table 4C.9).

4C.3.4 Transference numbers

The transference numbers of various ionic and molecular species for all mixing extents for all salt concentrations was calculated and averaged over all three independent runs.

System (% Li)	t_{Li}	t_{Na}	t_{FSI}
0	-	0.50	0.50
10	0.06	0.50	0.44
25	0.16	0.40	0.44
50	0.34	0.23	0.43
75	0.50	0.12	0.38
100	0.66	-	0.34

Table 4C.10: Transference numbers of various species at 303 K temperature and 1 bar pressure at 1:1 concentration of salt:solvent. Data averaged over three independent runs.

System (% Li)	t_{Li}	t_{Na}	t_{FSI}
0	-	0.53	0.47
10	0.062	0.494	0.444
25	0.076	0.157	0.767
50	0.175	0.097	0.728
75	0.53	0.08	0.39
100	0.63	-	0.37

Table 4C.11: Transference numbers of various species at 303 K temperature and 1 bar pressure at 1:1.5 concentration of salt:solvent. Data averaged over three independent runs.

System (% Li)	t_{Li}	t_{Na}	t_{FSI}
0	-	0.39	0.61
10	0.086	0.318	0.596
25	0.178	0.246	0.576
50	0.307	0.172	0.521
75	0.444	0.0651	0.491
100	0.517	-	0.483

Table 4C.12: Transference numbers of various species at 303 K temperature and 1 bar pressure at 1:9.57 concentration of salt:solvent. Data averaged over three independent runs.

The transference numbers reported in Tables 4C.10, 4C.11, 4C.12 do not account for correlations between non-self ion-displacements. These have been calculated using self-diffusion coefficients alone. The true transference numbers account for these correlations. The calculation of this quantity requires multiple (of the order of 50), and long (hundreds of nanoseconds to microseconds) trajectories. These simulations and calculations would be too computationally expensive and were therefore beyond the scope of the thesis.

From Tables 4C.10, 4C.11, and 4C.12, we found that the transference numbers of Li-ions (t_{Li}) at all salt concentrations increases with increase in the percentage of Li-ions in the system. This increase in t_{Li} is simultaneously accompanied with a decrease in t_{Na}.

The trend in t_{FSI} with increase in percentage of Li-ions in the system is either one of mild decrease or is unsystematic. Therefore, with increase in the percentage of Li-ions in the electrolyte, Li-ions carry a increasingly larger fraction of the total current and Na-ions carry a decreasing fraction of the total current.

From the data of the three transport properties the following were concluded:

(a) The transport properties of all species increase with increase in the percentage of Li-ions present in the electrolyte. The ionic conductivity of the electrolyte increases with the percentage of Li-ions in the mixture.

(b) The transference number of Li-ions also increases with increase in the percentage of Li-ions in the mixture.

Taken together, this implied that with increase in the percentage of Li-ions in the electrolyte, an increasingly large current will be carried by Li-ions.

Therefore, replacing Na-ions systematically with Li-ions in HCEs has two effects:

(a) Replacing Na-ions with Li-ions leads to a systemic increase in the fluidity of the electrolyte. This is seen with increase in the diffusion coefficients of all species with increase in the percentage of Li-ions. This is also perhaps the main factor behind the increase in ionic conductivity with increase in Li-content. The effect of this was also seen in several analyses to follow.

(b) A mere increase in systemic fluidity starting from a pure-Na HCE was not all there was to Li-Na mixture electrolyte. The effect of replacing Na-ions with Li-ions is not only in the thinning of electrolyte, but also that Li-ions take up an increasing brunt of the current carrying load at increasingly larger conductivities attained with higher Li-content in the electrolyte. Li-ions are therefore outplaying other ions and are the key-players in improving the transport properties of the mixed electrolytes. The precise reason for this was beyond the scope of the present thesis but will definitely comprise our studies in the future.

We mainly focus on understanding the 1:1 HCE as a function of extent of alkali-ion mixing. Structure and transport in HCEs as a function of concentration has been explored in Chapter 3. Wherever found necessary, comparison with other salt concentrations have also been presented.

4C.3.5 Radial distribution functions and coordination numbers

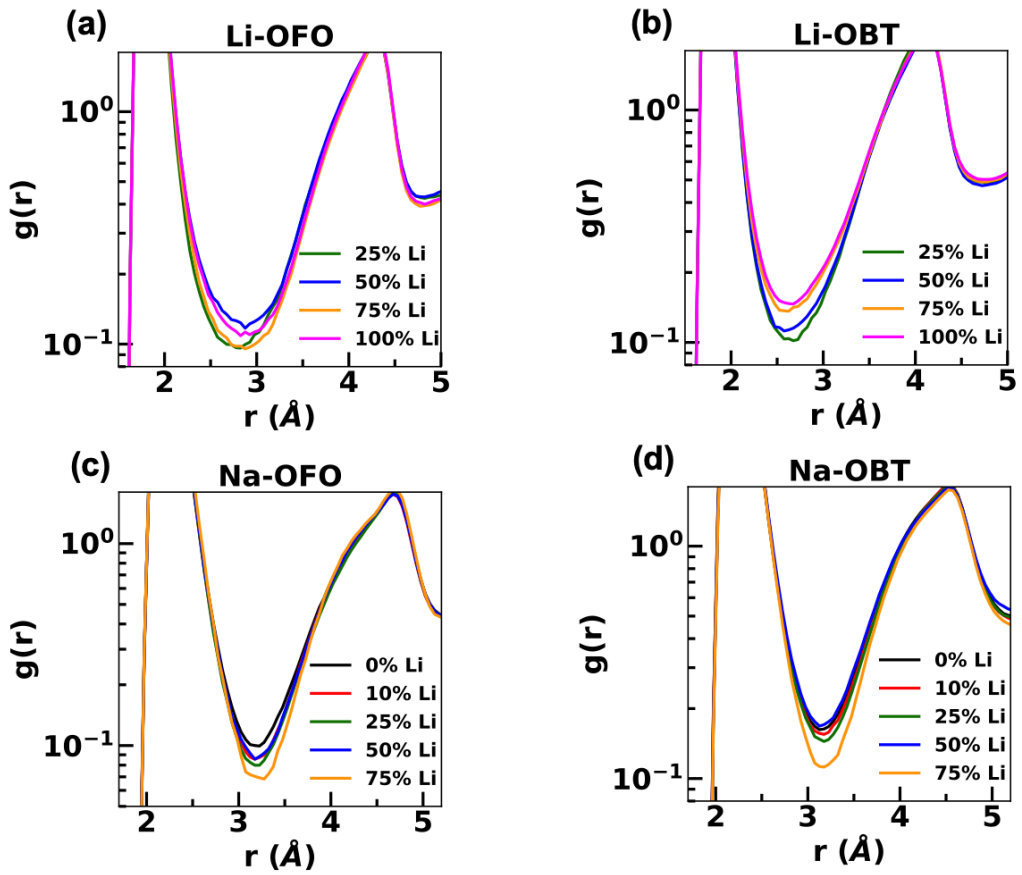

Figure 4C.5: Radial distribution function of significant alkali-ion-OFO (oxygen of sulfolane) and alkali-ion-OBT (oxygen of FSI) in 1:1 HCEs. Data averaged over three independent runs.

The radial distribution functions for alkali-ions in HCEs was focused upon. From Chapter 4B, we know that oxygens of sulfolane and FSI anions are the primary nearest neighbours to alkali-ions. Therefore, in this sub-chapter the alkali-ion-OFO (oxygen of sulfolane) and alkali-ion-OBT (oxygen of FSI) have been shown (Figure 4C.5).

System (% Li)	r_{solv} Li-OFO (Å)	r_{solv} Na-OFO (Å)	r_{solv} Li-OBT (Å)	r_{solv} Na-OBT (Å)	$n(r_{solv})$ Li-OFO	$n(r_{solv})$ Na-OFO	$n(r_{solv})$ Li-OBT	$n(r_{solv})$ Na-OBT
0	-	3.23	-	3.13	-	1.93	-	3.63
25	2.83	3.18	2.68	3.18	1.45	1.92	2.71	3.63
50	2.88	3.18	2.58	3.13	1.55	1.97	2.63	3.61
75	2.88	3.28	2.63	3.18	1.50	2.13	2.69	3.63
100	2.83	-	2.68	-	1.58	-	2.64	-

Table 4C.13: Position of the first solvation shell, r_{solv} (first minimum of RDF) and coordination number at first minimum for 1:1 HCEs. Data averaged over three independent runs.

Stronger interactions between Li-ion and FSI anion over Li-ion and sulfolane molecule is expected. This is why Li-OBT (oxygen of FSI anion) first minimum occurs at slightly shorter distances than the Li-OFO (oxygen of sulfolane molecule) first minimum (Figure 4C.5(a) and (b) and Table 4C.13). This is also why the coordination number at the first minimum (first solvation shell) is larger for Li-OFSI as compared to Li-OFO (Table 4C.13). Additionally, the first minimum becomes less deep with increase in Li-content even in the case of Li-OBT (Figure 4C.5(b)).

Li/Na-OFO/OBT and Li/Na-OFO/OBT RDF first minimum positions do not show any systematic shift with percentage of Li-ions (Figure 4C.5). The coordination number of Li-OSUL increases weakly with increase in the Li-content of the electrolyte. Na-ions tend to be a slightly more oblivious to the exact composition of the electrolyte than Li-ions due to the large solvation shell of Na-ions as compared to Li-ions.

Coordination numbers at first minimum suggest a slight overall increase in the sulfolane content and a small decrease in the FSI content in the solvation shells of Li-ions (Table 4C.13). This could imply a marginal decrease in the Li-anion interaction with increase in percentage of Li-ions. This decrease in interaction could possibly marginally aid in the enhancement of Li-ion transport.

4C.3.6 Solvation shell composition of alkali ions

Chapter 4B examined the difference between the solvation shells of Li and Na-ions in pure alkali-ion electrolytes. Here, we looked at the solvation shell composition distribution for each alkali-ion as a function of the extent of mixing at different total salt concentrations.

System				
10%Li	25%Li	50%Li	75%Li	100%Li
(OFO:OBT)- Percentage population				
(1,3) - 45.8	(1,3) - 34.2	(1,3) - 35.6	(1,3) - 32.6	(1,3) - 28.5
(2,2) - 27.0	(2,2) - 25.8	(2,2) - 26.0	(2,2) - 26.9	(2,2) - 26.0
(0,4) - 12.6	(0,4) - 19.1	(0,4) - 14.5	(0,4) - 14.9	(0,4) - 15.7
(2,3) - 4.0	(2,3) - 6.5	(3,1) - 5.2	(3,1) - 7.3	(3,1) - 9.6

Table 4C.14: Populations of solvation shell types of Li-ions for various extents of Li-Na mixing at salt:solvent = 1:1. OFO and OBT refer to oxygens of sulfolane and FSI anion, respectively. Only the significant populations have been listed.

System				
0%Li	10%Li	25%Li	50%Li	75%Li
(OFO:OBT)- Percentage population				
(2,4) - 17.9	(2,4) - 17.8	(2,4) - 18.1	(2,4) - 20.0	(2,4) - 20.2
(1,4) - 15.4	(1,4) - 17.2	(1,4) - 16.4	(3,3) - 15.5	(3,3) - 15.8
(2,3) - 14.0	(2,3) - 15.1	(3,3) - 15.8	(2,3) - 14.4	(1,5) - 13.1
(3,3) - 12.6	(1,5) - 10.1	(2,3) - 13.4	(1,4) - 13.6	(2,3) - 11.4
(1,5) - 11.6	(0,5) - 6.0	(4,2) - 7.6	(1,5) - 11.4	(1,4) - 10.4

Table 4C.15: Populations of solvation shell types of Na-ions for various extents of Li-Na mixing at salt:solvent = 1:1. OFO and OBT refer to oxygens of sulfolane and FSI anion, respectively. Only the significant populations have been listed.

From the top solvation shell populations, we observed that in agreement with the coordination numbers obtained from the RDFs (Table 4C.13), Li and Na-ions in HCEs have a larger anion content in the solvation shells than solvent content (Tables 4C.14 and 4C.15). From the top solvation shell populations, no clear trend in the solvation shell composition of Li or Na-ions as a function of Li-content of the electrolyte is seen (Tables 4C.14 and 4C.15).

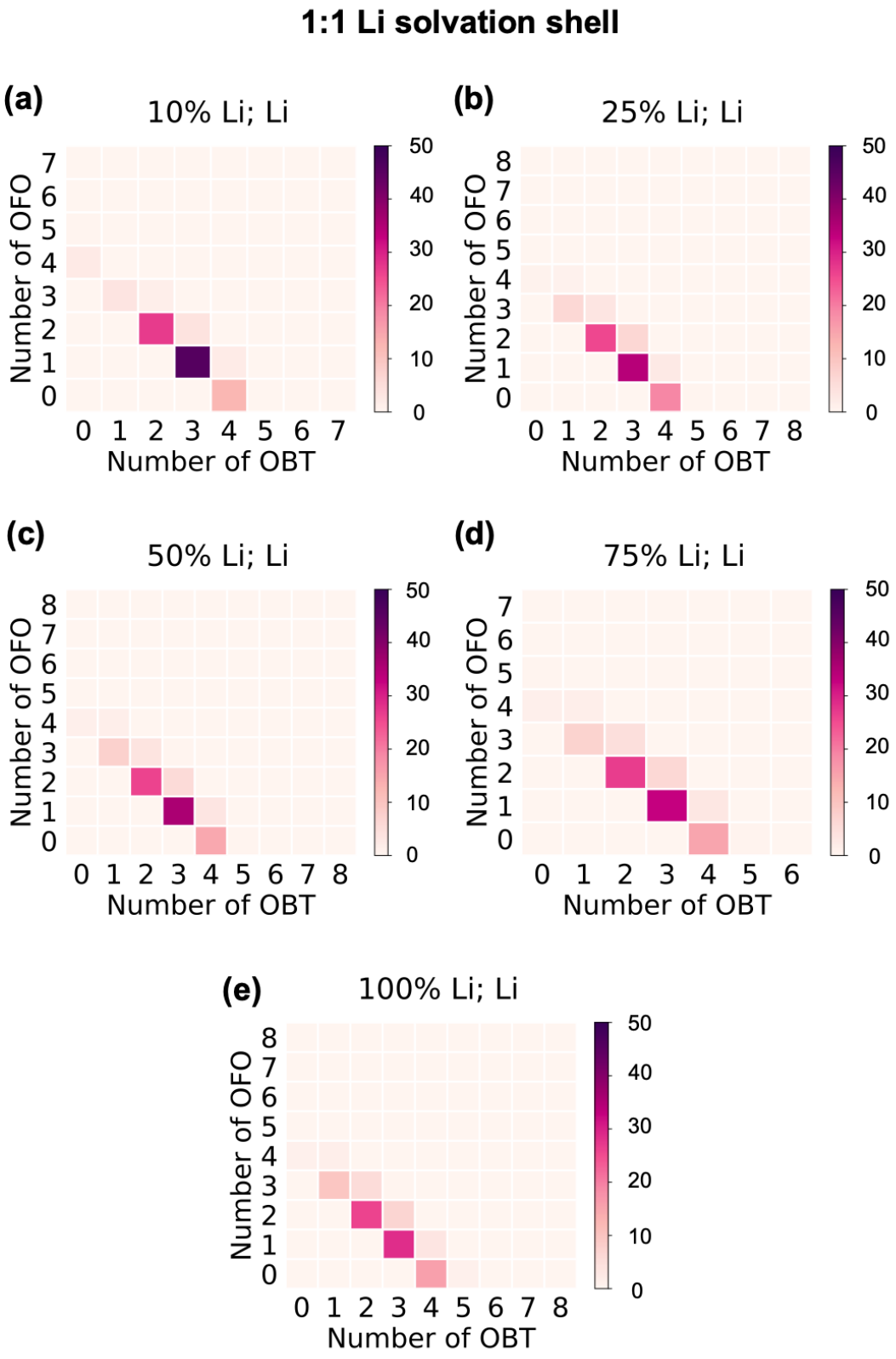

Figure 4C.6: Probability distribution of solvation shell composition of Li-ions for various extents of Li-Na mixing at salt:solvent = 1:1

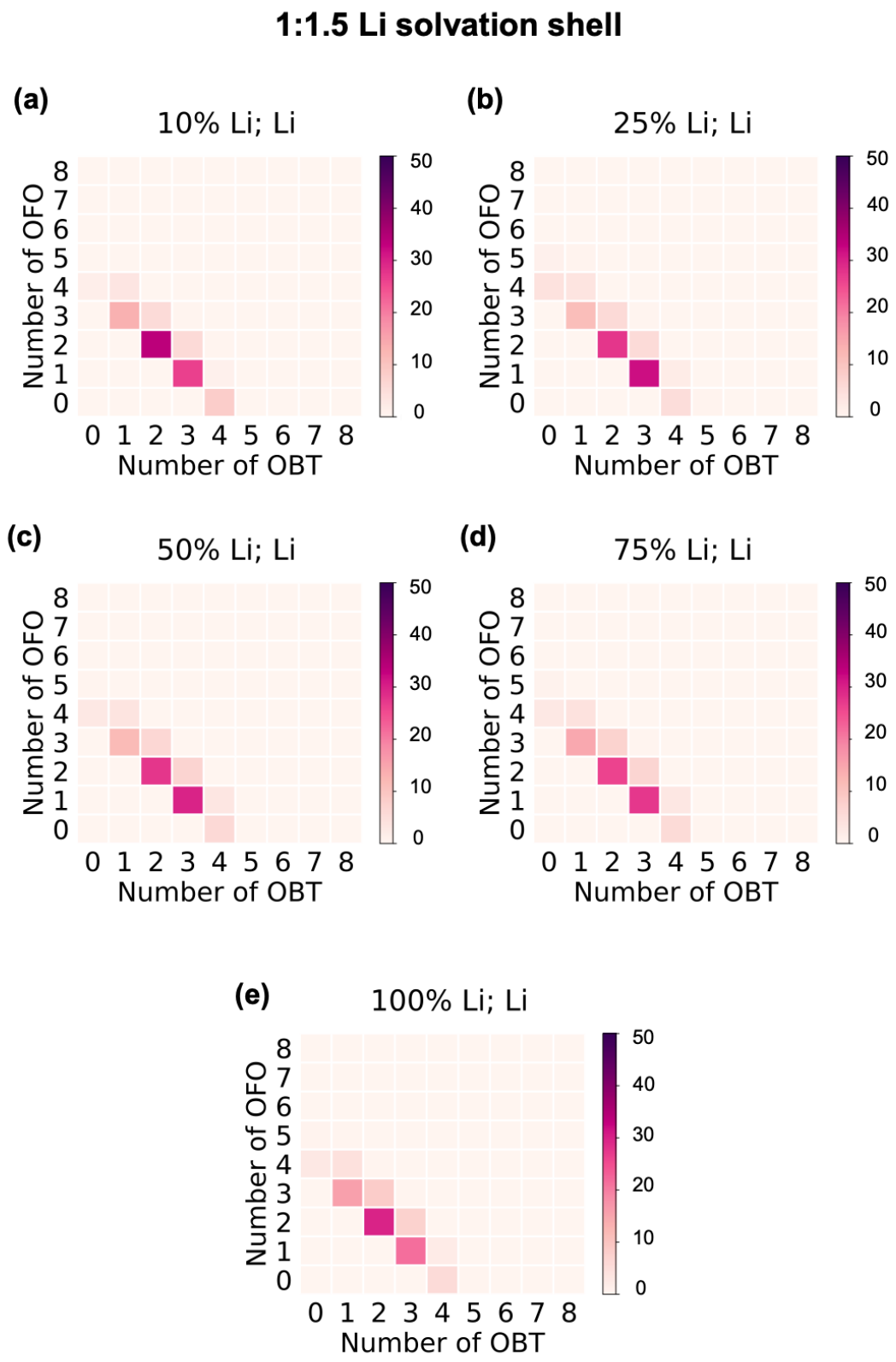

Figure 4C.7: Probability distribution of solvation shell composition of Li-ions for various extents of Li-Na mixing at salt:solvent = 1:1.5.

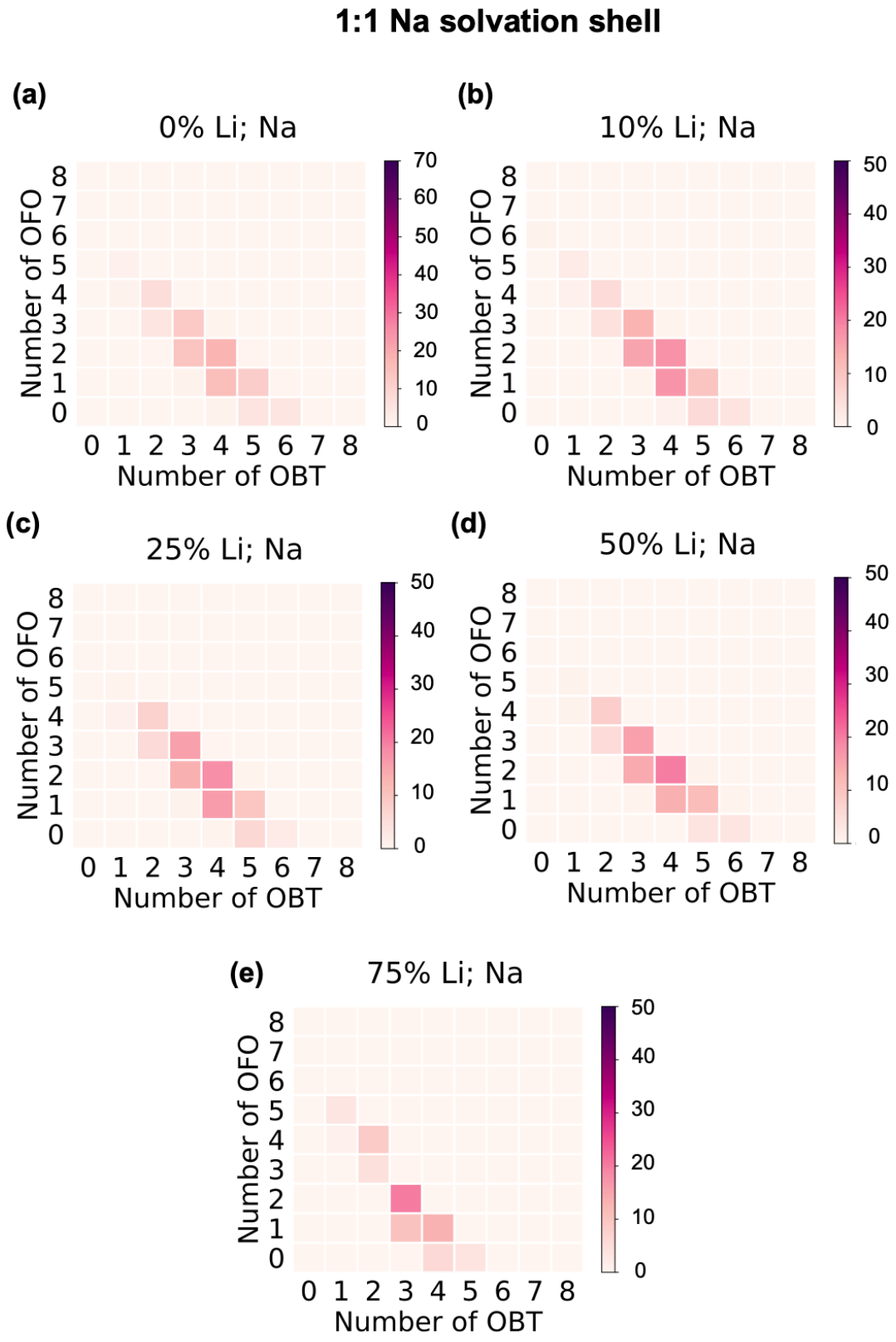

Figure 4C.8: Probability distribution of solvation shell composition of Na-ions for various extents of Li-Na mixing at salt:solvent = 1:1.

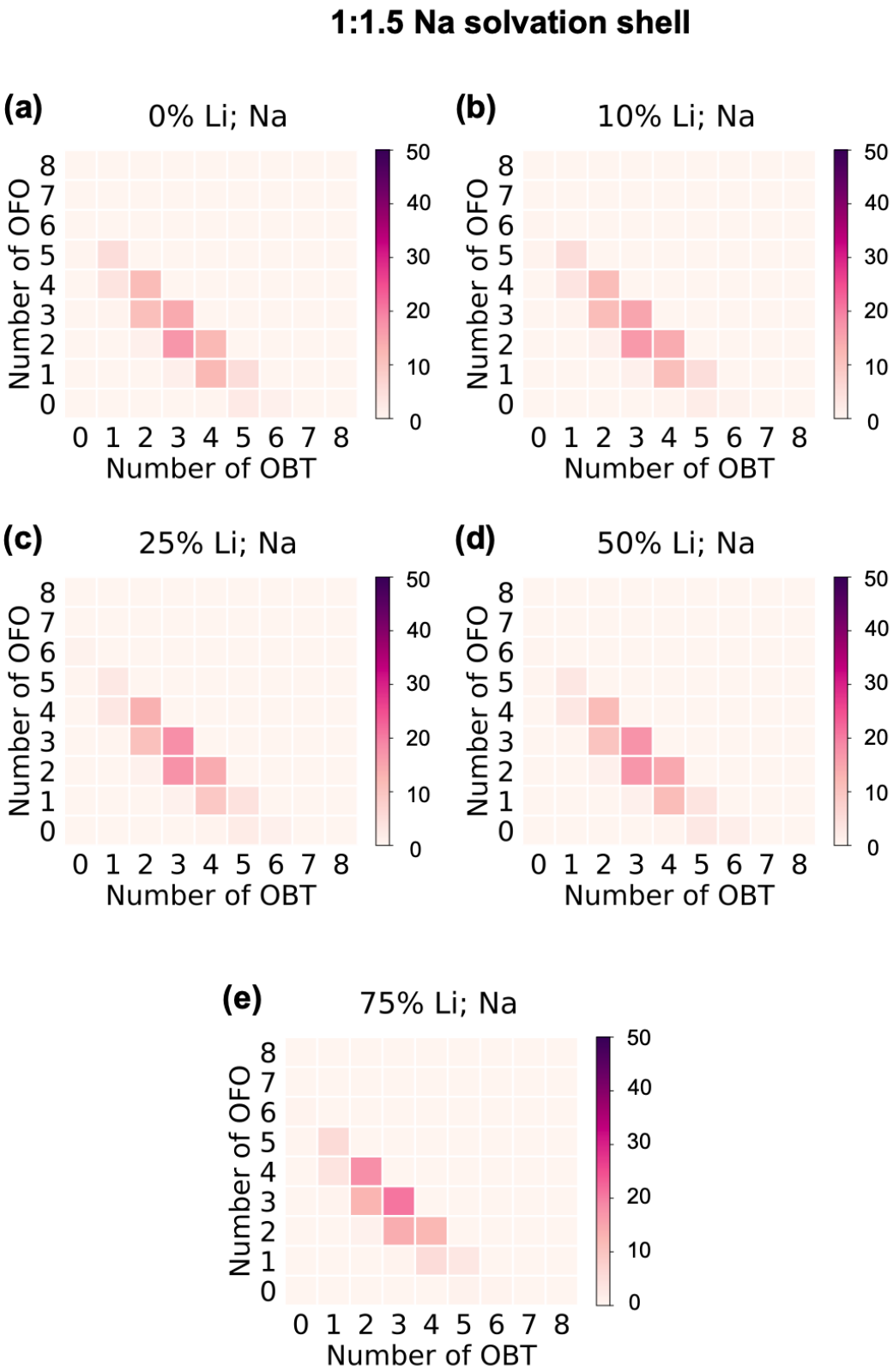

Figure 4C.9: Probability distribution of solvation shell composition of Na-ions for various extents of Li-Na mixing at salt:solvent = 1:1.5.

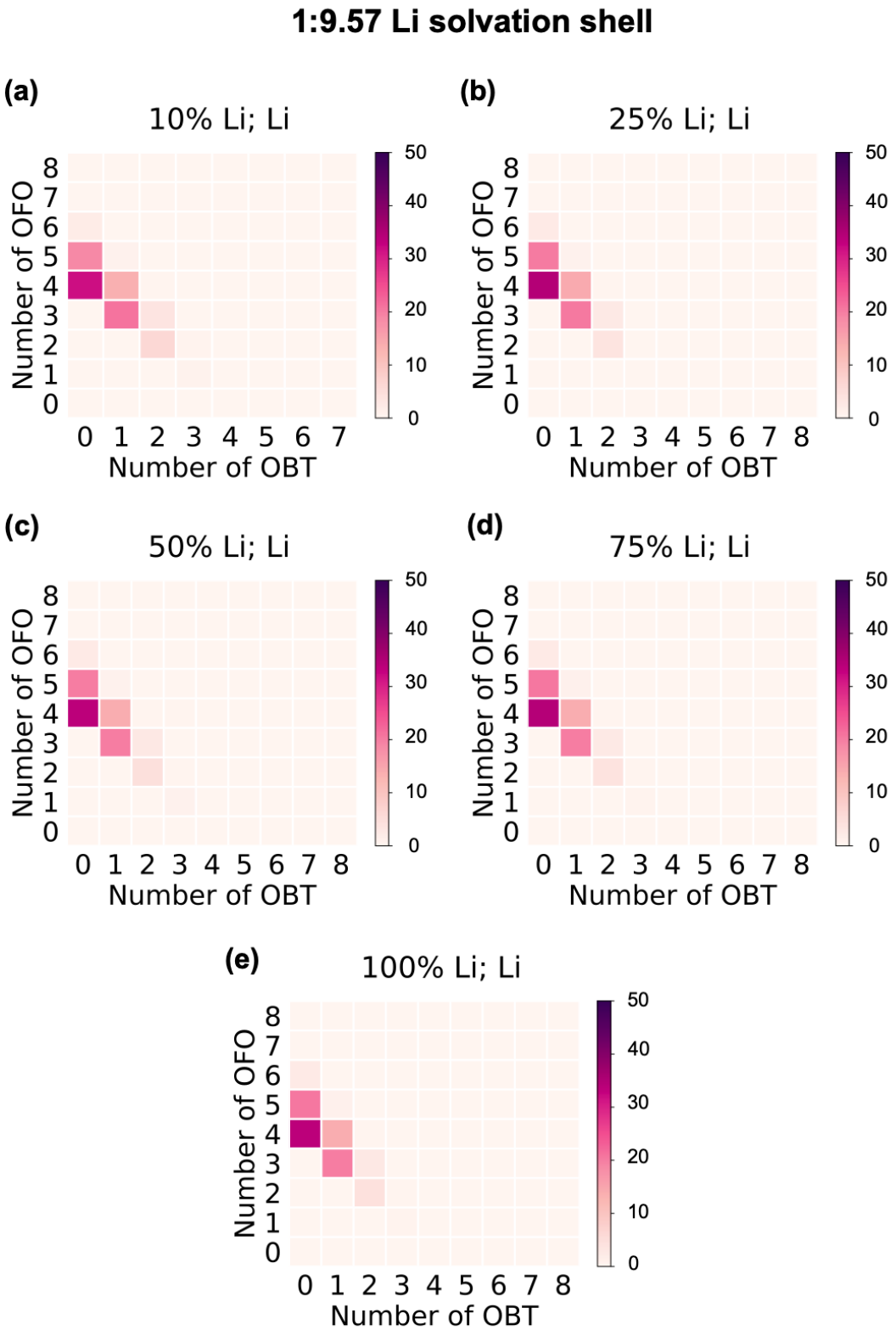

Figure 4C.10: Probability distribution of solvation shell composition of Li-ions for various extents of Li-Na mixing at salt:solvent = 1:9.57.

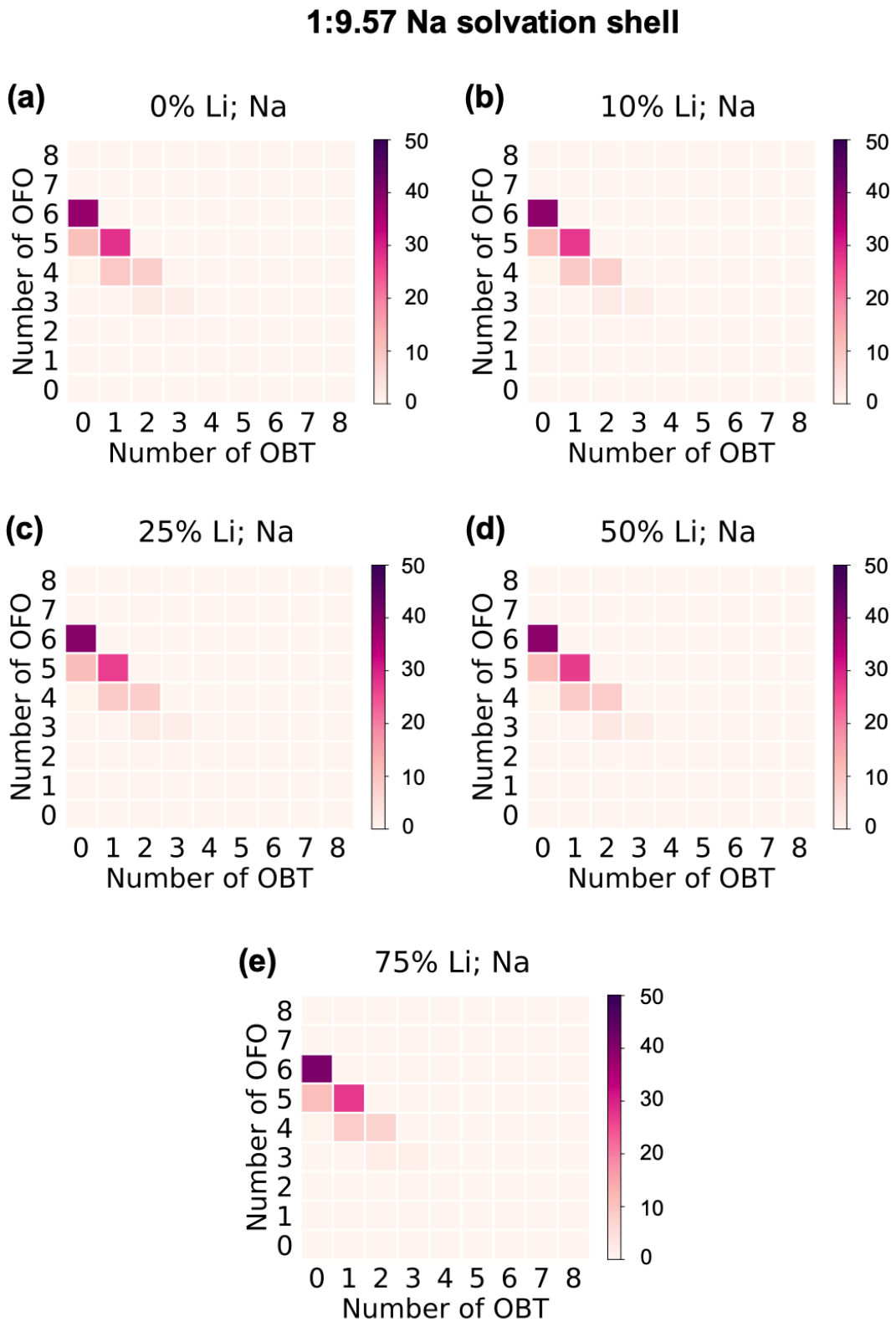

Figure 4C.11: Probability distribution of solvation shell composition of Na-ions for various extents of Li-Na mixing at salt:solvent = 1:9.57.

However, some other observations were made. Solvation shell composition distribution of Li-ions becomes more specific as the percentage of Li-ions in the mixture HCEs is decreased (Figures 4C.6 and 4C.7). We rationalise this in the following way. Na-ions have a broader solvation shell composition distribution (larger variety in significant solvation shell types) (Figures 4C.8 and 4C.9). The non-specificity in the solvation shell composition of Na-ions allows for Li-ions to adopt specificity in their solvation shell composition more when the more non-specific alkali-ion (Na-ions here), is in majority in the electrolyte.

Further, we observed that the solvation shell composition distribution for Na-ions does not change significantly with the percentage of Li-ions in the mixed electrolyte (Figures 4C.8 and 4C.9). Due to the large solvation shell of Na-ions, they tend to be a little more oblivious to the exact composition of the electrolyte in comparison to Li-ions.

At low salt concentration, the solvation shell type populations do not change very much for both Li and Na-ions as a function of mixing. All prominent solvation shell types of both alkali-ions was composed of predominantly solvent molecules. Thus, in LCEs, both Li and Na-ions show solvation shell composition specificity biased towards large solvent content (Figures 4C.10 and 4C.11). Changes in the alkali-ion composition are small changes compared with the excess solvent present in LCEs.

Li				Na			
System (%Li)	No. of sulfolane	No. FSI	Total	System (%Li)	No. of sulfolane	No. of FSI	Total
10	1.373	2.713	4.086	0	2.162	3.404	5.566
25	1.372	2.770	4.142	10	2.042	3.629	5.671
50	1.491	2.662	4.153	25	1.794	3.398	5.292
75	1.522	2.653	4.175	50	2.016	3.625	5.641
100	1.555	2.640	4.195	75	2.075	3.586	5.661

Table 4C.16: Population weighted average of the number of sulfolane molecules and number of FSI anions in the solvation shells of Li and Na-ions as a function of percentage of Li-ions in the HCEs. Salt:solvent = 1:1.

Subsequently, we examined the average number of solvent and FSI anion molecules (i.e., their centre of mass) present in the solvation shell of Li and Na-ions as a function of mixing by taking 1:1 HCEs as examples (Table 4C.16). For Li-ions, we found that as the percentage of Li-ions in the electrolyte is increased, the average number of sulfolane molecules in the solvation shell of Li-ions increases and the number of FSI anions in the solvation shell slightly decreases, consistent with Table 4C.13.

Na-ions on the other hand, showed no trend in the average number of sulfolane and FSI anions involved in the solvation shell as the percentage of Li-ions in the HCEs was

increased. Again, the non-specificity of the Na-ions allow the Li-ions to adopt specific solvation shell types.

4C.3.7 Self-part of the van Hove correlation function $G_s(r,t)$

Chapter 4B reported the self part of the van Hove correlation function for single alkali electrolytes at prototypical high and low salt concentrations. In this sub-chapter, we studied the effect of alkali-ion mixing on the self part of the van Hove correlation function of alkali ions.

Figures 4C.12 and 4C.13 show $G_s(r,t)$ for Li and Na-ions, respectively for 1:1 HCEs. As expected from diffusion coefficients, both Li and Na-ions are able to "hop+diffuse" to larger distances with increase in the Li-content of the electrolyte. Across the range of percentage Li-ions, a small fraction of Li and Na-ions reach up to approximately 2 times larger distances (Figure 4C.12 and 4C.13).

Signatures for alkali ion hopping for Li-ions are present but are smothered by signatures of increased diffusion of Li-ions with increase in Li-content of the electrolyte (Figure 4C.12). The ratio of diffusion coefficients of Li-ions to sulfolane molecules and FSI anions, and real time Li-ion hop trajectories, strongly suggest that Li-ion hopping was very much present in the pure 1:1 LiFSI in sulfolane electrolyte (Chapter 4B). From Figure 4C.13, it was clear that the propensity for Na-ion hopping also increases slightly with increase in Li-content in the electrolyte.

Hopping can be attributed as the predominant transport mechanism through which ions are able to reach larger radial distances than they would through diffusion alone ($G_s(r,t)$ in Appendix of Chapter 3).

Replacing Na-ions with Li-ions improves the diffusion coefficient of Li-ions more than it does of Na ions. From Chapter 4B, we know that Li-ions have a larger propensity to hop than Na-ions.

The effect of mixing of alkali-ions on the extent of non-diffusive dynamics (super-diffusive or hopping) in the electrolyte was studied and truly revealed the uniqueness of Li-ion transport over those of other ions. Study of $G_s(r,t)$ as a function of alkali-ion mixing proved instrumental in answering the questions raised in this sub-chapter. This is discussed in a later section.

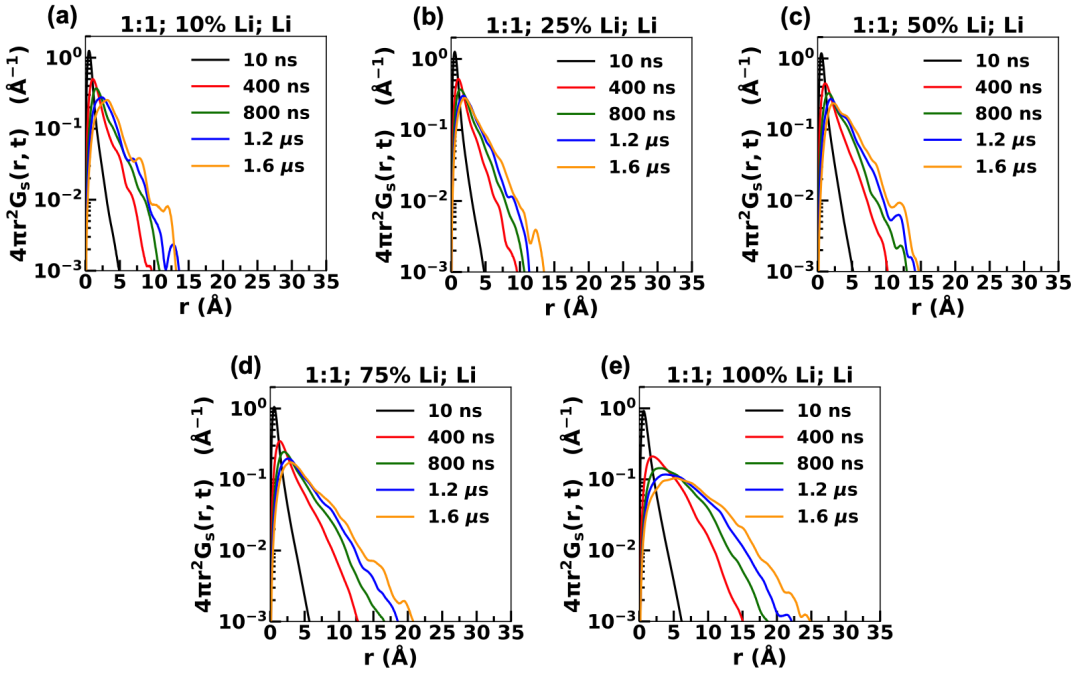

Figure 4C.12: Self-part of the van Hove correlation function, $G_s(r,t)$ for Li-ions as a function of the extent of mixing of the alkali-ions. Salt:solvent = 1:1 electrolytes. Data averaged over three independent runs.

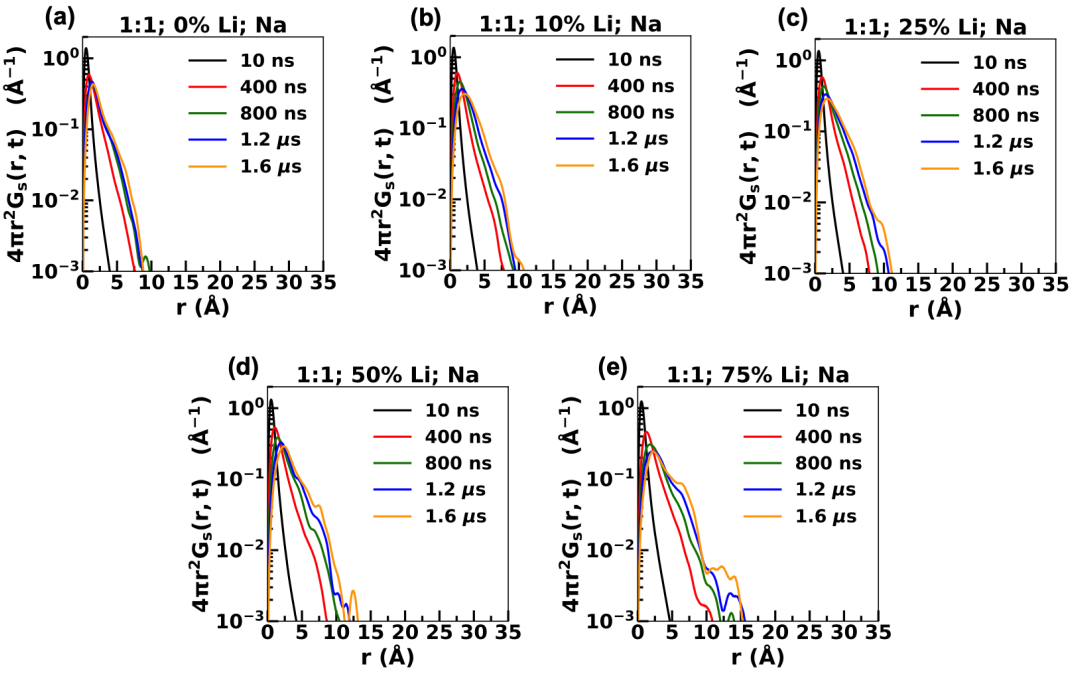

Figure 4C.13: Self part of the van Hove correlation function, $G_s(r,t)$ for Na-ions as a function of the extent of mixing of the alkali-ions. Salt:solvent = 1:1 electrolytes. Data averaged over three independent runs.

4C.3.8 Distinct-part of the van Hove correlation function G_d(r,t)

The distinct part of the van Hove correlation function, G_d(r,t), was used to understand how the propensity to "hop + diffuse" to a previously occupied alkali-ion site changed with the extent of mixing of the alkali ions.

A preference to "hop+diffuse" to previously occupied alkali-ion sites in seen for both Li and Na-ions in pure alkali electrolytes as well as their mixtures. This is indicated from a peak at $r = 0$ and a valley between $r = 0$ and the first peak (Figure 4C.14 and 4C.15).

Electrolytes composed of the top three highest percentages of Li-ions were considered to evaluate the transport of Li-ions through G_d(r,t). Electrolytes composed of the top three highest percentages of Na-ions were considered to evaluate the transport of Na-ions through G_d(r,t). This was done to have good statistics of the alkali-ions whose transport processes were under consideration.

As the Li-content of the electrolyte is decreased, the electrolyte becomes more sluggish and therefore alkali-ions tend to be more caged by their nearest neighbours. Diffusive motion becomes more difficult. Therefore transport of alkali-ions through hopping accounts for an increasing proportion of ion-motion, as the Li-content of the electrolyte is decreased. This makes the peak at $r = 0$ and a dip in between $r = 0$ and the first peak more distinct/deeper as Li-content is decreased in the electrolyte. In other words, as diffusion increases with increase in Li-content, this dip becomes shallower because the diffusive component of ion motion increases, and unlike hopping, diffusion has no site-preference (Figure 4C.14).

At any time-interval, Na-ions have a G_d(r,t) profile than would lie below that of Li-ions (Figures 4C.14 and Figure 4C.15). This is expected as Na-ion rich electrolytes are more sluggish than their Li-ion counterparts. The dip under consideration is also deeper in the Na-rich HCEs than the Li-rich HCEs under consideration (Figures 4C.14 and Figure 4C.15). Increase in the dip with increase in Na-content is expected because of the increase in the sluggishness of the electrolyte, making hopping to previously occupied sites more prominent.

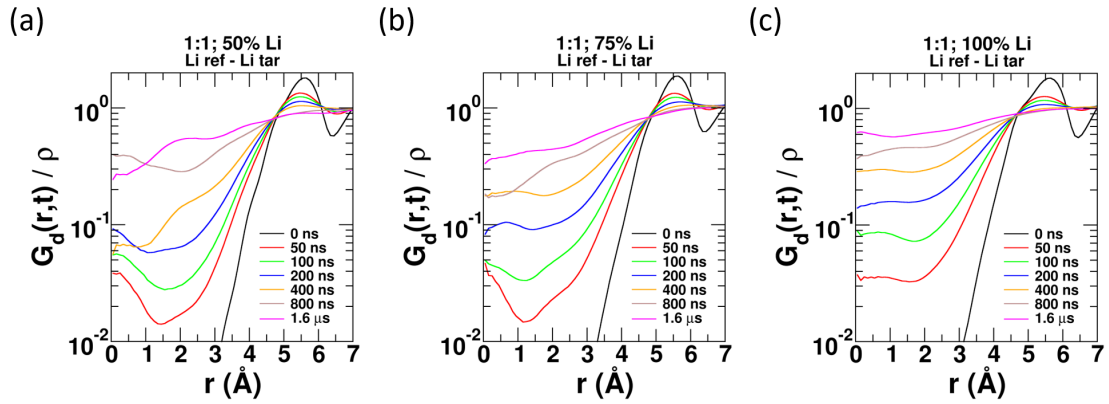

Figure 4C.14: Distinct part of the van Hove correlation function, $G_d(r,t)$, with Li-ions as both the reference (ref) and target (tar) ions. $G_d(r,t)$ is shown as a function of extent of mixing of the alkali-ions in three 1:1 HCEs.

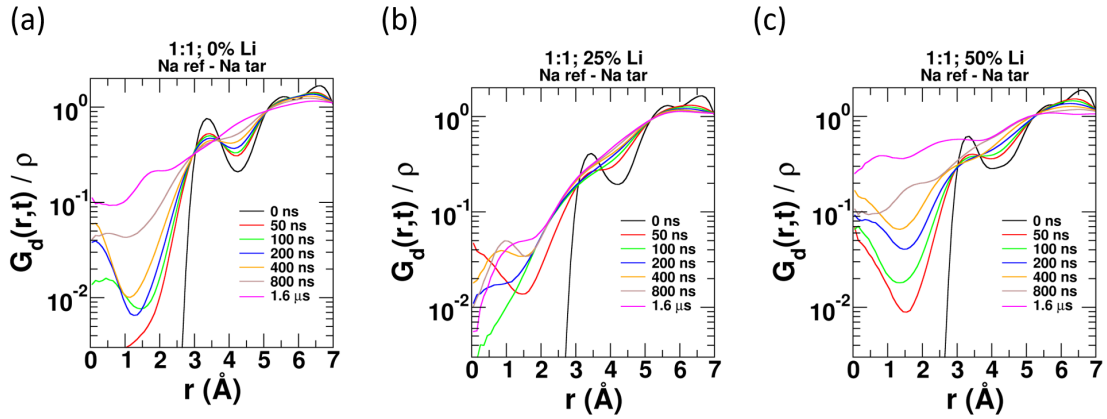

Figure 4C.15: Distinct part of the van Hove correlation function, $G_d(r,t)$, with Na-ions as both the reference (ref) and target (tar) ions. $G_d(r,t)$ is shown as a function of extent of mixing of the alkali-ions in three 1:1 HCEs.

When "hop+diffusion" between unlike alkali-ion sites were considered, we observed that Na-ions being less diffusive take a long time to reach a previously occupied Li-ion site. Corresponding $G_d(r,t)$ profiles show prominent dips between $r = 0$ and the first peak (Figure 4C.16(a) and (c)). Li-ions (being more diffusive than Na-ions) are easily able to diffuse to previously occupied Na-ion sites without the need to only do so through hopping. Therefore, the corresponding $G_d(r,t)$ profiles lack prominent dips between $r = 0$ and the first peak (Figure 4C.16(b) and (d)).

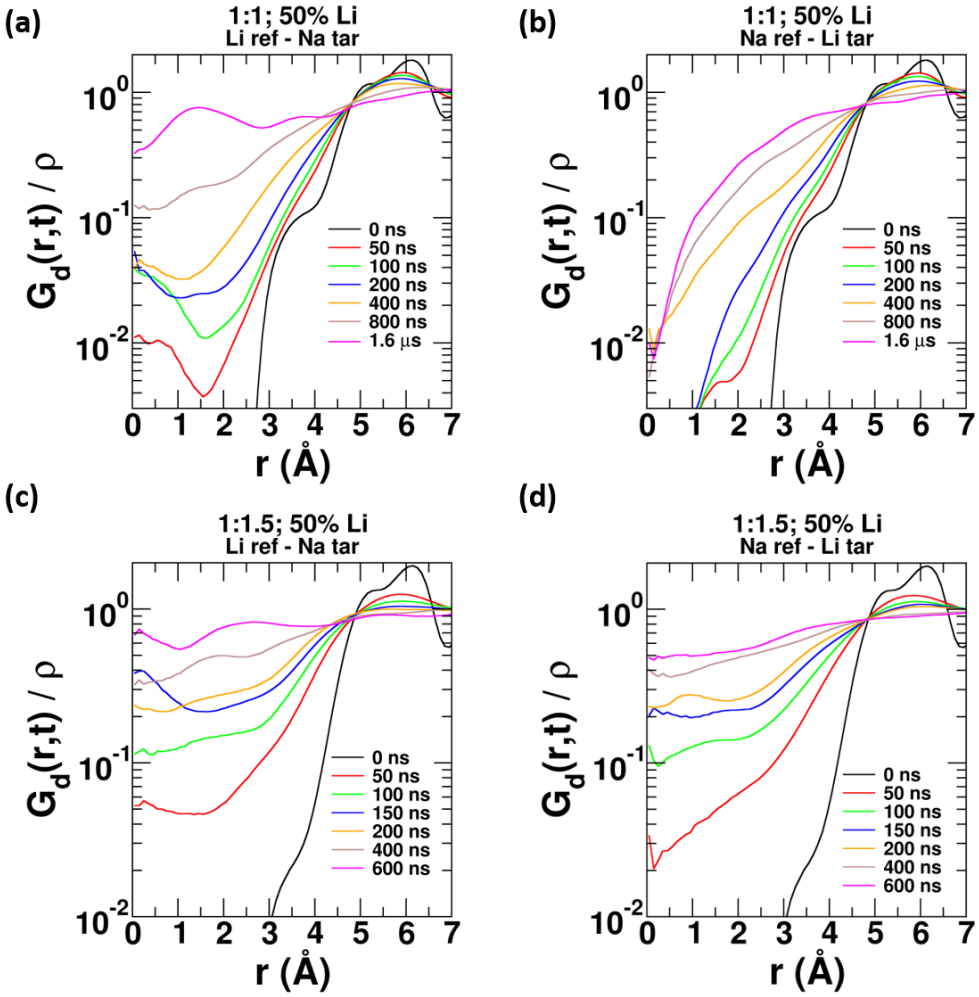

Figure 4C.16: Distinct part of the van Hove correlation function, G_d(r,t) with reference (ref) and target (tar) ions as stated in the sub-figures. G_d(r,t) is shown at 50 % Li-ions alkali-ion composition. Salt:solvent = 1:1 and 1:1.5.

4C.3.9 Non-Gaussian parameter α_2

The non-Gaussian parameter was studied for different ionic and molecular types present in the electrolytes across mixing extents of the two alkali ions. Data for the 1:1 HCE (where the differences were most stark) is shown. We found that with increase in Li-content in the electrolyte, the time corresponding to the maximum in α_2, t^*, roughly decreases for both Li and Na-ions (Figure 4C.17 (a) and (b)). In comparison to weak trends in α_2 for Li and Na-ions, no systematic trends were seen for FSI anions and sulfolane (SUL) molecules (Figure 4C.17 (c) and (d)). Alkali-ions are small and have high charge density in comparison to FSI anions, say. Small ions with high charge density have a well defined solvation shell. Such small ions (here Li and Na-ions) are expected to show transport

phenomenon which is more dependent on the local liquid environment around the alkali-ion. Hence, as opposed to FSI or SUL, alkali-ions are both more dynamically heterogenous and have heterogeneity that is more sensitive to Li-ion content/composition of the HCE.

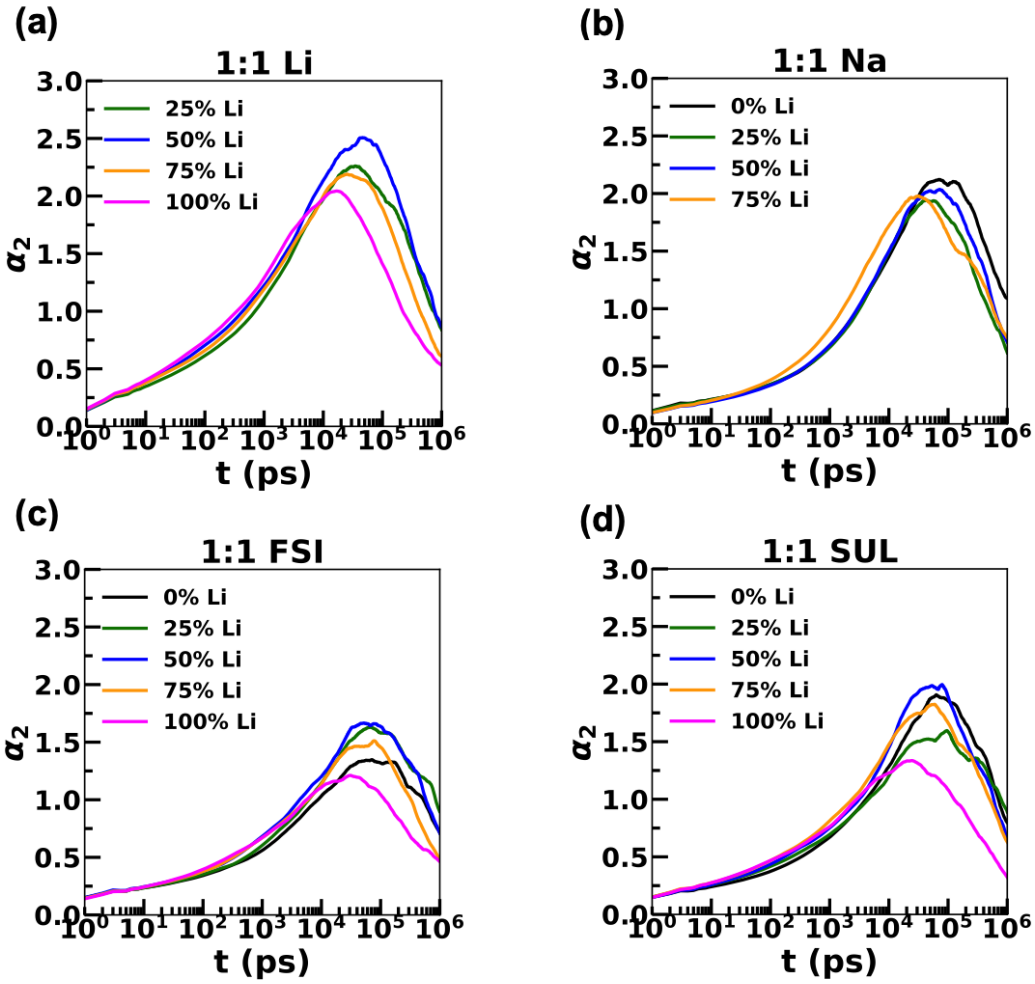

Figure 4C.17: Non-Gaussian parameter, α_2, for all ionic and molecular species for different extents of alkali-ion mixing in the 1:1 HCE. Data averaged over three independent runs.

4C.3.10 Cage relaxation time correlation function

Just as in the remainder of this thesis, ion transport has been seen to be heavily dependent on the structure of the electrolyte surrounding the ions. In order to understand the unique behaviour of Li-ions as a function of Li-content of the electrolyte, we examined the continuous cage relaxation time correlation function for Li and Na-ions as a function of alkali-ion mixing extent. The continuous cage relaxation time correlation function as

defined in Equation 4C.5, is one measure of how fast the cage identities of alkali-ions (considered here) change.

$$S(t) = \langle s(t_0 + t)m(t_0 + t)\rangle \tag{4C.5}$$

$s(t_0 + t) = 1$ if the nearest neighbours of the alkali-ion (cage-identity) were exactly the same at time $t_0 + t$ as they were at time t_0. Else $s(t_0 + t) = 0$. $m(t_0 + t) = 1$ if the nearest neighbours of an alkali-ion at time t_0 have remained exactly the same up to time $t_0 + t$ at every instant of a frequently dumped trajectory (here, 1 fs). Else $m(t_0 + t) = 0$.

From the continuous cage relaxation time correlation function of the alkali-ions, we found that the cages of Li-ions (Figure 4C.18(a)) relax slower than those of Na-ions (Figure 4C.18(b)). This can be expected since Na-ions have a larger and looser solvation shell in comparison with Li-ions (Chapter 4B), therefore, the cage-identities of Na-ions is lost faster than those of Li-ions on an average. One may naively therefore expect Na-ions to have larger transference numbers. As discussed in Chapter 4B, the larger solvation radius and a larger mass of Na-ions (relative to Li-ions), makes the diffusion of Na-ions (where nearest neighbours are dragged along with the central alkali-ion), slower. Further, the propensity for Na-ion hopping was also seen to be lower than that of Li-ions (Chapter 4B).

What was more interesting is that the $S(t)$ for Li-ions was found to be more sensitive to the increase in Li-content of the electrolyte than the $S(t)$ for Na-ions. This would mean that the cage identities of Li-ions were more sensitive to the Li-content of the electrolyte, favouring faster cage relaxation, than the cage identities of Na-ions (which were more indifferent to the Li-content of the electrolyte) (Figure 4C.18). This observation provides a structural relaxation rationale behind the increase in the transference numbers of Li-ions with increase in the percentage of Li-ions in the electrolyte.

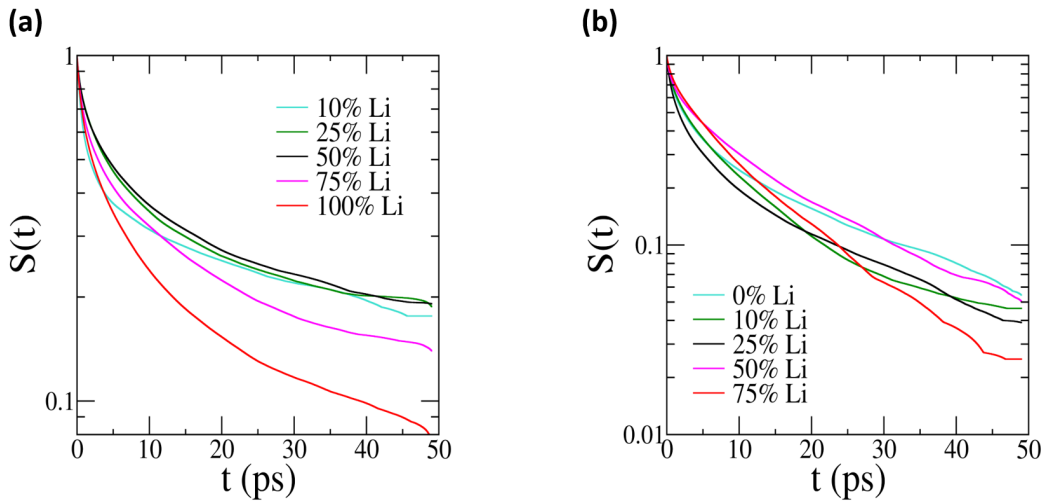

Figure 4C.18: Continuous cage relaxation time correlation function as a function of alkali-ion mixing extent in the 1:1 HCE for (a) Li-ions, and (b) Na-ions.

4C.4 Conclusions

Chapter 4B indicated that Na-ion HCEs are not a viable replacement for Li-ion HCEs due to their very low ionic conductivities. This sub-chapter started with a need for studying mixed cation electrolytes as well as a need to improve the conductivity of Na-ion HCEs. Starting from a pure-Na-ion based HCE, we found that mixing of alkali-ions by replacing a fraction of Na-ions with Li-ions greatly improves the ionic conductivity of the HCE. Replacing 25 % of the Na-ions with Li-ions improves ionic conductivity by close to a factor of two in the 1:1 HCE. Replacing 50 % of the Na-ions by Li-ions improves the ionic conductivity by close to a factor of four. We observed a monotonic improvement in transport properties in going from a purely Na-ion based HCE to a purely Li-ion HCE. We therefore did not observe a mixed-alkali effect [73–75]. Since the replacement of a fraction of Na-ions by Li-ions greatly improved the diffusion coefficients to the FSI anion as well, the mixed-cation technology can be used for dual-ion batteries if electrode materials can be appropriately chosen. Further, we noticed that replacing a fraction of Na-ions by Li-ions had a more pronounced effect in HCEs than LCEs. Furthermore, Li-ions were predicted to carry an increasingly large fraction of the total current the more Li-content there was in the electrolyte. Several analyses were carried out to understand the structure and transport of mixed-cation HCEs. The structural correlation to this observation was found in the fact that Li-ion cage identity was found to be more sensitive to the increase in the Li-ion content in the HCE than the sensitivity of Na-ion cages to the same (towards larger cage relaxation).

In dual-salt/mixed-cation electrolytes, a competition for solvent and anion molecules might be present between the two cations. In such a case, the solvation free energies of Li and Na-ions become important. Further, if HCEs are under consideration, the possibility of cation-pairs (homo-binuclear or hetero-binuclear pairs with sharing ligands) becomes larger. The solvation free energy of these complexes also becomes relevant to understand the propensity of formation of cation-pair clusters in HCEs. Chapter 5 is dedicated to understanding the solvation free energies of cation-pairs complexes of pure and mixed cation HCEs.

Bibliography

[1] Kang Xu. Nonaqueous liquid electrolytes for lithium-based rechargeable batteries. *Chemical Reviews*, 104(10):4303–4418, 2004.

[2] Larry J Krause, William Lamanna, John Summerfield, Mark Engle, Gary Korba, Robert Loch, and Radoslav Atanasoski. Corrosion of aluminum at high voltages in non-aqueous electrolytes containing perfluoroalkylsulfonyl imides; new lithium salts for lithium-ion cells. *Journal of Power Sources*, 68(2):320–325, 1997.

[3] Fusaji Kita, Akira Kawakami, Jin Nie, Takaaki Sonoda, and Hiroshi Kobayashi. On the characteristics of electrolytes with new lithium imide salts. *Journal of Power Sources*, 68(2):307–310, 1997.

[4] Larry A Dominey, Victor R Koch, and Tom J Blakley. Thermally stable lithium salts for polymer electrolytes. *Electrochimica Acta*, 37(9):1551–1554, 1992.

[5] J Barthel, M Wühr, R Buestrich, and HJ Gores. A new class of electrochemically and thermally stable lithium salts for lithium battery electrolytes: I. Synthesis and properties of lithium bis[1,2-benzenediolato(2-)-O,O′]borate. *Journal of the Electrochemical Society*, 142(8):2527, 1995.

[6] Kang Xu, Shengshui Zhang, T Richard Jow, Wu Xu, and C Austen Angell. LiBOB as salt for lithium-ion batteries: A possible solution for high temperature operation. *Electrochemical and Solid-State Letters*, 5(1):A26, 2001.

[7] Yukio Sasaki, Minoru Handa, Satoshi Sekiya, Katsuji Kurashima, and Kyohei Usami. Application to lithium battery electrolyte of lithium chelate compound with boron. *Journal of Power Sources*, 97:561–565, 2001.

[8] Kang Xu, Sheng S Zhang, Unchul Lee, Jan L Allen, and T Richard Jow. LiBOB: Is it an alternative salt for lithium ion chemistry? *Journal of Power Sources*, 146(1-2):79–85, 2005.

[9] Mengqing Xu, Ang Xiao, Weishan Li, and Brett L. Lucht. Investigation of Lithium Tetrafluorooxalatophosphate [$LiPF_4(C_2O_4)$] as a Lithium-Ion Battery Electrolyte for Elevated Temperature Performance. *Journal of The Electrochemical Society*, 157(1):A115, 2010.

[10] Noritoshi Nanbu, Koji Tsuchiya, Takatsugu Shibazaki, and Yukio Sasaki. Lithium Tris[3-fluoro-1,2-benzenediolato(2-)-O,O′] phosphate as a Novel Lithium Salt for Lithium Battery Electrolytes. *Electrochemical and Solid-State Letters*, 5(9):A202, 2002.

[11] Michael Eberwein, A Schmid, M Schmidt, Manfred Zabel, T Burgemeister, Josef Barthel, Werner Kunz, and Heiner J Gores. Synthesis and electrochemical properties of some lithium chelatophosphates. *Journal of the Electrochemical Society*, 150(7):A994, 2003.

[12] M Schmidt, U Heider, A Kuehner, R Oesten, M Jungnitz, N Ignat'ev, and P Sartori. Lithium fluoroalkylphosphates: A new class of conducting salts for electrolytes for high energy lithium-ion batteries. *Journal of Power Sources*, 97:557–560, 2001.

[13] Ziyu Song, Xingxing Wang, Hao Wu, Wenfang Feng, Jin Nie, Hailong Yu, Xuejie Huang, Michel Armand, Heng Zhang, and Zhibin Zhou. Bis(fluorosulfonyl)imide-based electrolyte for rechargeable lithium batteries: A perspective. *Journal of Power Sources Advances*, 14:100088, 2022.

[14] Charl J Jafta, Xiao-Guang Sun, Hailong Lyu, Hao Chen, Bishnu P Thapaliya, William T Heller, Matthew J Cuneo, Richard T Mayes, Mariappan Parans Paranthaman, Sheng Dai, et al. Insight into the solid electrolyte interphase formation in bis (fluorosulfonyl) imide based ionic liquid electrolytes. *Advanced Functional Materials*, 31(23):2008708, 2021.

[15] Karina Asheim, Per Erik Vullum, Nils Peter Wagner, Hanne Flåten Andersen, Jan Petter Mæhlen, and Ann Mari Svensson. Improved electrochemical performance and solid electrolyte interphase properties of electrolytes based on lithium bis (fluorosulfonyl) imide for high content silicon anodes. *RSC advances*, 12(20):12517–12530, 2022.

[16] Michel Armand, Peter Axmann, Dominic Bresser, Mark Copley, Kristina Edström, Christian Ekberg, Dominique Guyomard, Bernard Lestriez, Petr Novák, Martina Petranikova, et al. Lithium-ion batteries–Current state of the art and anticipated developments. *Journal of Power Sources*, 479:228708, 2020.

[17] Hong-Bo Han, Si-Si Zhou, Dai-Jun Zhang, Shao-Wei Feng, Li-Fei Li, Kai Liu, Wen-Fang Feng, Jin Nie, Hong Li, Xue-Jie Huang, et al. Lithium bis(fluorosulfonyl)imide (LiFSI) as conducting salt for nonaqueous liquid electrolytes for lithium-ion batteries: Physicochemical and electrochemical properties. *Journal of Power Sources*, 196(7):3623–3632, 2011.

[18] Jiangfeng Qian, Brian D Adams, Jianming Zheng, Wu Xu, Wesley A Henderson, Jun Wang, Mark E Bowden, Suochang Xu, Jianzhi Hu, and Ji-Guang Zhang. Anode-free rechargeable lithium metal batteries. *Advanced Functional Materials*, 26(39):7094–7102, 2016.

[19] Yuki Yamada, Keizo Furukawa, Keitaro Sodeyama, Keisuke Kikuchi, Makoto Yaegashi, Yoshitaka Tateyama, and Atsuo Yamada. Unusual stability of acetonitrile-based superconcentrated electrolytes for fast-charging lithium-ion batteries. *Journal of the American Chemical Society*, 136(13):5039–5046, 2014.

[20] Xiaodi Ren, Shuru Chen, Hongkyung Lee, Donghai Mei, Mark H Engelhard, Sarah D Burton, Wengao Zhao, Jianming Zheng, Qiuyan Li, and Michael S Ding. Localized high-concentration sulfone electrolytes for high-efficiency lithium-metal batteries. *Chem*, 4(8):1877–1892, 2018.

[21] Masashi Ishikawa, Toshinori Sugimoto, Manabu Kikuta, Eriko Ishiko, and Michiyuki Kono. Pure ionic liquid electrolytes compatible with a graphitized carbon negative

electrode in rechargeable lithium-ion batteries. *Journal of Power Sources*, 162(1):658–662, 2006.

[22] Bertrand Philippe, Rémi Dedryvère Dedryvère, Mihaela Gorgoi, Hakan Rensmo, Danielle Gonbeau, and Kristina Edström. Improved performances of nanosilicon electrodes using the salt LiFSI: a photoelectron spectroscopy study. *Journal of the American Chemical Society*, 135(26):9829–9842, 2013.

[23] Xinpeng Han and Jie Sun. Improved fast-charging performances of phosphorus electrodes using the intrinsically flame-retardant LiFSI based electrolyte. *Journal of Power Sources*, 474:228664, 2020.

[24] Elena Markevich, Gregory Salitra, Ariel Rosenman, Yosef Talyosef, F Chesneau, and Doron Aurbach. The effect of a solid electrolyte interphase on the mechanism of operation of lithium–sulfur batteries. *Journal of Materials Chemistry A*, 3(39):19873–19883, 2015.

[25] Satoshi Uchida and Masashi Ishikawa. Lithium bis(fluorosulfonyl)imide based low ethylene carbonate content electrolyte with unusual solvation state. *Journal of Power Sources*, 359:480–486, 2017.

[26] Kaoru Dokko, Daiki Watanabe, Yosuke Ugata, Morgan L Thomas, Seiji Tsuzuki, Wataru Shinoda, Kei Hashimoto, Kazuhide Ueno, Yasuhiro Umebayashi, and Masayoshi Watanabe. Direct evidence for Li ion hopping conduction in highly concentrated sulfolane-based liquid electrolytes. *The Journal of Physical Chemistry B*, 122(47):10736–10745, 2018.

[27] Yukihiro Okamoto, Seiji Tsuzuki, Ryoichi Tatara, Kazuhide Ueno, Kaoru Dokko, and Masayoshi Watanabe. High transference number of na ion in liquid-state sulfolane solvates of Sodium bis(fluorosulfonyl)amide. *J. Phys. Chem. C*, 124(8):4459–4469, 2020.

[28] Andreia SL Gouveia, Carlos ES Bernardes, Liliana C Tomé, Elena I Lozinskaya, Yakov S Vygodskii, Alexander S Shaplov, José N Canongia Lopes, and Isabel M Marrucho. Ionic liquids with anions based on fluorosulfonyl derivatives: from asymmetrical substitutions to a consistent force field model. *Physical Chemistry Chemical Physics*, 19(43):29617–29624, 2017.

[29] Anirban Mondal and Sundaram Balasubramanian. Quantitative prediction of physical properties of imidazolium based room temperature ionic liquids through determination of condensed phase site charges: A refined force field. *The Journal of Physical Chemistry B*, 118(12):3409–3422, 2014.

[30] Anirban Mondal and Sundaram Balasubramanian. A molecular dynamics study of collective transport properties of imidazolium-based room-temperature ionic liquids. *J. Chem. Eng. Data*, 59(10):3061–3068, 2014.

[31] Jürg Hutter, Marcella Iannuzzi, Florian Schiffmann, and Joost VandeVondele. CP2K: Atomistic simulations of condensed matter systems. *Wiley Interdisciplinary Reviews: Computational Molecular Science*, 4(1):15–25, 2014.

[32] John P Perdew, Kieron Burke, and Matthias Ernzerhof. Generalized gradient approximation made simple. *Phys. Rev. Lett.*, 77(18):3865, 1996.

[33] Stefan Grimme. Semiempirical gga-type density functional constructed with a long-range dispersion correction. *J. Comput. Chem.*, 27(15):1787–1799, 2006.

[34] Stefan Goedecker, Michael Teter, and Jürg Hutter. Separable dual-space gaussian pseudopotentials. *Phys. Rev. B*, 54(3):1703, 1996.

[35] Christian Hartwigsen, Sephen Gœdecker, and Jürg Hutter. Relativistic separable dual-space gaussian pseudopotentials from H to Rn. *Phys. Rev. B*, 58(7):3641, 1998.

[36] Nidia Gabaldon Limas and Thomas A Manz. Introducing DDEC6 atomic population analysis: part 4. efficient parallel computation of net atomic charges, atomic spin moments, bond orders, and more. *RSC Adv.*, 8(5):2678–2707, 2018.

[37] Thomas A Manz and Nidia Gabaldon Limas. Introducing DDEC6 atomic population analysis: Part 1. Charge partitioning theory and methodology. *RSC Advances*, 6(53):47771–47801, 2016.

[38] Leandro Martínez, Ricardo Andrade, Ernesto G Birgin, and José Mario Martínez. Packmol: A package for building initial configurations for molecular dynamics simulations. *Journal of Computational Chemistry*, 30(13):2157–2164, 2009.

[39] Henk Bekker, HJC Berendsen, EJ Dijkstra, S Achterop, R Vondrumen, David VANDERSPOEL, A Sijbers, H Keegstra, and MKR Renardus. Gromacs-a parallel computer for molecular-dynamics simulations. In *4th International Conference on Computational Physics (PC 92)*, pages 252–256. World Scientific Publishing, 1993.

[40] Berk Hess, Henk Bekker, Herman JC Berendsen, and Johannes GEM Fraaije. LINCS: A linear constraint solver for molecular simulations. *J. Comput. Chem.*, 18(12):1463–1472, 1997.

[41] Mark James Abraham, Teemu Murtola, Roland Schulz, Szilárd Páll, Jeremy C Smith, Berk Hess, and Erik Lindahl. GROMACS: High performance molecular simulations through multi-level parallelism from laptops to supercomputers. *SoftwareX*, 1:19–25, 2015.

[42] William Humphrey, Andrew Dalke, and Klaus Schulten. VMD: visual molecular dynamics. *Journal of Molecular Graphics*, 14(1):33–38, 1996.

[43] Olalla G Sas, Gorica R Ivaniš, Mirjana Lj Kijevčanin, Begoña González, Angeles Domínguez, and Ivona R Radovič. Densities and derived volumetric properties of ionic liquids with $[Nf_2]$ and $[NTf_2]$ anions at high pressures *Journal of Chemical & Engineering Data, 63(4):954-964, 2018.*

[44] William M Haynes, David R Lide, and Thomas J Bruno. *CRC Handbook of Chemistry and Physics*. CRC press, 2016.

[45] Naoaki Yabuuchi, Kei Kubota, Mouad Dahbi, and Shinichi Komaba. Research development on sodium-ion batteries. *Chemical Reviews*, 114(23):11636–11682, 2014.

[46] KM Abraham. Prospects and limits of energy storage in batteries. *The Journal of Physical Chemistry Letters*, 6(5):830–844, 2015.

[47] Takayuki Shibata, Wataru Kobayashi, and Yutaka Moritomo. Sodium ion diffusion in layered naxmno2 ($0.49 \leq x \leq 0.75$): Comparison with Na_xCoO_2. *Applied Physics Express*, 7(6):067101, 2014.

[48] KM Abraham. How comparable are sodium-ion batteries to lithium-ion counterparts? *ACS Energy Letters*, 5(11):3544–3547, 2020.

[49] Berk Hess, Carsten Kutzner, David Van Der Spoel, and Erik Lindahl. Gromacs 4: algorithms for highly efficient, load-balanced, and scalable molecular simulation. *Journal of Chemical Theory and Computation*, 4(3):435–447, 2008.

[50] Tom Darden, Darrin York, and Lee Pedersen. Particle Mesh Ewald: An n log (n) method for Ewald sums in large systems. *J. Chem. Phys.*, 98(12):10089–10092, 1993.

[51] Herman JC Berendsen, JPM van Postma, Wilfred F Van Gunsteren, ARHJ DiNola, and Jan R Haak. Molecular dynamics with coupling to an external bath. *The Journal of Chemical Physics*, 81(8):3684–3690, 1984.

[52] Shūichi Nosé. A molecular dynamics method for simulations in the canonical ensemble. *Molecular Physics*, 52(2):255–268, 1984.

[53] Michele Parrinello and Aneesur Rahman. Polymorphic transitions in single crystals: A new molecular dynamics method. *Journal of Applied physics*, 52(12):7182–7190, 1981.

[54] Oleg Borodin, Julian Self, Kristin A Persson, Chunsheng Wang, and Kang Xu. Uncharted waters: Super-concentrated electrolytes. *Joule*, 4(1):69–100, 2020.

[55] F Wohde, M Balabajew, and B Roling. Li^+ Transference Numbers in Liquid Electrolytes Obtained by Very-Low-Frequency Impedance Spectroscopy at Variable Electrode Distances. *Journal of The Electrochemical Society*, 163(5):A714, 2016.

[56] Yang Dong, Shengli Di, Fangbo Zhang, Xu Bian, Yuanyuan Wang, Jianzhong Xu, Liubin Wang, Fangyi Cheng, and Ning Zhang. Nonaqueous electrolyte with dual-cations for high-voltage and long-life zinc batteries. *Journal of Materials Chemistry A*, 8(6):3252–3261, 2020.

[57] Yunpei Zhu, Jun Yin, Xueli Zheng, Abdul-Hamid Emwas, Yongjiu Lei, Omar F Mohammed, Yi Cui, and Husam N Alshareef. Concentrated dual-cation electrolyte strategy for aqueous zinc-ion batteries. *Energy & Environmental Science*, 14(8):4463–4473, 2021.

[58] Yunpei Zhu, Yongjiu Lei, Zhixiong Liu, Youyou Yuan, and Husam N Alshareef. An unconventional full dual-cation battery. *Nano Energy*, 81:105539, 2021.

[59] Mariya Kalapsazova, Hristo Rasheev, Ekaterina Zhecheva, Alia Tadjer, and Radostina Stoyanova. Insights into the function of electrode and electrolyte materials in a hybrid lithium–sodium ion cell. *The Journal of Physical Chemistry C*, 123(18):11508–11521, 2019.

[60] Radostina Stoyanova, Violeta Koleva, and Antonia Stoyanova. Lithium versus mono/polyvalent ion intercalation: Hybrid metal ion systems for energy storage. *The Chemical Record*, 19(2-3):474–501, 2019.

[61] Hu-Rong Yao, Ya You, Ya-Xia Yin, Li-Jun Wan, and Yu-Guo Guo. Rechargeable dual-metal-ion batteries for advanced energy storage. *Physical Chemistry Chemical Physics*, 18(14):9326–9333, 2016.

[62] Svetlana Ivanova, Ekaterina Zhecheva, Rositsa Kukeva, Diana Nihtianova, Lyuben Mihaylov, Genoveva Atanasova, and Radostina Stoyanova. Layered P3-Na_x $Co_{1/3}Ni_{1/3}Mn_{1/3}O_2$ versus Spinel $Li_4Ti_5O_{12}$ as a Positive and a Negative Electrode in a Full Sodium–Lithium Cell. *ACS Applied Materials & Interfaces*, 8(27):17321–17333, 2016.

[63] Chunlei Jiang, Yue Fang, Wenyong Zhang, Xiaohe Song, Jihui Lang, Lei Shi, and Yongbing Tang. A multi-ion strategy towards rechargeable sodium-ion full batteries with high working voltage and rate capability. *Angewandte Chemie*, 130(50):16608–16612, 2018.

[64] Xiao-Tong Xi, Wen-Hao Li, Bao-Hua Hou, Yang Yang, Zhen-Yi Gu, and Xing-Long Wu. Dendrite-free lithium anode enables the lithium//graphite dual-ion battery with much improved cyclic stability. *ACS Applied Energy Materials*, 2(1):201–206, 2018.

[65] Maria Kalapsazova, Gregorio F Ortiz, Jose L Tirado, Oleksandr Dolotko, Ekaterina Zhecheva, Diana Nihtianova, Lyuben Mihaylov, and Radostina Stoyanova. P3-Type layered sodium-deficient nickel–manganese oxides: a flexible structural matrix for reversible sodium and lithium intercalation. *ChemPlusChem*, 80(11):1642–1656, 2015.

[66] M Kalapsazova, R Stoyanova, and E Zhecheva. Structural characterization and electrochemical intercalation of Li^+ in layered $Na_{0.65}Ni_{0.5}Mn_{0.5}O_2$ obtained by freeze-drying method. *Journal of Solid State Electrochemistry*, 18(8):2343–2350, 2014.

[67] M Kalapsazova, R Stoyanova, E Zhecheva, G Tyuliev, and D Nihtianova. Sodium deficient nickel–manganese oxides as intercalation electrodes in lithium ion batteries. *Journal of Materials Chemistry A*, 2(45):19383–19395, 2014.

[68] Maria L Kalapsazova, Ekaterina N Zhecheva, Georgi T Tyuliev, Diana D Nihtianova, Lyuben Mihaylov, and Radostina K Stoyanova. Effects of the Particle Size Distribution and of the Electrolyte Salt on the Intercalation Properties of P 3-$Na_{2/3}Ni_{1/2}Mn_{1/2}O_2$. *The Journal of Physical Chemistry C*, 121(11):5931–5940, 2017.

[69] Qi Li, Yu Qiao, Shaohua Guo, Kezhu Jiang, Qinghao Li, Jinpeng Wu, and Haoshen Zhou. Both cationic and anionic co-(de) intercalation into a metal-oxide material. *Joule*, 2(6):1134–1145, 2018.

[70] Kang Xu. Electrolytes and interphases in Li-ion batteries and beyond. *Chemical Reviews*, 114(23):11503–11618, 2014.

[71] Hui Dong, Yifei Li, Yanliang Liang, Guosheng Li, Cheng-Jun Sun, Yang Ren, Yuhao Lu, and Yan Yao. A magnesium–sodium hybrid battery with high operating voltage. *Chemical Communications*, 52(53):8263–8266, 2016.

[72] Nella M Vargas-Barbosa and Bernhard Roling. Dynamic ion correlations in solid and liquid electrolytes: how do they affect charge and mass transport? *ChemElectroChem*, 7(2):367–385, 2020.

[73] S Balasubramanian and KJ Rao. Preferential paths in alkali ion migration and the mixed alkali effect in silicate glasses. *The Journal of Physical Chemistry*, 97(35):8835–8838, 1993.

[74] S Balasubramanian and KJ Rao. A molecular dynamics study of the mixed alkali effect in silicate glasses. *Journal of Non-Crystalline Solids*, 181(1-2):157–174, 1995.

[75] KJ Rao, S Balasubramanian, and KV Damodaran. A molecular dynamics investigation of the structures and mixed alkali effect in sulfate glasses. *Journal of Solid State Chemistry*, 106(1):174–183, 1993.

Chapter 5

Study of cation pair clusters in high concentration electrolytes

5.1 Introduction

The subject matter of this chapter was motivated from an interesting observation from the classical MD simulations described in Chapter 4B. Therein, we noticed a pre-peak in the Na-Na RDF (at salt:solvent = 1:1), at around 3.5 Å. A similar pre-peak is present in the Na-Na RDF in the high concentration electrolyte (HCE) at salt:solvent = 1:1.5 (Figure 5.1(a)) as well. This pre-peak is much less prominent in the low concentration electrolyte (LCE) of concentration 1:9.57 (Chapter 4B). This pre-peak is located at much smaller radial distances than the expected alkali-alkali RDF first peak distance (peaks centered at 5.5 Å or more). Also, while these peaks are present in the Na-based electrolyte, they seem to be absent in the Li-based electrolyte (Chapter 4B). The presence of a pre-peak in Na-Na RDFs is unprecedented because the presence of Na-ion pairs a short distance apart (say, 3.5 Å), would imply a large Coulombic repulsion between the cations. This made us wonder whether this pre-peak was an artifact of the force field. However, the intensity and prominence of this pre-peak was too large for us to ignore. Whether such a pre-peak was truly present needed to be investigated. In other words, whether a substantial number of Na-Na cation pairs can truly be expected in HCEs required confirmation.

Further, alongside a Na-Na pre-peak, Na-NBT (nitrogen of FSI) and Na-FBT (fluorine of FSI) pre-peaks were also observed and could not be ignored in HCEs (salt:solvent = 1:1, Chapter 4B, and 1:1.5, Figure 5.1(b)-(c)). These observations too required to be first validated and understood. Validation for the presence of such cation pairs forms the first part of this chapter. A study into the characteristics and propensity of formation of such

cation pair complexes forms the second part of this chapter.

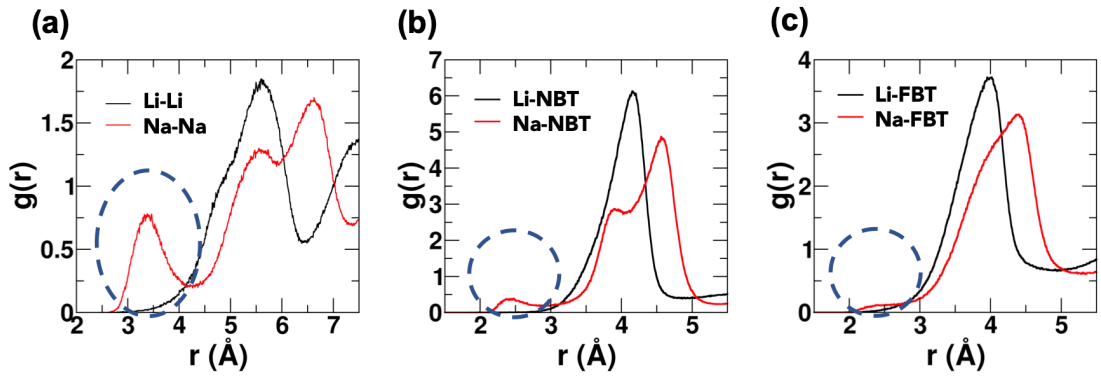

Figure 5.1: Interesting RDFs from classical MD simulations at concentration of salt:solvent = 1:1.5 for the following pairs: (a) alkali-alkali, (b) alkali-NBT (nitrogen of FSI), and (c) alkali-FBT (fluorine of FSI).

The accuracy of classical MD simulations is limited by the force fields being used. Nonetheless, a molecular picture example of a Na-Na cation pair from classical MD simulations carried out at salt:solvent = 1:1.5 is shown in Figure 5.2.

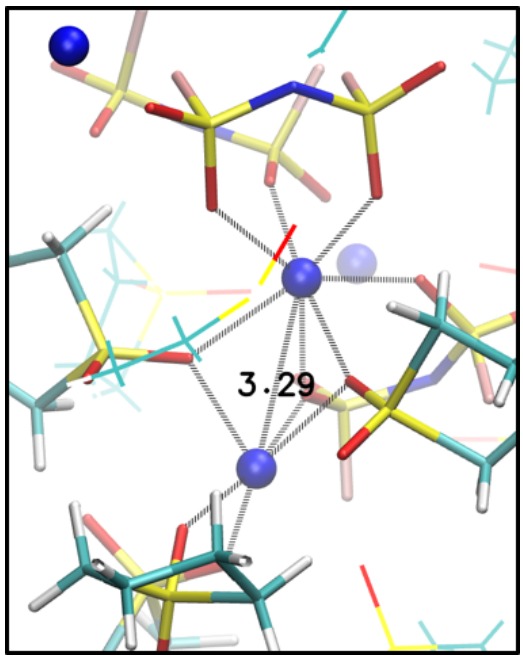

Figure 5.2: Snapshot from classical MD simulations of a Na-Na cation pair for NaFSI in sulfolane HCE at salt:solvent = 1:1.5 concentration. Na ions are shown in blue. Na-Na distance is in Å.

To our delight, some experimental evidences for cation pair complexes were found in literature. For example, Muldoon et al were the first to report an electrochemically

active cation pair complex, $[Mg_2(\mu\text{-}Cl_3\text{-}(THF)_6)]^{2+}$ in a magnesium/sulfur (Mg/S) battery electrolyte [1, 2]. The cation pair complex consists of two Mg ions in octahedral geometry where the three chloride ions serve as shared/bridging ligands and the three THF molecules serve as non-shared ligands [2, 3]. Such bulkly cation complexes along with their counter-anions would diffuse slowly as compared to mono-nuclear/mono-cation complexes. Therefore, these complexes could impair the transport properties of a low salt concentration electrolyte (LCE) where vehicular diffusion is the primary mode of transport of charge. In HCEs however, alkali-ions have the option of hopping out of their cages. A cation pair complex would mean that an alkali-ion also has a nearest neighbour alkali ion site to "hop+diffuse" to (as seen in Chapter 3). Therefore, such cation pair complexes may serve as building blocks of aggregate (AGG) structures [4, 5] or networks [6, 7] proposed for HCEs. These cation pair complexes may then aid alkali-ion transport made possible through the proximity of alkali-ion sites in HCEs. However, investigating the effect of cation pair complex on the transport properties of HCEs (as opposed to LCEs) was beyond the scope of the current thesis but is a question we wish to investigate in the future.

Experimental evidence for the presence of such cation pairs improved our confidence in the observations made from force field based classical MD studies carried out in this thesis. At the same time, the experimental evidence taken together with our observations from classical MD simulations made our definition for cation pairs fairly clear (Figure 5.3).

A cation pair complex can be defined as:

(a) A pair of cations which are located at short distances.

(b) Such pairs most definitely share ligands (solvent molecules or anions) common in their solvation shell. The Coulombic stabilisation these shared ligands bring to the Coulombic repulsion between the cations, makes the formation of these complexes plausible.

(c) The cations of these pairs also coordinate to some ligands they do not share in common with the other cation of the cation pair. These non-shared ligands satisfy the coordination number of the cations involved in the pair.

The cations forming the pair taken together with the shared and non-shared ligands constitute the cation pair complex.

Cation pair complexes have been studied in Ref. 8. However, in the aforementioned study, only solvent containing complexes were considered since the PF_6^- was barely present in the cation's solvation shell [8]. In HCEs, however, anions have a very prominent presence in the cation's solvation shell. Hence, a study of cation pair complexes (when presence is confirmed) containing shared anions is imperative. Furthermore, the FSI anion considered

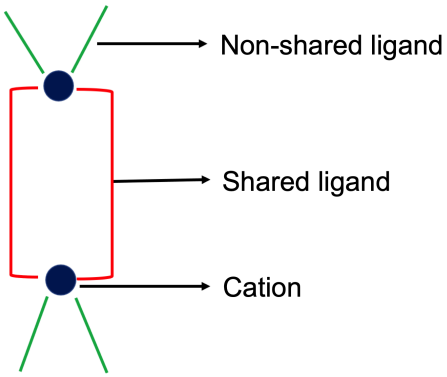

Figure 5.3: A schematic of a cation pair complex.

in this study was rather interesting. It is a non-spherical long anion which can elongate along its length when between the cations of the pair (unlike PF_6^-). Also, there are several donor atoms along the length of FSI (OBT, NBT, and FBT) that could possibly coordinate to the cations. This too made such cation pair complexes worth studying.

5.2 Methodology and Simulation Details

5.2.1 *Ab-initio* molecular dynamics simulations

To confirm if the Na-Na pairs seen in the empirical force field MD trajectories are genuine in HCEs and not artifacts of the force-field we used, we performed *ab-initio* MD simulations (AIMD) of the bulk electrolytes at salt:solvent = 1:1.5 concentration. Li-Li RDFs from classical MD seem to indicate the absence of any short-distance Li-Li pairs. We also investigated whether this is indeed so through AIMD simulations. We report two AIMD runs each for either alkali-ion system.

To perform the AIMD simulations, the procedure followed is as given below:

(a) A cation pair complex was identified from the MD simulation trajectory of Li and Na HCE at salt:solvent=1:1.5. A snapshot corresponding to the distance between the cations being close to the distance (r) of the center of the RDF pre-peak (of Na-Na say) was selected.

The classical MD simulations from which these snapshots were chosen had system details provided in Table 5.1

System and salt:solvent ratio	No. of Li-ions	No. of Na-ions	No. of FSI anions	No. of sulfolane molecules	Density (g/cc)	NPT equilibrated box length (Å)
LiFSI:SUL = 1:1.5	160	0	160	240	1.628	39.16
NaFSI:SUL = 1:1.5	0	160	160	240	1.686	39.24

Table 5.1: System details of the classical MD NVT trajectory from which snapshots were chosen.

(b) All residues belonging to a box approximately 20 Å in size around that cation pair were selected such that charge neutrality of the system was maintained and electrolyte composition was maintained at salt:solvent=1:1.5 as closely as possible. The snapshot carved out for the Li-ion HCE had a concentration of salt:solvent=1:1.5. That for the Na-ion HCE had a concentration of salt:solvent= 1:1.58.

(c) The selected snapshots were subjected to energy minimization, then NVT thermalization at 303 K for 10 ns using Nosé-Hoover thermostat, then NPT equilibration for 100 ns using Nosé-Hoover thermostat and Berendsen barostat, and finally NVT production at 303 K using Nose-Hoover thermostat for 100 ns in the force field used in Chapter 4. Frames at $t = 0$ ns and $t = 100$ ns from the NVT run were chosen for *ab-initio* geometry optimization (AIGO) calculations. The frames at $t = 0$ ns and $t = 100$ ns were chosen at random from either alkali-ion system to start the AIGO calculation. At the end of the classical MD simulations it was seen that one snapshot each for either alkali-ion system had a cation pair and the remaining snapshot of either system did not have a cation pair to start with (Figure 5.4).

The two independent snapshots that were used as starting points for the AIGO (thereafter AIMD simulations) for each alkali-ion system were taken from the same classical MD NVT trajectory spaced out 100 ns in time. Therefore, the two LiFSI in sulfolane AIMD simulations have exactly the same composition, the same number of molecules of each type, and the same density as that of the NPT equilibrated classical MD run the snapshots were taken from. Similarly, the two NaFSI in sulfolane AIMD simulations have exactly the same composition, the same number of molecules of each type, and the same density as that of the NPT equilibrated classical MD run the snapshots were taken from.

The system details of the box from classical MD used for AIGO calculations and thereafter AIMD NVT simulations are given in Table 5.2.

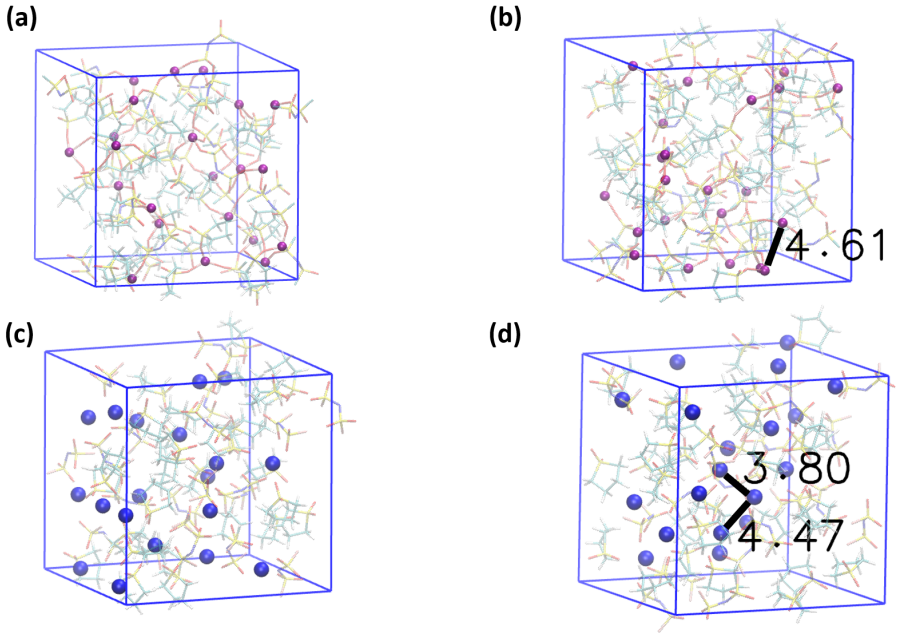

Figure 5.4: The four snapshots used as starting points of AIMD simulations. (a) and (b) are Li-systems. (c) and (d) are Na-systems. Distances marked are in Å.

System	Salt:Solvent	No. of Li^+	No. of Na^+	No. of FSI^-	No. of SUL	Cubic box length (Å)	Density in AIMD simulations (g/cc)	No. of valence electrons
LiFSI in sulfolane trial 1	22:33 = 1:1.5	22	0	22	33	20.20	1.628	2662
LiFSI in sulfolane trial 2	22:33 = 1:1.5	22	0	22	33	20.20	1.628	2662
NaFSI in sulfolane trial 1	19:30 = 1:1.58	0	19	19	30	19.65	1.633	2476
NaFSI in sulfolane trial 2	19:30 = 1:1.58	0	19	19	30	19.65	1.633	2476

Table 5.2: System details for AIGO and AIMD calculations.

(d) The two selected snapshots for the lithium and sodium systems (two each) were then geometry optimized using bulk density functional theory (DFT) calculations.

(e) The *ab-initio* geometry optimized (AIGO) snapshots hence obtained were used as

starting points for our NVT AIMD calculations at 350 K (Figure 5.4). A slightly elevated temperature was used in our AIMD calculations (350 K as opposed to 303 K in our classical MD calculations) for two reasons.

(i) In order to allow the system to sample more configurational space within a short amount of AIMD time. This is important since AIMD calculations for an appreciable system size (Table 5.2) is computationally expensive.

(ii) Cation pairs are more likely to exist and sustain over long durations at the highest salt concentrations investigated in Chapter 4 (salt:solvent=1:1) and at lower temperatures (say 303 K). If signatures for the presence of cation pairs are confirmed at a slightly more dilute HCE than salt:solvent=1:1, i.e, 1:1.5, here, and at a higher temperature (350 K here), the presence of these cation pairs can be undoubtedly expected in higher concentration electrolytes at a lower temperature.

Details of *ab-initio* calculations

The snapshots chosen from classical MD were DFT optimized using CP2K software [9] (version 7.1) with the Perdew, Burke, and Ernzerhof (PBE) exchange-correlation functional [10], and Grimme's D3 empirical van der Waals corrections [11]. Valence electrons were represented by short ranged, double-ζ valence polarized basis set, viz., DZVP-MOLOPT-SR-GTH, with an energy cutoff of 500 Ry. The core electrons and nuclei were accounted for using the Geodecker-Teter-Hutter pseudopotentials [12, 13]. A convergence criterion of 10^{-7} a.u. for the gradient of electronic wave functions was used. These details are common to the the geometry optimization and AIMD calculations. The system details for AIMD calculations were given in Table 5.2.

In addition, for the AIMD NVT simulations, a timestep of 0.5 fs was used to generate a trajectory of 52 ps. Temperature was controlled at 350 K using a canonical sampling through velocity rescaling (CSVR) type of thermostat [14].

5.2.2 Quantum cation pair cluster calculations

Cation pair complexes/clusters were built in the Gaussview software (version 5.0) [15] and optimized using the Gaussian 16 software [16]. The number of ligands shared between the two alkali ions were varied. Ligands are either solvent molecules or anions. In this case, the solvent is sulfolane, and the anion is FSI. The shared ligands were placed roughly

symmetrically between the two alkali-ions. For larger number of shared ligands, multiple initial configurations were used to confirm trends.

Optimizations were performed in gas-phase with frequency calculations. In all reported optimized structures, it was ensured that no imaginary frequencies were found. The level of theory and basis set used for the calculations was B3LYP/6-31g(d,p) [17, 18]. The Grimme's dispersion (D3) correction was employed [19]. Basis set superposition error in the Gibbs free energy was also corrected for using the Boys and Bernardi method [20]. For each calculation, the following two quantities were calculated: (i) Gibbs free energy of formation or solvation, and (ii) inter-alkali ion distance.

5.3 Results and Discussions

5.3.1 Results from AIMD simulations

AIMD simulations show that a pre-peak corresponding to Li-Li cation pairs do exist as was not apparent from the force field used in Chapter 4 or in Figure 5.1(a). The force field used was unable to capture this. From AIMD, it is clear that the pre-peak corresponding to Li-Li cation pairs occurs at distances smaller than that of Na-Na cation pairs, as one would expect considering the smaller size and tighter solvation shell of Li-ions compared to Na-ions (Figures 5.5(a) and (b)).

As we know, alkali cation pairs are able to stay intact for some period of time, only because the repulsive force between them (two positive charges at short distance), is compensated amply by the sharing of solvent molecules and anions between them. Since Na-ions have a looser and larger solvation shell than Li-ions, this would possibly allow for more conformations of the shared anions while maintaining the Na cation complex (Na-ions+shared ligands) intact. This thereby should increase the propensity of formation of Na-cation pairs as opposed to Li-cation pairs from an entropic standpoint. This is reflected in the larger pre-peak in the RDF of Na-Na as compared to that of Li-Li whether in AIMD or in the force field (Li-Li pre-peak in the force field is not present) (Figures 5.5(a) and (b)). The RDF peak postions of alkali-OBT, and the pre-peak positions of alkali-NBT or alkali-FBT are comparable (Figure 5.5 (c)-(h)).

From Chapter 4B, we know that Li and Na-ions are primarily surrounded by OBT (oxygen of FSI) and OFO (oxygen of sulfolane) in their first solvation shell. This is true for

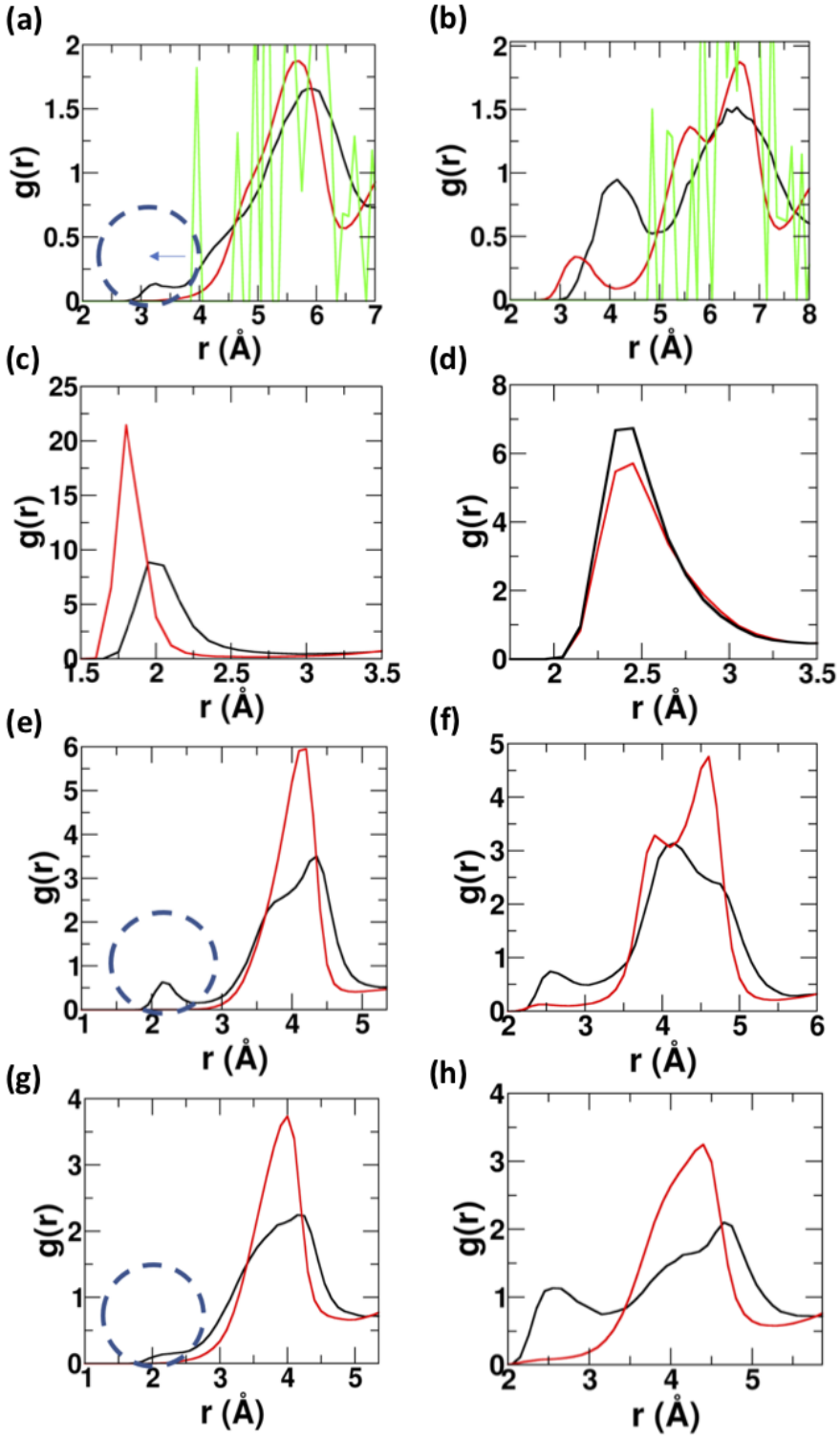

Figure 5.5: RDFs obtained from AIMD and force-field based simulations in Li and Na salt:solvent=1:1.5 HCE for select ion-pairs: (a) Li-Li, (b) Na-Na, (c) Li-OBT, (d) Na-OBT, (e) Li-NBT, (f) Na-NBT, (g) Li-FBT, (h) Na-FBT. Black - AIMD. Red- Force field. Green - single frame RDF for *ab-initio* geometry optimized frame. Other RDFs averaged over both AIMD runs for each system.

alkali-ions that are a part of cation pair complexes as well. Figure 5.5(c) and (d) shows the RDFs for Li-OBT and Na-OBT pairs, respectively. However, some cation pairs interact with atoms of FSI which are otherwise not the primary coordinating atoms of the ligand. The comparable first peak distance of alkali-OBT (Figure 5.5 (c) and (d)) with the pre-peaks seen in alkali-NBT or alkali-FBT (Figures 5.5(e)-(f) and (g)-(h)) in AIMD simulations confirm that alkali ions of some cation pairs can have a weak interaction with nitrogen (NBT) and fluorine (FBT) atoms of FSI in addition to that with OBT.

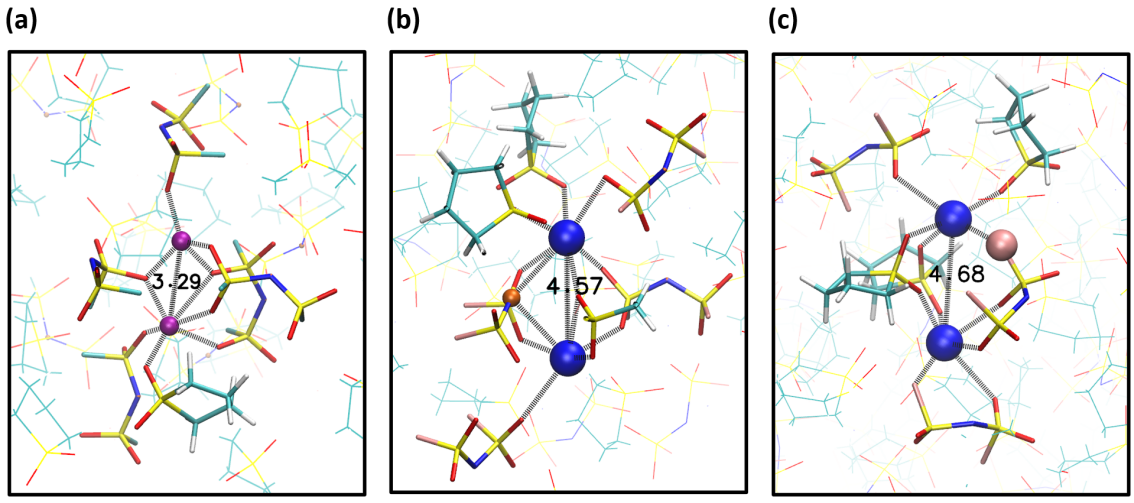

Figure 5.6: Representative snapshots from AIMD simulations. (a) Li-Li cation pair with shared ligands (3 anions here). The two Li-ions are also surrounded by ligands they do not share in common. (b) Na-Na cation pair where the nitrogen atom (orange atom) of the shared FSI anion is also involved in coordinating to both Na-ions. (c) Na-Na cation pair where the fluorine atom (light pink atom) of a shared FSI anion is involved in coordinating with one of the Na-ions. Distances marked are in Å.

We found that the insights gleaned from the RDFs obtained from AIMD simulations are corroborated well with what we found from visualizing several AIMD configurations. Figure 5.6(a) is an example of a Li-Li cation pair extracted from AIMD simulations. This pair has three shared anions. Figure 5.6(b) is an example of a snapshot from AIMD simulations where a nitrogen atom of a shared FSI is involved in coordination with both Na-ions of the cation pair. Figure 5.6(c) is an example of a cation pair where a fluorine atom of a shared FSI is involved in coordination in place of OBT. The fluorine atom, however, is seen to coordinate only with one of the Na-ions in this snapshot.

In order to understand further from AIMD simulations, we examined the number of cation pairs present in the HCEs as a function of AIMD simulation time (Figure 5.7). The cut-off distance within which two Li-ions were termed a cation pair was chosen to be 3.8 Å.

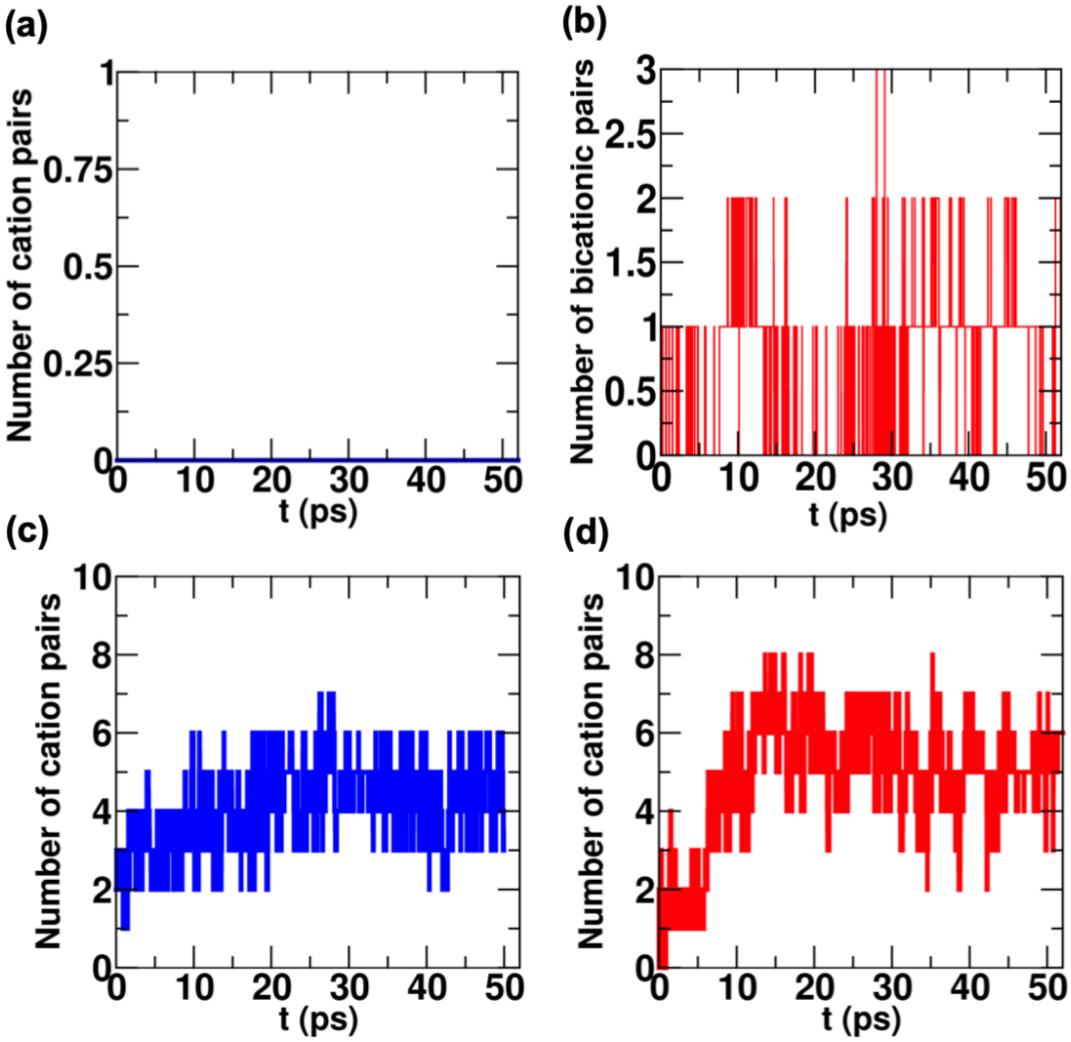

Figure 5.7: Number of cation pairs as a function of AIMD simulation time for two independent trials of either alkali-ion HCE. (a) and (b) LiFSI in sulfolane at salt:solvent=1:1.5. (c) and (d) NaFSI in sulfolane at salt:solvent=1:1.58. The cut-off distance within which two Li-ions were termed a cation pair was chosen to be 3.8 Å. The cut-off distance within which two Na-ions were termed a cation pair was chosen to be 4.8 Å.

The cut-off distance within which two Na-ions were termed a cation pair was chosen to be 4.8 Å. The position of the alkali-alkali minimum after the pre-peak was considered to be cut-off distance (Figure 5.5 (a) and (b)). The average number of cation pairs (after equilibration) from the two independent runs of LiFSI in sulfolane (1:1.5) shown in Figure 5.7(a) and (b) are 0 and 0.75, respectively. These numbers for the two independent runs of NaFSI in sulfolane (1:1.58) are 4.44 and 5.4, respectively.

Based on these, the following points are to be noted:

(a) Average number of short distance Li-ion pairs can be non-zero in contrast to what one may have falsely concluded from force field based classical MD simulations alone. Although one independent run of LiFSI in sulfolane shows no cation pair, we know that Li-cation pairs exist for two reasons. First, the independent run-averaged Li-Li RDF obtained from AIMD shows a pre-peak (Figure 5.5(a)). Second, the independent run in which a pre-existing cation pair (Figure 5.7 (b)) already existed, persists through the AIMD simulation.

(b) From the average number of cation pairs formed, we inferred that Na-ions have a larger propensity of formation of cation pairs than Li-ions. This may be expected since Na-ions have a larger solvation shell radius than those of Li-ions. This allows first shell members of Na-ions to be farther from Na-ions than in the case of Li-ions. Therefore, Na-ions while still staying slightly farther apart from each other than Li-ions can form cation pairs with shared ligands in between them. Na-Na pairs being further apart, also reduce the inter-alkali and inter-shared ligand repulsion more than corresponding Li-Li pairs. In the former case, the shared ligands have a larger volume over which they may arrange themselves spatially to minimize repulsion.

A more concrete and detailed study of the various kinds of cation clusters that can form is better studied through quantum chemical calculations rather than those from MD simulations. To this end, we perform quantum calculations of cation clusters as described in the methods section.

5.3.2 Quantum chemical calculations on cation pairs in gas phase

Solvation energy of cation complex formation and inter alkali-ion distance

Quantum chemical geometry optimization and frequency calculations were conducted. This allowed us to analyse the optimized geometry, calculate the free energy of formation of

various clusters, as well as look at inter-alkali ions distances in the geometry optimized cluster. Details of the level of theory has been specified in the "Methodology and Simulation Details" section.

Three sets of quantum chemical cluster calculations were carried out:

(i) Clusters with shared solvent molecules alone. Here, the number of shared solvent molecules was varied between one and four.

(ii) Clusters with shared anions alone. Here, the number of shared anions was varied between one and four.

(iii) Clusters with solvent molecules and anions. Here, the number of solvent molecules and anions were varied such that the total number of shared ligands remained four.

For every cation complex/cluster calculation carried out, three alkali-ion pair types were considered, viz., Li-Li, Li-Na, and Na-Na.

The initial and geometry optimized cation complex geometries for some representative cluster calculations for only solvent, only anion, and for a combination of solvent molecules and anions are shown in Figures 5.11, 5.12 and 5.13, respectively.

The free energy of solvation/formation of these complexes are calculated as:

$$\begin{aligned}\Delta G_{sol} = G(M_{\alpha}^{p+}M_{\beta}^{q+}(SUL)_x(FSI)_{n-x}) - G(M_{\alpha}^{p+}) \\ - G(M_{\beta}^{q+}) - xG(SUL) - (n-x)G(FSI)\end{aligned} \tag{5.1}$$

ΔG_{sol} is the free-energy of solvation or the free energy of formation of the cation complex. M_{α} and M_{β} are metal ions that form the cation complex of charge p^+ and q^+, respectively. SUL is the solvent molecule. FSI is the bis(fluorosulfonyl)imide anion. n is the number of ligands present in the cation complex. $G(M_{\alpha}^{p+}M_{\beta}^{q+}(SUL)_x(FSI)_{n-x})$ is the free energy of the cation complex. The free energy of the individual components are subtracted from this quantity.

The free energy of solvation/formation and the inter cation distance for the three sets of cation complexes are tabulated in Tables 5.3, 5.4 and 5.5.

The observations and inferences made from these calculations were the following:

(a) With increase in number of shared solvent molecules and anions (ligands), the free energy of solvation becomes more negative and the complex becomes more stabilized (Tables 5.3 and 5.4) (Figures 5.11, 5.12 and 5.13 are structures of representative complexes). In general, the larger the number of shared ligands, greater is the reduction in the repulsion between cations, and more stabilized is the cation complex.

(b) However, when the number of shared ligands is high, the ligands have steric and Coulombic repulsion (in the case of anions) between each other. When the inter-ligand repulsion partially overshadows the stabilization rendered to the cation complex, a non-monotonicity is seen in the trend of ΔG_{solv} (Figures 5.8 (a) and (c)).

(c) The inter-anion repulsion of a (no.of solvents, no. of anions) = (0,4) complex can be reduced by exchanging one of the anions with a solvent molecule (Figure 5.9). Amongst $n = 4$ complexes, there exists a non-monotonicity in free energy. A combination of (no. of solvents, no. of anions) for which the free-energy of formation is most negative, is (1,3) (Figure 5.9). Three initial configurations were used as starting points for the geometry optimization and frequency calculations. Each data point of Figure 5.9 corresponds to the free energy of solvation of the configuration yielding the most negative free energy of formation.

The non-monotonicity in Figures 5.8(c) and (d) was also confirmed in the same manner. Starting from three initial configurations each for (0,3) and (0,4), the configuration of minimum optimized energy was used for calculation of ΔG_{sol} and inter-alkali distance.

(d) With increase in the number of shared ligands, the inter alkali distance decreases. Inter alkali distances for some cation complexes are shown in Tables 5.3 and 5.4, and in Figures 5.8(b) and (d).

When the inter-ligand repulsion partially overshadows the stabilization rendered to the cation complex, a non-monotonicity is seen in the trend of inter-cation distances.

(e) The free energy of solvation for anion containing complex is more negative than for that of solvent containing complex for the same number of shared ligands (solvent or anion) (Figure 5.8).

(f) The inter alkali distance for anion containing complex is shorter than a solvent containing complex for the same number of shared ligands (solvent or anion) (Figures 5.8(b) and (d)).

This is to be expected since anions, being negatively charged, counter the Coulombic repulsion of cations more than solvent molecules are able to. This leads to greater stabilisation of anion containing complexes. The superior stabilisation of anion complexes over solvent complexes is maintained despite allowing for the cations to come closer together.

(g) A more negative value for the free energy of formation of a cation pair complex indicates greater stabilisation of that complex. However, a more negative value for the free energy of formation does not imply a larger propensity of formation of such a

complex. For example, Table 5.4 indicates that the ΔG_{sol} of a Li-Li cation complex is more negative than that for Li-Na complex, which in turn is more negative than that of a Na-Na complex of the same number of shared anions. However, the propensity of formation of a cation pair complex is dictated by the excess stabilisation of the cation pair complex over the two mono-cation complexes taken together ($\Delta G_{sol,bi-cation}$ - $\sum \Delta G_{sol,mono-cation}$) and not the free energy of formation of the cation-pair complex just by itself. $\Delta G_{sol,mono}$ is the free energy of formation of the mono-cation/nuclear complexes from its constituents. For example, for two shared anion cation pair complexes, $\Delta G_{sol,bi-cation}$ - $\sum \Delta G_{sol,mono-cation}$ is more negative for Na-Na complex than that of Li-Li complex (Figure 5.10). This implies that the Na-Na two anion complex has a higher propensity of formation than the Li-Li two anion complex even though ΔG_{solv} of Na-Na (two anion complex) is less negative than the Li-Li (two anion complex) (Table 5.4). A higher propensity of formation of Na-Na complexes as compared to Li-Li complexes was seen from AIMD simulations (Figure 5.5 and 5.7). Na-ions have a larger solvation shell. Therefore, Na-ions are able to stay further apart than Li-ions whilst still being a part of a cation pair complex. First, this reduces the Na-Na repulsion to some extent. Second, a larger coordination number of Na-ions as compared to Li-ions implies the possibility of a larger number of shared ligands in Na-Na cation pair complexes than Li-. Larger number of shared ligands connecting a pair of Na-ions spaced further than Li-ions makes Na-Na cation pair complexes more probable than Li-Li cation pair complexes.

(h) Lastly, generally, we found that the bi-cation heteronuclear complexes (Li-Na) have solvation free energies of formation, inter-cation distance, and propensity of formation, intermediate to those of the bi-cation homonuclear complexes (Li-Li and Na-Na).

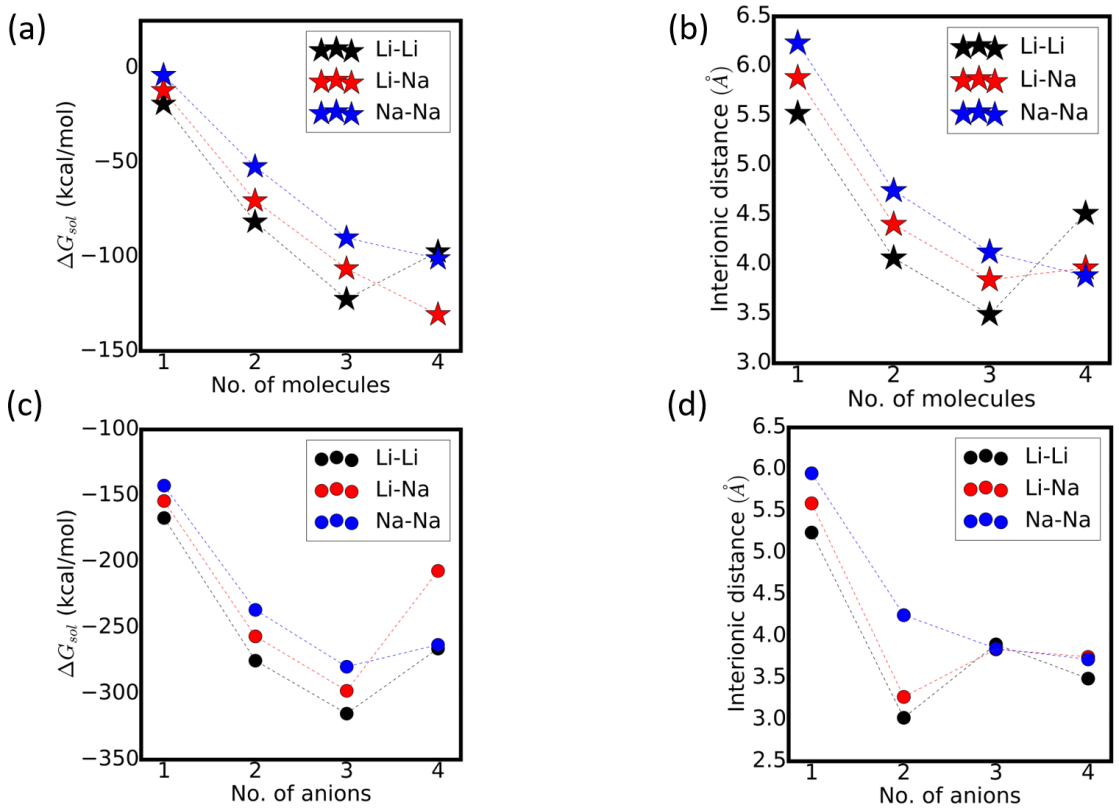

Figure 5.8: (a) Free energy of solvation and (b) inter-alkali distance for complexes as a function of number of solvent (sulfolane) molecules. (c) Free energy of solvation and (d) inter alkali distance for complexes as a function of number of anion (FSI) molecules.

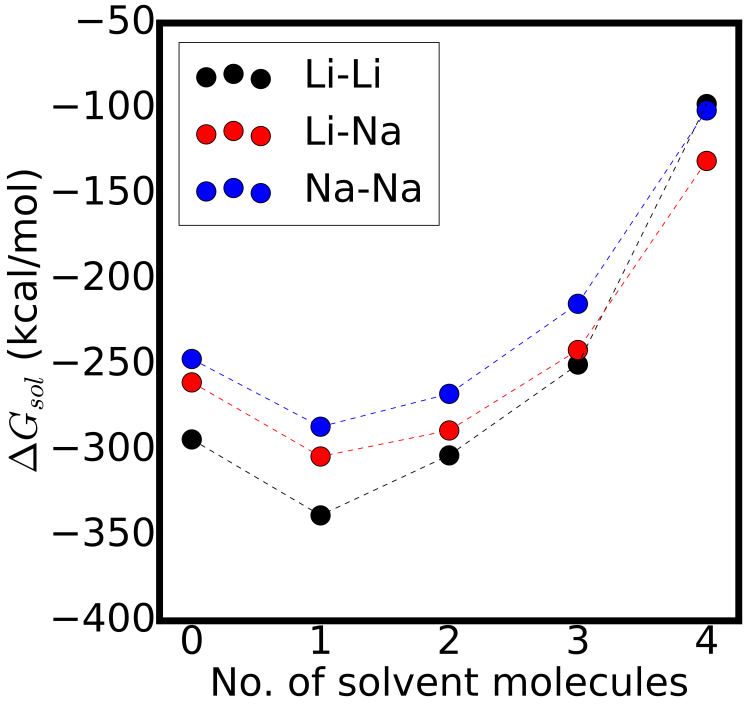

Figure 5.9: The free energy of solvation of all cation pair complexes containing a total of four ligands which can either be solvent molecules or anions.

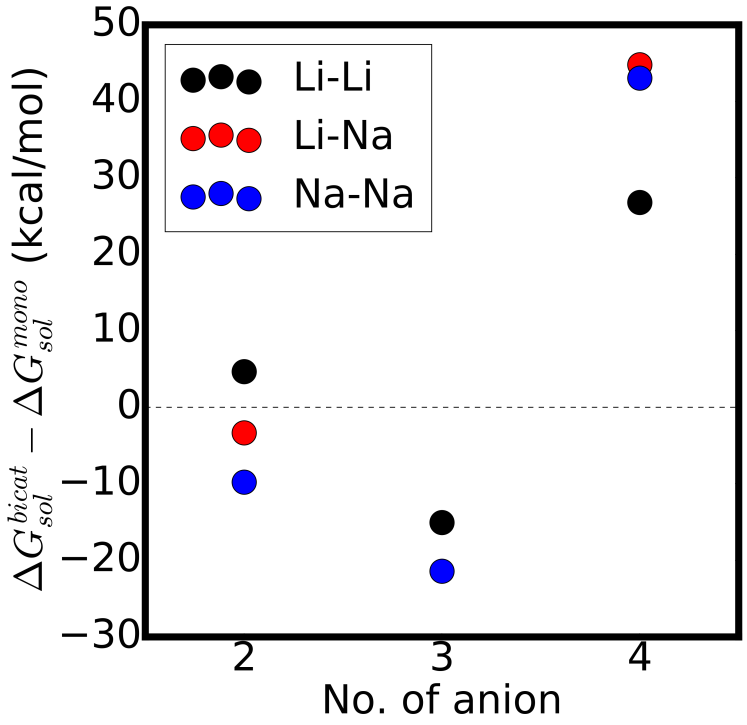

Figure 5.10: Difference between the free energy of formation/solvation of cation pair or bi-nuclear complexes and the mono-cation or mono-nuclear complexes.

No. of solvent	Li-Li		Li-Na		Na-Na	
	ΔG_{sol} kcal/mol	Distance Å	ΔG_{sol} kcal/mol	Distance Å	ΔG_{sol} kcal/mol	Distance Å
1	-19.21	5.52	-12.06	5.88	-3.96	6.23
2	-81.69	4.06	-70.44	4.40	-52.34	4.74
3	-122.64	3.49	-106.48	3.84	-90.12	4.12
4	-97.44	4.51	-130.76	3.96	-101.14	3.88

Table 5.3: Free energy of solvation, ΔG_{sol} and inter-cation distance as a function of number of sulfolane molecules. All the solvent molecules are shared between the alkali-ions.

No. of anions	Li-Li		Li-Na		Na-Na	
	ΔG_{sol} kcal/mol	Distance Å	ΔG_{sol} kcal/mol	Distance Å	ΔG_{sol} kcal/mol	Distance Å
1	-167.08	5.24	-154.23	5.59	-142.56	5.95
2	-275.11	3.02	-256.69	3.27	-236.70	4.25
3	-315.23	3.90	-297.92	3.84	-279.74	3.85
4	-293.79	3.49	-260.38	3.75	-246.71	3.72

Table 5.4: Free energy of solvation, ΔG_{sol} and inter-cation distance as a function of number of FSI anions. All the anions are shared between the alkali-ions.

No. of (solvent,anion)	Li-Li		Li-Na		Na-Na	
	ΔG_{sol} kcal/mol	Distance Å	ΔG_{sol} kcal/mol	Distance Å	ΔG_{sol} kcal/mol	Distance Å
(4,0)	-97.44	4.51	-130.75	3.96	-101.14	3.88
(3,1)	-249.97	3.65	-241.48	3.67	-214.37	3.91
(2,2)	-303.10	3.96	-288.56	4.08	-267.14	4.02
(1,3)	-463.86	3.66	-303.82	3.46	-286.37	3,72
(0,4)	-293.79	3.49	-260.38	3.75	-246.71	3.72

Table 5.5: Free energy of solvation, ΔG_{sol} and inter-cation distance as a function of number of solvent and FSI anions. All combinations of ligands which sum to four were considered.

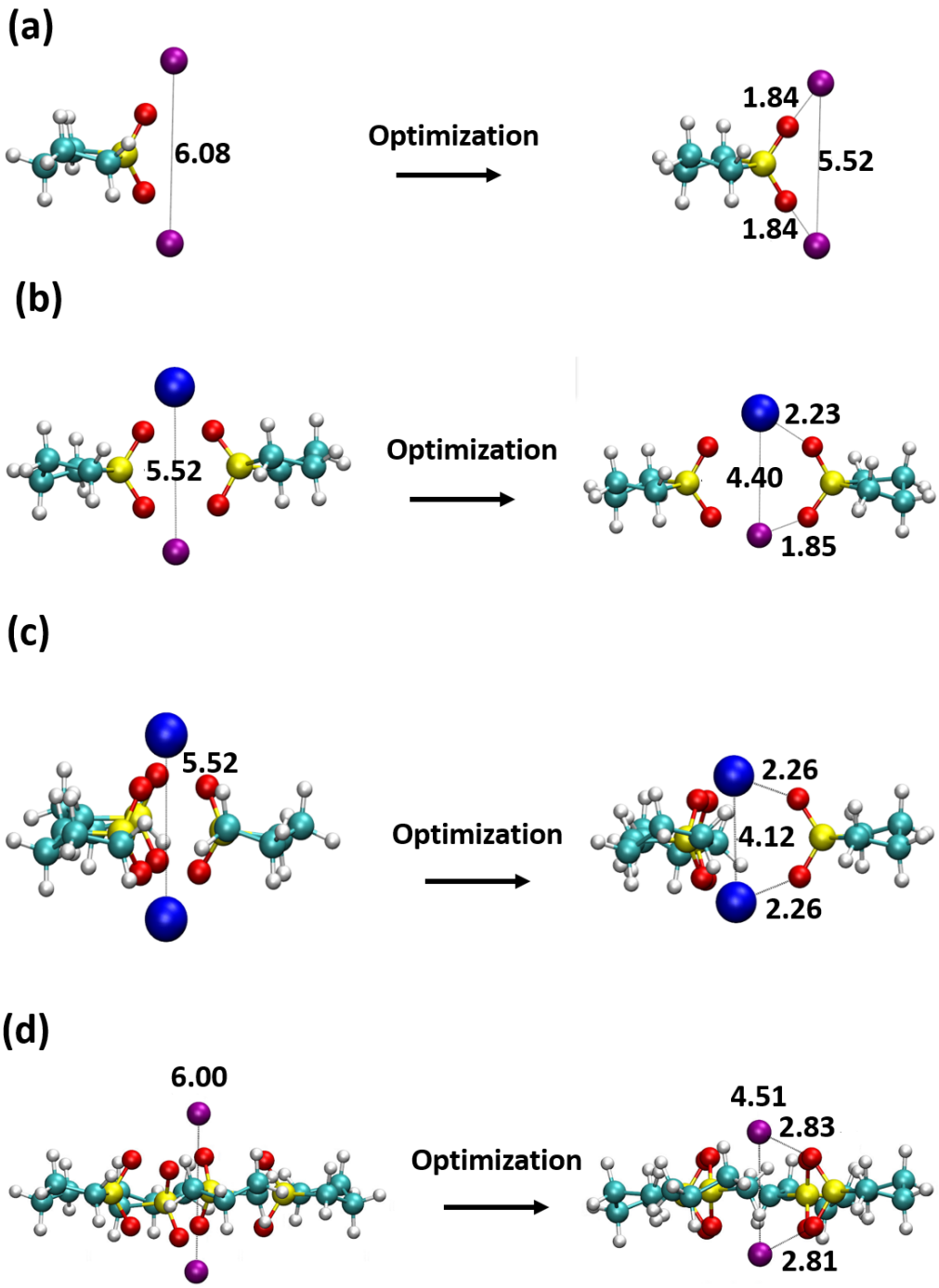

Figure 5.11: The initial and geometry optimized configurations of cation pair complexes containing different number of solvent (sulfolane) molecules as ligands: (a) one sulfolane in Li-Li complex, (b) two sulfolanes in Li-Na complex, (c) three sulfolane in Na-Na complex, and (d) four sulfolane in Li-Li complex. Purple - Li-ion, blue - Na-ion, red - oxygen, cyan - carbon, yellow - sulfur, and white - hydrogen. Representative distances marked in Å units. Configurations shown are the ones for that initial-final configuration pair which yielded the most negative energy for the optimised configuration.

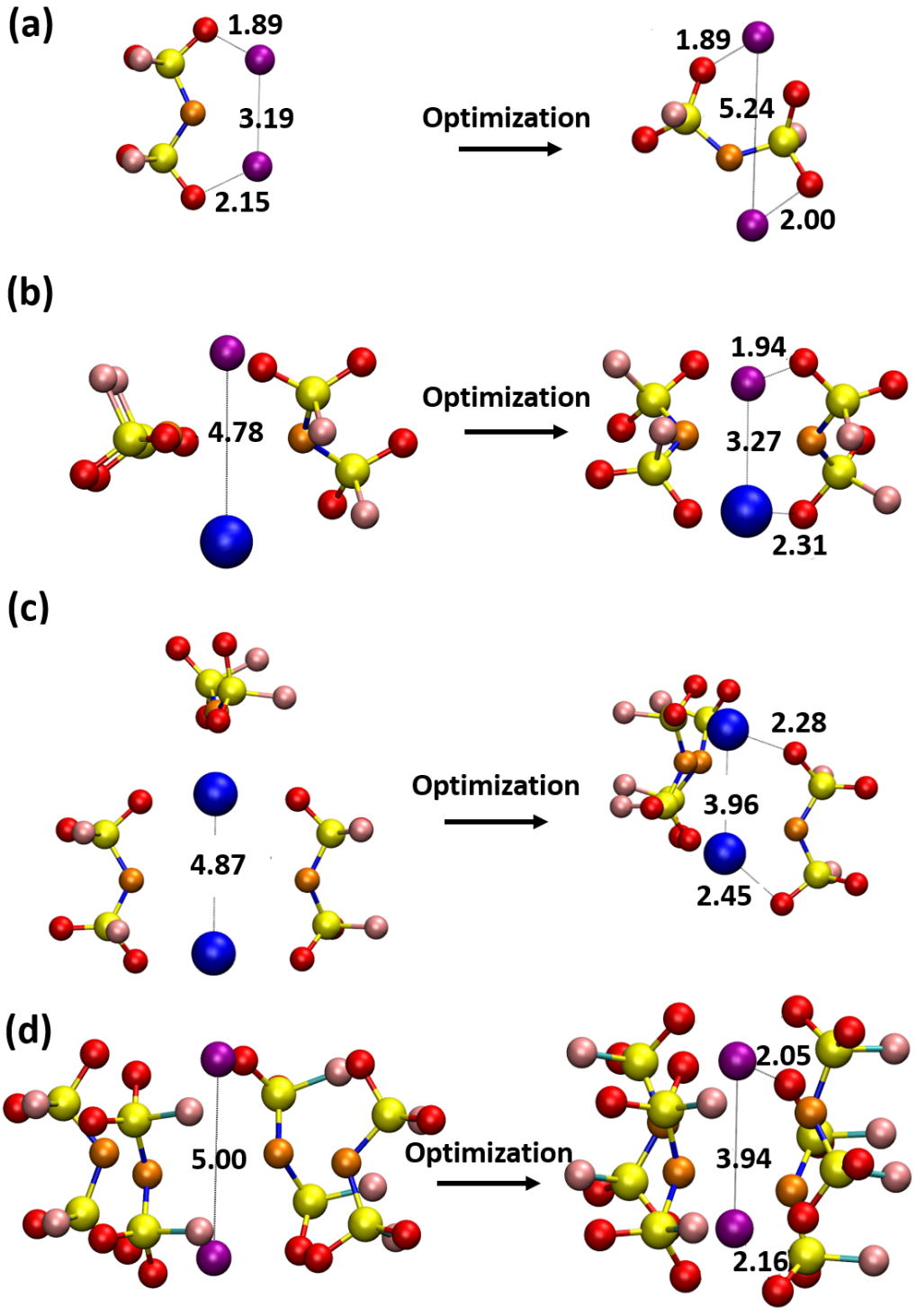

Figure 5.12: The initial and geometry optimized configurations of cation pair complexes containing different number of anions (FSI) as ligands: (a) one anion in Li-Li complex, (b) two anions in Li-Na complex, (c) three anions in Na-Na complex, and (d) four anions in Li-Li complex. Purple - Li-ion, blue - Na-ion, red - oxygen, yellow - sulfur, pink - fluorine, and orange - nitrogen. Representative distances marked in Å units. Configurations shown are the ones for that initial-final configuration pair which yielded the most negative energy for the optimised configuration.

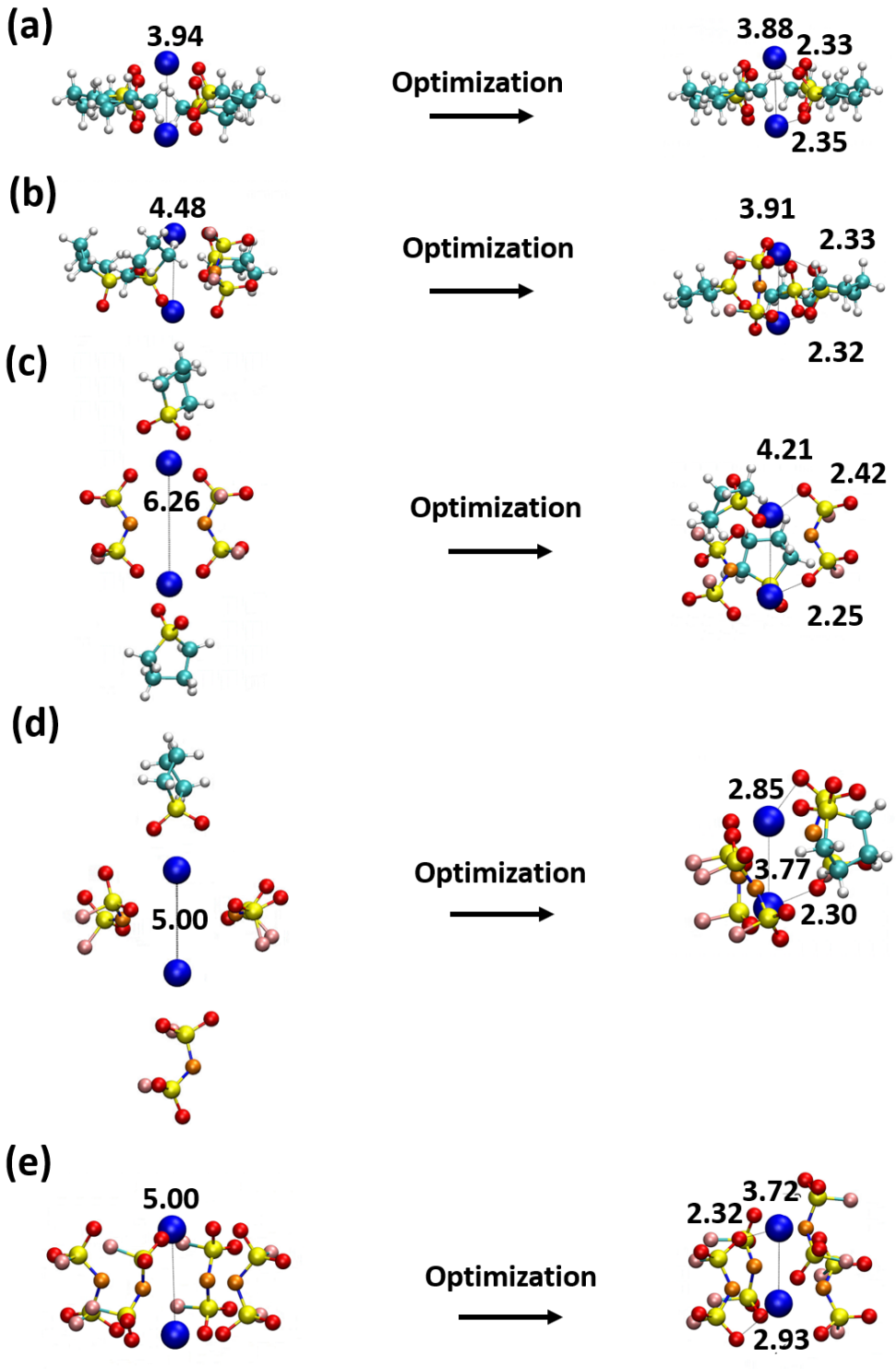

Figure 5.13: The initial and geometry optimized configurations of all Na-Na complexes containing solvent molecules and/or anions such that they have total of four ligands. The (No. of SUL, No. of FSI) Na-Na complexes investigated are (a) (4,0), (b) (3,1), (c) (2,2), (d) (1,3), and (e) (0,4). Blue - Na-ion, red - oxygen, yellow - sulfur, cyan - carbon, white - hydrogen, pink - fluorine, and orange - nitrogen. Representative distances marked in Å units. Configurations shown are the ones for that initial-final configuration pair which yielded the most negative energy for the optimised configuration.

5.4 Conclusions

In this chapter, to the best of our knowledge, the first evidence for the existence of stable cation pairs in HCEs through classical MD was reported. The presence of these cation pair complexes was confirmed through AIMD simulations. Na-Na cation pairs were easily predicted from the RDFs of classical MD. While the RDFs obtained from the force field based classical MD simulations did not show any appreciable signatures for Li-Li cation pairs, AIMD simulations confirm the presence of both Li-Li and Na-Na cation complexes. Atoms of FSI anions such as nitrogen and fluorine which are not commonly found to coordinate with alkali-ions in monoculear (mono-cation) complexes were seen to coordinate with alkali-ions in some cation complexes considered. The Li-NBT (nitrogen of FSI) and Li-FBT (fluorine of FSI) associations in cation complexes were also seen in RDFs from AIMD simulations. Hence, more subtle structural features need to be confirmed through AIMD simulations. Force field based classical MD simulations alone cannot be relied upon. Furthermore, quantum gas phase calculations of cation complex clusters revealed that anion containing clusters in general have more negative free energy of solvation and shorter inter-alkali distances. However, when the number of shared anions became too large (four, say), the inter-anion repulsion of four closely spaced negatively charged anions destabilised the cation complex partially. It was found that replacing one out of four anions with one solvent molecule improved the stability of the complex by reducing inter-ligand repulsion. Through our studies, we were able to both confirm the presence of cation complexes in HCEs and characterize properties of a range of investigated cation complexes. The effect of presence of cation complexes on alkali-ion hopping and diffusion and thereby the transport properties of HCEs are interesting questions we wish to address in the future. Furthermore, the extent to which such cation complexes extend in space or aggregate together in an HCE (as opposed to their detrimental presence in LCEs) can make for another riveting study.

Bibliography

[1] Hee Soo Kim, Timothy S Arthur, Gary D Allred, Jaroslav Zajicek, John G Newman, Alexander E Rodnyansky, Allen G Oliver, William C Boggess, and John Muldoon. Structure and compatibility of a magnesium electrolyte with a sulphur cathode. *Nature Communications*, 2(1):1–6, 2011.

[2] John Muldoon, Claudiu B Bucur, Allen G Oliver, Tsuyoshi Sugimoto, Masaki Matsui, Hee Soo Kim, Gary D Allred, Jaroslav Zajicek, and Yukinari Kotani. Electrolyte roadblocks to a magnesium rechargeable battery. *Energy & Environmental Science*, 5(3):5941–5950, 2012.

[3] Wanfei Li, Shuang Cheng, Jian Wang, Yongcai Qiu, Zhaozhao Zheng, Hongzhen Lin, Sanjay Nanda, Qian Ma, Yan Xu, Fangmin Ye, Meinan Liu, Lisha Zhou, and Yuegang Zhang. Synthesis, Crystal Structure, and Electrochemical Properties of a Simple Magnesium Electrolyte for Magnesium/Sulfur Batteries. *Angewandte Chemie International Edition*, 55(22):6406–6410, 2016.

[4] Jiangtao Hu, Yuchen Ji, Guorui Zheng, Weiyuan Huang, Yuan Lin, Luyi Yang, and Feng Pan. Influence of electrolyte structural evolution on battery applications: Cationic aggregation from dilute to high concentration. *Aggregate*, 3(1):e153, 2022.

[5] Zhou Yu, Nitash P Balsara, Oleg Borodin, Andrew A Gewirth, Nathan T Hahn, Edward J Maginn, Kristin A Persson, Venkat Srinivasan, Michael F Toney, Kang Xu, et al. Beyond local solvation structure: nanometric aggregates in battery electrolytes and their effect on electrolyte properties. *ACS Energy Letters*, 7(1):461–470, 2021.

[6] Fangfang Chen and Maria Forsyth. Elucidation of transport mechanism and enhanced alkali ion transference numbers in mixed alkali metal–organic ionic molten salts. *Physical Chemistry Chemical Physics*, 18(28):19336–19344, 2016.

[7] Michael McEldrew, Zachary AH Goodwin, Sheng Bi, Alexei A Kornyshev, and Martin Z Bazant. Ion clusters and networks in water-in-salt electrolytes. *Journal of The Electrochemical Society*, 168(5):050514, 2021.

[8] Hristo Rasheev, Radostina Stoyanova, and Alia Tadjer. Dual-Metal Electrolytes for Hybrid-Ion Batteries: Synergism or Antagonism? *ChemPhysChem*, 22(11):1110–1123, 2021.

[9] Jürg Hutter, Marcella Iannuzzi, Florian Schiffmann, and Joost VandeVondele. CP2K: Atomistic simulations of condensed matter systems. *Wiley Interdisciplinary Reviews: Computational Molecular Science*, 4(1):15–25, 2014.

[10] John P Perdew, Kieron Burke, and Matthias Ernzerhof. Generalized gradient approximation made simple. *Phys. Rev. Lett.*, 77(18):3865, 1996.

[11] Stefan Grimme. Semiempirical gga-type density functional constructed with a long-range dispersion correction. *J. Comput. Chem.*, 27(15):1787–1799, 2006.

[12] Stefan Goedecker, Michael Teter, and Jürg Hutter. Separable dual-space gaussian pseudopotentials. *Phys. Rev. B*, 54(3):1703, 1996.

[13] Christian Hartwigsen, Sephen Gœdecker, and Jürg Hutter. Relativistic separable dual-space gaussian pseudopotentials from H to Rn. *Phys. Rev. B*, 58(7):3641, 1998.

[14] Giovanni Bussi, Davide Donadio, and Michele Parrinello. Canonical sampling through velocity rescaling. *The Journal of Chemical Physics*, 126(1):014101, 2007.

[15] Roy Dennington, Todd Keith, John Millam, et al. Gaussview, version 5. 2009.

[16] MJ ea Frisch, GW Trucks, HB Schlegel, GE Scuseria, MA Robb, JR Cheeseman, G Scalmani, VPGA Barone, GA Petersson, HJRA Nakatsuji, et al. Gaussian 16, 2016.

[17] Axel D Becke. Density-functional thermochemistry. I. The effect of the exchange-only gradient correction. *The Journal of Chemical Physics*, 96(3):2155–2160, 1992.

[18] Chengteh Lee, Weitao Yang, and Robert G Parr. Development of the Colle-Salvetti correlation-energy formula into a functional of the electron density. *Physical Review B*, 37(2):785, 1988.

[19] Stephan Ehrlich, Jonas Moellmann, Werner Reckien, Thomas Bredow, and Stefan Grimme. System-dependent dispersion coefficients for the DFT-D3 treatment of adsorption processes on ionic surfaces. *ChemPhysChem*, 12(17):3414–3420, 2011.

[20] Samuel F Boys and FJMP Bernardi. The calculation of small molecular interactions by the differences of separate total energies. Some procedures with reduced errors. *Molecular Physics*, 19(4):553–566, 1970.

Chapter 6

Effect of propylene carbonate addition on the structure of dilute zinc-based aqueous electrolytes– a combined quantum mechanical and molecular dynamics approach

6.1 Introduction

Up to this point, the thesis has focused on understanding the intermolecular structure and transport phenomena of high concentration electrolytes (HCEs). Despite many advantages, HCEs continue to suffer from some shortcomings which are not possible to ignore, viz., low ionic conductivity owing to their high viscosity, and high cost due to the large amounts of salt used in making them [1]. Replacing carbonate solvents with water (aqueous electrolytes) intrinsically ensures non-flammability [2], without the need to increase salt concentration in the electrolyte to ensure non-volatility. Further, the highly polar nature, high dielectric constant, low viscosity, and the flexible and transitory nature of the hydrogen bond network

The work presented in this chapter was performed in collaboration with Dr. Premkumar Senguttuvan's group, Jawaharlal Nehru Centre for Advanced Scientific Research, Bangalore, India. Relevant experimental data from their group has been reported here for the sake of completeness. A majority of the work reported in this chapter was published in *J. Mat. Chem. A* **2022**, *10*, 12597-12607 (https://doi.org/10.1039/D2TA01501C) with the title "Two for one: propylene carbonate co-solvent for high performance aqueous zinc-ion batteries – remedies for persistent issues at both electrodes".

in water allow for making battery electrolytes with very high ionic conductivities. The high polarity and large dielectric constant of water also allow for a variety of salts to dissolve in it [2]. Lastly, unlike other organic solvents that need to be synthesised, water is readily available in abundance [3]. For all of these reasons therefore, having investigated HCEs, the exploration of aqueous electrolytes seems promising.

Although aqueous batteries may immediately seem like the solution to most problems to battery technology today, this is far from the truth as yet. Aqueous electrolytes have their own severe deficiencies. The main issues with dilute rechargeable aqueous zinc batteries (RAZBs) are the following: small electrochemical potential window [2], parasitic reactions on the zinc anode [4], dendritic growth on the zinc anode [5], low Coulombic efficiency leading to shorter battery lifespan [6], and partial dissolution of cathode material [4]. These issues acutely affect the applicability of RAZBs. The underlying reasons for these deficiencies are as follows. We know that water is thermodynamically unstable near the zinc deposition potential close to the anode [7]. This leads to parasitic reactions involving hydrogen evolution reaction (HER). This in turn increases the local pH near the anode and initiates the formation of $Zn(OH)_2$ and ZnO. These form a zinc-insulating and passivating layer which reduce the utilization of zinc in the battery, reduces cycling life, and promotes dendritic growth. As for commonly used and promising oxide-based cathodes, free water molecules attack and tend to dissolve the cathode material [7].

There are two main ways to overcome these issues: (a) Modifications to the zinc anode by the use of nanostructured zinc [8] and modification of protective interlayers [9, 10] of the anode, and (b) electrolyte engineering [4] to reduce water content in the zinc solvation shell. The latter is both a more tractable line of approach to solving this problem and can attempt to remedy the problem at both electrodes.

To remedy the persistent issues at anode and cathode through electrolyte engineering, it is necessary to:

(a) Reduce the number of solvating water molecules around zinc, and also to reduce the fraction of free water molecules (bulk water). This ensures that there is a smooth zinc-ion conducting solid electrolyte interface (SEI) on the anode which is derived less from the reduction of water. Such an SEI is also more impenetrable by water, and hence more protected from parastic reactions [7].

(b) Since free water molecules attack and tend to dissolve the cathode material [7], the fraction of free water must also be reduced in the electrolyte.

The route of electrolyte engineering has been pursued along two main directions:

(a) Through the use of high concentration aqueous electrolytes (water-in-salt electrolytes (WIS) [11]). Here, an anion-derived SEI can reduce dendritic growth and offer high

Coulombic efficiency. This gain will come at the cost of losing out on very high-ionic conductivity. Also, the use of large amounts of salt dramatically increases the battery cost.

(b) Through the addition of organic additives (or co-solvent) to the water solvent, which scavenge water from the zinc solvation shells. This leads to the formation of a relatively more anion and organic derived zinc solvation shell, the reduction of which in turn increases the anion and carbonate content of the SEI and thereby the battery performance [3, 4, 12–15]. One does not however want to add too much of the organic co-solvent into the water-based electrolyte for two main reasons. Large amounts of organic co-solvent would

(i) decrease the ionic conductivity of the aqueous electrolyte significantly, and

(ii) make the electrolyte flammable, thereby robbing the aqueous-based electrolyte of the primary advantages that made them an attractive option for battery electrolytes.

As a part of electrolyte engineering, several organic additives such as dimethyl carbonate (DMC) [14], methanol [6], dimethyl sulfoxide(DMSO) [15], triethyl phosphate (TEP) [12, 16], acetonitrile [17], glucose [13], ethylene glycol [18], urea [19], diethyl ether [20], dimethyl ether [21] and propylene carbonate (PC) (added in large quantities [22], 90% by volume) have been tried and have yielded good results in terms of significantly reducing the water content in the zinc solvation shell. The work on PC [22] appeared in literature after we had completed our studies using PC. This chapter is dedicated to providing molecular-level explanations for the experimentally obtained improvement in electrochemical battery performance upon addition of small amounts (20 weight %) of a promising organic co-solvent, viz., propylene carbonate (PC) (Prof. Senguttuvan's group). PC is a more commonplace solvent for use in batteries in comparison to additives/co-solvents aforementioned. At the same time, from our computational studies, we find that it proved to be a co-solvent that is required in only small amounts to cause discernible change in the zinc solvation shell structure. This change was enough to result in electrochemical performance at par with larger amounts of aforementioned additives/co-solvents, in general.

In the present chapter, the electrolyte is composed of zinc triflate ($Zn(OTf)_2$) salt, water solvent, and propylene carbonate (PC) (main) or dimethyl carbonate (DMC) (for comparison) co-solvent (Figure 6.1).

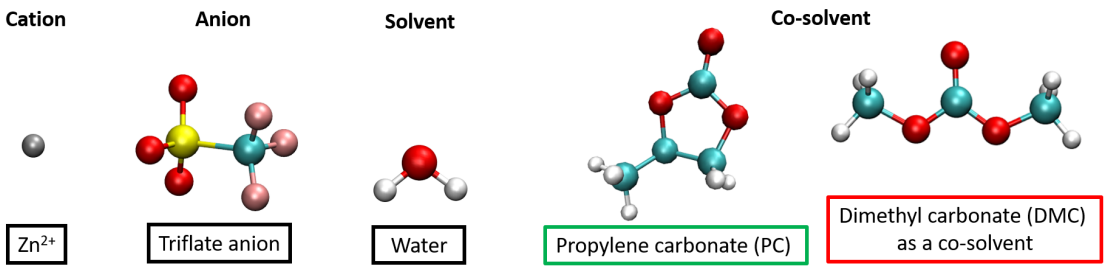

Figure 6.1: Molecular structures of zinc (Zn^{2+}) cation, triflate ($CF_3SO_3^-$) anion, water (H_2O) solvent, and propylene carbonate (PC) or dimethyl carbonate (DMC) co-solvent. Grey - Zn^{2+}, red - oxygen, yellow - sulphur, cyan - carbon, pink - fluorine, white - hydrogen.

The following systems were studied using MD simulations:

(a) TW: 1 M $Zn(OTf)_2$ in water,

(b) PC10 TW: 1 M $Zn(OTf)_2$ in water (90% by weight) and propylene carbonate (PC) (10% by weight),

(c) PC20 TW: 1 M $Zn(OTf)_2$ in water (80% by weight) and PC (20% by weight),

(d) PC30 TW: 1 M $Zn(OTf)_2$ in water (70% by weight) and PC (30% by weight), and

(e) to understand the effectiveness of PC as a co-solvent, a DMC based system was also simulated. DMC-TW: 1 M $Zn(OTf)_2$ in water with the same number of molecules of each type as PC20 TW– however, using DMC in the place of PC.

TW, PC10 TW (in some studies), PC20 TW, DMC20 TW (in some studies), and water systems were experimentally investigated [23].

We briefly discuss some important experimental results from Prof. Senguttuvan's group published in Ref. 23 to put our computational studies into perspective. Several definitions of various quantities and techniques relevant to experiments have been provided in Chapter 1.

Fourier transform infrared (FTIR) spectroscopy was used to investigate the solvation structure of water–PC–$Zn(OTf)_2$ hybrid electrolytes. A shift to higher wavenumbers of O-H vibration upon the progressive addition of PC was seen [23]. This shift implies the disruption of water–water hydrogen bonding and the emergence of interaction between PC, Zn^2+ and H_2O. Similarly, the C=O stretching frequencies also shift to lower wavenumbers going from pure PC to PC in water, indicating the strong hydrogen bonding of the carbonyl group of PC with water. These spectroscopic results indicate the strong interactions between

H_2O, Zn^{2+} and PC species, which are expected to modulate the primary solvation sheath of the $Zn(H_2O)^{2+}$ aqua complex in electrolytes. To confirm inferences from experiments, in our computational investigations, we study PC-water interactions and the solvation shell composition of Zn^{2+} ions.

To explore the impact of the solvation structure on the reversible Zn plating/stripping behavior, cyclic voltammetry (CV) measurements were performed using Zn|Ti cells [23]. The Zn plating process in the PC20 TW electrolyte occurs at a relatively lower reduction potential than in the reference TW electrolyte. Such a change in Zn plating overpotential can be attributed to the formation of the in situ solid-electrolyte interphase (SEI) and nucleation–growth of zinc electrodeposits.

A stable SEI derived from OTf^- anion-PC decomposition was observed in experiments of PC20 TW [23]. These show the presence of organic and inorganic products derived from OTf^- anion-PC decomposition on the Zn anode cycled in the PC20 TW electrolyte. The surface morphology of these samples revealed the formation of zinc dendrites in TW electrolyte, whilst a smooth morphology was observed in case of PC20 TW electrolyte. We computationally calculate reduction potential of various ionic and molecular species/pairs relevant here to shed some light on the possible compositions of the SEI observed in experiments.

Through our computational investigations, we correlate these observations on the cathode to PC-water interactions.

In this chapter, computationally, through radial distribution functions, and coordination numbers, we evaluate the averaged zinc-solvation shell compositions. We calculate the populations of various zinc solvation shell types, the reduction potentials of various chemical species involved in reduction, and quantify the interaction of water with PC. We understand our results on the zinc-solvation shell from MD simulations through quantum chemical binding energy and free energy of formation calculations. In most analyses, we draw a comparison between using PC and another commonplace battery solvent, viz., dimethyl carbonate (DMC), to evaluate the relative effectiveness of the two co-solvent carbonates.

6.2 Methodology and Simulation Details

6.2.1 Molecular dynamics simulations

Force-field

The bonded and non-bonded force field parameters used for triflate anion, PC, and DMC were the General Amber force-field (GAFF) parameters, generated by Antechamber software [24]. Their molecular structures are shown in Figure 6.1.

Restrained Electrostatic Potential (RESP) charges were adopted for the different atom types of these molecules [25]. Water was modeled using TIP-3P [26]. The Lennard-Jones parameters and charge used for zinc ion are of Amber99sb-ildn [27], and are provided in Table 6.1. Charge on zinc ion was taken to be +2.

Atom type	σ (Å)	ϵ (kcal mol^{-1})	Charge (e^{-})
Zn	1.95998	0.0125	2.0

Table 6.1: Force field parameters for zinc used in MD simulations.

Method

PACKMOL software (Version 18.002) [28] was used to generate random initial configurations for all systems. System details are as in Table 6.2. GROMACS-2018.3 package [29] was used to evolve particle trajectories in time. A timestep of 1 fs and the leap-frog algorithm were used to integrate the equations of motion. The Coulomb and Lennard-Jones (LJ) cut-off distances were chosen according to the GAFF to be 10 Å. 1-2 and 1-3 non-bonded interactions are absent. Non-bonded interactions between 1-4 atom pairs were scaled by 0.5 for LJ interactions and by 0.8333 for Coulomb interactions. For all other atom pairs, a scale factor of 1.0 was used for both kinds of non-bonded interactions. Long range interactions were included using the particle-particle mesh Ewald method [30]. LINCS constraints were used for all intramolecular bonds involving hydrogens [31]. Periodic boundary conditions were applied. Arithmetic mean and geometric mean were used as combination rules for LJ sigma and epsilon, respectively. V-rescale thermostat [32] was employed for all simulations with a coupling time-constant of 0.5 ps. The thermostat was coupled to the system once every 10 MD steps. Long range temperature and pressure corrections were employed.

Three independent configurations for each system were packed, energy minimized, and evolved in time. **All analyses are averaged over the results of three independent runs.** The random configurations were first energy minimized in the force field. Thereafter, the temperatures of the all the systems were ramped from 0 K to 298 K under constant volume conditions at the rate of 0.1 K/ps, and then equilibrated at 298 K for 2 ns. Following this, NPT equilibration runs at 1 bar pressure for a duration of 5 ns were performed for each system using Berendsen barostat [33] with a coupling time-constant of 2.0 ps. The barostat was coupled to these systems once every ten steps. Subsequently, NPT production runs of duration 10 ns were run using Parrinello-Rahman barostat [30, 34]. The time-constant for pressure coupling was 2.0 ps. The Parrinello-Rahman barostat was coupled to the system at every step. Finally, the average density obtained during NPT production was used as initial configurations for NVT runs generated for 50 ns. GROMACS-2018.3 [29] modules and FORTRAN codes developed in-house were used to analyze NVT particle trajectories.

System	n_{OTf^-}:n_{PC}:n_{H_2O} carbonate	No. of water molecules	No. of box molecules	Equilibrated length (Å)
TW	1:0:56	0	8960	67.14
PC10 TW	1:1:51	160	8160	67.02
PC20 TW	1:2:45	320	7200	66.50
DMC-TW	1:2:45	320	7200	66.34
PC30 TW	1:2.42:31.76	486	6432	66.43

No. of Zn^{2+} ions = No. of $Zn(OTf)_2$ = 160 for all systems. No. of triflate ions = 320 for all systems.

Table 6.2: Details of systems simulated using MD.

Agreement level of force-field used with experiments

The validity of the force field used was checked by comparing simulation densities against the densities obtained from experiments (wherever available). See Table 6.3.

System	$\rho_{simulation}$ (g/cc)	$\rho_{experiment}$ (g/cc)	$\Delta\rho\%$
TW	1.204	1.208	-0.33
PC10 TW	1.222	1.225	-0.24
PC20 TW	1.245	1.235	0.81
DMC-TW	1.236	–	–
PC30 TW	1.263	–	–

Table 6.3: Density obtained in simulations compared against experimental values.

6.2.2 Quantum chemical DFT calculations

We calculate the binding energies of some pairs of molecules and the reduction potentials of some single molecules and some pairs of molecules quantum chemically. In this section, we provide the details used in performing these calculations. The results of these calculations are provided in the results and discussion section.

Binding energy calculations in implicit solvent model

All quantum chemical calculations were performed using the Gaussian 16 package [35] and all visualizations for these calculations were carried out in GaussView (version 5.0.9) [36]. To obtain an estimate of the strength of interaction between the zinc-ion and other components of the electrolyte, we calculate the binding energy of various species with the zinc ion in the implicit Solvation Model Based on Density (SMD) [37] using water solvent. Like Dong et al. [14] the systems were geometry optimized at the B3LYP level of theory and using the 6-311G(d) basis set for all atoms barring zinc. For zinc, a B3LYP level of theory and the SDD basis set was employed. D3 version of Grimme's dispersion corrections were employed for these calculations [38]. Frequency calculations confirmed the absence of any imaginary frequency. The binding energy E_b of complex containing components 1 and 2 was calculated as: $E_b = E_{1,2} - E_1 - E_2$, where E is the energy of the optimized structure.

Reduction Potentials

The free energy of formation [$\Delta G_{S,298} = G_{S,298}(X^-) - G_{S,298}(X)$] of X^- from X for some complexes in implicit solvent phase (water) was calculated using the SMD [37]. X represents a molecule, ion or a zinc complex that can undergo reduction. Both X and X^- were optimized in the same way as was done for binding energy calculations. The optimized structure of X was used as the starting configuration for the optimization of X^- with the addition of an electron. D3 version of Grimme's dispersion corrections were employed for these calculations [38]. The reduction potentials of the complexes were obtained therefrom using the following expression [14]

$$E_{red} = -(\Delta G/F) - 3.656V \tag{6.1}$$

where F is the Faraday constant.

6.3 Results and Discussions

6.3.1 Radial distribution functions and coordination numbers

Altering the zinc-ion solvation shell has attracted much attention in the recent past as a promising way forward in resolving the issues faced by conventional aqueous zinc-ion batteries [13–15, 39, 40]. The addition of small amounts of PC to the aqueous zinc electrolyte solution is a similar attempt at the same, resulting in significantly improved electrochemical battery performance. Atomistic MD simulations have been performed to investigate the altered electrolyte structure in general and the zinc solvation shell composition in particular. Various radial distribution functions (RDFs) around zinc and running coordination numbers are displayed in Figure 6.2. Peaks at 1.92 and 1.88 Å in the RDFs of all the electrolytes correspond to Zn – OW (i.e., Zn – O of H_2O) and Zn – OTf (i.e., Zn – O of triflate anion) distances, respectively, in the Zn^{2+} primary solvation shell (Figure 6.2(a) and (c)). In PC-based electrolytes, the carbonyl oxygen (OC) is present at a distance of 1.95 Å from Zn^{2+} (Figure 6.2(b)). Coordination number analysis of the average composition of Zn^{2+} primary solvation shell is provided in Table 6.4.

System	Average zinc solvation shell composition
TW	$Zn^{2+}[(H_2O)_{5.53}(OTf^-)_{0.47}]$
PC10 TW	$Zn^{2+}[(H_2O)_{5.27}(PC)_{0.14}(OTf^-)_{0.59}]$
PC20 TW	$Zn^{2+}[(H_2O)_{5.25}(PC)_{0.24}(OTf^-)_{0.51}]$
PC30 TW	$Zn^{2+}[(H_2O)_{5.00}(PC)_{0.37}(OTf^-)_{0.64}]$

Table 6.4: Average composition of Zn^{2+} primary solvation shell.

These observations are interesting, as the addition of a small amount of PC (say, 20 weight %) increases the amount of OTf^-, and expels nearly 0.3 water molecules from the zinc solvation shell. In tripling the weight percent of PC in the electrolyte (from PC10 TW to PC30 TW), the PC content of the zinc solvation shell is also tripled, approximately (Figure 6.2(b)). Example of a zinc environment in PC20 TW with triflate anion and PC participating in its primary solvation shell, replacing two of six water molecules present in TW is shown in Figure 6.3.

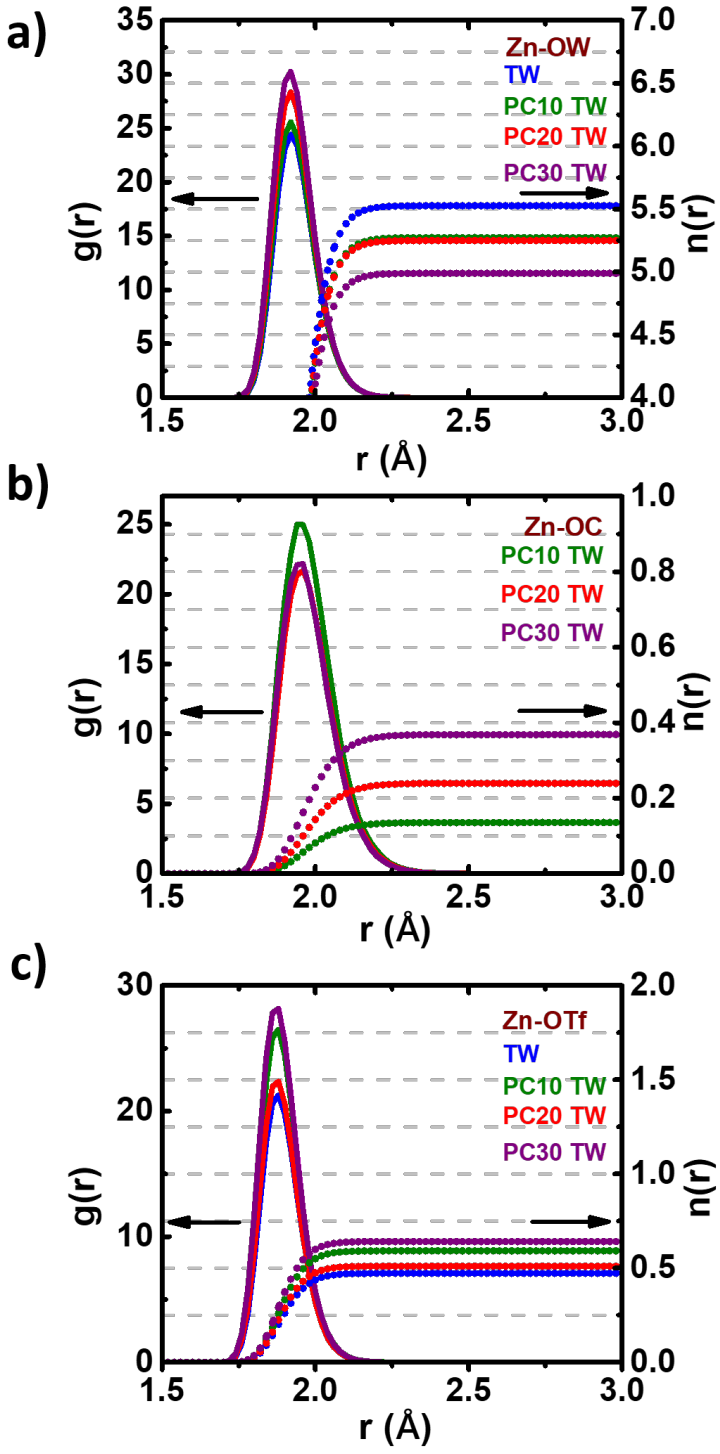

Figure 6.2: Radial distribution functions (RDF) (left axis) and running coordination numbers (CN) (right axis) for a) Zn – OW (i.e., Zn – O of H_2O), b) Zn – OC (i.e., carbonyl O of PC) and c) Zn – OTf (i.e., Zn – O of triflate anion).

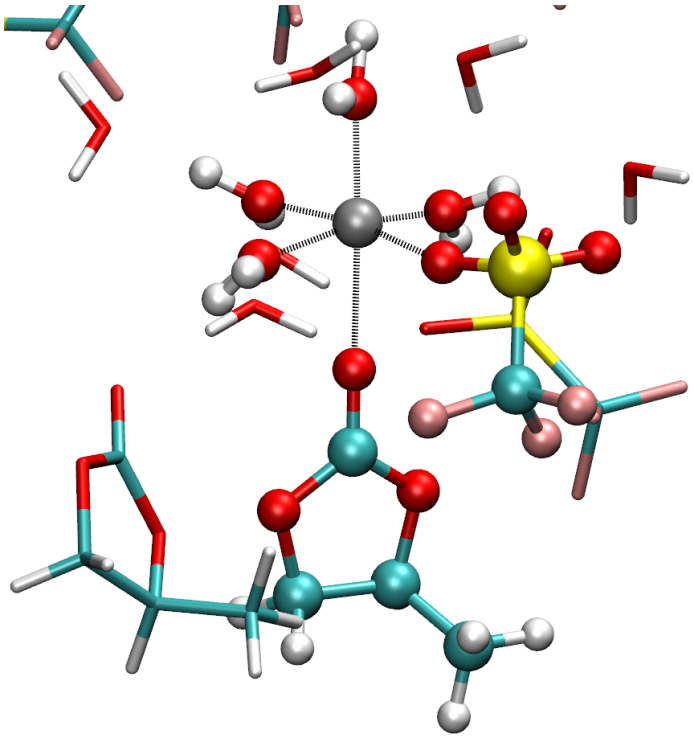

Figure 6.3: A representative zinc environment in PC20 TW. Atom colors: Red - oxygen, white - hydrogen, cyan - carbon, grey - zinc ion, yellow - sulphur, pink - fluorine.

6.3.2 Organization of water molecules around PC

PC is a polar molecule with a large dipole moment of 4.94 D [41]. Radial distribution functions (RDF) and coordination numbers (CN) between different atom pairs or center of masses (Figure 6.4) shows that water organizes around PC, and significantly interacts with it through hydrogen bonding (Also see results on hydrogen bonding). Thus, say in the PC20 TW electrolyte, on average, as many as 2.6 water molecules are present in the first coordination shell of the carbonyl oxygen of PC (see Figure 6.4(b) for the corresponding RDF whose first peak integrates to a value of 2.6 at the first minimum of 3.5 Å; donor O – acceptor O distance in hydrogen bonds). PC scavenges these water molecules both from the bulk solution and from the zinc solvation shell to bring them into its own first coordination shell (Figure 6.5). This leads to a partial water depletion at zinc which is compensated by an increased insertion of PC and OTf^- into the zinc solvation shell (Figures 6.2(b) and (c)). Such a replacement of water molecules with organic co-solvent molecules and anions is in good agreement with recent reports [3, 6, 12–15, 39, 42]. As one might expect, there are 12 water molecules around the PC centre of mass (COM) (Figure 6.4(c)).

Organization of water around the PC molecules must reduce the free (bulk-like) water percentage. We study this in the next section.

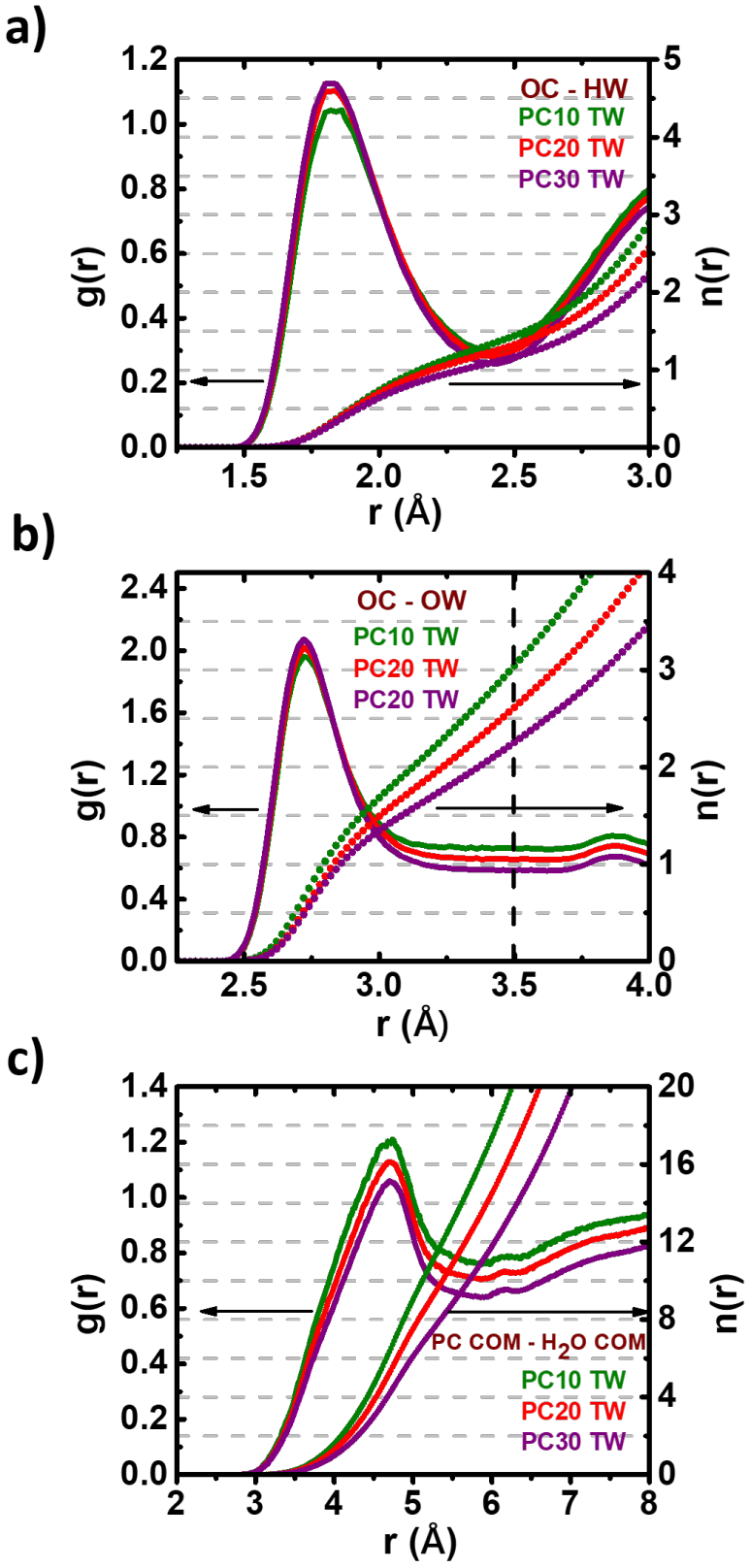

Figure 6.4: Radial distribution functions (RDF) (left axis, solid lines) and running coordination numbers (CN) (right axis, dotted lines) for a) OC – HW (hydrogens of water), b) OC – OW and, c) the center of mass (COM) of PC – COM of H_2O.

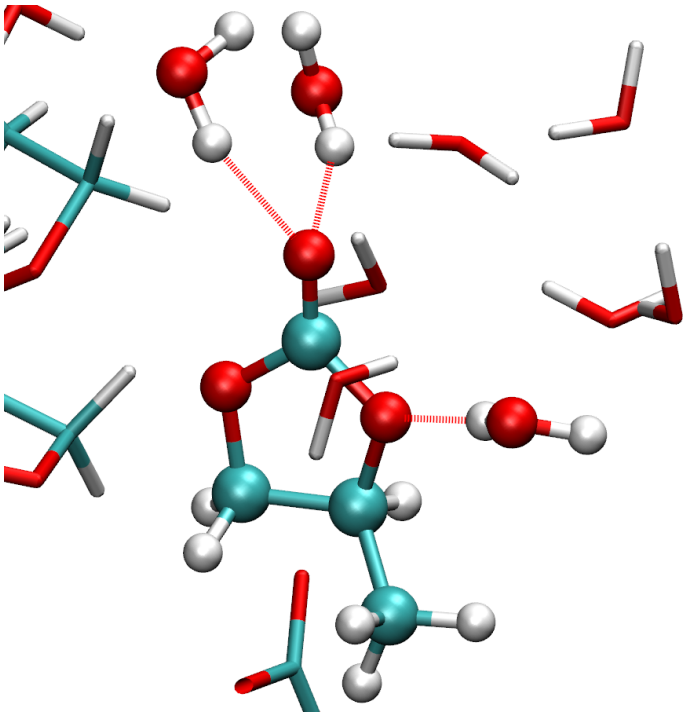

Figure 6.5: A snapshot of PC20 TW-MD simulation showing PC forming hydrogen bonds with water molecules.

6.3.3 Percentage of free water molecules

A free water molecule is defined as one which only has other water molecules as its nearest neighbors, i.e., a water molecule not coordinating or interacting with zinc ions, PC molecules, or triflate anions, in a PC based electrolyte, say. The cutoff interaction distance between OW and Zn was taken to be 2.5 Å. Water and PC were considered to interact through hydrogen bonds. The carbonyl oxygen atoms (OC) were considered to be the hydrogen bond acceptors of the carbonates used. The cutoff distance for OW and OC interaction was therefore taken to be 3.5 Å. The oxygens of the triflate anions interact with the hydrogens of water molecules. This again made the cutoff of 3.5 Å for OW to OTf distance, a suitable choice. We find that the percentage of free water decreases from TW to PC30 TW (Table 6.5). This reduction is due to water molecules getting increasingly coordinated to PC with increase in the latter's proportion in the electrolyte. As discussed earlier, this reduction of free water percentage is crucial in reducing the reductive reactivity of water at the anode and in reducing the extent of dissolution of the cathode.

System	Percentage of free water
TW	68
PC10 TW	64
PC20 TW	58
PC30 TW	55

Table 6.5: Free water percentages across different concentrations of PC in the electrolyte.

6.3.4 Hydrogen bonds among water molecules

In MD trajectories, setting the hydrogen bond distance (donor oxygen to acceptor oxygen) criterion to be 3.5 Å, and the hydrogen bond angle (O-H–O) criterion to be between 130^o to 180^o, we tabulate our results in Table 6.6.

System	Number of H-bonds
TW	1.96
PC10 TW	1.90
PC20 TW	1.83
PC30 TW	1.78

Table 6.6: Average number of water-water hydrogen bonds per water molecule.

PC interacts with water through hydrogen bonding. The hydrogen bonds formed between PC and water comes at the cost of partially breaking the water-water hydrogen bond network, consistent with the reduction in the percentage of 'free water' in the solution and the average number of hydrogen bonds per water molecule. A higher weight percent of PC in the solution results in a larger disruption of the water-water hydrogen bonding network. The organic co-solvent (PC here) lowers the solvent's (water here) activity.

Having studied the reason for carbonate and triflate insertion into the zinc solvation shell and a quantitative measure for water-PC interactions leading to free water reduction, we were interested in quantitatively estimating the prevalence of triflate and carbonate containing zinc-ion clusters vis-a-vis the standard hexa aquo zinc complex. This aspect is investigated in the next section.

6.3.5 Zinc solvation shell compositions and percentage populations

The nature of zinc-ion primary solvation shell is dependent on the number of water molecules, PC molecules, and triflate anions present in the electrolyte solution. The solvation shell of all zinc ions over the last 45 ns of NVT trajectories were determined to arrive at the population of various zinc solvation shell types. The populations were averaged over three independent runs. In order for a water molecule or a PC molecule or a triflate anion to be a part of a zinc ion's solvation shell, the distance between OW of water and Zn, or OC of PC and Zn, or any OTf of triflate anion and Zn, was required to be less than or equal to 2.5 Å.

The occurrence probability of various types of zinc solvation shell is displayed in Figure 6.6. An examination of the coordination shell and its reduction potential (next section) is relevant to understand the character of the SEI, which is likely to be a product of reduction of such species. The addition of PC to TW diversifies the composition of the zinc solvation shell (increased population of triflate and carbonate containing complexes) and significantly reduces the probability amplitude of the hexa-aquo complex (Figure 6.6, Table 6.7).

TW	PC10 TW	PC20 TW (n_{H_2O}:n_{PC}:n_{OTf}) - Pop(%)	PC30 TW
(6:0:0) - 60	(6:0:0) - 43.12	(6:0:0) - 43.75	(6:0:0) - 30.00
(5:0:1) - 33.54	(5:0:1) - 35.62	(5:0:1) - 24.79	(5:0:1) - 30.62
(4:0:2) - 5.62	(5:1:0) - 7.29	(5:1:0) - 14.79	(5:1:0) - 14.37
(3:0:3) - 0.83	(4:0:2) - 6.67	(4:0:2) - 8.12	(4:1:1) - 12.08
(5:0:0) - 1.29x10^{-3}	(4:1:1) - 5.42	(4:1:1) - 5.42	(4:0:2) - 5.62
(4:0:1) - 3.89x10^{-4}	(3:0:3) - 1.25	(4:2:0) - 1.25	(3:1:2) - 2.08
(3:0:2) - 2.78x10^{-5}		(3:1:2) - 1.25	(3:2:1) - 1.67
			(4:2:0) - 1.87
			(3:0:3) - 1.04

Table 6.7: Zinc-solvation shell compositions across four electrolytes.

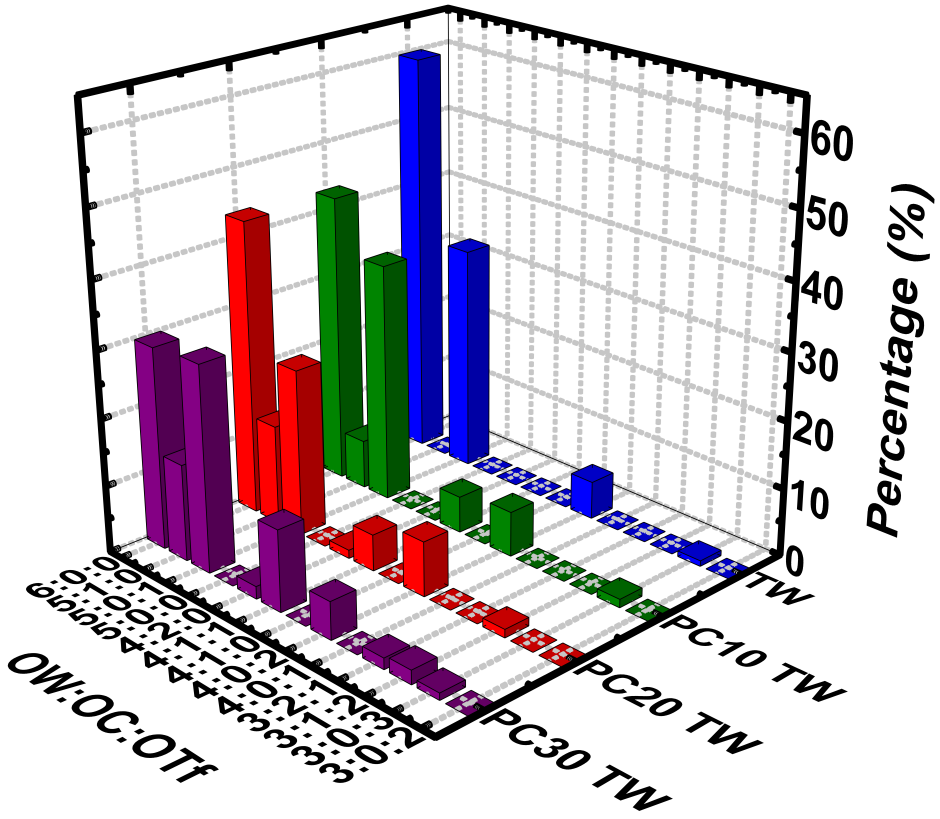

Figure 6.6: Populations of all zinc primary solvation shell compositions in TW, PC10 TW, PC20 TW, DMC, and PC30 TW electrolytes.

The interpretation of zinc solvation shell population study can be understood in light of reduction potentials discussed in the next section.

6.3.6 Reduction potentials

Having looked at populations of various solvation shell types for zinc ions, it is useful to look at how the reduction potentials of the fundamental units of some of these zinc complexes compare to that of Zn^{2+}. The methods for the calculation of the same are given in the methods section. Although a separate section is devoted to the comparison between PC and DMC, for the sake of convenience, in this case DMC has been included in here. Figure 6.7 and Table 6.8 tell us that bare triflate anion, PC, and DMC have a much lower reduction potential (-2.79 V, -2.34 V, and -2.44 V, respectively) compared to the Zn^{2+}/Zn redox couple. Therefore, Zn^{2+} ions will preferentially undergo reduction before triflate anion or PC or DMC. Interestingly however, $Zn^{2+}OTf^{-}$ (0.13 V), Zn^{2+}PC (0.23 V), and Zn^{2+}DMC (0.21 V) have a higher reduction potential compared to Zn^{2+}/Zn redox couple,

and therefore preferentially undergo reduction in comparison to zinc. This can potentially allow for the formation and deposition of fluoride and carbonate derivatives of zinc as SEI instead of oxide and hydroxide derivatives of zinc predominantly formed in the absence of carbonate.

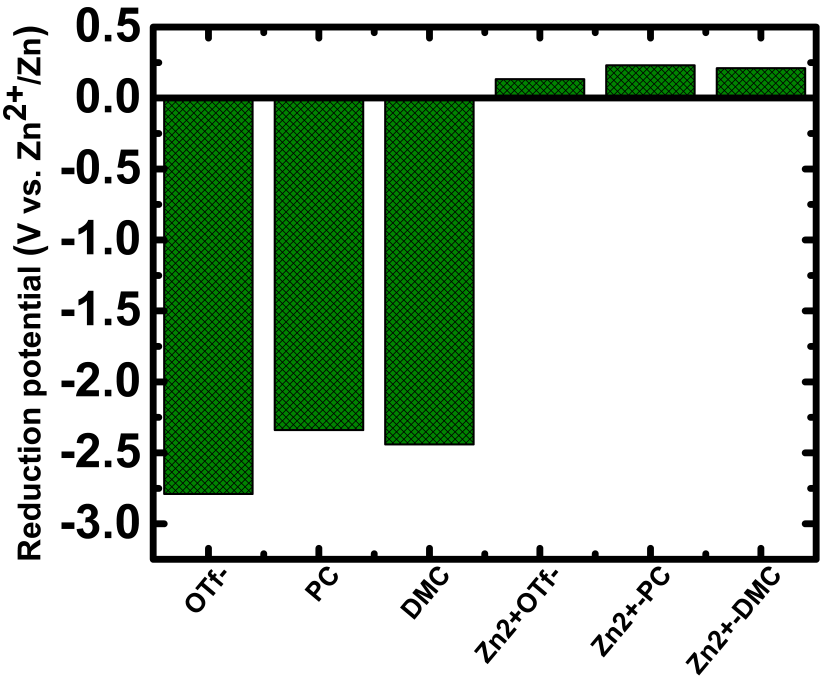

Figure 6.7: The calculated reduction potentials of free OTf^-, free PC, free DMC, $Zn^{2+}OTf^-$, Zn^{2+}PC and Zn^{2+}DMC species.

Chemical species	Calculated reduction potential (E_{red}) (V)
OTf^-	-2.79
PC	-2.34
DMC	-2.44
$Zn^{2+}OTf^-$	0.13
Zn^{2+}PC	0.23
Zn^{2+}DMC	0.21

Table 6.8: The calculated reduction potentials of various chemical species.

Taking the zinc solvation shell composition populations together with reduction potentials, the reduction potentials of 0.23 V for Zn^{2+}PC (akin to number ratio - OW:OC:OTf = 5:1:0, for example), and 0.13 V for $Zn^{2+}OTf^-$ (akin to number ratio - OW:OC:OTf = 5:0:1 for example), are higher than that of the Zn^{2+}/Zn redox couple, and will therefore preferentially undergo reduction in comparison to zinc (Figures 6.6, 6.7, and Table 6.7),

similar to the scenario in Ref. 14 for DMC. Increased presence of PC and OTf^- in the zinc-ion primary solvation shell (Figure 6.6) and the preferred reduction of such complexes over zinc (Table 6.8), can potentially lead to the formation of a more PC and OTf^-- derived SEI (fluoride and carbonate derived SEI). This will have a protective effect on the electrode, leading to improved electrochemical performance over TW. This is at par with the W4D1 (55 weight percent DMC) system of Ref. 14 through the presence of PC only at 20 weight percent in the electrolyte.

We performed quantum chemical calculations to verify the stability of the Zn^{2+}–(H_2O/PC/DMC/OTf^-) pairs and to rationalize these results.

6.3.7 Binding energies in implicit solvent model

Quantum chemical calculations have been performed to verify the stability of Zn^{2+}–(H_2O/PC/DMC/OTf^-) pairs. The binding energies of Zn^{2+}-PC (-18.14 kcal mol^{-1}) and Zn^{2+}– OTf^- (-18.78 kcal mol^{-1}) pairs are comparable to each other and relatively closer to Zn^{2+}–H_2O (-22.87 kcal mol^{-1}) in comparison to Zn^{2+}-DMC (-16.89 kcal mol^{-1}) (Figure 6.8). This supports the introduction of PC and OTf^- in the Zn^{2+} primary solvation shell as well as the larger PC content than DMC content in the Zn^{2+} solvation shell seen in our MD results.

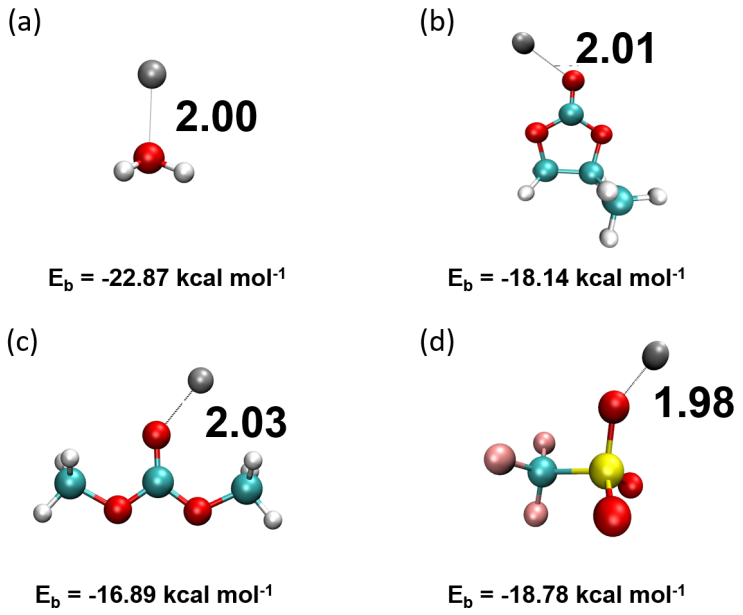

Figure 6.8: Binding energies calculated using SMD [37] with implicit water representation of (a) Zn^{2+}-H_2O, (b) Zn^{2+}-PC, (c) Zn^{2+}-DMC, and (d) Zn^{2+}-OTf^-. Distances are in units of Angstrom (Å).

Focussing on electrolytes with PC as a co-solvent, the binding energy of Zn^{2+}-H_2O (-22.87 kcal mol-1) is larger than that of Zn^{2+}-PC (-18.14 kcal mol-1), and Zn^{2+}-OTf^- (-18.78 kcal mol-1). This, coupled with the fact that the proportion of water in the electrolyte is largest, is reflected in n_{OW}:n_{OC}:n_{OTf} = 6:0:0 being the most probable zinc solvation shell type (Figure 6.6), and water being the predominant participant in interactions with zinc, even in non-hexa-aquo complexes. The values of the binding energies are comparable, thereby not precluding the formation of zinc complexes containing PC and OTf^-, rather the comparability of the energies make complexes such as n_{OW}:n_{OC}:n_{OTf} = 5:0:1, 5:1:0, second and third most probable according to our MD simulations. Quantum chemical calculations of the free-energy of formation ($\Delta_f G$) of n_{OW}:n_{OC}:n_{OTf} = 6:0:0, 5:0:1, 5:1:0 complexes in gas phase (below) have also been calculated (Figure 6.9). These reveal that the formation of PC and OTf^- containing complexes are possible and support our MD results. PC and OTf^- entering the zinc solvation is a function of the amount of PC in the electrolyte, binding and free energies, and temperature. Both these quantum chemical calculations (gas and SMD phases) have their own limitations as does the force field used for MD simulations. However, the presence of PC and OTf^- in the zinc solvation shell (in as small quantities as 17% ($1/6^{th}$) in the most probable zinc solvation shells (barring 6:0:0)) is either shown or strongly considered plausible by all of them.

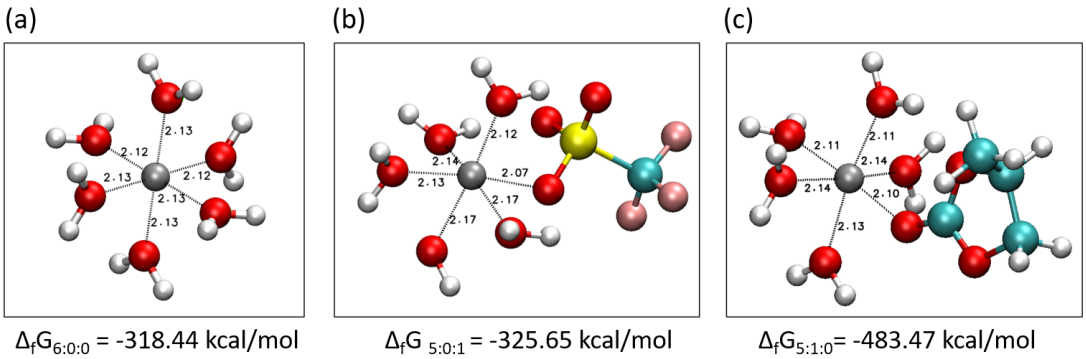

Figure 6.9: Gas-phase free energy for: n_{OW}:n_{OC}:n_{OTf} = (a) 6:0:0, (b) 5:0:1, and (c) 5:1:0.

6.3.8 Propylene carbonate versus dimethyl carbonate

PC and DMC are both widely used solvents in batteries and therefore, apart from others, for this reason too, they become attractive co-solvents in aqueous electrolytes. However, results reported in Ref. 14 were not at the same weight percent of DMC as the studies conducted by Prof. Senguttuvan's (and our) studies on PC. Neither are the experimental conditions such as current density nor the mass loading at the cathode exactly the same

between the two studies. Therefore, making a definitive statement about the efficacy of the two carbonates across the studies is therefore, difficult. For a direct one-on-one comparison, Prof. Senguttuvan's group prepared two electrolytes, viz., containing PC20 TW and DMC20 TW and performed full-cell studies at the same current density and the same mass loading of the cathode (4 mg cm^{-2}). The capacity retention of the PC20 TW was far superior in comparison to DMC20 TW [23].

In order to find the plausible reasons for the improved electrochemical performance of PC over DMC, we simulated a $Zn(OTf)_2$-DMC-H_2O (DMC-TW) in the same molecular ratio as the PC20 TW system. We use the same molecular ratio and not the same weight percent (as in experiments) across the PC and DMC electrolytes. This was so because, maintaining the same number of interaction sites (Zn, OW, OC, OTf, say) across the electrolytes is required for a fair comparison when it comes to gleaning molecular level insights from simulations.

First, from Figure 6.10(a), we find that approximately 0.16 additional water molecules are expelled from the zinc ion solvation shell by PC in lieu of DMC. Although the extent of the carbonate entering the zinc solvation shell is small at low carbonate concentrations, from Figure 6.10(b), we find that at the same molecular ratio of PC and DMC in their respective electrolytes, approximately 2.4 times more PC is able to enter the zinc solvation shell than DMC. The above observations can be summarized using the average solvation shell composition formulae for the DMC-TW and PC20 TW electrolytes from Table 6.9.

System	Average zinc solvation shell composition
PC20 TW	$Zn^{2+}[(H_2O)_{5.25}(PC)_{0.24}(OTf^{-})_{0.51}]$
DMC-TW	$Zn^{2+}[(H_2O)_{5.41}(PC)_{0.1}(OTf^{-})_{0.49}]$

Table 6.9: Average composition of Zn^{2+} primary solvation shell in PC20 TW and DMC-TW electrolytes.

Second, unlike PC20 TW wherein PC's OC coordinates to 2.6 water molecules, DMC's OC coordinates to only 2.15 water molecules. This difference can be clearly attributed to the lower dipole moment of DMC (0.91 D) [43] in comparison to that of PC (4.94 D) [41].

Third, we find that the free-water percentages for both electrolytes are the same (Table 6.10). At first glance, this may seem surprising since PC has seemed to be a better carbonate to use as an organic co-solvent as compared to DMC up to this point. Here, we note from Table 6.9 that PC scavenges out more water from the zinc solvation shell in comparison to DMC. This should lead to more free-water in the DMC-TW than PC20 TW. However, PC's OC coordinates with 2.6 water molecules as opposed to 2.15 water molecules in the case of OC of DMC. The two effects seem to compensate for each other to yield the same free-water percentage in both electrolytes.

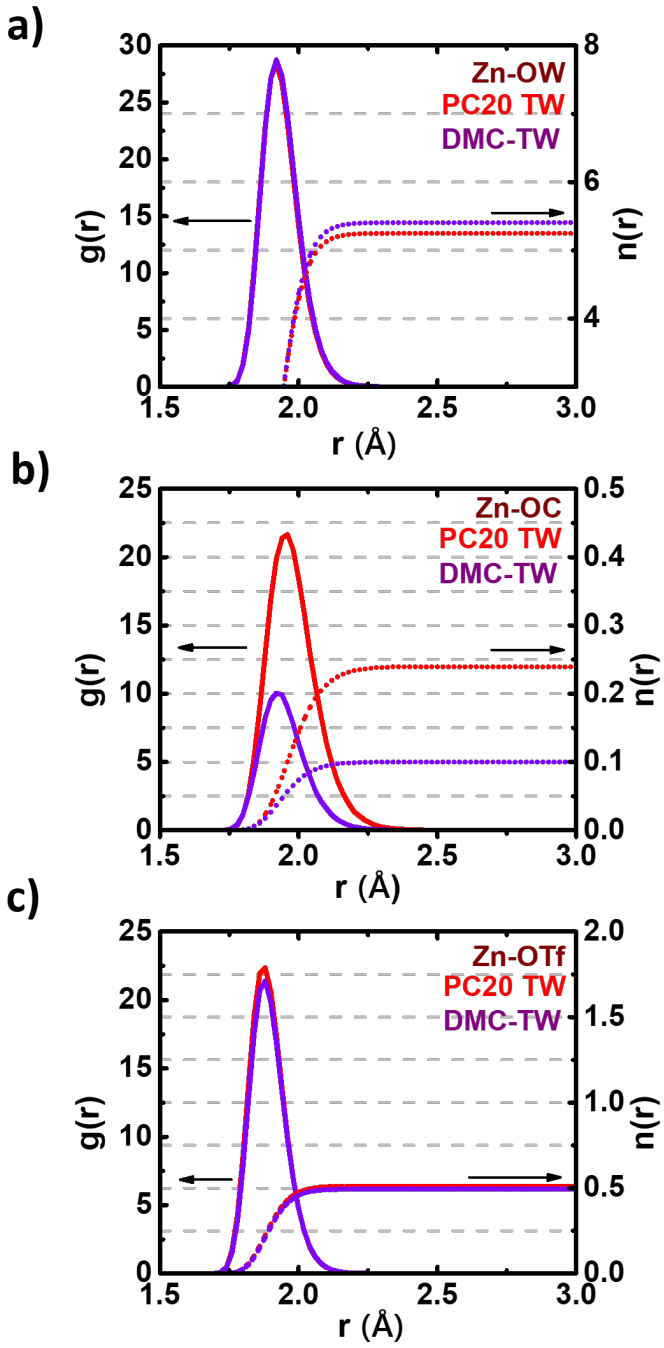

Figure 6.10: Comparison of MD simulation results of DMC based and PC based zinc-water-triflate electrolyte solutions, at the same molecular ratios of $Zn(OTf)_2$:carbonate solvent:H_2O.

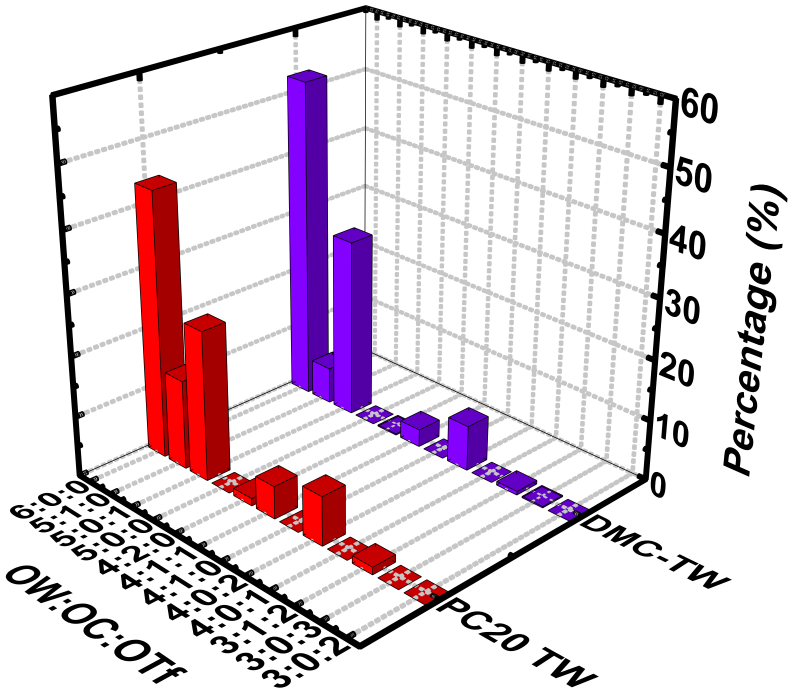

Figure 6.11: Populations of all zinc primary solvation shell compositions in PC20 TW and DMC-TW electrolytes.

System	Percentage of free water
PC20 TW	58
DMC-TW	58

Table 6.10: Free water percentages for PC20 TW and DMC-TW electrolytes.

Fourth, we find that the number of hydrogen bonds between water molecules per water molecule is larger in the PC20 TW electrolyte than the DMC-TW electrolyte (Table 6.11). Stronger interactions between PC-water vis-a-vis DMC-water can be inferred. An additive/co-solvent that engages more water molecules is suited.

System	Number of H-bonds
PC20 TW	1.83
DMC-TW	1.81

Table 6.11: Average number of water-water hydrogen bonds per water molecule

Fifth, we look at the populations of different zinc solvation shell types in the PC20 TW and DMC-TW electrolytes.

PC20 TW (n_{H_2O}:n_{PC}:n_{OTf}) - Pop(%)	DMC-TW
(6:0:0) - 43.75	(6:0:0) - 52.92
(5:0:1) - 24.79	(5:0:1) - 29.58
(5:1:0) - 14.79	(4:0:2) - 7.50
(4:0:2) - 8.12	(5:1:0) - 6.04
(4:1:1) - 5.42	(4:1:1) - 2.92
(3:1:2) - 1.25	(3:1:2) - 0.62
(4:2:0) - 1.25	(3,0,3) - 0.21

Table 6.12: Zinc solvation shell compositions across PC20 TW and DMC-TW electrolytes.

Two interesting observations can be made from Figure 6.11 and Table 6.12: (a) The population of the hexa-aquo (6:0:0) complex is approximately 10% less in the PC20 TW in comparison with DMC-TW. This observation implies that PC has been able to desirably convert a larger number of hexa-aquo complexes from hexa-aquo to ones that contain PC and/or triflate, as opposed to DMC. (b) The population of any carbonate containing complex is larger in the PC based-electrolyte when compared with the DMC-based electrolyte (up to 9% more in (5:1:0)). This implies that PC is able to enter the zinc solvation shell more easily as than DMC. The higher population of PC containing zinc-ion complexes than DMC containing zinc-ion complexes when taken together with the fact that the reduction potentials of both Zn^{2+}PC and Zn^{2+}DMC are higher in comparison to the Zn^{2+}/Zn couple imply that the carbonate containing zinc-ion complexes are likely to reduce before zinc and that the carbonate derived part of the SEI is likely to be a little more in the PC-based electrolyte than the DMC-based electrolyte. As discussed earlier, increasing the fraction of carbonate and anion-derived SEI is favourable for better battery performance.

These results indicate that the use of PC over DMC is favourable. These observations find their footing in part because liquid PC has a higher static dielectric constant and molecular dipole moment (64.9, 4.94 D) [41] in comparison to DMC (3.087, 0.91 D) [43], i.e. PC is more polar than DMC.

6.4 Conclusions

This work was performed in collaboration with Prof. Senguttuvan's group. Experimentally, infrared (IR) and Raman spectroscopy hinted at changes in the zinc solvation shell. However, these changes could be elaborated upon through MD simulations. X-ray photoelectron spectroscopy (XPS) determined the chemical composition of the SEI on the zinc anode

cycled in PC20 TW as being composed of organic (C-F, C-O, and C-S) and inorganic ($ZnCO_3$ and ZnF_2) products. Scanning-electron microscope (SEM) images show the smooth deposition of these products on the zinc anode. Cyclic voltammetry, voltage-capacity studies, Galvanostatic Zn plating/stripping experiments, and cycling-stability were performed to determine the battery performance. These proved that even in small quantities (20% by weight), the presence of PC in the aqueous electrolyte significantly curbed the hydrogen evolution reaction (HER), reduced dendritic growth on the zinc anode and the erosion of the V_2O_5 cathode. These improved the Coulombic efficiency and cycling stability of the battery greatly. The advantage of improving the electrochemical performance of the battery using small amounts of organic additives is that one can largely maintain the high ionic conductivity and non-flammability of aqueous electrolytes. From our simulations, we were able to arrive at the molecular explanations for the experimental findings. We find that the addition of PC in the electrolyte has two main effects:

(a) PC enters the zinc solvation shell and promotes the entry of triflate anion into the zinc solvation shell as well. The population of the hexa-aquo complexes is significantly reduced as the proportion of PC in the electrolyte increases and the zinc solvation shell composition is thus diversified. The reduction potential of Zn^{2+}PC and $Zn^{2+}OTf^{-}$ are also larger than that of the Zn^{2+}/Zn couple. Taken together, these results would mean that addition of PC in the aqueous electrolyte will result in a significant fraction of non-hexa-aquo (i.e. PC or OTf containing) complexes which will preferentially undergo reduction to form a smoother (less dendrites), more hydrophobic (hence protective) carbonate and anion-derived SEI on the zinc anode.

(b) The addition of PC in the electrolyte decreases the fraction of free (bulk) water in the electrolyte. This happens as PC scavenges water molecules from the zinc solvation shell and bulk liquid through its interactions with water via hydrogen bonds. This reduction of free water reduces the dissolution of the V_2O_5 cathode.

Therefore using PC as a co-solvent to water remedies issues at both electrodes and we have been able to understand the molecular underpinnings for the same.

Bibliography

[1] Yuki Yamada, Jianhui Wang, Seongjae Ko, Eriko Watanabe, and Atsuo Yamada. Advances and issues in developing salt-concentrated battery electrolytes. *Nature Energy*, 4(4):269–280, 2019.

[2] Rezan Demir-Cakan, M Rosa Palacin, and Laurence Croguennec. Rechargeable aqueous electrolyte batteries: from univalent to multivalent cation chemistry. *Journal of Materials Chemistry A*, 7(36):20519–20539, 2019.

[3] Zhen Hou, Hong Tan, Yao Gao, Menghu Li, Ziheng Lu, and Biao Zhang. Tailoring desolvation kinetics enables stable zinc metal anodes. *Journal of Materials Chemistry A*, 8(37):19367–19374, 2020.

[4] Qiu Zhang, Yilin Ma, Yong Lu, Xunzhu Zhou, Liu Lin, Lin Li, Zhenhua Yan, Qing Zhao, Kai Zhang, and Jun Chen. Designing Anion-Type Water-Free Zn^{2+} Solvation Structure for Robust Zn Metal Anode. *Angewandte Chemie*, 133(43):23545–23552, 2021.

[5] Qi Zhang, Jingyi Luan, Yougen Tang, Xiaobo Ji, and Haiyan Wang. Interfacial design of dendrite-free zinc anodes for aqueous zinc-ion batteries. *Angewandte Chemie International Edition*, 59(32):13180–13191, 2020.

[6] Junnan Hao, Libei Yuan, Chao Ye, Dongliang Chao, Kenneth Davey, Zaiping Guo, and Shi-Zhang Qiao. Boosting Zinc Electrode Reversibility in Aqueous Electrolytes by Using Low-Cost Antisolvents. *Angewandte Chemie*, 133(13):7442–7451, 2021.

[7] Boya Tang, Lutong Shan, Shuquan Liang, and Jiang Zhou. Issues and opportunities facing aqueous zinc-ion batteries. *Energy & Environmental Science*, 12(11):3288–3304, 2019.

[8] Yinxiang Zeng, Xiyue Zhang, Ruofei Qin, Xiaoqing Liu, Pingping Fang, Dezhou Zheng, Yexiang Tong, and Xihong Lu. Dendrite-free zinc deposition induced by multifunctional CNT frameworks for stable flexible Zn-ion batteries. *Advanced Materials*, 31(36):1903675, 2019.

[9] Nannan Zhang, Shuo Huang, Zishun Yuan, Jiacai Zhu, Zifang Zhao, and Zhiqiang Niu. Direct Self-Assembly of MXene on Zn Anodes for Dendrite-Free Aqueous Zinc-Ion Batteries. *Angewandte Chemie International Edition*, 60(6):2861–2865, 2021.

[10] Longsheng Cao, Dan Li, Tao Deng, Qin Li, and Chunsheng Wang. Hydrophobic Organic-Electrolyte-Protected Zinc Anodes for Aqueous Zinc Batteries. *Angewandte Chemie International Edition*, 59(43):19292–19296, 2020.

[11] Yuyan Wang, Xiaotang Meng, Jinfeng Sun, Yang Liu, and Linrui Hou. Recent Progress in "Water-in-Salt" Electrolytes Toward Non-lithium Based Rechargeable Batteries. *Frontiers in Chemistry*, 8:595, 2020.

[12] Sailin Liu, Jianfeng Mao, Wei Kong Pang, Jitraporn Vongsvivut, Xiaohui Zeng, Lars Thomsen, Yanyan Wang, Jianwen Liu, Dan Li, and Zaiping Guo. Tuning the Electrolyte Solvation Structure to Suppress Cathode Dissolution, Water Reactivity, and Zn Dendrite Growth in Zinc-Ion Batteries. *Advanced Functional Materials*, 31(38):2104281, 2021.

[13] Peng Sun, Liang Ma, Wanhai Zhou, Meijia Qiu, Zilong Wang, Dongliang Chao, and Wenjie Mai. Simultaneous regulation on solvation shell and electrode interface for dendrite-free Zn ion batteries achieved by a low-cost glucose additive. *Angewandte Chemie*, 133(33):18395–18403, 2021.

[14] Yang Dong, Licheng Miao, Guoqiang Ma, Shengli Di, Yuanyuan Wang, Liubin Wang, Jianzhong Xu, and Ning Zhang. Non-concentrated aqueous electrolytes with organic solvent additives for stable zinc batteries. *Chemical Science*, 12(16):5843–5852, 2021.

[15] Longsheng Cao, Dan Li, Enyuan Hu, Jijian Xu, Tao Deng, Lin Ma, Yi Wang, Xiao-Qing Yang, and Chunsheng Wang. Solvation structure design for aqueous Zn metal batteries. *Journal of the American Chemical Society*, 142(51):21404–21409, 2020.

[16] Ahmad Naveed, Huijun Yang, Jun Yang, Yanna Nuli, and Jiulin Wang. Highly reversible and rechargeable safe Zn batteries based on a triethyl phosphate electrolyte. *Angewandte Chemie International Edition*, 58(9):2760–2764, 2019.

[17] Xueyang Song, Huibing He, Mohammad Hossein Aboonasr Shiraz, Hongzheng Zhu, Ali Khosrozadeh, and Jian Liu. Enhanced reversibility and electrochemical window of Zn-ion batteries with an acetonitrile/water-in-salt electrolyte. *Chemical Communications*, 57(10):1246–1249, 2021.

[18] Nana Chang, Tianyu Li, Rui Li, Shengnan Wang, Yanbin Yin, Huamin Zhang, and Xianfeng Li. An aqueous hybrid electrolyte for low-temperature zinc-based energy storage devices. *Energy & Environmental Science*, 13(10):3527–3535, 2020.

[19] Jingwen Zhao, Jian Zhang, Wuhai Yang, Bingbing Chen, Zhiming Zhao, Huayu Qiu, Shanmu Dong, Xinhong Zhou, Guanglei Cui, and Liquan Chen. "Water-in-deep eutectic solvent" electrolytes enable zinc metal anodes for rechargeable aqueous batteries. *Nano Energy*, 57:625–634, 2019.

[20] Weina Xu, Kangning Zhao, Wangchen Huo, Yizhan Wang, Guang Yao, Xiao Gu, Hongwei Cheng, Liqiang Mai, Chenguo Hu, and Xudong Wang. Diethyl ether as self-healing electrolyte additive enabled long-life rechargeable aqueous zinc ion batteries. *Nano Energy*, 62:275–281, 2019.

[21] Guoqiang Ma, Licheng Miao, Yang Dong, Wentao Yuan, Xueyu Nie, Shengli Di, Yuanyuan Wang, Liubin Wang, and Ning Zhang. Reshaping the electrolyte structure and interface chemistry for stable aqueous zinc batteries. *Energy Storage Materials*, 47:203–210, 2022.

[22] Fangwang Ming, Yunpei Zhu, Gang Huang, Abdul-Hamid Emwas, Hanfeng Liang, Yi Cui, and Husam N Alshareef. Co-Solvent Electrolyte Engineering for Stable Anode-Free Zinc Metal Batteries. *Journal of the American Chemical Society*, 144(16):7160–7170, 2022.

[23] Bhaskar Kakoty, Rishikesh Vengarathody, Srimayee Mukherji, Vinita Ahuja, Anjana Joseph, Chandrabhas Narayana, Sundaram Balasubramanian, and Premkumar Senguttuvan. Two for one: propylene carbonate co-solvent for high performance aqueous zinc-ion batteries–remedies for persistent issues at both electrodes. *Journal of Materials Chemistry A*, 2022.

[24] Junmei Wang, Wei Wang, Peter A Kollman, and David A Case. Automatic atom type and bond type perception in molecular mechanical calculations. *Journal of Molecular Graphics and Modelling*, 25(2):247–260, 2006.

[25] Christopher I Bayly, Piotr Cieplak, Wendy Cornell, and Peter A Kollman. A well-behaved electrostatic potential based method using charge restraints for deriving atomic charges: The RESP model. *The Journal of Physical Chemistry*, 97(40):10269–10280, 1993.

[26] William L Jorgensen, Jayaraman Chandrasekhar, Jeffry D Madura, Roger W Impey, and Michael L Klein. Comparison of simple potential functions for simulating liquid water. *The Journal of Chemical Physics*, 79(2):926–935, 1983.

[27] Marina Macchiagodena, Marco Pagliai, Claudia Andreini, Antonio Rosato, and Piero Procacci. Upgraded AMBER force field for zinc-binding residues and ligands for predicting structural properties and binding affinities in zinc-proteins. *ACS Omega*, 5(25):15301–15310, 2020.

[28] Leandro Martínez, Ricardo Andrade, Ernesto G Birgin, and José Mario Martínez. Packmol: A package for building initial configurations for molecular dynamics simulations. *Journal of Computational Chemistry*, 30(13):2157–2164, 2009.

[29] Mark James Abraham, Teemu Murtola, Roland Schulz, Szilárd Páll, Jeremy C Smith, Berk Hess, and Erik Lindahl. GROMACS: High performance molecular simulations through multi-level parallelism from laptops to supercomputers. *SoftwareX*, 1:19–25, 2015.

[30] Tom Darden, Darrin York, and Lee Pedersen. Particle Mesh Ewald: An n log (n) method for Ewald sums in large systems. *J. Chem. Phys.*, 98(12):10089–10092, 1993.

[31] Berk Hess, Henk Bekker, Herman JC Berendsen, and Johannes GEM Fraaije. LINCS: A linear constraint solver for molecular simulations. *J. Comput. Chem.*, 18(12):1463–1472, 1997.

[32] Giovanni Bussi, Davide Donadio, and Michele Parrinello. Canonical sampling through velocity rescaling. *The Journal of Chemical Physics*, 126(1):014101, 2007.

[33] Herman JC Berendsen, JPM van Postma, Wilfred F Van Gunsteren, ARHJ DiNola, and Jan R Haak. Molecular dynamics with coupling to an external bath. *The Journal of Chemical Physics*, 81(8):3684–3690, 1984.

[34] Michele Parrinello and Aneesur Rahman. Polymorphic transitions in single crystals: A new molecular dynamics method. *Journal of Applied physics*, 52(12):7182–7190, 1981.

[35] M. J. Frisch, G. W. Trucks, H. B. Schlegel, G. E. Scuseria, M. A. Robb, J. R. Cheeseman, G. Scalmani, V. Barone, G. A. Petersson, H. Nakatsuji, X. Li, M. Caricato, A. V. Marenich, J. Bloino, B. G. Janesko, R. Gomperts, B. Mennucci, H. P. Hratchian, J. V. Ortiz, A. F. Izmaylov, J. L. Sonnenberg, D. Williams-Young, F. Ding, F. Lipparini, F. Egidi, J. Goings, B. Peng, A. Petrone, T. Henderson, D. Ranasinghe, V. G. Zakrzewski, J. Gao, N. Rega, G. Zheng, W. Liang, M. Hada, M. Ehara, K. Toyota, R. Fukuda, J. Hasegawa, M. Ishida, T. Nakajima, Y. Honda, O. Kitao, H. Nakai, T. Vreven, K. Throssell, J. A. Montgomery, Jr., J. E. Peralta, F. Ogliaro, M. J. Bearpark, J. J. Heyd, E. N. Brothers, K. N. Kudin, V. N. Staroverov, T. A. Keith, R. Kobayashi, J. Normand, K. Raghavachari, A. P. Rendell, J. C. Burant, S. S. Iyengar, J. Tomasi, M. Cossi, J. M. Millam, M. Klene, C. Adamo, R. Cammi, J. W. Ochterski, R. L. Martin, K. Morokuma, O. Farkas, J. B. Foresman, and D. J. Fox. Gaussian 16 Revision C.01, 2016. Gaussian Inc. Wallingford CT.

[36] Todd Keith Roy Dennington and John Millam. GaussView. *Semichem Inc*, 2009.

[37] Aleksandr V Marenich, Christopher J Cramer, and Donald G Truhlar. Universal solvation model based on solute electron density and on a continuum model of the solvent defined by the bulk dielectric constant and atomic surface tensions. *The Journal of Physical Chemistry B*, 113(18):6378–6396, 2009.

[38] Stephan Ehrlich, Jonas Moellmann, Werner Reckien, Thomas Bredow, and Stefan Grimme. System-dependent dispersion coefficients for the DFT-D3 treatment of adsorption processes on ionic surfaces. *ChemPhysChem*, 12(17):3414–3420, 2011.

[39] Nan Wang, Yang Yang, Xuan Qiu, Xiaoli Dong, Yonggang Wang, and Yongyao Xia. Stabilized rechargeable aqueous zinc batteries using ethylene glycol as water blocker. *ChemSusChem*, 13(20):5556–5564, 2020.

[40] Huihui Yan, Xikun Zhang, Zhengwei Yang, Maoting Xia, Chiwei Xu, Yiwen Liu, Haoxiang Yu, Liyuan Zhang, and Jie Shu. Insight into the electrolyte strategies for aqueous zinc ion batteries. *Coordination Chemistry Reviews*, 452:214297, 2022.

[41] Richard Payne and Ignatius E Theodorou. Dielectric properties and relaxation in ethylene carbonate and propylene carbonate. *The Journal of Physical Chemistry*, 76(20):2892–2900, 1972.

[42] Doudou Feng, Faqing Cao, Lei Hou, Tianyu Li, Yucong Jiao, and Peiyi Wu. Immunizing aqueous Zn batteries against dendrite formation and side reactions at various temperatures via electrolyte additives. *Small*, 17(42):2103195, 2021.

[43] R Naejus, D Lemordant, R Coudert, and P Willmann. Excess thermodynamic properties of binary mixtures containing linear or cyclic carbonates as solvents at the temperatures 298.15 K and 315.15 K. *The Journal of Chemical Thermodynamics*, 29(12):1503–1515, 1997.

Chapter 7

Summary and Future Outlook

Being the main medium of storage of energy, batteries are critical to the adoption and widespread usage of alternative sources of power to replace fossil fuels. Research in improving battery technology focus both on the electrodes and the electrolytes. The work presented in this thesis has focused on the latter. In particular, using computational methods, we have studied aspects of high concentration electrolytes (HCE), which overcome some of the shortcomings of the low concentration electrolytes (LCE). At present, LCEs are more commonly used. We have used sulfolane, a promising polar aprotic organic solvent in order to study the structure and transport phenomena in HCEs. The study of HCEs forms the bulk of the work presented in this thesis. In addition to the study of HCEs, a particular combination of organic and aqueous solvents is also explored in the dilute salt concentration limit.

7.1 Summary

In the introductory **Chapter 1**, we set the scene by giving an outline of the current state of knowledge of HCE structure and transport phenomena. We also discussed some computational tools and statistical quantities used in this thesis.

In **Chapter 2**, we derived a parameter set for an effective force field that quantitatively captures the transport and physicochemical properties of liquid sulfolane. Specifically, we derived non-bonded Lennard-Jones parameters and average DDEC6 atomic-site charges for sulfolane in its liquid phase. These can be used in classical molecular dynamic simulations. In order to carry over the force field developed here for sulfolane to the study of transport phenomenon in sulfolane-based HCEs, it was particularly important to arrive at accurate predictions of transport in sulfolane itself. Our refined force field was shown to achieve this better than other common force fields.

Due to the large viscosity of HCEs, their ionic conductivity is low, and a molecular-level understanding of the transport mechanism in them remains incomplete. We use the refined force field for sulfolane obtained in Chapter 2 to study various concentrations of $LiBF_4$ in sulfolane battery electrolytes in **Chapter 3**. Having achieved near quantitative agreement to experimental values in transport properties, Li-ion hopping was confirmed to be one possible transport mechanism of ions in HCEs. Further, Li-ions were found to bear an affinity to *hop+diffuse* to previously occupied Li-ion sites. Anion-rich nano-heterogeneities in a marginally solvent-rich HCE was found to comprise of Li-ions bridged by anions. To the best of our knowledge, we derive the first ever liquid-state non-H^+ ion-hopping free energy barrier, and characterise its transition state. Lastly, we perform MD simulations of crystalline HCEs as a parallel to liquid HCEs to further our understanding of the hopping mechanism in the two.

Chapter 3 used Li-ion based HCEs as their object of study, where lithium is a metal that is relatively scarce in the Earth's crust. **Chapter 4** takes up Na-ion based HCEs, sodium being the closest alternative to lithium, and a metal that is far more abundant than lithium. **Chapter 4A** presents a refined force field for the bis(fluorosulfonyl)imide (FSI) anion. This improved FSI force field is suitable for use across Li and Na-ion based battery electrolytes, and in combination with ionic liquid cations such as $[C_2MIM][FSI]$. This force field predicts density to a similar accuracy as the CL&P force field, but predicts transport properties such as diffusion coefficients and ionic conductivity to much better. The refined FSI force field is used in **Chapter 4B** to do a comparative study of the structure and transport of Li-ion and Na-ion based HCEs. We showed that the diffusion coefficients and ionic conductivity in Na-ion based electrolytes are an order of magnitude lower than those in Li-ion based ones, particularly at high salt concentrations. This is due to the larger solvation radius of the former. We also found that ions in Li-based HCEs have a greater propensity to hop than their Na-ion counterparts. This is due to the higher Einstein frequency of Li-ions. Despite the abundance of sodium in the Earth's crust, the very poor conductivity of pure Na-ion HCEs make them an unviable option for immediate application. In **Chapter 4C**, we studied a mixed alkali electrolyte to overcome the poor transport properties of pure Na based HCEs discovered in the previous sub-chapter. We found a monotonic improvement in transport properties as the fraction of Na-ions replaced by Li-ions is increased; an effect that is found to be more pronounced in HCEs than in LCEs. We found that Li-ions carry an increasing fraction of the current as more Na-ion were replaced by Li-ions. We also discovered that the structural underpinings of the above was linked to the sensitivity of the alkali-ion cage identity's dependence on the lithium content of the electrolyte. While Li-ion cages loosened with increase in lithium content of the electrolyte, Na-ion cages were largely indifferent to the same.

In **Chapter 5**, we examined ligand-bridged bicatonic complexes that form in pure and mixed cation solvents, such as those discussed in Chapters 4B and 4C, respectively. Using AIMD simulations, we showed (to the best of our knowledge) the first evidence for the presence of stable cation pair complexes in both Na-based (as predicted from RDFs) and Li-based (not predicted by RDFs) HCEs. We also find that such complexes are more likely to be composed of Na-ions than Li-ions. It is also seen that some FSI anion atoms that do not usually coordinate with monocationic/mononuclear alkali ion complexes do so in some of the cation pair complexes. We found evidence of Li-NFSI and Li-FFSI associations in cation complexes, although these subtler features need further examination. A study of free energies of formation showed that anion containing clusters have shorter inter-alkali distances and are more stable than solvent containing complexes. It was also found that when the number of shared ligands is large ($\sim\geq 4$), the cationic complex stability decreases; this may be remedied by replacing one of the anions by a solvent molecule.

A possible means by which to overcome many of the limitations of HCEs is to replace the carbonate solvents of electrolytes with water. Dilute aqueous electrolytes, however, have their own shortcomings, stemming primarily from parasitic reactions at the anode. The final chapter of this thesis, **Chapter 6**, describes a work done in collaboration with experimentalists, in which we show that, and theoretically explain why, the addition of propylene carbonate (PC) as a cosolvent to water remedies many of the limitations of a pure aqueous electrolyte such as that found in rechargeable aqueous zinc ion batteries. Experiments have shown that even a relatively small amount of PC in the aqueous electrolyte greatly improved the Coulombic efficiency and cycling stability of the battery. Classical MD simulations reason that such an effect is due to two factors.

(a) PC enters the zinc solvation shell and greatly increases the fraction of non-hexa-aquo complexes. Non-hexa aquo complexes preferentially undergo reduction to form a smoother and more hydrophobic carbonate and anion-derived SEI on the zinc anode.

(b) PC scavenges H_2O molecules from the zinc solvation shell and the bulk liquid through its interactions with water via hydrogen bonds. This reduces the free water content of the electrolyte and thus the dissolution of the cathode.

7.2 Future Outlook

Several interesting and potentially fruitful avenues exist to extend the work done in this thesis.

The force field obtained in **Chapter 2** for sulfolane may, by means of minor modifications, be extended to capture the transport and physicochemical properties of the whole class of sulfones. As an extension to **Chapter 3**, of particular interest would be to study the characteristics of "higher-order" hops that involve multiple ligand exchanges and chain-like networks and aggregates. As part of a deeper exploration of the hopping mode of transport, we also need to experiment with different salt and solvent choices to determine the best combinations to reduce the activation barriers to hopping without reducing salt concentrations and losing the benefits of HCEs. Rotational van Hove correlation functions for anions and solvent molecules may expose their role in promoting Li-ion hopping and ligand exchange. This may also therefore prove to be a worthwhile subject of investigation.

Chapter 4 showed how the ionic conductivity of Na-ion HCEs can be improved through replacing some fraction of Na-ions with Li-ions. It would be interesting to find out if starting from a pure Li-ion HCE, the replacement of some fraction of Li-ions with some other cation can improve the transport properties of Li-ion based HCEs even further such that the main shortcoming of low ionic conductivity in HCEs is addressed. Replacing a fraction of Li-ions with some other cation whose metal form is abundant would significantly reduce the cost of Li-ion HCE-based batteries as well.

Another potentially constructive direction to extend the exploration of cation pair complexes initiated in **Chapter 5** is to estimate the populations of various types of cation pair clusters from classical MD simulations. Further, it is worth investigating whether some ligand-bridged cation pairs join to form networks or aggregates which enhance the conduction of alkali-ions in the electrolyte.

In **Chapter 6** we saw that even when the electrolyte is composed of PC at 30% by weight, the amount of water displaced from the zinc-solvation shell on an average, is very little. The affinity of zinc-ions for water is very large. Therefore, it is meaningful to hunt for a co-solvent with small and polar molecules, which form a liquid with a high dielectric constant comparable to water. Water molecules need to be paralleled in these crucial aspects. The molecules of such a co-solvent would be stronger competitors to water molecules for a place in the zinc-ion solvation shell than PC molecules. The hunt for an appropriate co-solvent must therefore continue.

Appendix A

Appendix to Chapter 2

A.1 Determination of gas-phase DDEC6 charges

Gas-phase DDEC6 charges [1] were obtained from single molecule quantum chemical gas-phase optimization, followed by wave-function determination, both of which were carried out in Gaussian 16 [2]. This procedure is in contrast with the procedure used to obtain charges in Ref. 3. Subsequently in our procedure, charge-partitioning was carried out using Chargemol software [4] using the wavefuction file as input. The charges obtained were averaged over all atoms of the same atom-type to obtain average gas-phase DDEC6 charges given in Table A.1.

Atom type	q (e)
SFO	1.21259
OFO	-0.62659
CS1	-0.32635
CS2	-0.12475
HC1	0.14217
HC2	0.09352

Table A.1: Single-molecule gas-phase atomic-site DDEC6 charges, q (e), used in the MD run from which independent snapshots were chosen for liquid-phase DDEC6 charge calculation. These gas-phase DDEC6 charges were also used for total potential energy calculation for potential energy surfaces of the refined force field presented in figure 2.2 of chapter 2.

A.2 Charge distribution obtained in liquid-phase DDEC6 charge calculation

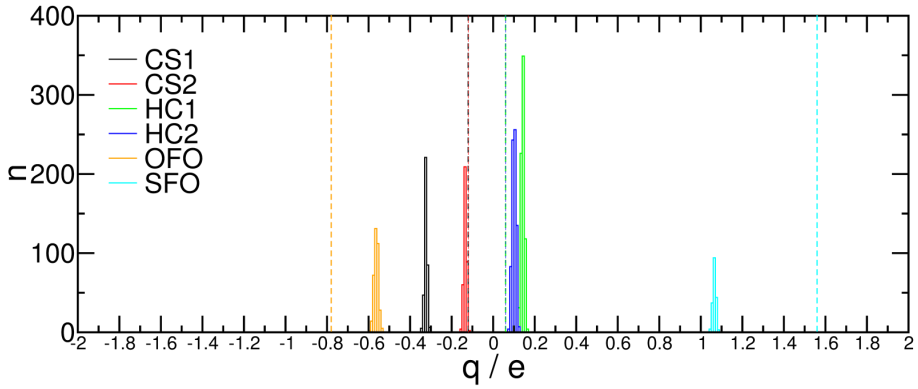

Figure A.1: Distribution of charges, (q) according to atom types, obtained from seven liquid phase snapshots, energy minimized within quantum density functional theory. Subsequently, the electron density obtained thus, was used to derive atomic site charges. n is the count of a bin of width 0.01 e. Dashed lines represent the charges of the force field from which the current force field was developed [3]. Snapshots were chosen from the MD simulation as described in the main manuscript at temperature T = 303 K and pressure p = 1 bar. The narrow distributions of the site charges justify the use of a non-polarizable force field. Differences in the mean values of liquid phase site charges from the corresponding gas phase values indicates the need to derive charges from condensed phase simulations.

A.3 Bonded parameters

The equilibrium values of bond lengths and angles of sulfolane were obtained from the geometry optimization of a single-molecule, at MP2/aug-cc-pvdz level of theory (see Tables A.2 and A.3). The bond and angle force-constants were used as given in Ref. 3.

Bond type	r_0	k_b
SFO-OFO	1.497	10660.832
SFO-CS1	1.893	3941.328
CS1-CS2	1.534	2242.624
CS2-CS2	1.545	2242.624
CS1-HC1	1.099	2769.808
CS2-HC2	1.016	2769.808

Table A.2: Bond parameters used in the refined force field. Equilibrium bond-length r_0 (Å) and force-constant k_b (kJ·mol^{-1}·Å^{-2}) of equation 2.1 of chapter 2.

Angle type	θ_0	k_θ
OFO–SFO–OFO	120.77	1941.38
OFO–SFO–CS1	109.34	1740.54
CS1–SFO–CS1	95.83	1631.76
CS2–CS1–SFO	104.46	1389.09
CS1–CS2–HC2	110.80	313.21
CS2–CS1–HC1	113.98	313.21
HC1–CS1–HC1	111.06	276.14
HC2–CS2–HC2	108.12	276.14
CS2–CS2–HC2	110.80	313.21
CS2–CS2–CS1	106.12	836.80
SFO–CS1–HC1	106.23	313.21

Table A.3: Angle parameters used in the refined force field. Equilibrium angle θ_0 (degree) and force-constant k_θ (kJ·mol^{-1}·rad^{-2}) of equation 2.1 of chapter 2.

A.4 Additional MD details

Temperature	Force field	NPT averaged box-length (Å)
303	Force field of Ref. 3	49.8647
303	OPLS	50.3709
303	This work	49.8082
313	This work	49.9531
323	This work	50.1071
348	This work	50.5048
373	This work	50.9340
398	This work	51.3757

Table A.4: Averaged box-sizes from NPT production from different force fields. Box-lengths for simulations using the refined force field at different temperatures and at pressure p = 1 bar are also reported. These box-sizes were used for NVT runs on which majority of the analyses were conducted.

A.5 Example of block average calculation: density

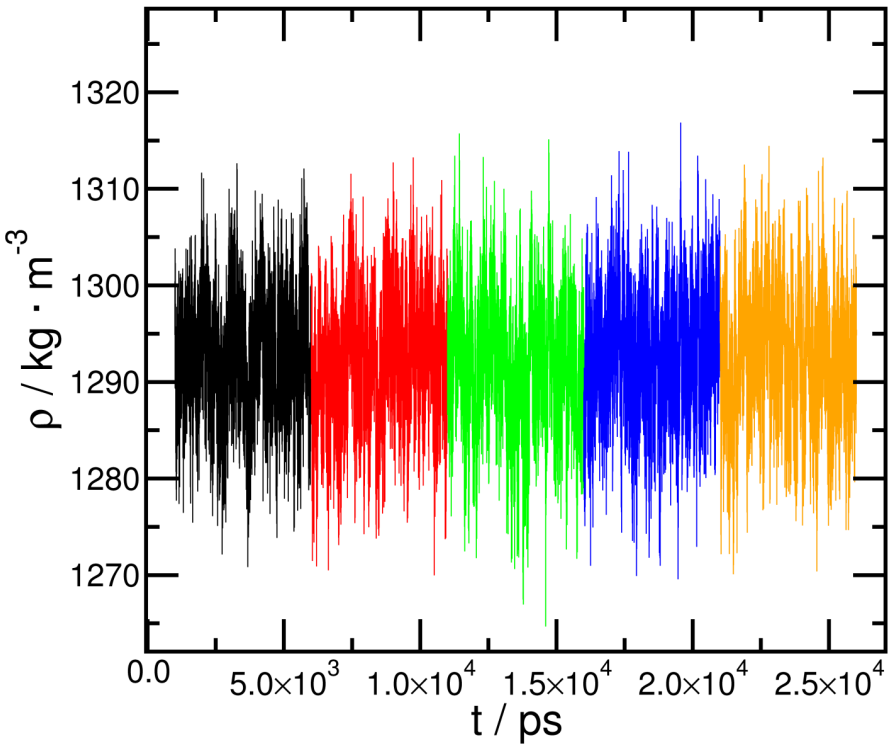

Figure A.2: Density as a function of time (from 1 ns to 26 ns) of the NPT production run of the refined force field reported in this work. The run was conducted at temperature T = 303 K, and pressure p = 1 bar. Each block is represented by a different color. The blocks are assumed to be independent as in Ref. 5.

Average density, $\rho = \frac{\sum_{i=1}^{N_{blocks}} \rho_{i,avg}}{N_{blocks}}$

Standard deviation on the average density is $U = \left(\frac{\sum_{i=1}^{N_{blocks}} (\rho_{i,avg} - \rho)^2}{N_{blocks}(N_{blocks}-1)} \right)^{1/2}$

Here, $\rho_{i,avg}$ is the average density of block i, N_{blocks} is the number of blocks = 5 (in this case). Number of timesteps comprising each independent block, S_{prod} = 5000 density points (one per picosecond). ρ is the mean density averaged over individual blocks. ρ is reported along with calculated uncertainty U in an interval form in chapter 2 with a confidence level of 0.95 (k=2).

A.6 Additional radial distribution function plots

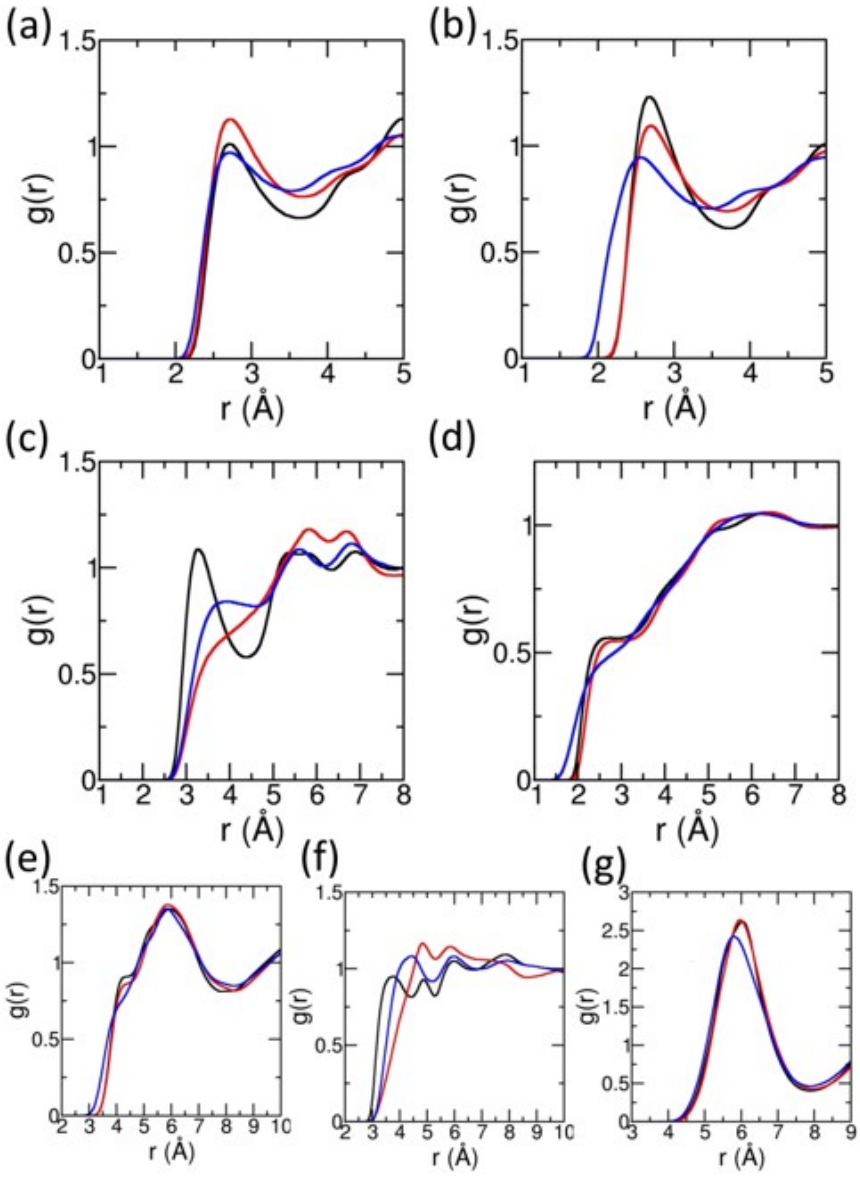

Figure A.3: Intermolecular radial distribution function between the following groups of atoms - (a) OFO-HC2, (b) OFO-any H, (c) OFO-OFO, (d) any H-any H, (e) any C-any C, (f) SFO-OFO, and (g) Center of ring - Center of ring. Black - Ref. 3, red - OPLS, and blue - this work.

A.7 Details for single-molecule volume calculation

The volume of a single MP2/aug-cc-pvdz optimized molecule was calculated in a method similar to that in Ref. 6, i.e. a Monte-Carlo method for calculating volume was employed. The volume calculation was carried out in the Gaussian 16 [2] software, using the 'volume 'keyword. The electron-density was obtained through a calculation performed using B3LYP/6-311++g(d,p) level of theory and basis-set. The convergence criterion requested was 10^{-6} for energy and 10^{-7} for RMS density. A density envelope used was 0.001 e/bohr^3. Since, molecular volume of sulfolane was calculated only to obtain a rough estimate of its size, we do not report this number as a true estimate of its size.

A.8 Uncertainty calculation for heat of vaporization

Average heat of vaporization $\Delta H = \frac{\sum_{i=1}^{N_{sample}} \Delta H_{i,avg}}{N_{sample}}$;

Standard deviation on the average heat of vaporization is $U = \left(\frac{\sum_{i=1}^{N_{sample}} (\Delta H_{i,avg} - \Delta H)^2}{N_{sample}(N_{sample}-1)} \right)^{1/2}$

Here, $\Delta H_{i,avg}$ is the average heat of vaporization of independent run i, calculated from the average total energy of the sulfolane molecule $E_{gas,i}$ in the i^{th} run. N_{sample} is the number of independent runs = 3 (in this case). S_{prod} = 30000 is the number of total energy points per independent run (one every picosecond). E_{liq}, the average total energy of a sulfolane molecule in the liquid state, was obtained from a single NVT run in the respective force field and is a constant across the independent calculations of ΔH for a given force field. ΔH is the mean heat-of-vaporization averaged over three independent runs. ΔH with calculated uncertainty U is reported in an interval form in the main manuscript with a confidence level of 0.95 (k=2).

A.9 Calculation of Surface Tension - Details

To calculate surface tension, a pre-equilibrated cubic simulation box containing 800 molecules was stretched along the z-axis (150 Å) by approximately three times its size along the x or y–axis ($\approx$ 50 Å). Surface tension was estimated from three independent NVT runs (N_{sample} = 3), of run length 10 ns each. i.e., S_{prod} = 10000000 timesteps. Three independent runs of duration of 100 ns (S_{prod} = 100000000) was needed for the simulations using the force field of Ref. 3 to account for the time required for the various pressure

components to equilibrate in this high viscosity force field. Components of the pressure tensor were saved at every timestep (1 fs). Surface tension, γ, was calculated using the relation $\gamma = l_z/4(2P_{zz} - P_{xx} - P_{yy})$ as in Ref. 7, where P_{xx}, P_{yy} and P_{zz} are the diagonal components of the stress tensor, and l_z is the length of the simulation box along the z–axis.

A.10 Shear viscosity

A.10.1 Calculation of shear viscosity

The shear viscosity(η) was calculated from the Green-Kubo relation as given in Ref. 8 and defined in equation A-1. Here, $P_{\alpha\beta}$ is the $\alpha\beta$ off-diagonal ($\alpha \neq \beta$) component of the pressure tensor. k_B is the Boltzmann constant, T is temperature, V is the volume of the system, and t is time. An example for the pressure tensor correlation function is shown in Figure A.4.

$$\eta(t) = \frac{V}{k_B T} \int_0^t \langle P_{\alpha\beta}(t') \cdot P_{\alpha\beta}(0) \rangle dt' \tag{A-1}$$

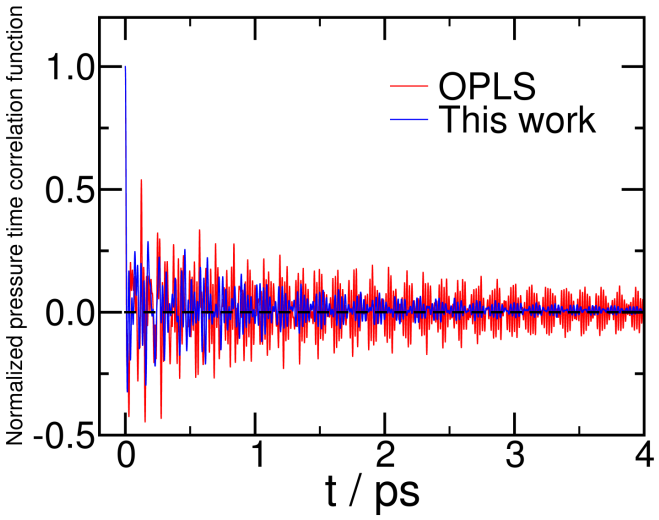

Figure A.4: The pressure tensor correlation function for the OPLS force field and from this work at state point temperature T = 303 K, and pressure p = 1 bar.

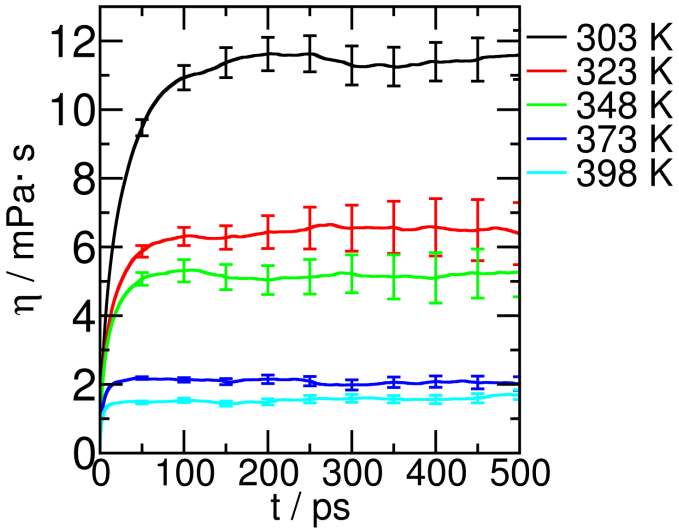

Figure A.5: Graphical representation of equation A-1 as a function of temperature. Data from the force field refined in this study

A.10.2 Calculation of mean shear viscosity and uncertainty on the mean - Details

Five independent trajectories for viscosity calculation corresponding to each force field were performed with pressure components dumped every timestep (1 fs). Each run was in turn divided into four blocks for viscosity calculation from equation A-1, while considering each block to be independent. A total of twenty independent runs of length 5 ns each were obtained. Error bars on the running integral obtained from averaging over twenty independent running integrals was calculated at an interval of 50 ps. To report a single value for viscosity, we consider the mean running integral of viscosity up to 500 ps. We divide the steady portion of the running integral (200 ps to 500 ps) into three blocks (N_{sample} = 3) of 100 ps duration each (S_{prod} = 100000 steps). Through block averaging method, we arrive at the mean shear viscosity, and the uncertainty on the average, just as we did for density.

A.11 Diffusion constant

A.11.1 Defining the diffusive regime

The mean-squared displacement ($\langle|\Delta\mathbf{r}|^2\rangle$) grows with time-interval (t) according to a general expression: $\langle|\Delta\mathbf{r}|^2\rangle = 6Dt^{\beta}$. Here, β is an exponent determining the regime of dynamics of the system, and D is the self-diffusion constant. When exponent β reaches ≈ 1 in time interval t, the system is said to have entered the diffusive regime from a sub-diffusive regime.

$$\beta(t) = \frac{d\log(\langle|\Delta\mathbf{r}|^2\rangle)}{d\log(t)} \tag{A-2}$$

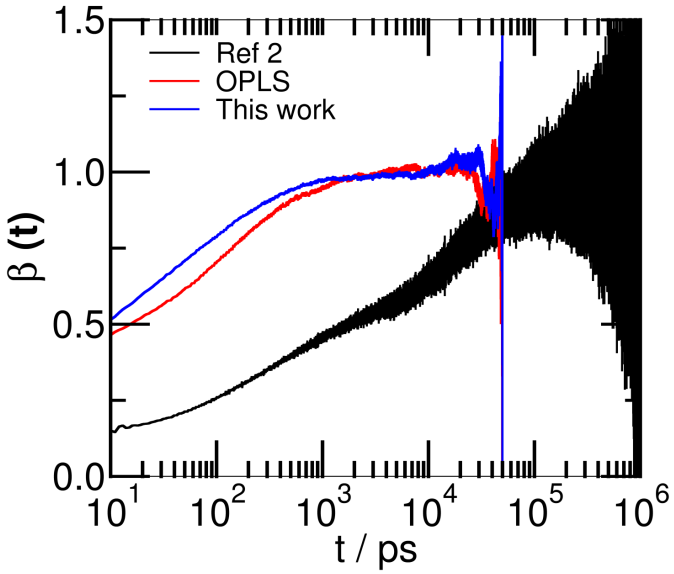

Figure A.6: β as a function of time is used to determine the diffusive regime in each force field studied. Data at temperature T = 303 K, and pressure p = 1 bar.

A.11.2 Calculation of mean diffusion constant & uncertainty on mean

The $\beta(t) \approx 1$ of MSD was divided into three blocks ($N_{blocks} = 3$) of duration 8 ns each ($S_{prod} = 8000$ one point per picosecond). The blocks were considered to be independent. The slope ($6Dt$) of MSD in these blocks were averaged to arrive at the self-diffusion constants D quoted in Tables 2.10 and 2.11 of chapter 2. In the liquid modelled with the force field of Ref. 3, sulfolane was found to be extremely sluggish and sub-diffusive, with a nominally estimated diffusion constant which was at least two orders of magnitude less than the experimental value at 303 K. For this force field alone, a $1\mu s$ run was required to obtain a sufficient run-length in the diffusive regime for calculating the self-diffusion constant. In this case, MSD (200 ns to 500 ns) was divided into three blocks of length 100 ns each (S_{prod} = 100000). The calculation of uncertainty U on the block averaged diffusion constant was calculated in a manner very similar to the calculation of uncertainty for density.

Bibliography

[1] Thomas A Manz and Nidia Gabaldon Limas. Introducing DDEC6 atomic population analysis: Part 1. Charge partitioning theory and methodology. *RSC Advances*, 6(53):47771–47801, 2016.

[2] MJ ea Frisch, GW Trucks, HB Schlegel, GE Scuseria, MA Robb, JR Cheeseman, G Scalmani, VPGA Barone, GA Petersson, HJRA Nakatsuji, et al. Gaussian 16, 2016.

[3] Kaoru Dokko, Daiki Watanabe, Yosuke Ugata, Morgan L Thomas, Seiji Tsuzuki, Wataru Shinoda, Kei Hashimoto, Kazuhide Ueno, Yasuhiro Umebayashi, and Masayoshi Watanabe. Direct evidence for Li ion hopping conduction in highly concentrated sulfolane-based liquid electrolytes. *The Journal of Physical Chemistry B*, 122(47):10736–10745, 2018.

[4] Nidia Gabaldon Limas and Thomas A Manz. Introducing DDEC6 atomic population analysis: part 4. efficient parallel computation of net atomic charges, atomic spin moments, bond orders, and more. *RSC Adv.*, 8(5):2678–2707, 2018.

[5] Yushan Zhang, Yong Zhang, Mark J McCready, and Edward J Maginn. Evaluation and refinement of the general amber force field for nineteen pure organic electrolyte solvents. *J. Chem. Eng. Data*, 63(9):3488–3502, 2018.

[6] Nicholas J Brooks, Franca Castiglione, Cara M Doherty, Andrew Dolan, Anita J Hill, Patricia A Hunt, Richard P Matthews, Michele Mauri, Andrea Mele, Roberto Simonutti, et al. Linking the structures, free volumes, and properties of ionic liquid mixtures. *Chem. Sci.*, 8(9):6359–6374, 2017.

[7] Gustavo A Orozco, Othonas A Moultos, Hao Jiang, Ioannis G Economou, and Athanassios Z Panagiotopoulos. Molecular simulation of thermodynamic and transport properties for the H_2O+NaCl system. *J. Chem. Phys.*, 141(23):234507, 2014.

[8] Yong Zhang, Akihito Otani, and Edward J Maginn. Reliable viscosity calculation from equilibrium molecular dynamics simulations: A time decomposition method. *J. Chem. Theory Comput.*, 11(8):3537–3546, 2015.

Appendix B

Appendix to Chapter 3

B.1 System details

B.1.1 System composition and thermodynamic state details

The system details used for various concentrations simulated here are as in Table B.1.

Salt concentration (M)	Molar ratio $LiBF_4$:SUL	No. of $LiBF_4$ molecules	No. of sulfolane molecules	Temperature (K)	Force-field used	NPT equilibrated box length Å
5.76	1:1.35	160	216	303	This work	35.58
5.76	1:1.35	160	216	303	Ref. 1	35.84
4.26	1:2.00	160	320	303	This work	39.50
4.26	1:2.00	160	320	333.15	This work	39.58
4.26	1:2.00	160	320	363.15	This work	39.70
3.04	1:3.00	160	480	303	This work	44.14
2.36	1:4.00	160	640	303	This work	47.79
1.25	1:8.00	160	1280	303	This work	59.16
1.00	1:10.08	208	2096	303	This work	69.65
1.00	1:10.08	208	2096	303	Ref. 1	69.77
0.51	1:20.00	208	4160	303	This work	86.70
0.21	1:50.00	16	800	303	This work	49.88
0.00	0:800	0	800	303	This force-field [2]	49.81

Table B.1: System details

Li-BF4-SUL crystal

Watanabe et al. were able to grow single crystals of the LiBF4:SUL binary mixture at 1:1 mole fraction from the liquid of the same composition (7.93 M salt concentration) [1]. The melting point of the crystal is around 40^0C. In this work, we have carried out unbiased and biased MD simulations of the 1:1 $LiBF_4$:SUL crystal to study the coordination environment

of the Li-ions and the free energy of hop events. Table B.2 lists the details of the equilibrated simulation box of the crystal studied in this work.

Nomenclature	Molar ratio $LiBF_4$:SUL (l,m,n)	No. of $LiBF_4$ molecules	No. of sulfolane molecules	Temperature (K)	Force-field used	NPT equilibrated box dimensions (x, y, z) (Å)
Cryst-216	1:1 (12,6,3)	864	864	303	This work	61.69, 51.81, 58.91
Cryst-216	1:1 (12,6,3)	864	864	223	experimental	61.87, 53.12, 55.01
Cryst-120	1:1 (8,5,3)	480	480	303	This work	41.13, 43.18, 58.91
Cryst-120	1:1 (8,5,3)	480	480	223	experimental	41.25, 44.27, 55.01

Table B.2: System details. The supercells were created by replicating the unitcell ℓ, m, and n times along the a, b, and c lattice vectors respectively.

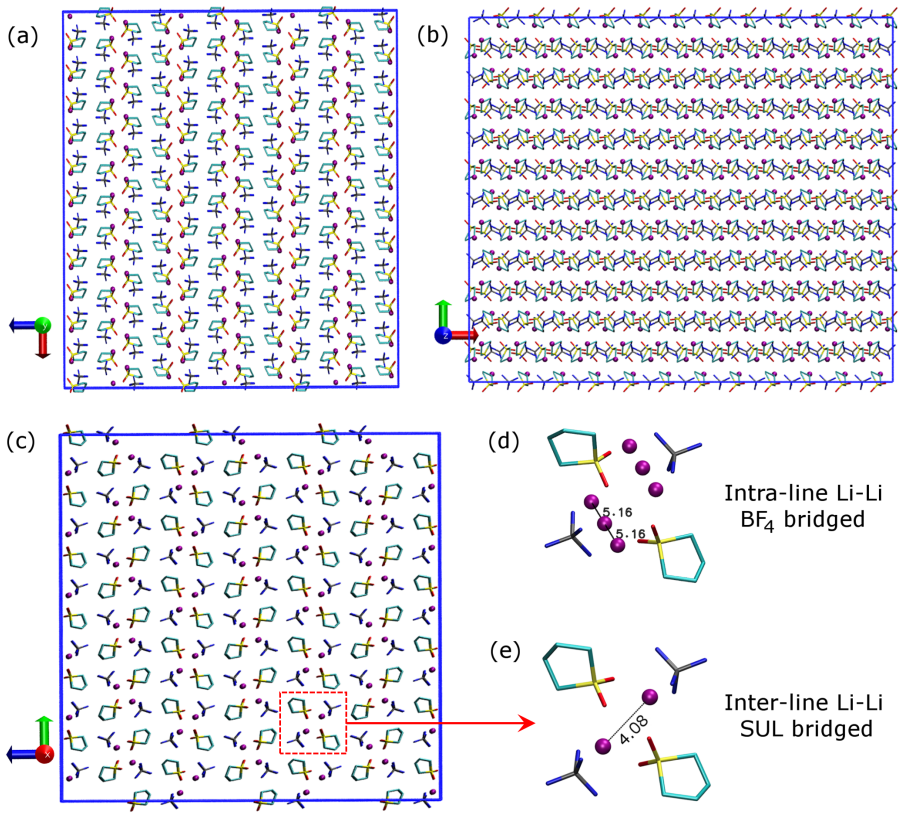

Figure B.1: The orthographic projections of the $12 \times 8 \times 3$ supercell of the experimental $LiBF_4$:SUL = 1:1 crystal structure along (a) Y axis, (b) Z axis and (c) X axis. The red, green and blue arrows (shown at the side of the projections) represent the X, Y and Z axis respectively. The X,Y,Z axes are along a,b,c lattice vectors respectively. The Li-ions are arranged in a straight line along the X axis and two such Li-ion lines which are nearest to each other are bridged by sulfolane molecules. The Li-ions which are bridged by a common ligand (BF_4) within each line are referred to as "intra-line" Li-Li and the Li-ions bridged by a common ligand (SUL) across two lines are referred to as "inter-line" Li-Li. Local coordination of Li-ions showing (d) intra-line Li-Li distance to be 5.16 Å, and (e) inter-line Li-Li distance to be 4.08 Å. The experimental crystal structure was taken from Ref. 1.

B.2 Analysis

B.2.1 Density

Concentration (M)	Molar ratio $LiBF_4$:SUL	Force-field	T (K)	ρ_{sim} (g/cc)	ρ_{exp} (g/cc) [1]
5.76	1:1.35	This work	303	1.516	1.475
5.76	1:1.35	Ref. 1	303	1.477	1.475
4.26	1:2.00	This work	303	1.460	1.424
4.26	1:2.00	This work	333.15	1.431	1.400
4.26	1:2.00	This work	363.15	1.402	1.378
3.04	1:3.00	This work	303	1.403	1.381
2.36	1:4.00	This work	303	1.400	1.356
1.25	1:8.00	This work	303	1.354	1.314
1.00	1:10.08	This work	303	1.343	1.304
1.00	1:10.08	Ref. 1	303	1.326	1.304
0.51	1:20.00	This work	303	1.322	1.284
0.21	1:50.00	This work	303	1.306	1.271
0.00	0:800.00	Ref. 2	303	1.292	1.263 [3]
0.00	0:800.00	Ref. 1	303	1.297	1.263 [3]

Table B.3: Density from simulations and those reported in experiments reported in Ref. 1 (unless otherwise stated) at pressure P = 1 bar.

B.2.2 Ionic conductivity

We used the Einstein relation (Equation A-1) [4] to compute the ionic conductivity at pressure P = 1 bar.

$$\Lambda = \frac{N_0 e^2}{6nk_BT} \lim_{t\to\infty} \frac{d}{dt} \sum_i \sum_j z_i z_j \langle [\mathbf{R_i}(t) - \mathbf{R_i}(0)] \cdot [\mathbf{R_j}(t) - \mathbf{R_j}(0)] \rangle \qquad \text{(A-1)}$$

Here, Λ is the molar conductivity, and $\mathbf{R}_i$(t) and $\mathbf{R}_j$(t) are the position vectors of the ith and jth ions at time interval t. Angular brackets refers to average over all possible time origins. z_i and z_j are the charge of the ith and jth ions. N_0 is the Avogadro constant, e, the elementary charge, n, the number of formula units of ions (number of cation-anion pairs), k_B, the Boltzmann constant, and T, the temperature. The value for ionic conductivity was

calculated by examining the linear region's slope of the total ionic displacement correlation (mostly of the last 50% of the first half of the data). This total ionic displacement correlation was found through the addition of individual contributions to it viz., cation-cation, cation-anion, and anion-anion displacement correlations. Example for the displacement correlation part of Equation A-1, averaged over all time origins, at 5.76 M, is shown in Figure B.2.

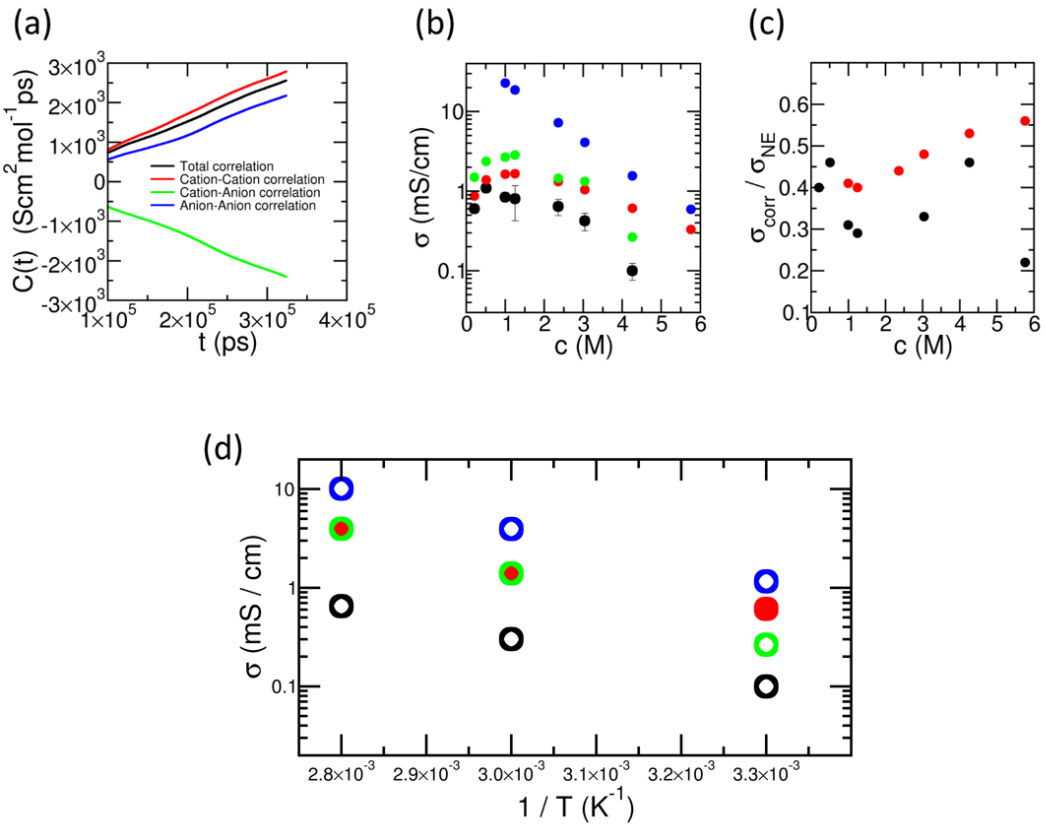

Figure B.2: (a) Individual ionic displacement correlation contributions to the total ionic conductivity. (b) Ionic conductivities from various methods; Black - inclusive of correlations from our simulations, red - experimentally reported in Ref. 1, green - NE conductivity from simulations, and blue - NE conductivity from experimental diffusion constants reported in Ref. 1. (c) Ratio of conductivity with correlations to NE conductivity from our simulations (black), and experimentally reported true conductivity to experimental NE conductivity (red) [1]. (d) Temperature dependence of ionic conductivity from simulations of this work and from experiments in Ref. 1. Black - simulation with correlation, red - experiment with correlation, green - Nernst Einstein conductivity from simulation, and Nernst Einstein conductivity from experiment.

We also calculated the simple molar Nernst-Einstein (NE) ionic conductivity (which ignores correlations between displacement of distinct ions) which is defined in Equation A-2).

$$\Lambda = \frac{N_0 e^2}{k_B T}(D_{cation} + D_{anion}) \tag{A-2}$$

Here, D_{cation} and D_{anion} are the self-diffusion coefficients of the cation (Li-ion) and BF_4 anion respectively.

To arrive at an estimate for the degree of ionic displacement correlations present in our systems as a function of salt concentration, we calculated the ratio of the ionic conductivity obtained from Equation A-1 to the NE conductivity obtained from the self-diffusion constants calculated from our simulations (see Section Self-diffusion constant). Correspondingly, we also calculated the same ratio from the experimentally reported data [1]. Data for the same is tabulated in Table B.4 and depicted in Figure B.2(b)-(c). The Li-Li displacement correlation contributes to a greater extent (see Figure B.2(a)) to the total conductivity than the anion-anion one, as expected at high salt concentrations. This tallies with the transference number of lithium reported in experiments (Table B.6).

The behaviour of ionic conductivity with concentration is captured well in our MD simulations (see Figure B.2(b)). Barring 5.76 M, in agreement with experiments (Figure B.2(c)), our simulations predict a high degree of correlation between inter-ionic displacements (ratio ≤ 0.7). Data for the two lowest concentrations were unavailable in experiments. However looking at the trend, we suspected that the ratio exhibits a non-monotonic behaviour close to 1 M. This non-monotonicity or increase in the ratio for concentrations greater than 1 M may be due to Li-ion hopping. The fact that Li-ion hopping becomes gradually more prominent as the concentration is raised above 1 M, implies that a larger fraction of ions tend to hop out of their cage through the exchange of ligands, leading to progressively less correlated ion transport.

Figure B.2(d) shows ionic conductivity at three temperatures (30 K apart) at 4.26 M. The activation energy calculated from the Arrhenius equation applied to our simulations (E_a = 3.21 kcal/mol) is in good agreement with that from experiments (E_a = 3.08 kcal/mol). Although the activation energy barrier calculated from ionic conductivity has several contributing factors which span over long length and timescales, it is important to note that the hopping energy barriers calculated from our simulations (where barriers are calculated for a very localized ion-jump over short length (1 to 4 Å) and timescales (1 to 4 ps)) are also in the range of 2 to 4 kcal/mol.

c(M)	MR	T(K)	$\sigma_{sim,corr}$	σ_{exp}	$\sigma_{sim,NE}$	$\sigma_{exp,NE}$	$\frac{\sigma_{sim,corr}}{\sigma_{sim,NE}}$	$\frac{\sigma_{exp}}{\sigma_{exp,NE}}$
5.76	1:1.35	303	0.005	0.33	0.02	0.59	0.25	0.56
4.26	1:2.00	303	0.10	0.61	0.26	1.16	0.38	0.52
4.26	1:2.00	333.15	0.30	1.72	1.40	3.94	0.21	0.44
4.26	1:2.00	363.15	0.65	3.64	3.95	10.1	0.16	0.36
3.04	1:3.00	303	0.42	1.04	1.33	2.16	0.32	0.48
2.36	1:4.00	303	0.64	1.32	1.45	2.97	0.44	0.44
1.25	1:8.00	303	0.80	1.66	2.84	4.16	0.28	0.40
1.00	1:10.08	303	0.84	1.63	2.68	3.95	0.31	0.41
0.51	1:20.00	303	1.09	1.38	2.36	-	0.46	-
0.21	1:50.00	303	0.60	0.87	1.49	-	0.40	-

c: concentration. MR: Molar ratio ($LiBF_4$:SUL). Ionic conductivity (Eq. A-1): $\sigma_{sim,corr}$. All σ are in units of (mS/cm).

Table B.4: Ionic conductivity of the electrolyte calculated from our simulations compared against experimental data of Ref. 1 at various concentrations of $LiBF_4$. NE is the Nernst-Einstein conductivity. Calculating the ionic conductivity in simulations employing the force-field of Ref. 1 was attempted, however, the highly sluggish nature of the system in this force-field did not permit an accurate estimate within our computational timescales investigated by us.

B.2.3 Self-diffusion constant

The mean-squared displacement (MSD) of ions and molecules were calculated using Equation A-3.

$$\langle|\mathbf{\Delta r}|^2\rangle(t) = \langle|\mathbf{R_i(t)} - \mathbf{R_i(0)}|^2\rangle \tag{A-3}$$

Angular brackets represent average over all molecules of the same type and that over all time origins. The self-diffusion constant was calculated from the slope of MSD, using Equation A-4.

$$\langle|\mathbf{\Delta r}|^2\rangle(t) = 6Dt \tag{A-4}$$

Here, D is the self-diffusion constant.

We learn the following from Figure B.3(a): One, the electrolyte at 5.76 M is much more sluggish than at 1 M. Two, although not sufficiently evident from the figure, when viewed alongside Table B.5, we see that the Li-ions diffuse faster than both BF_4 anions and sulfolane molecules at 5.76 M. However, at 1 M, they are slower than the sulfolane molecules.

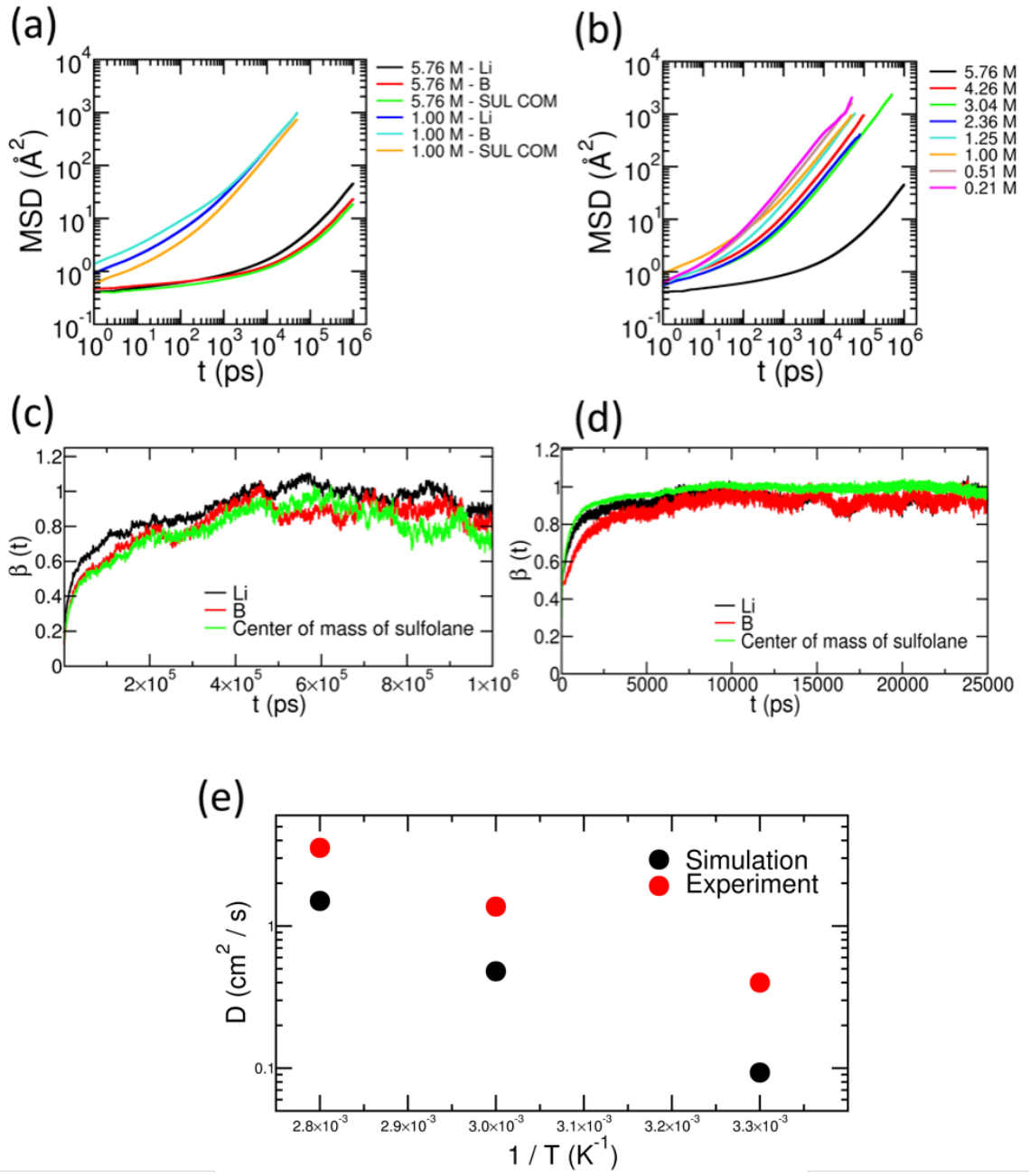

Figure B.3: (a) Mean-squared displacement (MSD) of Li-ion, Boron atom and the center of mass (COM) of sulfolane at two representative concentrations of 5.76 M and 1.00 M. (b) MSD of Li-ions at all concentrations. The factor β which defines the diffusive regime, for Li ion, boron atom and the COM of sulfolane at (c) 5.76 M and (d) 1.00 M. (e) Temperature dependence of self-diffusion constant of Li-ions at 4.26 M concentration of $LiBF_4$ in sulfolane.

Figure B.3(b) compares Li ion MSD at different concentrations. The solution at 5.76 M is far more sluggish than the remaining salt concentrations, although the MSD follows the expected trend with decrease in salt concentration. Table B.5 provides values of self-diffusion constant obtained from the present simulations and those from experiments

reported in Ref. 1. To accurately determine the diffusion constant of all species, we performed long runs for the system to attain the diffusive regime. To determine the diffusive regime in time and to know if a trajectory is long enough, we look for the duration of time where $\beta(t) = \frac{dlog(MSD)}{dlog(t)} \approx 1$. We calculate the slope of the MSD in Equation A-4 over this duration of time to calculate D. From Figure B.3(c) and (d), we see that quantity β at 5.76 M reaches a value close to unity at time intervals more than two orders of magnitude larger than that at 1 M.

c(M)	FF	T(K)	D_1	D_2	D_3	D_4	D_5	D_6	$\frac{D_3}{D_1}$	$\frac{D_4}{D_2}$	$\frac{D_5}{D_1}$	$\frac{D_6}{D_2}$
5.76	*	303	0.007	0.15	0.003	0.10	0.003	0.08	0.43	0.67	0.43	0.53
4.26	*	303	0.09	0.40	0.06	0.26	0.05	0.25	0.67	0.65	0.56	0.62
4.26	*	333.15	0.48	1.37	0.40	1.10	0.33	1.03	0.83	0.80	0.69	0.75
4.26	*	363.15	1.50	3.55	1.20	3.37	1.05	2.97	0.8	0.95	0.7	0.84
3.04	*	303	0.59	0.96	0.48	0.77	0.47	0.85	0.81	0.80	0.80	0.88
2.36	*	303	0.84	1.60	0.65	1.46	0.63	1.69	0.77	0.91	0.75	1.05
1.25	*	303	2.90	3.80	2.60	4.11	2.50	4.96	0.90	1.08	0.86	1.30
1.00	*	303	3.26	4.50	3.26	5.12	2.46	6.11	1.00	1.14	0.75	1.36
0.51	*	303	5.28	NA	5.99	NA	6.00	NA	1.13	NA	1.14	NA
0.21	*	303	7.44	NA	9.71	NA	8.17	NA	1.30	NA	1.10	NA
0.00	[2]	303	–	–	–	1.19	†	–	–	–	–	–
0.00	[1]	303	–	–	–	0.06	†	–	–	–	–	–

c: concentration. FF = Force field. $D_1 = D_{\text{Li,sim}}$ ($\times 10^{-7}$cm^2/s), $D_2 = D_{\text{Li,exp}}$ ($\times 10^{-7}$cm^2/s), $D_3 = D_{BF_4,sim}$ ($\times 10^{-7}$cm^2/s), $D_4 = D_{BF_4,exp}$ ($\times 10^{-7}$cm^2/s), $D_5 = D_{\text{SUL,sim}}$ ($\times 10^{-7}$cm^2/s), $D_6 = D_{\text{SUL,exp}}$ ($\times 10^{-7}$cm^2/s). * this work. † 14.72 extrapolated from Ref. 1.

Table B.5: Self-diffusion constant from the present simulations and from experiments reported in Ref. 1 at various concentrations of $LiBF_4$ at pressure P = 1 bar. Calculating the diffusion-constant from force-field of Ref. 1 was attempted, however due to the highly viscous nature of the electrolyte as represented by this force-field, β did not increase more than 0.7 and thus the system remained sub-diffusive within the simulation times investigated.

Although the difference in the self-diffusion coefficients obtained from our simulations and as reported in experiments of Ref. [1] is large at high concentrations, we believe that the difference has been reduced by orders of magnitude (and to computable values) by employing the force-field for sulfolane reported in Ref. [2], relative to attempts in the literature.

Transference numbers

Transference numbers of Li-ions ($t_{Li} = \frac{D_{Li}}{D_{Li}+DBF_4}$) (Table B.6) are enhanced with increase in concentration of Li-salt in line with literature on HCEs [1, 5, 6].

c(M)	Molar ratio $LiBF_4$/SUL	t_{sim}	t_{exp}
5.76	1:1.35	0.70	0.60
4.26	1:2	0.60	0.61
3.04	1:3	0.55	0.55
2.36	1:4	0.56	0.52
1.25	1:8	0.53	0.48
1.00	1:10.08	0.50	0.47
0.51	1:20	0.47	NA
0.21	1:50	0.43	NA

Table B.6: Transference numbers of Li-ions, t_{Li}, from simulations and experiments in Ref. 1

The transference numbers reported in Table B.6 do not account for correlations between non-self ion-displacements. These have been calculated using self-diffusion coefficients alone. The true transference numbers ($t_+, correlated$) account for these correlations. $t_+, correlated$ can be defined as : $t_+, correlated = \frac{\sigma_{--}\sigma_{++}-\sigma_{+-}{}^2}{\sigma_{--}(\sigma_{++}+\sigma_{--}-2\sigma_{+-})}$ [7]. Here, σ_{++}, σ_{--}, and σ_{+-} are the three components of ionic conductivity or the transport coefficients stemming from cation-cation, anion-anion, and cation-anion displacement correlations, respectively. The calculation of $t_+, correlated$ require multiple (of the order of 50), and long (hundreds of nanoseconds to microseconds) trajectories. These simulations and calculations would be too computationally expensive and were therefore beyond the scope of the thesis.

B.2.4 Non-Gaussian parameter

The non-Gaussian parameter is defined as:

$$\alpha_2(t) = \frac{3\langle \Delta \mathbf{R}(t)^4 \rangle}{5\langle \Delta \mathbf{R}(t)^2 \rangle^2} - 1 \tag{A-5}$$

Here, $\Delta \mathbf{R}$(t) is the displacement of a Li-ion over time-interval t. Average taken over all time origins possible for time interval t.

B.2.5 Self-part of the van Hove correlation function

The self-part of the van Hove correlation function is defined in Equation A-6.

$$G_s(r,t) = (1/N)\sum_{i=1}^{N}\langle\delta(|\mathbf{R_i}(t) - \mathbf{R_i}(0)| - r)\rangle \tag{A-6}$$

N is the total number of molecules of a particular type and r is the radial distance from $\mathbf{R}(0)$ for any particle of the chosen type. Remaining symbols are as defined in the previous section. Average taken over all time origins possible for time intervals t.

Figure B.4 shows $G_s(r,t)$ of Li-ions for a range of concentrations barring 5.76 M and 1 M whose data are presented in Chapter 3.

$G_s(r,t)$ for purely diffusive motion is defined in Equation A-7 [8].

$$G_s(r,t) = \frac{e^{\frac{-r^2}{4Dt}}}{4Dt^{\frac{3}{2}}} \tag{A-7}$$

In addition to the conclusions drawn from $G_s(r,t)$, Figure B.4 makes the systematically growing prominence of Li-ion hopping with increase in salt concentration, amply clear.

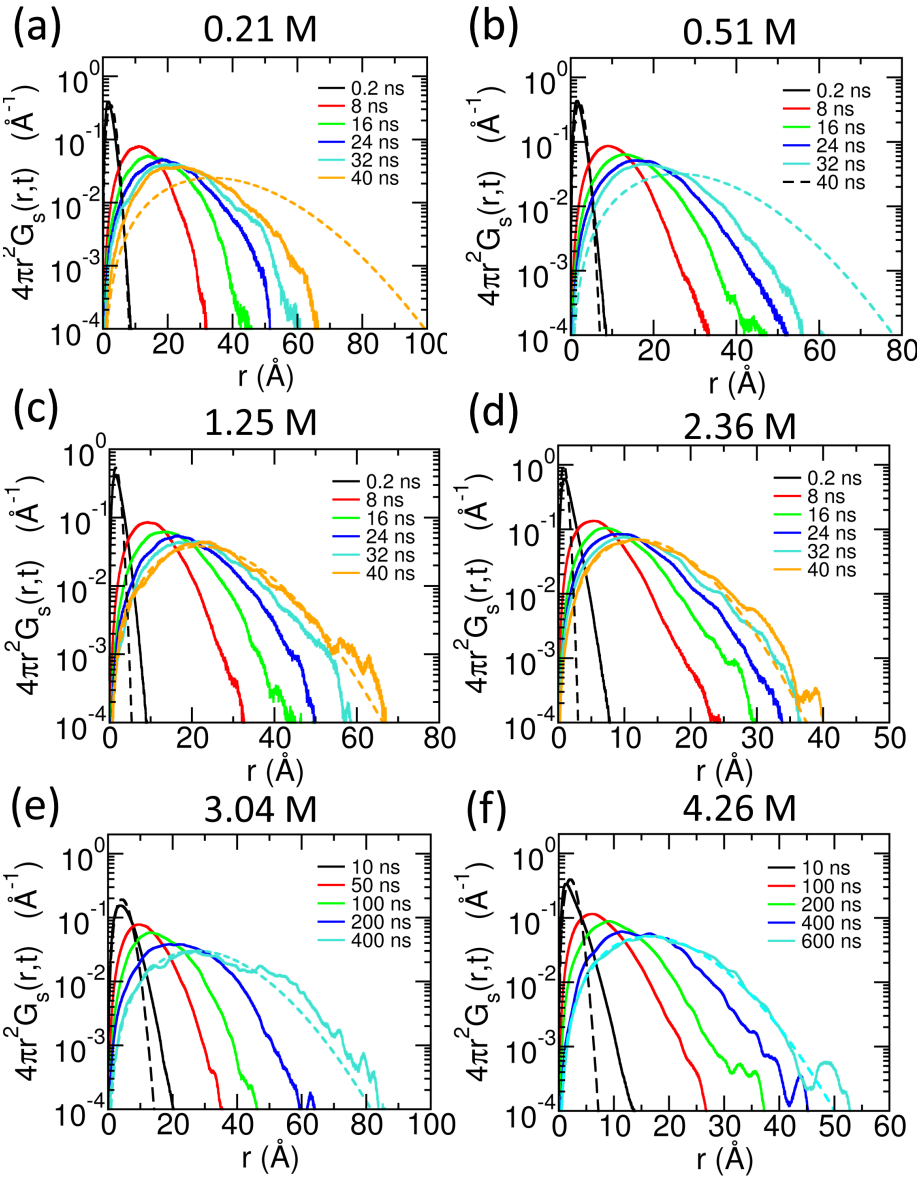

Figure B.4: (a)-(f) $G_s(r,t)$ for the different concentrations studied. $G_s(r,t)$ defined in Equation A-6 and $G_s(r,t)$ from Equation A-7 are represented by solid and dashed lines of the same color, respectively. Data reported at 303 K and 1 bar.

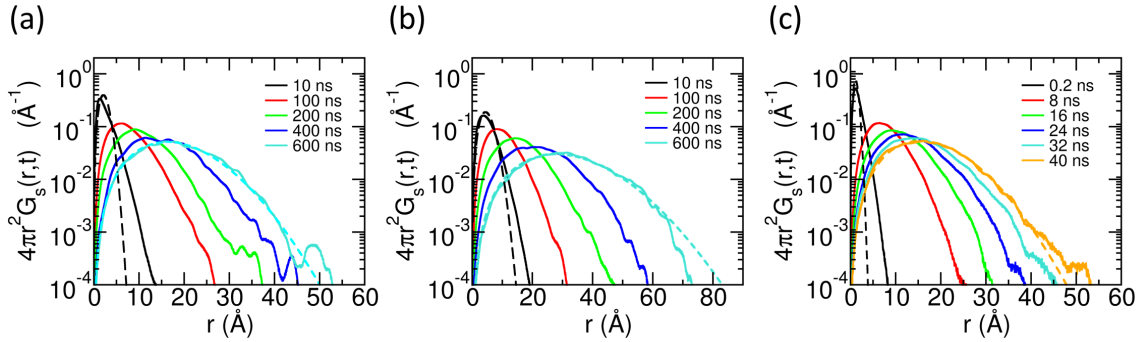

Figure B.5: $G_s(r,t)$ at 4.26 M at temperatures (a) T = 303 K, (b) T = 333.15 K, and (c) T = 363.15 K.

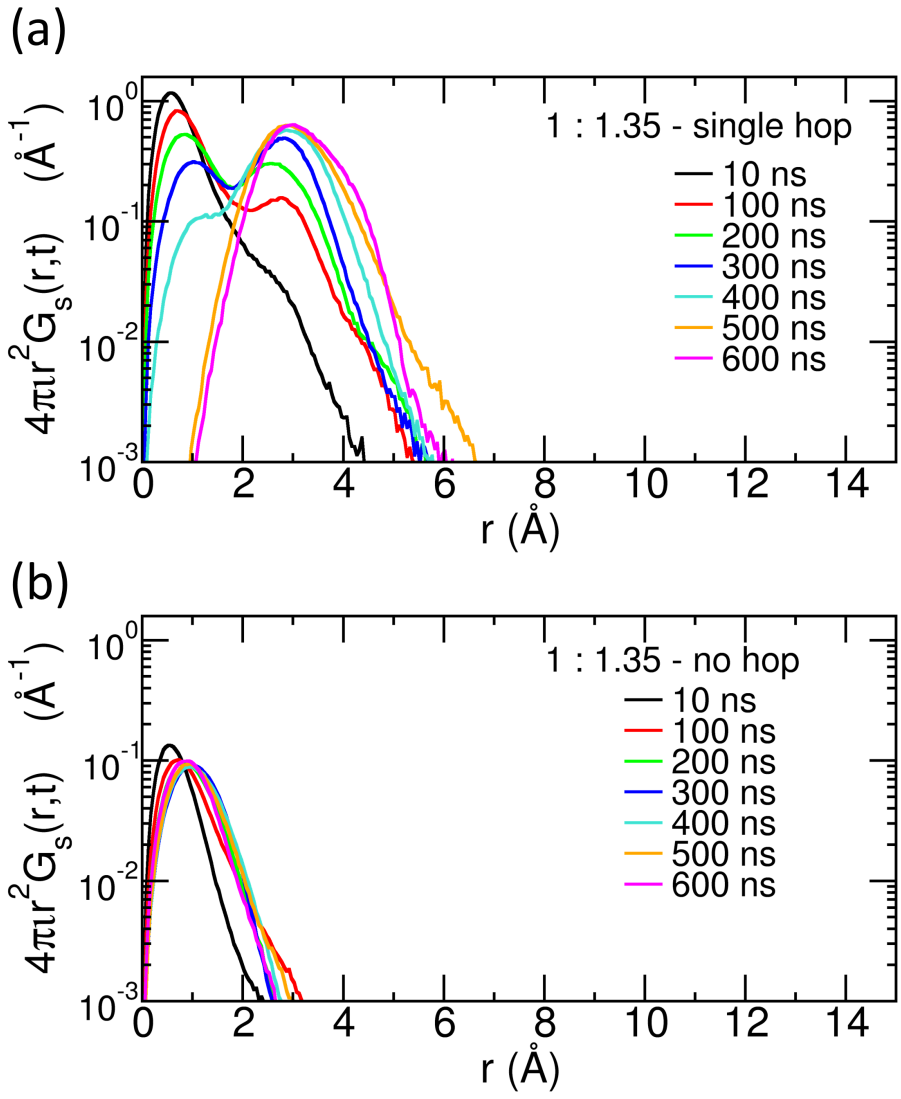

Figure B.6: Single-particle $G_s(r,t)$ for two different Li-ions at 5.76 M. A particle that typically performs (a) one hop and (b) no hop over the time interval of 600 ns.

Decreasing Li-salt concentration decreases the contribution of hopping to Li-ion transport (Figure B.4), and increases the distance over which the Li-ions are able to travel in the same interval of time. Increasing temperature has an effect very similar to the decrease in concentration (compare Figure B.5(b) with Figure B.4(e), and Figure B.5(c) with Figure B.4(d)).

At high concentrations, the dynamical heterogeneities in the molecular motions are large. This can be understood from investigating the single-particle $G_s(r,t)$ of Li-ions. Apart from Li-ions that hop multiple times, there are ions which hop once (Figure B.6(a)) and those that do not hop at all (Figure B.6(b)) over the long time intervals investigated.

B.2.6 Distinct-part of the van Hove correlation function

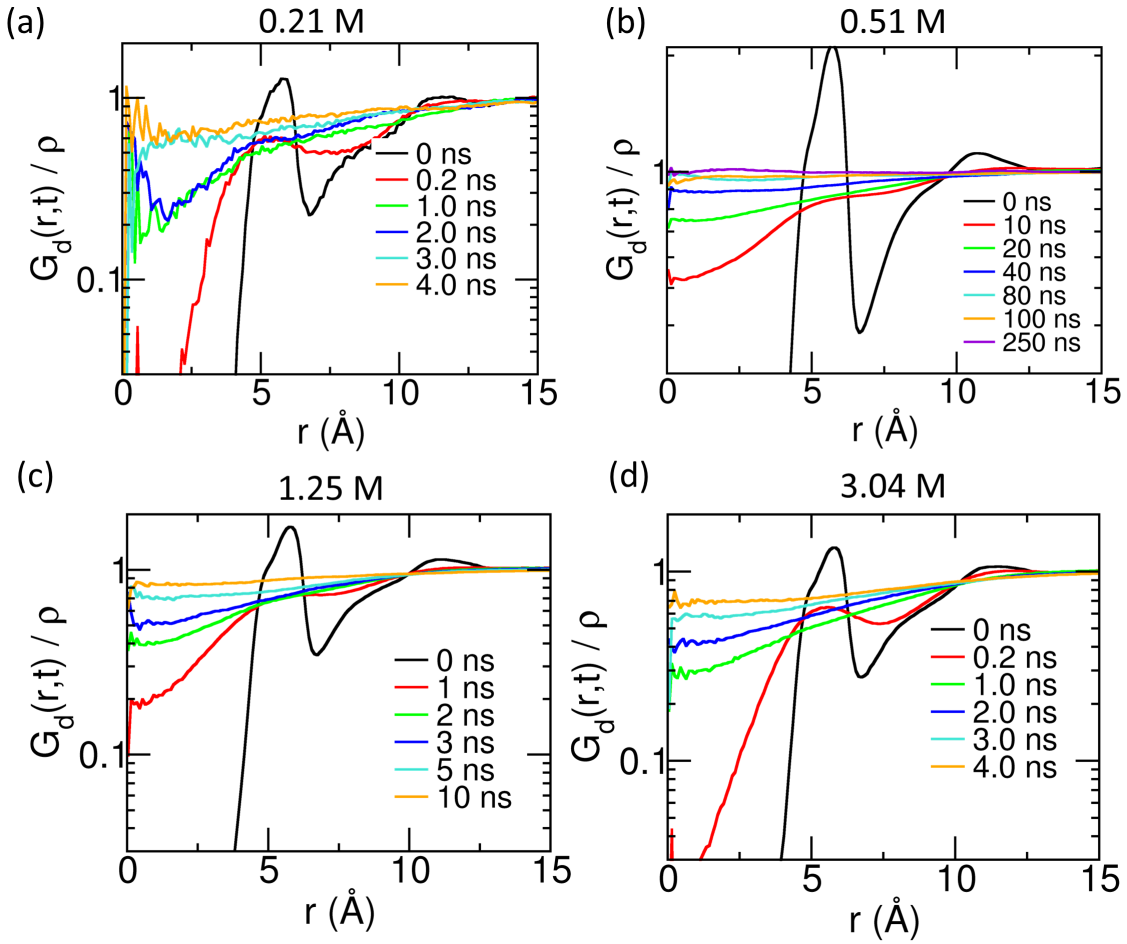

Figure B.7: $G_d(r,t)$ of Li-Li ions of the remaining salt concentrations at various time intervals at temperature T = 303 K and pressure P = 1 bar.

$$G_d(r,t) = (1/N)\sum_{i=1}^{N}\sum_{j\neq i}\langle\delta(|\mathbf{R_j}(t) - \mathbf{R_i}(0)| - r) \tag{A-8}$$

In a system of N Li-ions, considering the ith Li-ion at position $\mathbf{R}(0)$ at time origin 0, the radial distribution at time interval t of the remaining $N-1$ Li-ions ($j \neq i$) around the position $\mathbf{R}(0)$ is calculated. All symbols have their meanings as defined in prior sections. Average taken over all time origins possible for time interval t. $G_d(r,t)$ for concentrations other than for those shown in Chapter 3 are presented in Figure B.7.

The tendency to hop+diffuse to previously occupied Li-ion sites decreases with increase in temperature (Figure B.8).

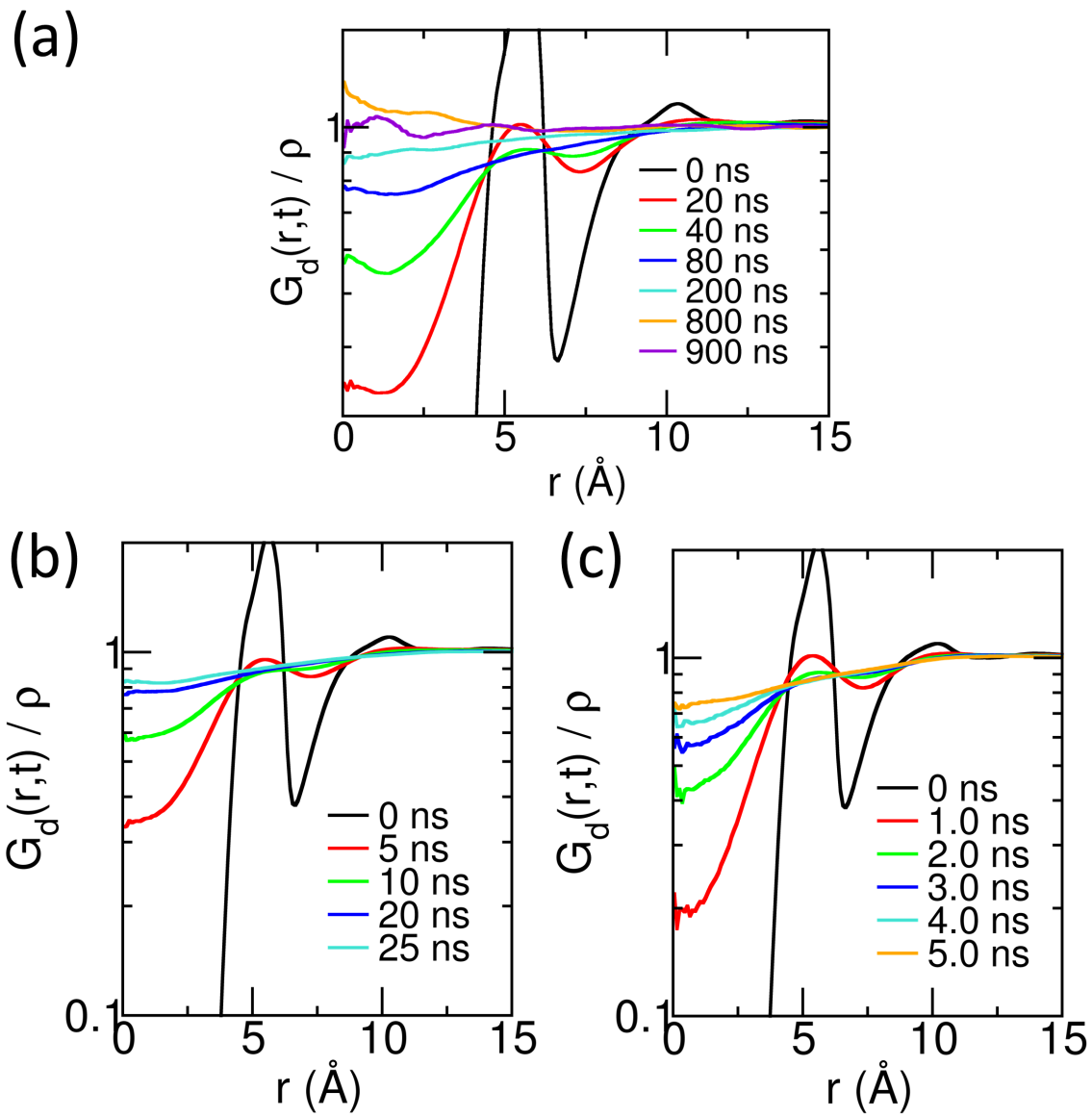

Figure B.8: $G_d(r,t)$ at 4.26 M, pressure P = 1 bar, and at temperatures (a) 303 K, (b) 333.15 K, and (c) 363.15 K.

B.2.7 Distribution of anions vs solvent molecules in the first solvation shell of Li-ions

Figure B.9(a)-(d) show that when the number of solvent molecules per solute (salt) molecules is eight or larger, the most preferred Li-ion first solvation shell composition is (O:F) = (4:0). A first solvation shell comprising exclusively of solvent molecules is most probable at these concentrations.

When there are between two and four solvent molecules per solute molecule, however, the most probable solvation shell composition is (O:F) = (3:1) and its relative probability increases with increase in salt concentration (Figure B.9(e)-(g)).

The relative probability of (O:F) = (2,2) also increases with increase in concentration until it becomes the most probable solvation structure at 5.76 M ($LiBF_4$:SUL=1:1.35) (Figure B.9 (h)), akin to the nearest neighbor structure in the $LiBF_4$:SUL=1:1 crystal (Figure B.1).

The concentration at which the changes in the composition of the solvation shell of Li-ions occur is dependent on the accuracy of the force-field. However, we expect that the qualitative trends and to a fair extent, the quantitative trends of these results should match with experiments.

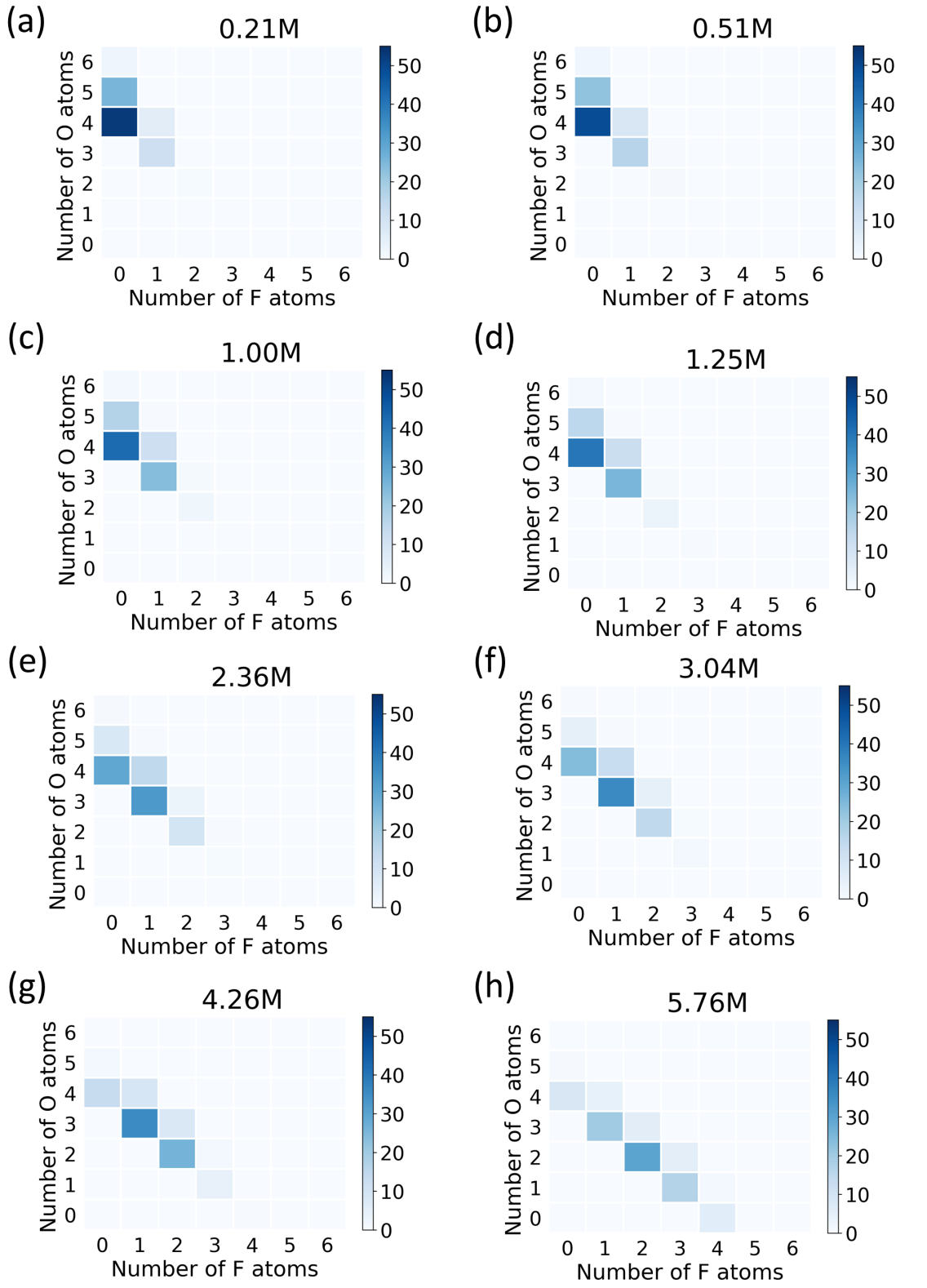

Figure B.9: The percentage composition of the first solvation shell of Li-ions at all concentrations.

B.2.8 Radial distribution functions (RDF) and coordination numbers.

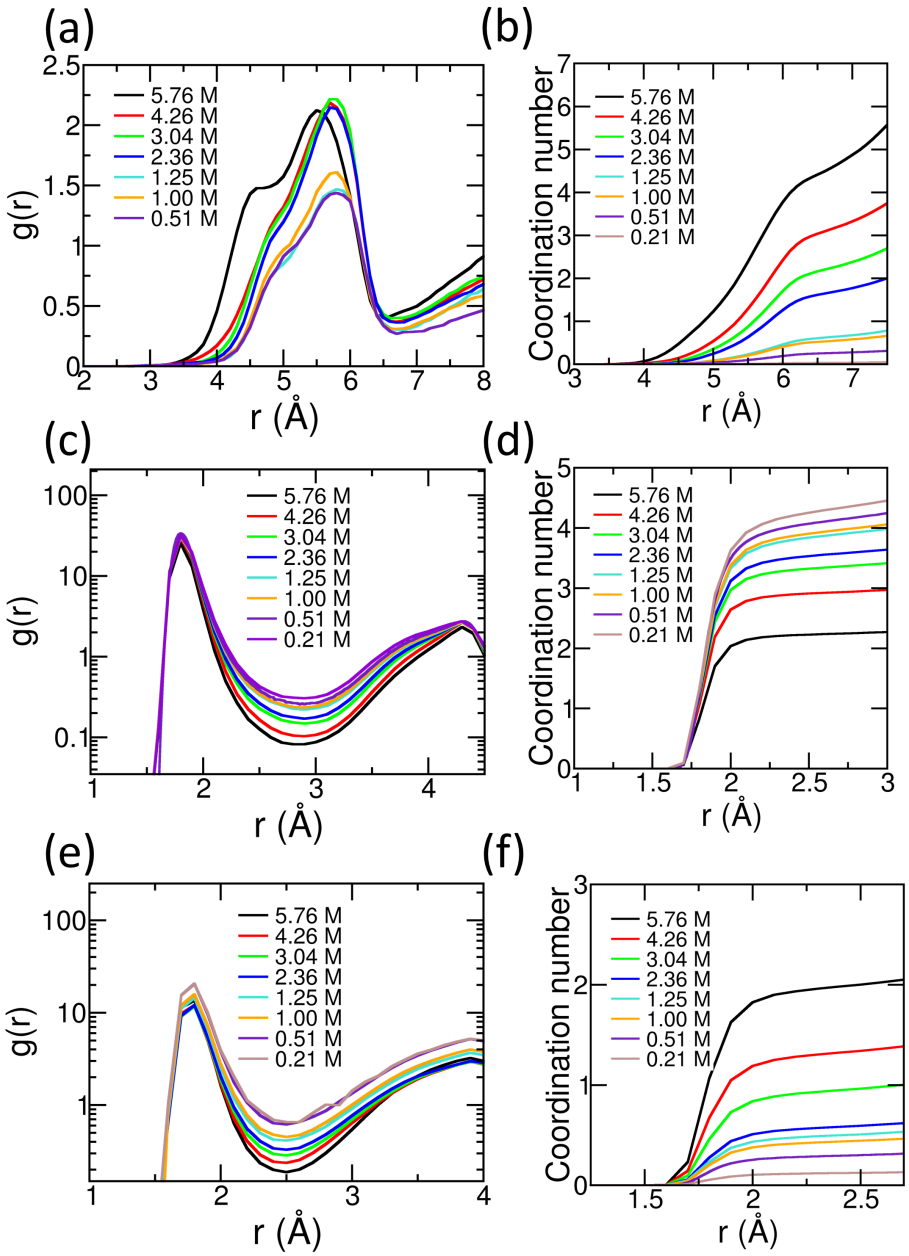

Figure B.10: Radial distribution functions (RDF) and running coordination numbers respectively of the following atom pairs - (a) & (b) Li-Li, (c) & (d) Li-O and (e) & (f) Li-F.

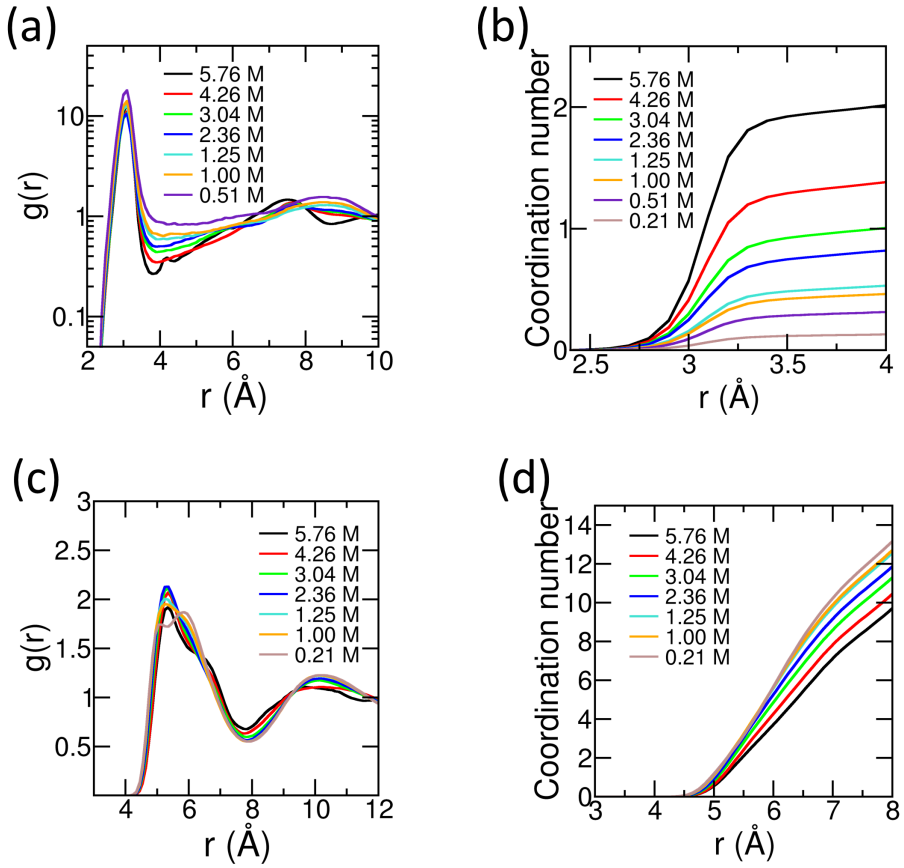

Figure B.11: Radial distribution functions (RDF) and running coordination numbers respectively of the following atom pairs - (a) & (b) Li-B, and (c) & (d) Sulfolane COM-Sulfolane COM.

Figure B.10(a), i.e., the Li-Li RDF, as expected, shows that with increase in salt concentration, the first peak shifts to the left (5.75 Å to 5.5 Å). Further, with an increase in salt concentration, a shoulder at around 4.7 Å emerges and is most prominent at 5.76 M concentration. This shoulder peak implies that there are two kinds of Li-ion environments on average at two slightly different distances around a central Li-ion. To understand what these two distances imply, we compare this RDF with the Li-Li RDF from a crystal of 1:1 composition. On examination of the near neighbor environment in the crystal, we see that the peak at around 5.5 Å distance is representative of Li-ions bridged by BF_4 anions in the crystal. We call this distance an *intra-line* distance. The left shoulder around 4.6 Å is representative of Li-ions bridged by a sulfolane molecule. We call this distance an *inter-line* distance in the crystal. Although two types of Li-ion environments exist even in liquids, the bridging environments which distinguish them in the crystal are not maintained in the liquid phase.

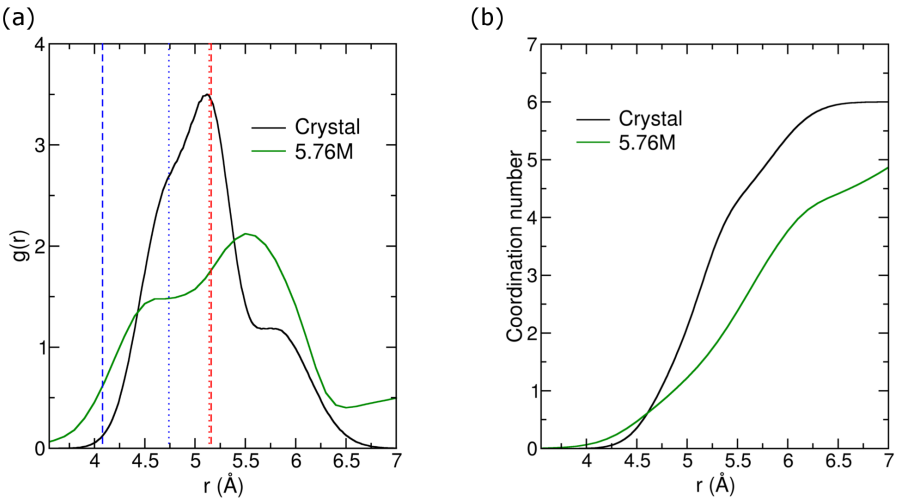

Figure B.12: Comparison of (a) radial distribution functions (RDF) and (b) running coordination numbers respectively of the crystal and of the 5.76 M liquid for Li-Li atom pairs. The blue and the red dashed vertical lines indicate the inter-line (4.08 Å) and intra-line (5.16 Å) Li-Li distance respectively in the experimental crystal structure. The blue and the red dotted vertical lines indicate the inter-line (4.74 Å) and intra-line (5.14 Å) Li-Li distance respectively in the crystal simulations in this work. The left shoulder in the crystal's Li-Li RDF is due to the inter-line Li-Li pairs and the main peak is due to the intra-line Li-Li peak. The presence of two humps in the 5.76 M liquid indicates the presence of two kinds of Li-ion environments.

Due to the larger size of a sulfolane molecule in comparison to the BF_4 ion, and also to the fact that the interactions of Li-ions with the former are weaker due to its charge neutral character, the Li-O first solvation shell distance (Figure B.10(c)) is larger than the Li-F first solvation shell distance (Figure B.10(e)). We also observe that these distances do not vary much with change in salt concentration.

With an increase in salt concentration, the Li-B first solvation shell radius becomes progressively better defined (Figure B.11(a)), as can be seen from the decrease of the value at the first minimum. With an increase in salt concentration, the first solvation shell radius of sulfolane COM - sulfolane COM moves very slightly to the left (Figure B.11(c)). As expected, the number of Li-ions coordinating a Li-ion in the first solvation shell increases with salt concentration (Figure B.10(b)). The first solvation structure of BF_4 anions and sulfolane molecules around a Li-ion pertaining to Figure B.11 can be better understood in Section B.2.7. Finally, as expected, we observe that the number of sulfolane COMs in the first solvation shell of Li-sulfolane COM reduces with an increase in salt concentration.

B.2.9 Computational details for Steered molecular dynamics runs

Li-hoppers were chosen from the equilibrium MD trajectory at 5.76 M. The initial and final positions of the Li-ions before and after the hop were identified. For a given Li-hopper, the vector connecting its initial and final positions was fixed as the pull direction. Independent runs had randomly assigned initial velocities for all atoms obtained from the Maxwell distribution at 303 K. In each run, the chosen lithium ion was pulled at a constant velocity with magnitudes in the range 0.05 to 0.5 Å/ps for different Li-ions. The force constant for the harmonic potential was taken to be in the range 2390 to 23900 kcalmol^{-1}ang^{-2}. An absolute reference point was used as the starting point for each of the four Li-ion's SMD run. The displacement of the center of mass of the system was removed at every step to remove any effects of the external force on the center of mass of the system (the system is at equilibrium). A time step of 1 fs was used to evolve the trajectories of all atoms with time. Positions of all atoms were dumped at every time step.

From the work done for the Li-ion to go from the initial state A to the final state B over a large number of runs. The total number of runs for each studied Li-hopper ranged from 1000 to 4000 runs. For each such Li-ion, the runs were divided into four blocks. The free energy profile estimated from each of the blocks pertaining to a given Li-ion, where averaged to arrive at the free energy profile and error-bars (standard deviation) shown in Figure 5. The free energy profile was calculated using the Jarzynski equality [9–12] defined below (Equation A-9).

$$e^{-\beta \Delta F_{AB}} = \langle e^{-\beta W_{AB}} \rangle \tag{A-9}$$

Here, ΔF is the equilibrium free energy difference between states A and B, W is the non-equilibrium work done to take the Li-ion from state A to B, and $\beta = \frac{1}{k_B T}$. Symbols have their usual meaning. An average is taken over all runs in one block of runs to arrive at the free energy profile ($\Delta F(z)$), where z is the reaction coordinate of the Li-ion. Here z is the component of the displacement from state A of the Li-ion along the fixed pull-direction. Profiles obtained from different blocks (of equal number of runs each) were averaged to arrive at the average free energy profile for a hop and to estimate the errors involved in the calculation.

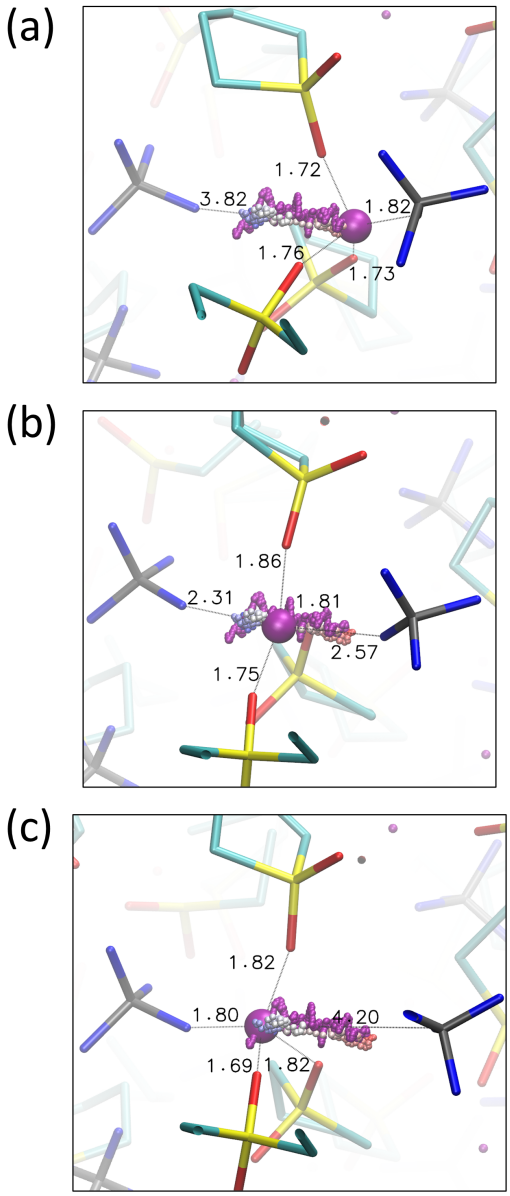

Figure B.13: A representative SMD trajectory shown with purple spheres is presented along with the equilibrium MD trajectory (shown from red spheres to blue spheres with progression of time). Snapshots shown correspond to the Li-ion (a) before the hop, (b) at the transition state, and (c) after the hop.

Free Energy profile of Li-ion hopping in Li-BF4-SUL crystal

Li-ion hopping in the crystal was studied using Cryst-120 system (Table B.2). From the NVT equilibrated configuration, one randomly chosen Li-ion (and one randomly chosen BF_4 ion to maintain charge neutrality) were removed to create a defect. This defect configuration was then equilibrated in the NVT ensemble for 100 ns.

There are two different kinds of Li-ions neighboring the Li defect position. Two intra-line Li-ions (bridged by BF_4 ions) and two inter-line Li-ions (bridged by SUL molecules). The average intra-line and inter-line Li-Li distance in an NVT simulation are around 5.14 Å and 4.74 Å respectively. So, it is expected that these two kinds of Li-ions would show different hopping free energy profiles.

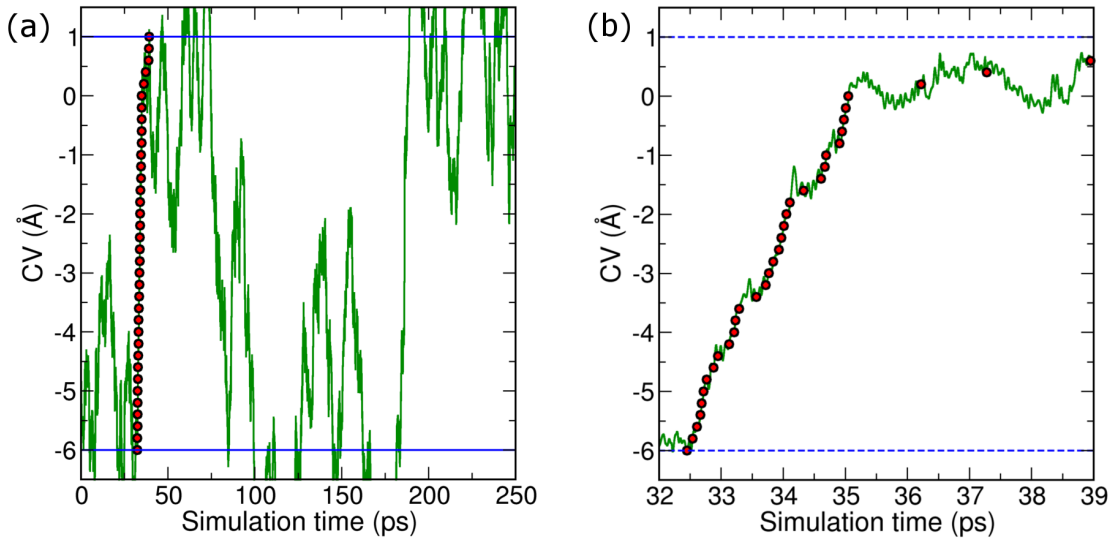

Figure B.14: The evolution of the collective variable (CV) over (a) the entire course of a metadynamics simulation, and (b) the short duration of the hop in the metadynamics run. The red circles represent the snapshots chosen as the window centers to carry out subsequent umbrella sampling simulations. This particular CV evolution is one of 10 independent metadynamics runs for an intra-line hop. Similar runs were carried out for inter-line hop as well.

The free energy profiles of each kind are obtained from a two step process. First, hops of each kind were constructed using metadynamics [13] simulations independently. The bias was applied on the Li-ion neighboring the defect position and in the direction towards the defect. The distance between the Li-ion and the defect position along the direction of the hop was chosen as the collective variable. A Gaussian potential of height 0.50 kJ/mol and sigma 0.005 Å was added, every 50 fs. Walls were added to keep the Li-ion from over-shooting the defect position and disturbing the rest of the system. Multiple independent metadynamics simulations, each starting from a different initial configuration,

were performed to generate 10 hops of each kind. Each of these hops were examined visually to select the best hop to be studied further via Umbrella Sampling. Note that the metadynamics simulations were performed only to generate the hop trajectories and not to obtain the free energy profile.

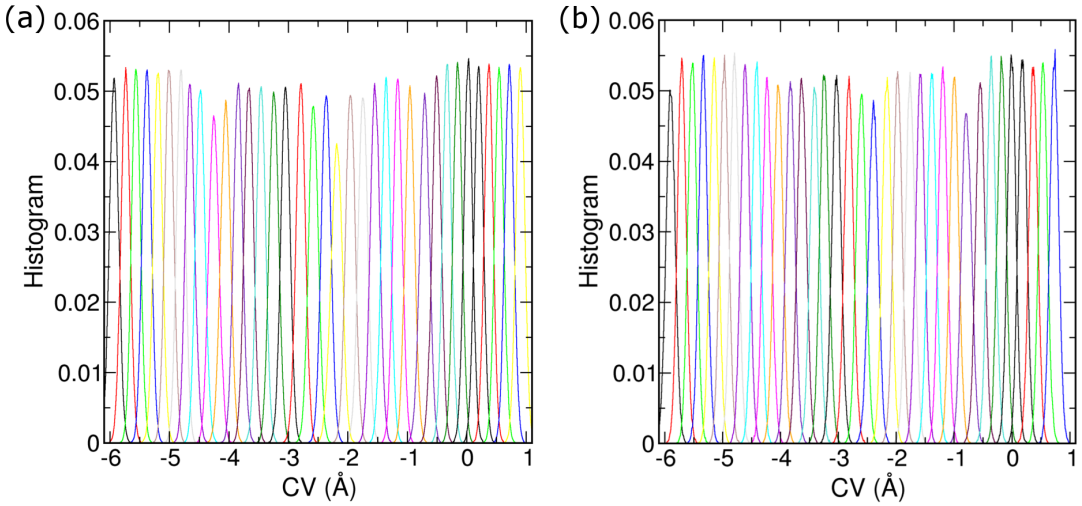

Figure B.15: The histograms of the collective variable (CV) for all the windows of (a) intraline hop, and (b) interline hop. The histograms of neighboring windows show good overlap which is necessary for smooth convergence of the free energy profile using WHAM.

These hop trajectories are then used to estimate the free energy profiles by using the Umbrella Sampling method [14]. The same distance collective variable used in the metadynamics step was used. A total of 36 windows were created to sample the collective variable from -6 Å to +1 Å with 0 Å indicating the defect position. The starting configurations for each window was sampled from a metadynamics run as shown in Figure B.15. Each window was run for 1 ns with the collective variable sampled every 1 fs. A harmonic restraint with a force constant of 40000 kJ/nm^2 was used to sample each window. Weighted Histogram Analysis Method (WHAM) was used to construct the free energy profile from the individual window histograms [15]. All the simulations are run in NVT ensemble at 303 K in order to enable a direct comparison with the liquid phase hopping. The umbrella sampling and metadynamics simulations were run using GROMACS [16–18] patched with the open-source, community developed PLUMED library [19], version 2.4.4 [20].

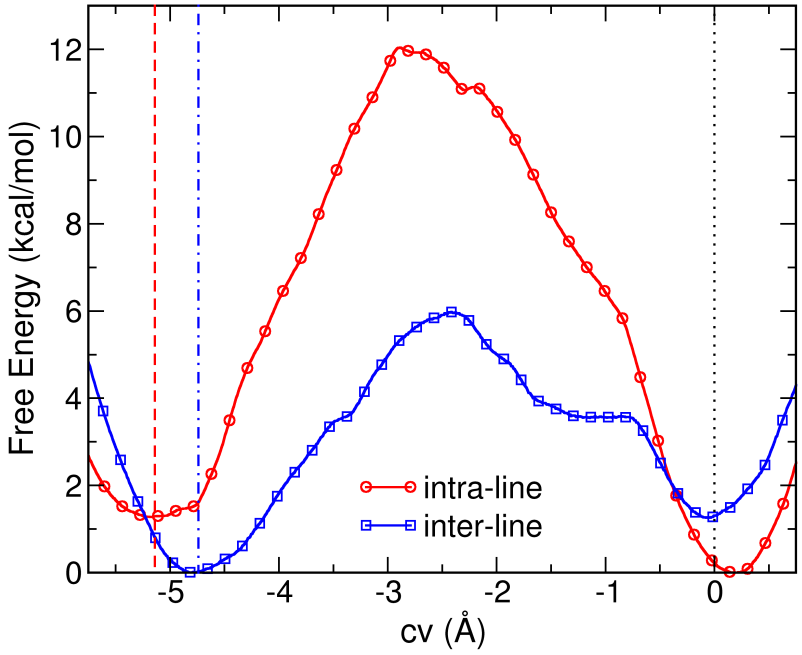

Figure B.16: The free energy profile of a Li-ion's intra-line hop (red) and inter-line hop (blue). The collective variable is the distance of the hopping Li-ion from the defect position along the hopping direction. The vertical black dotted line shows the defect position (0 Å). The red and blue vertical lines show the intra-line (5.14 Å) and inter-line Li-Li (4.74 Å) distance. The error bars are within the symbol size and are hence not shown.

Figure B.16 compares the free energy profile of intra-line (BF_4 bridged) and inter-line (SUL bridged) hops. The intra-line hop being longer, shows a barrier height of 50 kJ/mol when compared to 25 kJ/mol barrier height for the inter-line hop. This would mean that inter-line hops are more favorable in the crystal phase, consistent with our observations of the equilibrium NVT trajectory of the defective crystal, where only inter-line hops were observed in 100 ns (data not shown). In the context of hopping in HCEs, these results indicate that a variety of hop types can be operating simultaneously each with its own transition state and barrier height.

B.2.10 Details for the cage-relaxation time correlation functions

The continuous cage-relaxation time correlation function we use is defined in Equation A-10.

$$S(t) = \langle s(t_0 + t)m(t_0 + t)\rangle \tag{A-10}$$

$s(t_0 + t)$ is assigned a value of 1, if the nearest neighbors to a Li-ion at time $t_0 + t$ were exactly the same as those at time t_0. In other words, $s(t_0 + t)$ = 1, if the composition of the cage of the Li-ion is exactly the same at time t_0 and time $t_0 + t$. Else $s(t_0 + t)$ is assigned a value, 0. $m(t_0 + t)$ is assigned a value 1, if the composition of a Li-ion cage is exactly the same at every timestep in the interval, from time t_0 up to $t_0 + t$. Here $\langle\rangle$ refers to an average over all time origins for a time interval of t and an average over all Li-ions present in the system. Whether a ligand atom is a nearest neighbor of a Li-ion is decided by imposed cut-offs. In line with the Li-O and Li-F g(r)s in Figures B.10(c)&(e), the cut-off distances used for oxygen and fluorine atoms are 2.5 Å and 2.3 Å, respectively. $S(t)$ depends on the time between two consecutive snapshots. To obtain the most accurate continuous cage relaxation time correlation function, the time gap between two frames in this analysis was chosen to be the same as the MD timestep., i.e, 1 fs.

The intermittent cage-relaxation time correlation function, $C(t)$, allows for instantaneous changes in the coordination shell members of Li-ions and is defined in Equation A-11. The time gap between two frames for this calculation was taken to be 5 ps.

$$C(t) = \langle s(t_0 + t)\rangle \tag{A-11}$$

$S(t)$ and $C(t)$ were fit as in Equation A-12.

$$f(t) = \sum_{i=1}^{N} A_i e^{\frac{-t}{\tau_i}} \tag{A-12}$$

The fit for two representative salt concentrations is shown in Figure B.17. The fit parameters, A_i and τ_i are tabulated in Tables B.7 and B.8.

The continuous cage relaxation function S(t) (Eq. 4C.5) decays much faster at 1.00 M (5 ps) than at 5.76 M (16 ps) (Figure B.17 (a)). Unlike S(t), C(t) allows for reformation of the cage. The mean cage relaxation time at 5.76 M extracted from C(t) (300 ns) (Figure B.17(b)) is three orders of magnitude larger than than at 1 M (0.1 ns). Interestingly, it is from the order or magnitude of tens of nanoseconds onwards that the mildest features of hopping start to become evident in G_s(r,t) of 5.76 M (see Figure 2(b)). The huge increase in the mean cage relaxation time (intermittent) at 5.76 M concentration over the value at 1 M concentration is primarily due to the longest time component, τ_4 which is 470 ns and also

has a significant weight (around 62%). This component is contributed by molecules in the first coordination shell which diffuse out afar to later become part of the cage of the same lithium ion. Its significant increase arises from the rather slow, low wave vector viscous modes. Quantitative examination of these modes is beyond the scope of the current work. The ligand reaction times of 60-120 ps estimated in Ref. 21 falls between the mean cage relaxation times obtained from the continuous and intermittent cage lifetime correlation functions. Thus, although the first solvation Li-O and Li-F distances at these two concentrations are similar (Figure B.10 (c)-(f)), Li-ion cages at 5.76 M are much longer-lived than at 1 M.

Parameter	Concentration 5.76 M	Concentration 1.00 M
A_0	0.277	0.304
τ_0 (ps)	2.7	2.4
A_1	0.255	0.336
τ_1 (ps)	0.4	0.4
A_2	0.468	0.360
τ_2 (ps)	32.5	12.4
$\langle\tau\rangle$ (ps)	16.1	5.3

Table B.7: Fit parameters according to Equation A-12 for $S(t)$ data

Parameter	Concentration 5.76 M	Concentration 1.00 M
A_0	0.256	0.392
τ_0 (ps)	1.3	1.5
A_1	0.032	0.199
τ_1 (ps)	332.4	261.0
A_2	0.023	0.232
τ_2 (ps)	38.3	72.5
A_3	0.059	0.140
τ_3 (ps)	2610.3	15.2
A_4	0.629	0.037
τ_4 (ps)	470824.5	780.1
$\langle\tau\rangle$ (ps)	296494.1	100.2

Table B.8: Fit parameters according to Equation A-12 for $C(t)$ data

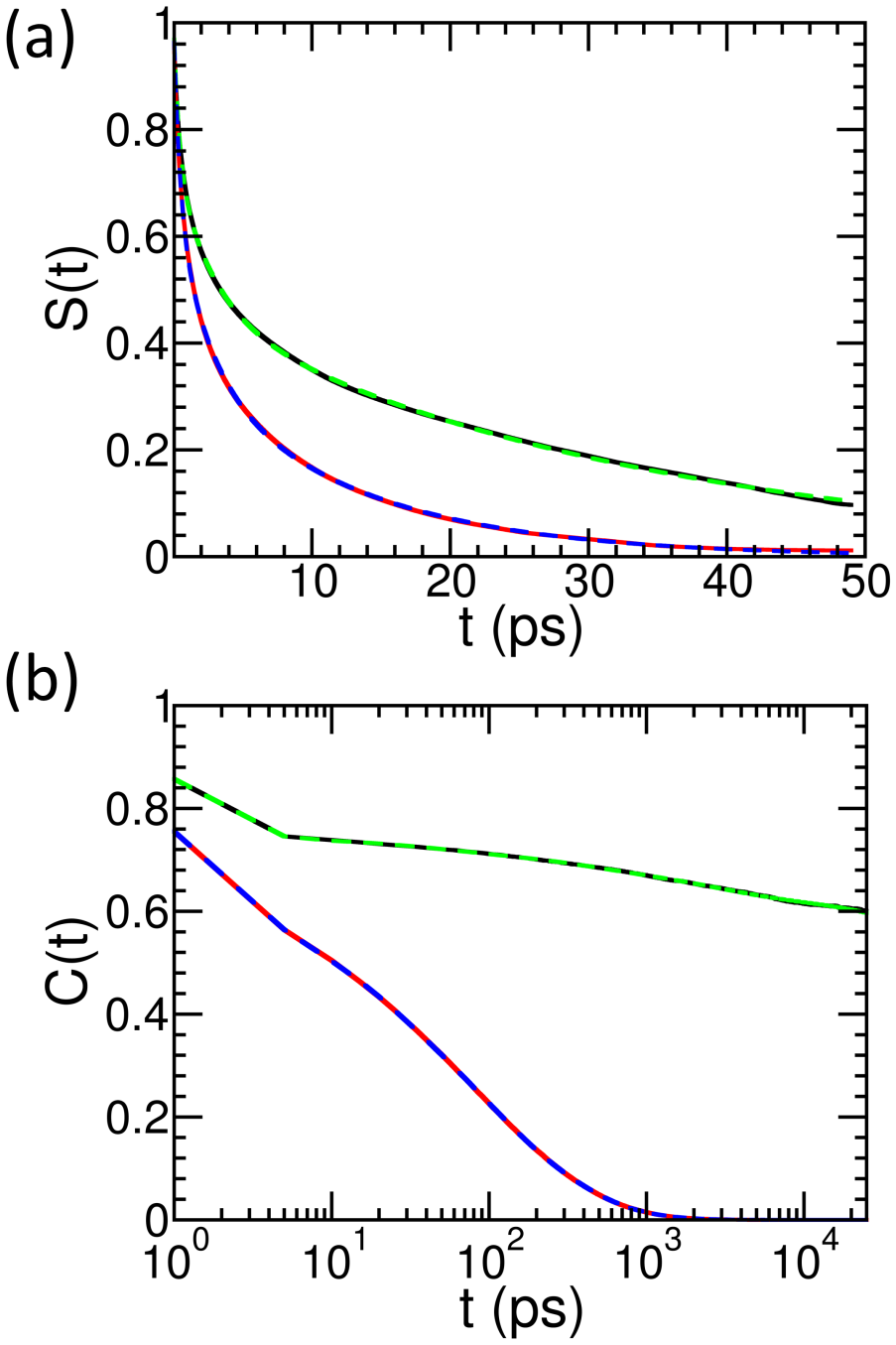

Figure B.17: Cage relaxation time correlation functions at two prototypical concentrations with functional fits. (a) Continuous cage relaxation time correlation function, $S(t)$, and (b) Intermittent cage relaxation time correlation function, $C(t)$. Black - 5.76 M and red - 1.00 M. Dashed lines are fits to the data.

B.2.11 Velocity time auto-correlation function (VACF)

The VDOS of Li ions (Figure B.18(b)) in the far-infrared region displays a hardening of the cage surrounding the ion, with increasing salt concentration, reflected as a blue shift in the low frequency feature. This is a consequence of the increased "clarity" of the Li-B g(r) as seen in Figure B.11(a). The same is also reflected in the VACF of the BF_4 anion (Figure 1.12(c)), where one finds the frequency of oscillations in the VACF to increase with salt concentration. The VACF for sulfolane is nearly independent of salt concentration, as the molecule, being large, barely interacts significantly with the ions.

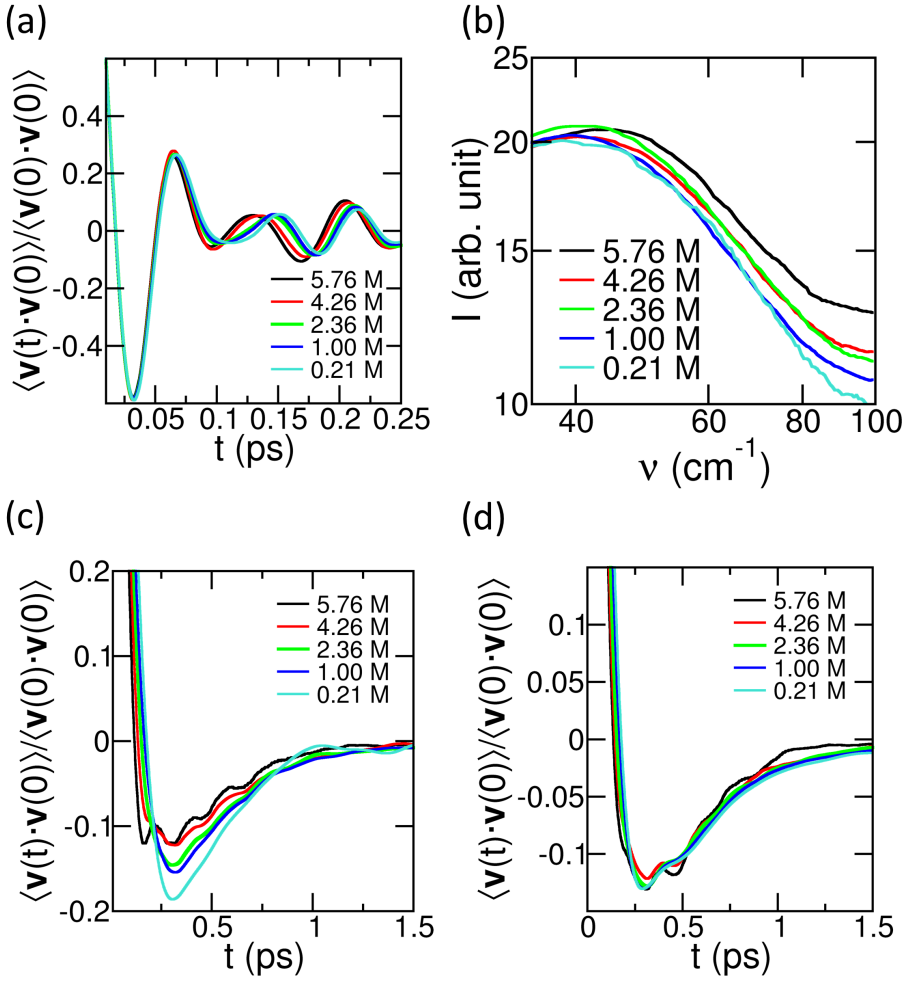

Figure B.18: Comparison of VACF at some representative salt concentrations. (a) Li-ion velocity auto-correlation function, (b) Vibrational density of states (VDOS) of Li-ions, obtained as the Fourier Transform of VACF, (c) BF_4 anion velocity auto-correlation, and (d) Sulfolane COM velocity auto-correlation function.

Bibliography

[1] Kaoru Dokko, Daiki Watanabe, Yosuke Ugata, Morgan L Thomas, Seiji Tsuzuki, Wataru Shinoda, Kei Hashimoto, Kazuhide Ueno, Yasuhiro Umebayashi, and Masayoshi Watanabe. Direct evidence for Li ion hopping conduction in highly concentrated sulfolane-based liquid electrolytes. *The Journal of Physical Chemistry B*, 122(47):10736–10745, 2018.

[2] Srimayee Mukherji, Nikhil VS Avula, and Sundaram Balasubramanian. Refined force field for liquid sulfolane with particular emphasis to its transport characteristics. *ACS Omega*, 5(43):28285–28295, 2020.

[3] Francisca Maria Rodrigues Mesquita, Filipe Xavier Feitosa, Martin Aznar, Hosiberto B de Sant'Ana, and Rílvia S Santiago-Aguiar. Density, viscosities, and excess properties for binary mixtures of sulfolane+ alcohols and sulfolane+ glycols at different temperatures. *J. Chem. Eng. Data*, 59(7):2196–2206, 2014.

[4] Wei Zhao, Frédéric Leroy, Berit Heggen, Stefan Zahn, Barbara Kirchner, Sundaram Balasubramanian, and Florian Müller-Plathe. Are there stable ion-pairs in room-temperature ionic liquids? Molecular dynamics simulations of 1-n-butyl-3-methylimidazolium hexafluorophosphate. *Journal of the American Chemical Society*, 131(43):15825–15833, 2009.

[5] Oleg Borodin, Liumin Suo, Mallory Gobet, Xiaoming Ren, Fei Wang, Antonio Faraone, Jing Peng, Marco Olguin, Marshall Schroeder, Michael S Ding, et al. Liquid structure with nano-heterogeneity promotes cationic transport in concentrated electrolytes. *ACS Nano*, 11(10):10462–10471, 2017.

[6] Fangfang Chen, Patrick Howlett, and Maria Forsyth. Na-ion solvation and high transference number in superconcentrated ionic liquid electrolytes: a theoretical approach. *The Journal of Physical Chemistry C*, 122(1):105–114, 2018.

[7] F Wohde, M Balabajew, and B Roling. Li^+ Transference Numbers in Liquid Electrolytes Obtained by Very-Low-Frequency Impedance Spectroscopy at Variable Electrode Distances. *Journal of The Electrochemical Society*, 163(5):A714, 2016.

[8] Junko Habasaki, Carlos Leon, and KL Ngai. *Dynamics of Glassy, Crystalline and Liquid Ionic Conductors: Experiments, Theories, Simulations*, volume 132. Springer, 2016.

[9] Christopher Jarzynski. Nonequilibrium equality for free energy differences. *Physical Review Letters*, 78(14):2690, 1997.

[10] Christopher Jarzynski. Equilibrium free-energy differences from nonequilibrium measurements: A master-equation approach. *Physical Review E*, 56(5):5018, 1997.

[11] Jan Liphardt, Sophie Dumont, Steven B Smith, Ignacio Tinoco Jr, and Carlos Bustamante. Equilibrium information from nonequilibrium measurements in an experimental test of Jarzynski's equality. *Science*, 296(5574):1832–1835, 2002.

[12] Sanghyun Park, Fatemeh Khalili-Araghi, Emad Tajkhorshid, and Klaus Schulten. Free energy calculation from steered molecular dynamics simulations using jarzynski's equality. *The Journal of Chemical Physics*, 119(6):3559–3566, 2003.

[13] Alessandro Laio and Michele Parrinello. Escaping free-energy minima. *Proceedings of the National Academy of Sciences*, 99(20):12562–12566, 2002.

[14] Johannes Kästner. Umbrella sampling. *WIREs Computational Molecular Science*, 1(6):932–942, 2011.

[15] Alan Grossfield. WHAM: the weighted histogram analysis method.

[16] Henk Bekker, HJC Berendsen, EJ Dijkstra, S Achterop, R Vondrumen, David VANDERSPOEL, A Sijbers, H Keegstra, and MKR Renardus. Gromacs-a parallel computer for molecular-dynamics simulations. In *4th International Conference on Computational Physics (PC 92)*, pages 252–256. World Scientific Publishing, 1993.

[17] Berk Hess, Carsten Kutzner, David Van Der Spoel, and Erik Lindahl. Gromacs 4: algorithms for highly efficient, load-balanced, and scalable molecular simulation. *Journal of Chemical Theory and Computation*, 4(3):435–447, 2008.

[18] Mark James Abraham, Teemu Murtola, Roland Schulz, Szilárd Páll, Jeremy C Smith, Berk Hess, and Erik Lindahl. GROMACS: High performance molecular simulations through multi-level parallelism from laptops to supercomputers. *SoftwareX*, 1:19–25, 2015.

[19] Massimiliano Bonomi, Giovanni Bussi, Carlo Camilloni, Gareth A. Tribello, Pavel Banáš, Alessandro Barducci, Mattia Bernetti, Peter G. Bolhuis, Sandro Bottaro, Davide Branduardi, Riccardo Capelli, Paolo Carloni, Michele Ceriotti, Andrea Cesari, Haochuan Chen, Wei Chen, Francesco Colizzi, Sandip De, Marco De La Pierre, Davide Donadio, Viktor Drobot, Bernd Ensing, Andrew L. Ferguson, Marta Filizola, James S. Fraser, Haohao Fu, Piero Gasparotto, Francesco Luigi Gervasio, Federico Giberti, Alejandro Gil-Ley, Toni Giorgino, Gabriella T. Heller, Glen M. Hocky, Marcella Iannuzzi, Michele Invernizzi, Kim E. Jelfs, Alexander Jussupow, Evgeny Kirilin, Alessandro Laio, Vittorio Limongelli, Kresten Lindorff-Larsen, Thomas Löhr, Fabrizio Marinelli, Layla Martin-Samos, Matteo Masetti, Ralf Meyer, Angelos Michaelides, Carla Molteni, Tetsuya Morishita, Marco Nava, Cristina Paissoni, Elena Papaleo, Michele Parrinello, Jim Pfaendtner, Pablo Piaggi, GiovanniMaria Piccini, Adriana Pietropaolo, Fabio Pietrucci, Silvio Pipolo, Davide Provasi, David Quigley, Paolo Raiteri, Stefano Raniolo, Jakub Rydzewski, Matteo Salvalaglio, Gabriele Cesare Sosso, Vojtěch Spiwok, Jiří Šponer, David W. H. Swenson, Pratyush Tiwary, Omar Valsson, Michele Vendruscolo, Gregory A. Voth, Andrew White, and The PLUMED consortium. Promoting transparency and reproducibility in enhanced molecular simulations. *Nature Methods*, 16(8):670–673, Aug 2019.

[20] Gareth A. Tribello, Massimiliano Bonomi, Davide Branduardi, Carlo Camilloni, and Giovanni Bussi. Plumed 2: New feathers for an old bird. *Computer Physics Communications*, 185(2):604 – 613, 2014.

[21] Masaki Okoshi, Chien-Pin Chou, and Hiromi Nakai. Theoretical analysis of carrier ion diffusion in superconcentrated electrolyte solutions for sodium-ion batteries. *The Journal of Physical Chemistry B*, 122(9):2600–2609, 2018.

List of Publications

1. Refined Force Field for Liquid Sulfolane with Particular Emphasis to Its Transport Characteristics.
   Mukherji, S; Avula N. V. S.; Balasubramanian, S*. *ACS Omega* **2020**, *5*, 28285–28295.

2. Hopping in High Concentration Electrolytes - Long Time Bulk and Single-Particle Signatures, Free Energy Barriers, and Structural Insights
   Mukherji, S; Avula N. V. S.; Kumar, R; Balasubramanian, S*. *J. Phys. Chem. Lett.* **2020**, *11*, 9613–9620.
   Erratum: Correction to "Hopping in High Concentration Electrolytes - Long Time Bulk and Single-Particle Signatures, Free Energy Barriers, and Structural Insights"
   Mukherji, S; Avula N. V. S.; Kumar, R; Balasubramanian, S*. *J. Phys. Chem. Lett.* **2020**, *11*, 10283–10283.

3. Two for one: propylene carbonate co-solvent for high performance aqueous zinc-ion batteries – remedies for persistent issues at both electrodes
   Kakoty, B; Vengarathody, R; **Mukherji, S**; Ahuja, V; Joseph, A; Narayana, C; Balasubramanian, S; Senguttuvan, P*. *J. Mat. Chem. A* **2022**, *10*, 12597-12607.

4. Enhancement of Transport Properties of Sodium High Concentration Electrolytes Through Lithium Doping: A Study of Mixed Alkali High Concentration Electrolytes
   Mukherji, S; Balasubramanian, S*. (Manuscript under preperation)

5. Study of Cation Pair Clusters in High Concentration electrolytes
   Mukherji, S; Brahma, D; Balasubramanian, S*. (Manuscript under preperation)

6. **Miscellaneous publication**: Strength of Mechanical Memories is Maximal at the Yield Point of a Soft Glass
   Mukherji, S*; Kandula, N; Sood, A. K.; Ganapathy, R* *Phys. Rev. Lett.*, **2019**, *122*, 158001.

Erratum

- In Chapter 4A, page 109, the following sentence was added: *"In this sub-chapter, the results from two force fields, viz., charge-scaled CL&P and the refined force field, were reported. The dihedral energy functional forms of the two force-fields are different. Therefore, the functional form for this term has not been included in Equation 4A.1. Under the heading "Refinement of dihedral parameters", please refer to Equations 4A.2 and Equation 4A.3 for the dihedral energy functional forms for charge scaled CL&P and the refined force field reported here, respectively."*

- In Chapter 4A, on page 113, the following sentence was added: *This functional form takes the place of the dihedral energy term in Equation 4A.1 for the charge-scaled CL&P force field.*

- In Chapter 4A, on page 114, the following sentence was added just before Equation 4A.3: *This functional form takes the place of the dihedral energy term in Equation 4A.1 for the refined force field.*

- On page 130, the following sentences have been added below Table 4B.9. *The transference numbers reported in Tables 4B.7, 4B.8, 4B.9 do not account for correlations between non-self ion-displacements. These have been calculated using self-diffusion coefficients alone. The true transference numbers ($t_{+,correlated}$) account for these correlations [54]. $t_{+,correlated}$ can be defined as : $t_{+,correlated} = \frac{\sigma_{--}\sigma_{++}-{\sigma_{+-}}^2}{\sigma_{--}(\sigma_{++}+\sigma_{--}-2\sigma_{+-})}$ [55]. Here, σ_{++}, σ_{--}, and σ_{+-} are the three components of ionic conductivity or the transport coefficients stemming from cation-cation, anion-anion, and cation-anion displacement correlations, respectively. The calculation of $t_{+,correlated}$ requires multiple (of the order of 50), and long (hundreds of nanoseconds to microseconds) trajectories. These simulations and calculations would be too computationally expensive and were therefore beyond the scope of the thesis.*

- One page 156, the following sentences have been added below Table 4C.12. *The transference numbers reported in Tables 4C.10, 4C.11, 4C.12 do not account for correlations between non-self ion-displacements. These have been calculated using*

self- diffusion coefficients alone. The true transference numbers account for these correlations. The calculation of this quantity requires multiple (of the order of 50), and long (hundreds of nanoseconds to microseconds) trajectories. These simulations and calculations would be too computationally expensive and were therefore beyond the scope of the thesis.

- Figure 5.9 on page 200 has been corrected.

- On page 259, the following sentences have been added below Table B.6 in Appendix B. *The transference numbers reported in Table B.6 do not account for correlations between non-self ion-displacements. These have been calculated using self-diffusion coefficients alone. The true transference numbers ($t_{+,correlated}$) account for these correlations. $t_{+,correlated}$ can be defined as : $t_{+,correlated} = \frac{\sigma_{--}\sigma_{++}-\sigma_{+-}{}^2}{\sigma_{--}(\sigma_{++}+\sigma_{--}-2\sigma_{+-})}$ [7]. Here, σ_{++}, σ_{--}, and σ_{+-} are the three components of ionic conductivity or the transport coefficients stemming from cation-cation, anion-anion, and cation-anion displacement correlations, respectively. The calculation of $t_{+,correlated}$ require multiple (of the order of 50), and long (hundreds of nanoseconds to microseconds) trajectories. These simulations and calculations would be too computationally expensive and were therefore beyond the scope of the thesis.*